Characterisation and Rapid Purification of a Superconducting Charge Qubit

Thesis submitted in accordance with the requirements of
the University of Liverpool for the degree of Doctor in Philosophy
by
Elias James Griffith

April 2007

Abstract

The work of this thesis focuses on stochastic methods for the simulation of superconducting charge qubits, also known as Cooper pair boxes, which are promising candidates for large scale quantum information processing. To aid non-physicists, a brief outline of the structure of quantum mechanics is provided using the Dirac formalism.

Using the so called 'Backreaction effect', we consider if any information can be obtained regarding the qubit behaviour, through detecting the changes observed in the frequency spectrum of the coupled biasing circuitry, modelled as a dissipative oscillator circuit. The process of modelling dissipative quantum systems is described, however an alternative approach called 'quantum trajectories' is used rather than the traditional Calderia-Leggett model, as the time evolution of a single 'trajectory' represents the evolution of an individual system coupled to a noisy environment. Through the noise generated by an excited qubit, the energy level structure of the qubit can be probed with a microwave drive field, by observing the noise power within the biasing circuit. We consider a biasing circuit of unusually high resonant frequency which can drive the qubit, this creates frequency splitting features that would not normally be observed.

Weak measurement is also examined as this is closely related to the stochastic 'quantum trajectories', where the measurement is recorded by the observer rather than lost to an environment. Weakly measuring a qubit does not completely collapse it and therefore 'quantum feedback' may be employed to alter the qubit controls favourably. In particular we consider the problem of purifying a weakly measured system rapidly; given a qubit in the completely mixed state what is the best feedback to become confident in the actual qubit state quickly. There are two optimal feedback protocols proposed by Jacobs [1] and by Wiseman and Ralph [2] for purifying qubits that have ideal controls. However, we adapt these protocols for the charge qubit, whose finite Hamiltonian resources and non-zero σ_x tunnelling term means the Bloch vector can not be easily held in the optimal location.

Contents

List of Figures

Acknowledgements

I would like to thank my mother and father for encouraging and looking after me so far, and also for letting me lurk around the house for three years longer than they needed to. I would also like to thank my PhD supervisor Jason Ralph, who has always been able to solve any problems I have had, and for better or for worse has encouraged my public speaking at conferences. I also thank the ever enthusiastic Charles Hill who has always patiently explained difficult concepts with practical examples.

I finally thank my fellow PhD students for being such interesting and welcome diversions from my work!

Chapter 1

Introduction

1.1 Why is quantum computation necessary?

Quantum computing is necessary because it allows a particular group of problems to be solved exponentially faster compared with using classical computers. Originally, these problems were limited to the world of quantum physics, as Richard Feynman suggested in 1982 that a quantum computer could be used to efficiently simulate quantum mechanical systems [9]. However, during the 1990's three *quantum algorithms* were designed which suggested that quantum computers could be used to solve problems that would be impractical for classical computers, these problems are of particular interest to governments and financial institutions as they both solve *and* create security related issues. Ignoring the complexities of building a classical parallel computer, if ten classical computers are working in parallel to solve a problem, then adding another computer should ideally increase the computation power by 10% as another storage element is ready for useage, this can be thought of as adding an extra axis (or dimension) to a ten dimenional space which is searched by the computer(s) for a solution. However, if ten quantum bits, or 'qubits', are working on the same problem and another qubit is added, the computation power *doubles* as the number of storage elements or dimensions *doubles*. This doubling of the so called *Hilbert space* for each qubit added allows an exponential number of axes to be examined simultanteously, for N qubits there are 2^N axes in the Hilbert space, wheras for a classical computer with N units there are only N axes. The vast number of axes can not all be measured at once, and in the physical world measuring a quantum computer yields a random result. However the quantum algorithms aim to maximise the probability of selecting the correct answer, hence the difficulty in designing suitable algorithms.

But why is building a working quantum computer so important that it attracts

interest from commercial companies and governments? There are at least two main reasons; Quantum cryptography and Shor's algorithm.

Quantum cryptography uses the property of entanglement and the random result of a measurement to infer the presence of eavesdroppers listening on a supposedly secure channel by detecting an unusual increase in the number or errors, this system would be indeed useful for banking and military communications. As these experiments are relatively basic compared with a many qubit quantum computer and can be done at room temperature with commercially available components, a working device has already been designed and marketed by French company MagiQ [10].

Most of the world's encryption schemes rely in some way on the difficulty of factoring large numbers, an example is the RSA 'public key' encryption system [11] creates the keys from numbers A, B and C where $A \times B = C$. The number C is transmitted along with an *encryption key* E created from A and B. The *decryption key* D is kept secret and can only be recreated by knowing A or B, hence if a computer can solve $A \times B = C$ to find A and B from C the message can be decoded by recreating decryption key D. The consequences of banking and miliary details being uncovered could give an organisation or government an advantage. In 1994 Peter Shor designed an algorithm which could factor numbers exponentially faster than classical algorithms, hence an encryption scheme that could take millions of years to decode could be broken in a matter of hours. Exposing banking, military and government secrets.

1.2 Quantum notation

The mathematics of quantum mechanics is examined further in chapter 2 however a brief overview is provided here to aid reading of the following material.

Dirac notation is a concise method used to write quantum states, $|0\rangle$ and $|1\rangle$ are called *kets* and are used to represent the *zero* and *one* quantum states. If a qubit with the $|0\rangle$ state is measured the outcome will always be 'zero', likewise $|1\rangle$ yields 'one', in general $|a\rangle$ will yield outcome 'a'. Alternatively, *bras* can be used to the same effect. Where $\langle 0|$, $\langle 1|$ and $\langle a|$ are the equivalent bras for the previous examples. The bra-ket relation $\langle X| = |X\rangle^\dagger$ is defined by the Hermitian conjugate $\dagger$. The Hermitian conjugate is the complex conjugate followed by a transpose (or vice versa).

Composite systems of more than one qubit are simply bras or kets containing a string representing the state of a set of qubits. For example, $|00010\rangle$ means all

the qubits are in the zero state except the fourth qubit which is in state $|1\rangle$.

Qubits can hold superpositions of $|0\rangle$ and $|1\rangle$, this is written as $\alpha|0\rangle + \beta|1\rangle$, if this qubit is measured it will yield either the outcome $|0\rangle$ with probability $|\alpha|^2$ or the outcome $|1\rangle$ with probability $|\beta|^2$. When composite systems are involved this is called *entanglement*, this increases the number of coefficients dramatically which gives quantum computers their potential power, for two qubits there are now four coefficients on the two physical devices. $\alpha|00\rangle + \beta|10\rangle + \gamma|01\rangle + \delta|11\rangle$.

Operators act on states, transforming them to new states. *Unitary* operators change the state coefficients (α and β) without affecting the overall magnitude of the state, so that the state probabilities ($|\alpha|^2$ and $|\beta|^2$) sum to one. Unitary operators cause rotations of the state vector. Other operators can be use to measure the system, these operators tend to have real eigenvalues are these correspond to physically measurable outcomes, such operators are called *Hermitian.*

1.3 Quantum computation algorithms

The design of quantum algorithms has proved very difficult as the result of over 20 years of research as only yielded three algorithms that are more efficient than their classical counterparts; The Deutsch-Jozsa algorithm [12], Shor's algorithm [13] and Grover's algorithm [14]. Despite this, there is considerable interest from government and commercial organisations to fund quantum computing research, this is mostly due to Shor's algorithm, which promises to break cryptographic schemes such as RSA [11] which are currently used for secure banking.

1.3.1 The Deutsch-Jozsa algorithm

The first quantum algorithm was designed in 1992 by David Deutsch and Richard Jozsa [12], it is the simplest of the three known quantum algorithms.

It solves a very specific problem: The experimentalist must decide if a black box is *constant* or *balanced.* If the box is *constant* then **all** the outputs are either 0 or 1. If the box is *balanced* then half are 0 and half are 1, over the input range (limited by the number of input wires).

Classically, this can be solved by either stepping through all possible inputs or by using randomly selected inputs, but as at least half the 2^N input range needs to be searched to confirm that either half are zeros or all the same value, this can be a slow process.

Whereas classically $2^{N-1} + 1$ steps are required to examine just over half the possible combinations, the Deutsch-Jozsa algorithm can determine *constant*

or *balanced* boxes with 100% certainity using just a single step (Note that the quantum result is deterministic, repeated measurements are **not** required for this algorithm!).

The algorithm makes use of the Hadamard gate, which is used to setup superpositions on all the inputs. The Hadamard gate is defined as a matrix as follows:

$$H = \frac{1}{\sqrt{2}} \begin{pmatrix} 1 & 1 \\ 1 & -1 \end{pmatrix} \tag{1.1}$$

Algorithm - [15]

1. Initialise $N+1$ qubits to $|00.....0\rangle$.

2. The Hadamard gate is applied to $N+1$ qubits to create a superposition state on N qubits corresponding to N input wires, and a $|1\rangle$ state which will be the answer qubit.

3. The experimenter needs to send the entangled state through the black box which will either contain gates to simulate a classical balanced box, or a (time delayed) pass-through to simulate the constant box. This is implemented as a function controlled phase shift:

$$|x\rangle \rightarrow (-1)^{f(x)}|x\rangle \tag{1.2}$$

4. Apply another Hadamard gate to the qubits.

5. Measure the answer qubit, if the result is 0 then the box was constant else if the result is 1 the box was balanced.

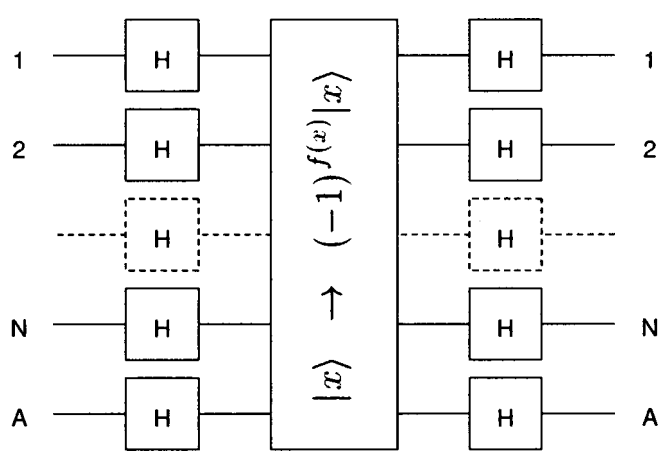

Figure 1.1: Quantum circuit for the Deutsch-Jozsa algorithm. Hadamard gates are applied at the first and last stage of the algorithm. Qubit **A** is measured to produce the answer.

1.3.2 Shor's algorithm

After 1994, Shor's algorithm was responsible for significant investment in the area of quantum computation, without it quantum computation would surely remain just an interesting concept. The reason why it is so important is that commercial cryptographic schemes rely on the difficulty of factoring numbers into their prime components, Shor's algorithm represents a threat as the factoring problem can be rephrased so a quantum computer can use the inverse quantum Fourier transform to search for factors with great speed. If numbers could be factored easily every banking transaction or military communication could be compromised.

The algorithm was verified experimentally in 2001 on a seven qubit NMR quantum computer [16], where the number 15 was factored into 5 and 3.

Multiplying two numbers is easy $A \times B = C$. However, only given C it is difficult to find the two numbers A and B that were multiplied to obtain C. Although many numbers can be factored in several ways, for example the number 12 can be factored into 2×6, $2 \times 2 \times 3$ and 3×4, however cryptographic schemes such as RSA [11] use the indivisible property of prime numbers to limit the factoring problem to two prime numbers, for example $77 = 7 \times 11$ has no other combination, given 77 and 7 it is very easy to find the third number 11. For very large numbers this problem becomes almost impossible classically without knowing two of the numbers, so one number can be kept secret whilst another is made public. It is the large size of the numbers involved (1024bit to 2048bit for current RSA) that prevents factoring with classical computers for decryption proposes.

In 1994 Peter Shor noticed that the quantum Fourier transform could be used once the factoring problem has been re-expressed as a period finding problem, hence Shor's algorithm has classical and quantum parts.

Algorithm - Factoring N [15]

1. (*Classical*) To ensure that the number we are trying to factor (N) is actually worth factoring, a random number R is generated between 0 and N and the greatest common divisor (GCD) between R and N is calculated. If $GCD(R, N) = 1$ then R is not a factor of N and can be used to seed the remainder of the algorithm.

2. (*Classical*) Assuming there must be only two factors. We can define a function whose period is related to N, Shor uses an exponential function which is modulo

N.

$$f(x) \;=\; R^x \pmod{N} \tag{1.3}$$

It is necessary to find T such that $f(x+T) = f(x)$, i.e. the period.

3. (*Quantum*) The inverse quantum Fourier transform is used to solve this. Create a composite system with a register of input $\log_2(N)$ qubits in the superposition state and an array of $\log_2(N)$ output qubits set to zero.

$$|\psi\rangle = \frac{1}{\sqrt{N}} \sum_x |x\rangle|0\rangle \tag{1.4}$$

The output qubits are modified such that they now store the quantum function $f(x)$, so there is now an x and y axis as it were.

$$|\psi\rangle = \frac{1}{\sqrt{N}} \sum_x |x\rangle|f(x)\rangle \tag{1.5}$$

The quantum Fourier transform is applied

$$U_{QFT}|x\rangle = \frac{1}{\sqrt{N}} \sum_y \exp\left(-i2\pi \frac{xy}{N}\right) |y\rangle \tag{1.6}$$

which leaves the system in a state that maxismises the probability that the output register contains the period T when the state is collapsed at measurement.

4a. (*Classical*) Checking T: If T is odd, then goto step 1. As $R^{\frac{T}{2}}$ required later would pose problems related to the square root.
4b. (*Classical*) Checking T: If T is even, then check $R^{\frac{T}{2}} = -1 \pmod{N}$, if this is true goto step 1.

5. (*Classical*) The factors of N should be $GCD(R^{\frac{T}{2}}+1, N)$ and $GCD(R^{\frac{T}{2}}-1, N)$.

The algorithm is an exponential speedup over classical equivalents, where the number of operations for Shor's algorithm is $(\log_2 N)^3$ operations.

1.3.3 Grover's algorithm

Grover's algorithm was designed by Lov Grover in 1997 [14], it is described as a searching algorithm, although the problem it actually solves is the repeated evaluation of a function $f(x)$ that yields a binary yes (1) or no (0) type answer (Eqs. 1.7 and 1.8). This repeated querying of the function $f(x)$ is akin to using 'brute force' methods to search for α, the correct value for x. By using Grover's algorithm, the average number of function evaluations required to find α is reduced from N to $\sqrt{N}$ queries.

$$f(x = \alpha) = 1 \tag{1.7}$$

$$f(x \neq \alpha) = 0 \tag{1.8}$$

The function $f(x)$ is represented by a unitary operator also known as the *oracle* which needs to satisfy the following:

$$\begin{aligned} U_o |x = \alpha\rangle &= -|x\rangle \\ U_o |x \neq \alpha\rangle &= |x\rangle \end{aligned} \tag{1.9}$$

This operator changes the phase of the α solution state by 180^o but does not affect the amplitude, also all the wrong solutions are not changed in any way. Each x value is assigned a state, therefore the number of searchable x values is limited by the number of qubits, where n qubits can evaluate 2^n possibilities.

$$|x\rangle = |0\rangle, |1\rangle, |2\rangle, \ldots |N-1\rangle \tag{1.10}$$

Algorithm - [15]

1. To start the algorithm a superposition of all possible states is created, so that the states are equiprobable (Fig. 1.2 **A1**).

2. The oracle operator U_o is applied to the array of qubits, this applies a 180^o phase shift to **only** the state amplitude corresponding to $|x = \alpha\rangle$, therefore this 'flips' a positive value to a negative value and vice versa (Fig. 1.2**A2**).

3. An operator U_m is now applied, as applying the oracle operator flip would undo the last step. This operator increases the magnitude of the state amplitude for $|x = \alpha\rangle$ and hence the increasing the probability of α being selected at measurement (Fig. 1.2 **A3**).

$$U_m = 2|\psi\rangle\langle\psi| - I \tag{1.11}$$

4. Repeat steps 2 and 3, for $\sqrt{N}$ iterations to ensure that the probability of selecting the correct state is maximised.

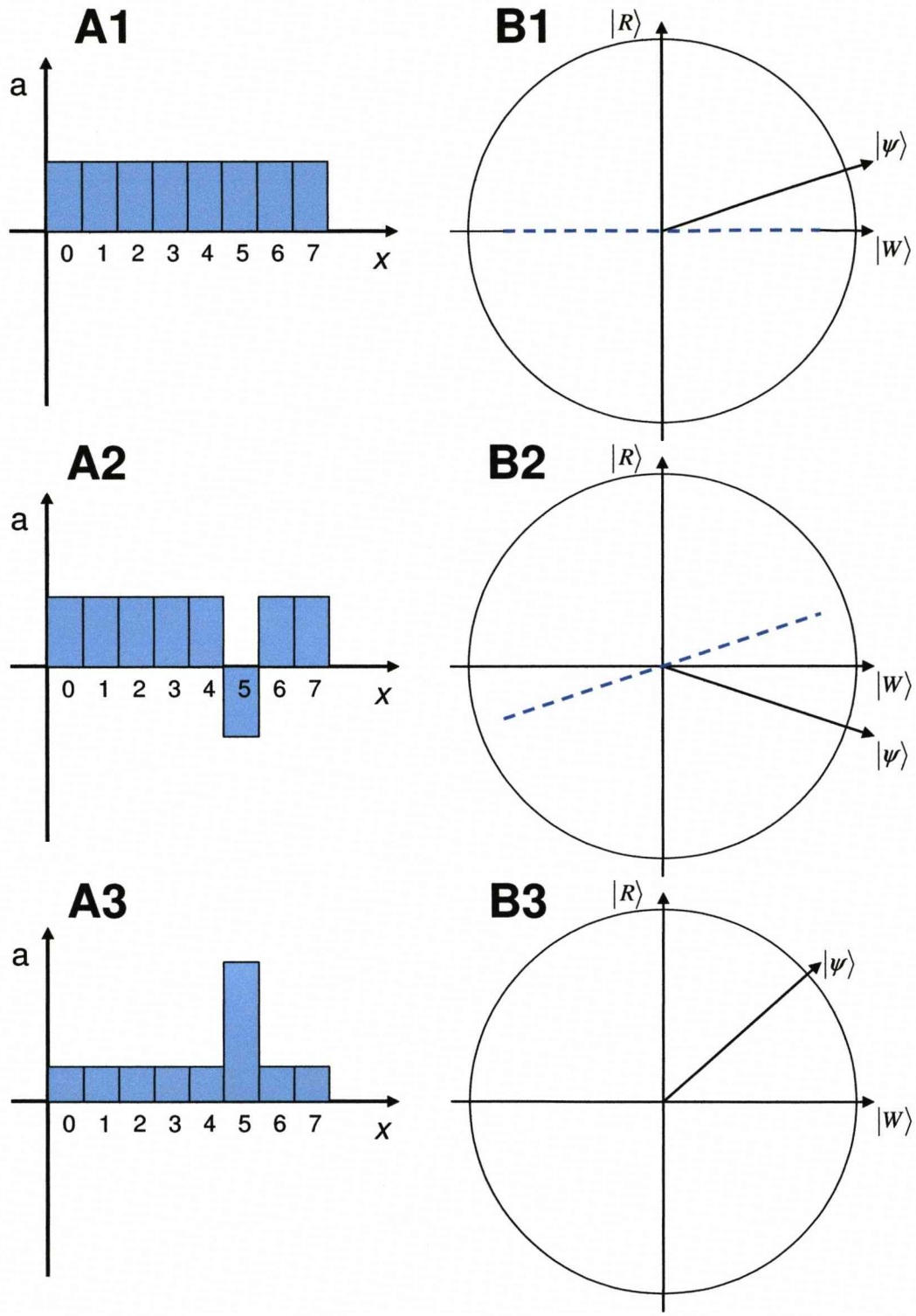

Figure 1.2: Two interpretations of Grover's algorithm for $\alpha = 5$. (**A**) Evolution of the individual state probabilities. (**B**) Grouping the $N = 8$ possible states into right $|R\rangle$ and wrong $|W\rangle$ states shows that Grover's algorithm gradually rotates the system state $|\psi\rangle$ towards the correct answer state $|R\rangle$, by reflecting the state about known axes, shown here as dashed lines.

An alternative explanation begins by grouping the N possible state vectors into two vectors 'right answers' $|R\rangle$ that satisfy equation 1.7, and 'wrong answers' $|W\rangle$ that satisfy equation 1.8. In this way, the problem can be simplified to two orthogonal vectors where the goal is to align the system state $|\psi\rangle$ with $|R\rangle$, (Fig. 1.2 **B1**).

Step 1 of the algorithm generates a superposition state which will contain many wrong answers and at least one correct answer, therefore the vector $|\psi\rangle$ will almost be in alignment with the 'wrong axis' $|W\rangle$, (Fig. 1.2 **B1**).

In step 2, the oracle operator U_o reflects the state vector $|\psi\rangle$ in the axis of all wrong answers $|W\rangle$ (as indicated by the blue dashed line in figure 1.2 **B1**), so there is a sign change in the $|R\rangle$ component of $|\psi\rangle$ (Fig. 1.2 **B2**).

It can now be seen that, applying operator U_o will undo the last step, so the system is now reflected about the **old** $|\psi\rangle$ axis (indicated by the blue dashed line in figure 1.2 **B2**). This sequence of two steps gradually rotates the state vector $|\psi\rangle$ towards the state $|R\rangle$ corresponding to the 'right answers' (Fig. 1.2 **B3**), and so when measurement occurs the correct state is measured. It can be seen that the rotation causes the $|R\rangle$ component of $|\psi\rangle$ to lengthen and the $|W\rangle$ component to contract hence the probability of **all** the correct answers increase and **all** the wrong answers decrease as per figure 1.2 **A3**.

The finite limit on the number of iterations ($\sqrt{N}$) is necessary as the process will eventually start to rotate the $|\phi\rangle$ away from the $|R\rangle$, but is faster that N operations as required by a classical approach.

1.4 Quantum computing technologies

There are many proposed technologies for implementing a quantum computer ready for useful 'quantum information processing'. In this section we describe the most significant technologies and summerise how these compare with superconducting charge qubits. Whilst there have been some successes, no technology has yet been able to best a classical computer at solving a problem, with the largest quantum computer proving:

$$15 = 3 \times 5 \tag{1.12}$$

Despite the simplistic result, this implementation of Shor's factoring algorithm on a seven qubit NMR computer is a great achievement as it proves that a quantum algorithm actually works [16].

1.4.1 Ion trap

First proposed by Cirac and Zoller [17], ion traps confine microscopic particles that are suitably isolated and cooled to create two-level qubits, these ions are manipulated, measured and cooled with lasers. Examples of suitable ions are Beryllium [18] and Calcium [19]. Each ion forms a qubit and is maintained in a cold low pressure environment to prevent decoherence due to collisions with atoms and photons. The simplest method for cooling is Doppler cooling, whereby a laser is focused on the ions along a particular axis, and the frequency of this laser is chosen to be detuned slightly from the energy gap of the ion. Assuming Brownian motion, if the ion stochastically moves toward the laser, the frequency of the laser appears to increase due to the Doppler effect such that the laser frequency becomes retuned with the ion energy gap resonates and emits a photon. Hence energy is lost and the ion cools over time.

The ions are suspended inside a 'trap', most ion trap based quantum computers use a linear quadrapole trap [20], in which a row of ions is held between four rod-like electrodes with a DC voltage (Fig. 1.3**A**), alternatively to enhance the ion confinement RF voltages are applied to the electrodes so that the potential very quickly shifts back and forth about the ion creating a pseudo parabolic potential (Paul trap). The rod electrodes are capped with ring electrodes to prevent the ions from escaping. An alternative trap design [21], uses a single ring with two point electrodes as endcaps (Fig. 1.3**B**).

The two states of the ion trap system are encoded in the ground energy level, and an excited energy. The qubit state is manipulated by focusing a short burst of laser radiation on to the ion to rotate the state. The qubits can be read out by directing laser pulses at each ion, to illuminate them for a camera [22] or photon counting device.

The Coulomb repulsion force couples the ions, where the positions of the ions are chosen to be at the nodes of the laser standing wave. These interactions can be controlled by laser frequency, through the so-called centre of mass mode, where the individual ions in a chain can be moved as a whole.

The advantage of an ion trap is the relative ease that the qubit can be isolated from the environment, meaning long coherence times in the order of seconds. In addition it may be possible to move the ions around a complex circuit for storage and coupling to other ions by lowering the electric fields that confine the ions (Fig. 1.3**C**). However, as with many quantum technologies the equipment used is unwieldy in comparison with solid-state devices.

Prominent ion trap research groups can be found at Oxford University (in-

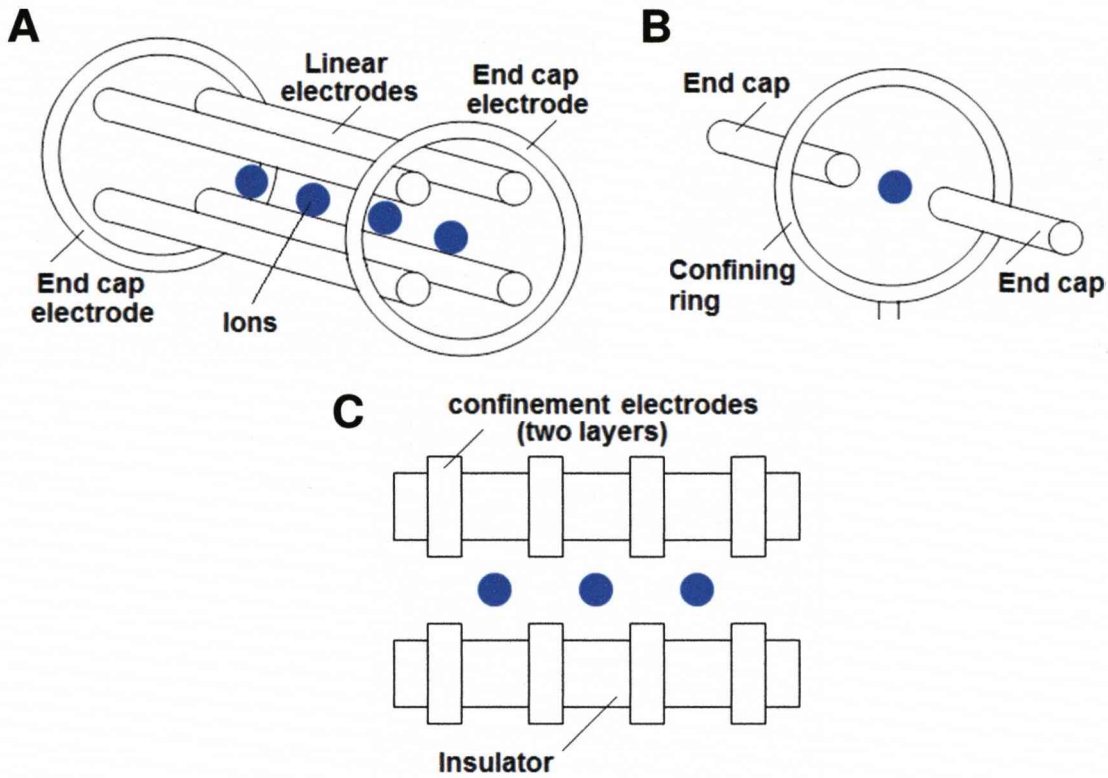

Figure 1.3: Examples of ion traps: (**A**) Linear trap (quadrapole). The ions are trapped in an electric field potential set up between four rod-like electrodes, an RF signal is applied to the rod electrodes to obtain finer confinement, whilst a DC potential is applied to the ring-like end caps to stop the ions escaping. (**B**) Spherical trap. Ions are trapped within a spherical volume surrounded by a ring electrode and capped with two pole electrodes. (**C**) Pole trap. A quadrapole-like construction that allows ions to be moved to neighbouring cells by changing the potential applied to the pole electrodes.

cluding ion traps designed at the University of Liverpool), the National Physical Laboratory (NPL, UK) and Innsbruck University (Austria).

1.4.2 NMR - Nuclear Magnetic Resonance

The discovery of NMR in 1946 [23] has allowed the exploration of molecular structures and dynamics, by using magnetic fields to induce changes in the spin of nuclei. Using Nuclear Magnetic Resonance for quantum imformation processing was suggested in 1993 by Lloyd [24] eventually led to the first practical demonstration of quantum computation, where spin-$\frac{1}{2}$ nuclei are used as robust qubits as they tend to be only affected by magnetic fields. As the magnetic fields are short distance effects, the qubit remains relatively uncoupled from the environment until a strong magnetic control field is applied. The system specifically uses

atoms with the particular property of a spin-$\frac{1}{2}$ nucleus, which is easiest imagined as a small bar magnet. This magnet can be either 'aligned' or 'anti-aligned' with an applied magnetic field, forming two distinct states, spin up and spin down, which can be assigned to $|0\rangle$ and $|1\rangle$. Since the nuclear spin is very small, it is quantum mechanical in nature.

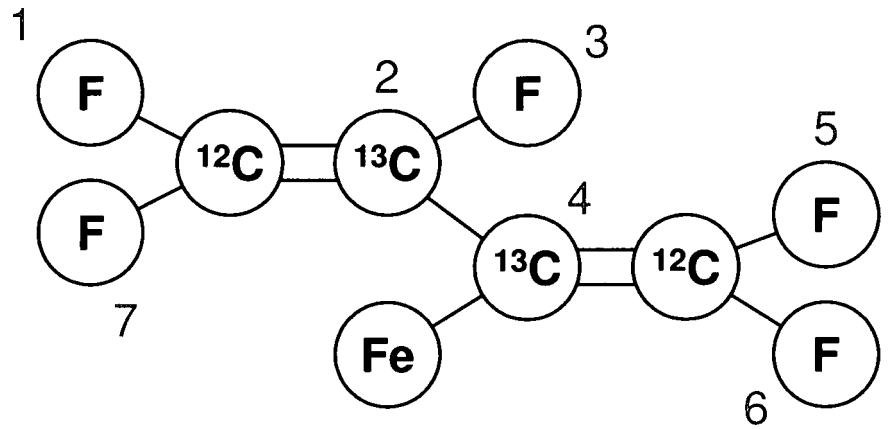

Figure 1.4: The molecule used by the largest working quantum computer to date., where the seven qubits are Fluorine and Carbon 13 atoms bonded together by Carbon 12. The main problem facing NMR is the creation of larger molecules.

Examples of the atoms used are Hydrogen, Carbon, and Fluorine; these are combined with inert atoms to form a molecule. This presents a significant problem, as the size and complexity of the molecule, and therefore the number of qubits, is limited. The most successful computer to date, the computer described by Vandersypen et al. [16] utilises a molecule comprising of Fluorine and Carbon, in which the seven qubit atoms are magnetically active with their spins separated by the inert Carbon atoms (Fig. 1.4). However the magnetic spin fields are too weak to measure directly, hence an ensemble of $\approx 10^{18}$ molecules performs the same calculation, the resulting large field is recorded. Single qubit operations, are realised by electromagnetic field control, whilst two qubit operations require some form of interaction which is provided by the shared chemical bonds in the molecule. The system has the advantage of long decoherence times of several seconds, compared with nanoseconds in solids. However, the main obstacle to overcome is maintaining coherent control over a set of coupled qubits as the size of the molecule is limited, and the use of intense and uniform fields is required to ensure that the ensemble qubits are all supplied the same control.

Prominent NMR research groups can be found at the Massachusetts Institute of Technology (MIT) and the Los Alamos National Laboratory.

1.4.3 Kane computer

The Kane computer [25] is a form of NMR, but uses a solid substrate rather than the liquid ensemble used by Vandersypen et al. [16]. Aside form NMR, there is a contribution from the electron spins of the electrons released by the presence of the impurity in the silicon lattice. This can be measured using Electron Paramagnetic Resonance (EPR) [26] a technique similar to NMR.

Similar to the magnetically active Fluorine bonded with inactive carbon for NMR computation, Kane proposed to use Phosphorous atoms embedded in an inert Silicon crystal substrate to keep the spins separated.

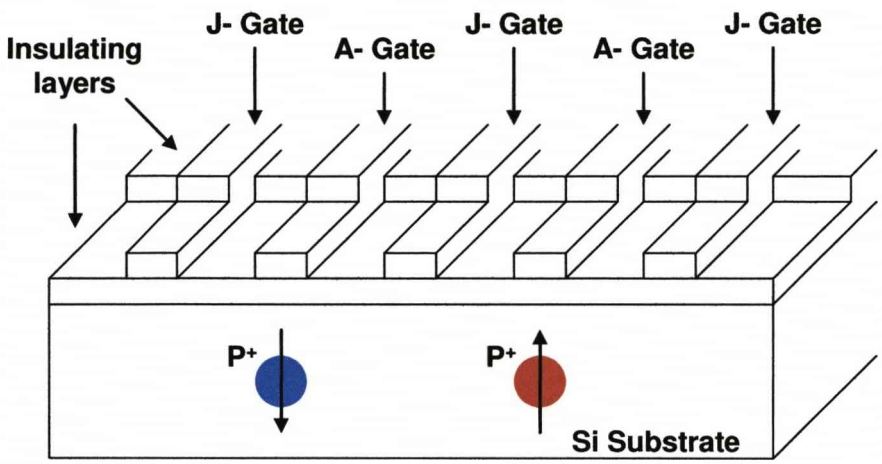

Figure 1.5: The Kane computer is a solid state implementation of NMR quantum computing, the magnetic spins are embedded in a Silicon substrate and controlled by metal srips (gates) on the surface.

The spins are manipulated by applying radio frequency pulses to electrodes above each nucleus (A-gates). Electrodes placed between the atoms control interactions between adjacent atoms (J-gates).

The Kane computer has the advantages of being solid, unlike the container of liquid required for a conventional NMR implementation. However, researchers fear the electrodes may melt under the high currents needed to generate magnetic fields required, and there is also unwanted leakage of the control fields to neighbouring atoms. In addition, the large number of surrounding Silicon atoms in the solid would destroy any coherence quickly.

Prominent research groups working with Kane computers can be found at the University of Queensland and University of Melbourne (Australia).

1.4.4 Quantum optics and the Quantum Electrodynamic Cavity (QED)

Quantum optics exploits perhaps the earliest observations of quantum theory, polarisation and the interference of photons (double slit experiment). It has been a most productive technology with secure quantum communication channels now available for purchase [10].

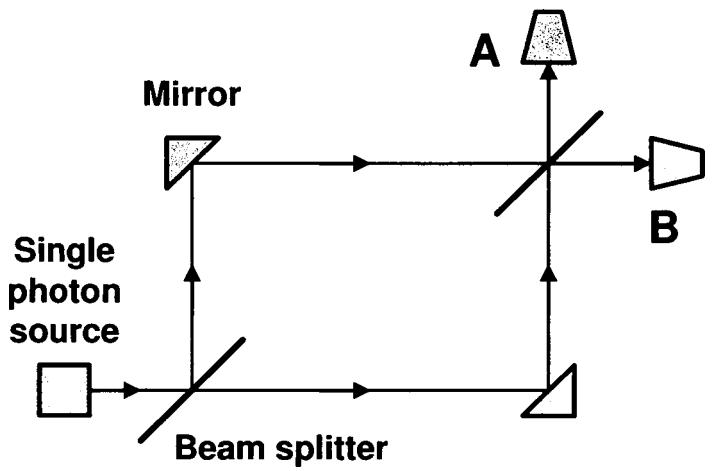

Figure 1.6: A beam splitter is used to create a superposition of two possible paths (states), if a detector is placed on either path it will register a hit 50% of the time. The second beam splitter recombines the state such that the photon is always measured at detector **A**, which is counter to classical thinking where **A** and **B** *should* be equiprobable.

Quantum optics experiments are performed on a light table at room temperature, making it the most accessible quantum technology with practical and commercial applications in secure communication. The photons travel throughout a circuit of mirrors, beamsplitters and devices to rotate the polarisation of an incoming photon as the quantum state is encoded as polarisation. Qubit states are altered by rotating the angle of polarisation with a variable wave plate.

Ideally a single photon source should be used to ensure that the photon that enters the system is the one entangled with other photons and not an independent photon following closely and then measured by mistake. To achieve this, experiments can be designed to detect faults by setting photon detectors along paths that two photons would always take, thus if a 'hit' is registered the result of the experiment can be ignored [27]. Reliable detection of photons has been a difficult issue as the single photons could be absorbed by any apparatus along the path of travel, and a failed detection can also be misinterpreted as a $|0\rangle$ result.

Linking quantum optics to the quantum effects of a microscopic object resulted in the Quantum ElectroDynamic (QED) cavity [28] which consists of a superconducting cavity filled with Caesium atoms, and surrounded by state preparation and measuring equipment such as lasers and phase detectors (Fig. 1.7).

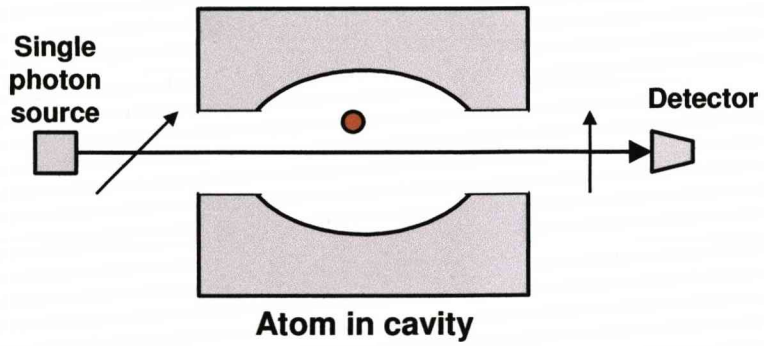

Figure 1.7: Atoms suspended in a cavity can be probed by passing prepared photons through the cavity and measuring the change in polarisation.

The device exploits the large optical non-linearities found in cavity QED. The atom used is coupled to the cavity mode for the efficient transfer of electromagnetic fields. Hence, the cavity is said to be a quantum-optical device. To perform calculations, the cavity is probed by passing polarised photons through the cavity (Fig. 1.7). On exiting, the photons are analysed for phase changes in their polarisation.

Quantum optics is a very popular research area as the experiments can be performed at room temperature and with equipment used for classical optics experiments, therefore numerous research groups exist.

1.4.5 Quantum Dots

The quantum dot [29] is a single trapped electron whose spin represents the qubit state. The electron can either be trapped between electrodes by electrostatic forces (Fig. 1.8**A**) or stored on a small 'island' of Silicon (Fig. 1.8**B**), photo-etched by conventional lithographic methods as per most solid state technologies it should be very **scalable** [30] in this way. The size of the island is reduced in all three dimensions to such an extent that it forms a three dimensional potential well whose wavefunction can only support a single electron, the extreme confinement quantises the states in which the electron can exist. The qubit state is defined as the spin of the trapped electron [3]. The state can be measured either using an electrometer such as the Single Electron Transistor (SET), or by tunnelling to a paramagnetic island which changes direction of magnetisation.

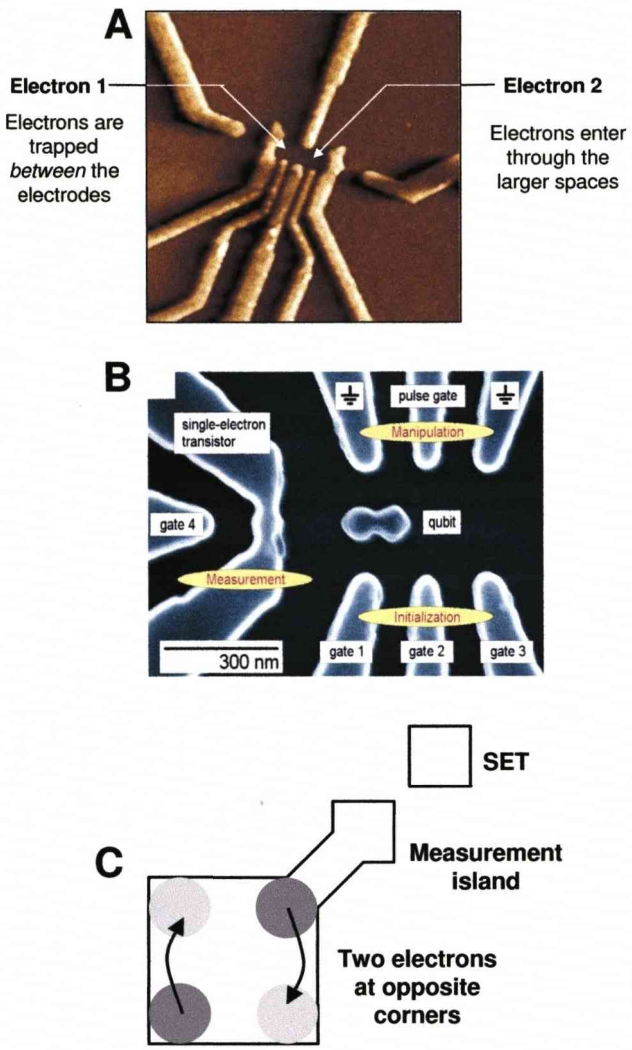

Figure 1.8: (**A**) The electrons can be trapped between electrodes (Delft spin qubit [3]) or (**B**) trapped on islands of silicon (Hitachi double dot [4]). (**C**) A scheme has also been proposed that measures the positions of two electrons pushed to the corners of an island [5]

An electrical gate barrier controls tunnelling between islands, or laser manipulation can be used. Single qubit operators are initiated using magnetic fields and the electric gating previously mentioned. The main disadvantage of this system is rapid decoherence, which is common to most solid-state qubits, but there are also unwanted internal states if there is more than one electron in the dot as these can entangle. However there has been research focusing on using two-electron quantum dots [5] where the positioning of the electrons at opposite corners of a square island is used as the computational states (Fig. 1.8**C**).

Quantum dot groups tend to have close ties to the semiconductor industry with groups at Hitachi (Cambridge) and IBM (New York).

1.4.6 Flux qubit - Persistent current qubit

A flux qubit is essentially a ring of superconducting material with a number of Josephson junctions segmenting it, and a magnetic flux threading the ring. A ring with one junction are usually referred to as the RF-SQUID (Superconducting Quantum Interference Device), however this configuration is also known as the 'Phase qubit' where the state is represented by the superconducting phase across the junction [31]. Rings with two junctions are called DC-SQUIDs and are used as sensitive magnetometers which can measure a flux qubit (see section 3.1.2). The flux qubit itself is a three junction ring that allows the direction of the 'persistent current' flowing around the ring to be reversed, the qubit state is encoded as direction of the current flow [6] which is on the order of microamperes.

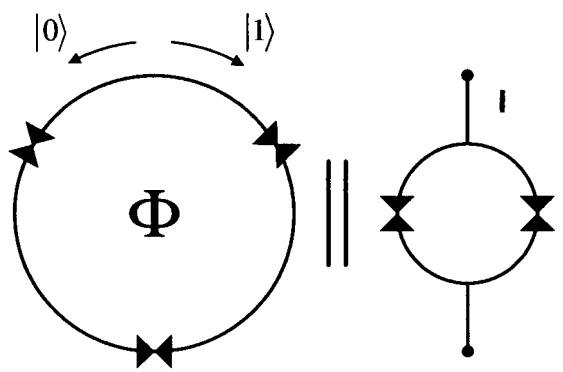

Figure 1.9: Although a flux qubit can be formed from a ring with a single junction, a three junction qubit was proposed by Mooij [6] that encodes the state as the direction of current flow. The qubit is measured with an inductively coupled DC-SQUID.

Flux qubits can be inductively coupled to other qubits or measurement devices, this is usually accomplished by placing the qubit rings inside a larger ring that forms the coupling inductance. Circular rings are difficult to fabricate by using conventional lithography, hence the qubit rings are physically rectangular although the circuit diagrams tend to be drawn as circles. Typical values for the circuit parameters can be found in reference [32].

Qubits that encodes states as charge can be disrupted by charges trapped in the materials used to fabricate superconducting circuits, whereas flux qubits are almost immune.

Experimental and theoretical work on flux qubits has been performed at both Delft University (Netherlands) and Sussex University (United Kingdom).

1.4.7 Quantronium qubit

The quantronium was developed at Saclay (France) by Vion *et al* in 2002 [33]. It is a hybrid device that operates in the regime between the Flux and Charge qubits, this distinction is defined by the ratio of the capactive charging energy E_C and the junction energy E_J, for a Flux qubit $E_J >> E_C$ and likewise for a Charge qubit $E_J << E_C$ however for a quantronium device $E_J \approx E_C$.

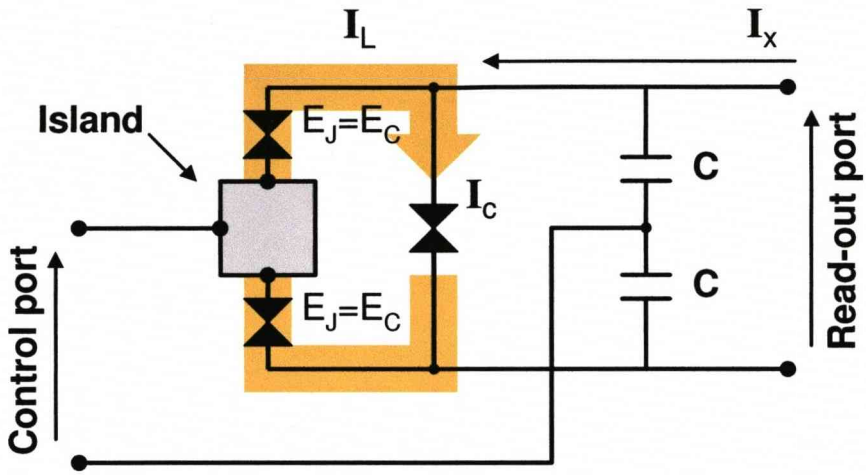

Figure 1.10: The Quantronium is a hybrid solid state qubit that operates between the charge and flux qubit regimes, although arguably it is more closely related to a charge qubit with junction energies comparable to the island charging energy. The charge induced on the island controls the phase and therefore the current in the loop indicated by the orange outline, this quantum variable is measured by pumping sufficient current into the system as to exceed the critical current of the third Josephson junction and thus create a non-zero voltage across the output.

The structure of a quantronium is essentially a Cooper pair box however the two Josephson junctions coupled to the island have energy E_J approximately equal to the charging energy of the island E_C, the 'box' forms part of a SQUID ring (flux qubit) which is used for measuring the qubit. The quantronium is controlled via a voltage capacitively coupled to the island, which alters the superconducting phase difference across the two coupled Josephson junctions and hence the total current I_L flowing in the orange loop. This loop current is 'read out' by forcing extra current I_X in through the 'read out' port until the critical current I_C of the 'read out' Josephson junction is exceeded and generates a finite voltage. Since I_X and I_C are known, I_L can be obtained using Kirchoff's current law $I_C = I_L + I_X$. The advantage of using the quantronium circuit is relative insensitivity to charge and phase fluctuations, as it operates between the charge and flux regimes.

1.4.8 Charge qubit - Cooper pair box

The superconducting charge qubit is also known as the Cooper pair box as the qubit state is represented by the presence or absence of an excess Cooper pair on a small box-like island. The design was proposed in 1987 by Buttiker [34], and in the simplest form it is a single Josephson junction linking a bulk superconductor, which is a reservoir of Cooper pairs, to an island small enough that the number of excess Cooper pairs on the island becomes discretised due to the Coulomb blockade effect [35]. The blockade effect occurs when the charging energy of the island E_C is large, so that once charged with a Cooper pair, the energy required to add extra Cooper pairs becomes prohibitively large, hence $E_C >> E_J$ for a charge qubit. The tunnelling of the 'free' Cooper pair is allowed by the Josephson junction, the frequency of which is defined by the Josephson junction energy E_J. Given two Josephson junctions connected together in a loop with the island, the pair is equivalent to a single junction with tunnelling energy $E_J(\Phi)$, a function of the magnetic flux Φ threading the loop. The qubit can also be controlled by applying a voltage bias across the structure (usually interpreted as a biasing charge n_g). However the island can also be irradiated by a microwave drive field to cause qubit excitation.

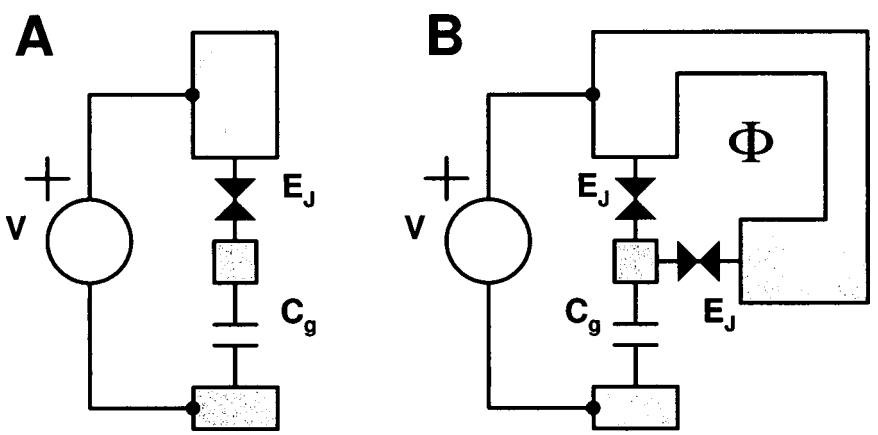

Figure 1.11: (**A**) Simple charge qubit has a single Josephson junction to allow tunnelling of a Cooper pair on to and off the island. (**B**) Two junctions connected in parallel is equivalent to a single junction but with adjustable tunnelling energy.

The charge qubit state is measured using a sensitive electrometer such as the Single Electron Transistor (SET) [36] which is capacitively coupled to the island.

The leading group working with Cooper pair boxes is NEC (Japan) who have experimentally shown coherent state oscillations in single [37] and coupled [38] charge qubits.

1.4.9 Unusual technologies

The following technologies would perhaps not be considered the mainstream, but should not be dismissed.

Heteropolymers

The heteropolymer computer is a linear chain of atoms used as memory. The state of each atom is pumped into an excited state with a laser. Similarly, instructions are also be transmitted by laser pulse, with the type of instruction performed on an atom being dependant on the properties of the pulse. The resulting answers are read using resonance florescence.

The individual atoms are distinguished from other atoms, as the energy levels of each object differ slightly due to interactions between the atoms in the chain. It is possible to transmit a classical bit between adjacent atoms in the chain, to load the quantum computer [24].
This method of using heteropolymers was designed and implemented by Teich [39].

Topological Quantum Computer

The topological quantum computer utilises the braiding properties of anyons, a type of composite particle formed in complex condensed matter systems. The anyon movement is restricted to a two-dimensional layer, and has the unusual property of no anyons crossing paths. The quantum information is encoded in their motion. The phenomenon is called quantum braiding. Averin et al [40] designed a device that can control the positions of the anyons and hence the braiding. Suggesting a design for a two qubit controlled NOT gate, and single gate operations.
The main advantage is expected to be immunity to errors, due to the stability of anyons.

Quantum electromechanical systems

The quantum electromechanical system proposed by Utami et al [7], is similar to a quantum dot device. However, the island is now a Buckminsterfullerene molecule suspended between three electrodes; a source, drain and gate electrode labeled in the same fashion as a classical MOSFET transistor (Fig. 1.12). The molecule behaves as a high frequency oscillator and a single electron is placed on the molecule using a charging current. Due to the Coulomb blockade effect only

one electron is present, as the charging energy to place a second is considered too large.

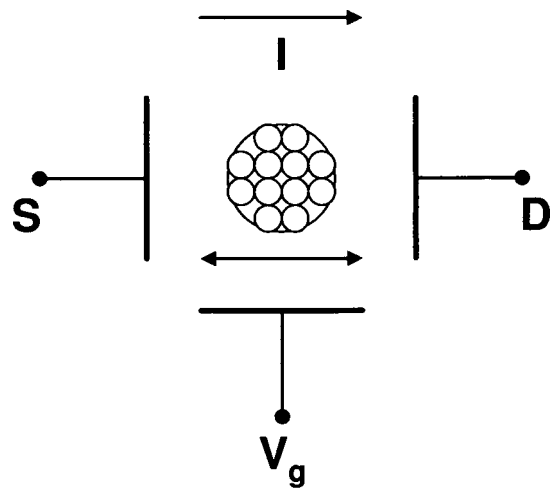

Figure 1.12: A quantum electromechanical system. [7]

The source and drain electrodes act as reservoirs, and so the qubit state is controlled by the applied gate voltage. This gate voltage is affected by conductance between the molecule and electrodes, and so then electrical system surrounding the fullerine molecule exhibits quantum effects caused by the quantum mechanical nature of the molecule's vibration in a typical environment temperature of 10mK. The system is observed through the drain-source current as a function of a bias voltage.

1.5 Technical challenges

In 1997 a list of criteria to evaluate the emerging quantum computing technologies was proposed by David DiVincenzo [41]. The so called 'DiVincenzo checklist' consists the following five criteria:

1. Hilbert space control

The qubit should be well characterised as the behaviour of the qubit states must be known. In addition, it should be possible to increase the number of qubits and hence the dimensions in the Hilbert space. This requires accuracy beyond that of classical systems, as quantum states tend to be defined in terms of the lowest two energies of a system they are very sensitive to disturbances. Characterisation is a significant problem for solid state systems due to the variation in fabrication of neighbouring qubits. However, solid state technologies

could employ existing lithographic manufacturing techniques to create very large number of qubits.

2. State preparation

The state vector must be initialised to a predetermined value. More difficult in some cases, the temperature must be brought low enough to force the system into the ground state. Qubits can be forced into a known state by making a projective measurement to instantly collapse the state, however a weak measurement scheme (considered in this thesis) requires a significant amount of time to pull the state vector into a known pure state. (The purification process proposed in this thesis depends on the measurement strength and may take dozens of rotations.)

3. Low decoherence

Qubits should be suitably isolated from sources of interference, which may disrupt the superposition, before the result of the calculation is measured. It is difficult to completely isolate a system and still be able to interact with it at the classical level, which how the outside world works. Solid state qubits are strongly coupled to the environment as the number of atoms in a macroscopic object is large, whereas microscopic systems such as ion traps are well isolated within a vacuum chamber. Decoherence times for solid state systems vary, with the most successful systems quoting $500ns$ [30, 37]. Given this, hundreds of qubit rotations can occur at these high frequencies (>10GHz).

4. Controlled unitary transformations

The qubits must be able to respond correctly to a sequence of precisely formed unitary transforms. Accuracy is required, if the transform is performed incorrectly the resultant uncertainty in the qubit state is equivalent to unwanted decoherence. Solid state qubits are controlled via a long series of amplifier and filter chains to connect a warm outside world to the very cold environment of a qubit.

5. State specific quantum measurements

The readout of a qubit state should be some classical binary string, the result of a sequence of quantum measurements. There needs to be a method of measuring the qubit, and not the environment or another unwanted qubit. For a solid state charge qubits a Single Electron Transistor (SET) can be used to measure the presence of a charge, alternatively for flux qubits a Superconducting QUantum Interference Device (SQUID) measures magnetic field.

Technology	Number of qubits (potential)	Decoherence time (order)	Control	Readout	Notes
Ion trap	1000s	Milliseconds seconds	Laser pulse	CCD camera	Promising technology, has many advantages. Scalable, by moving ions in a trap circuit
NMR	7+	Seconds to minutes	Simple magnetic field applied globally	Ensemble magnetic field is measured	Most successful technology to date with a working seven qubit quantum computer. Number of qubits is limited by size of molecule.
Kane	millions	Tens of seconds	Electric fields can crosstalk	Single Ion buried deep	Solid state NMR, although only one nucleus is used, and is embedded deep within a Silicon substrate.
QED/ Quantum optics	10s	hours	Off the shelf optics	Photon counter	Quantum Optics operate at room temperature. Requires large areas until miniaturisation is achieved.
Quantum dots	millions	microseconds	Remotely applied voltage	Electrometer coupled to qubit	Semiconductor implementation of Cooper pair boxes. Has internal state problems caused by dopants.
Flux	millions	nanoseconds	Remotely applied current	SQUID coupled to qubit	Dual of the Cooper pair box, (charging energies differ).
Quantronium	millions	nanoseconds	Remotely applied voltage	RF pulse & voltmeter	Suffers from less noise problems than charge or flux qubits. Qubit and readout are one device
Cooper pair box	millions	nanoseconds	Remotely applied voltage	Electrometer coupled to qubit	Susceptible to noise due to close coupling between environment, qubit and measurement device

Figure 1.13: Overview of the mainstream quantum computing technologies. Green indicates a current strength, whilst red indicates a weakness of a given technology.

1.5.1 Summary of Thesis

Quantum computing is a new paradigm in information processing. It is a large and rapidly growing field covering algorithm design to the construction of new and technologically demanding devices. In this thesis we concentrate on the problem of control and observation. In particular we have devised methods of characterising and purifying superconducting charge qubits also known as Cooper pair boxes (Sec. 1.4.8) by means of simulation with MatLab^{tm}.

For characterising a qubit we focus on a spectroscopic analysis of a two-level charge qubit coupled to a biasing circuit that behaves as an oscillator. This would normally be performed using a Single Electron Transistor to measure the qubit behaviour. However, we investigate the power spectra of the biasing circuitry which coupled the qubit behaviour to the biasing charge through capacitive coupling. We find that features in the frequency spectrum of the biasing circuitry could be used to determine the qubit's response to the bias control.

The experimentalist's knowledge of the true quantum state can be gradually lost by the process of decoherence where the qubit is somehow coupled to an unknown or random environment. Purifying the state removes the uncertainty of the actual state coefficients by measurement. This is usually not a concern for *projective measurements* as the qubit will collapse in to a known state, however here we consider *weak measurement* where the qubit state is only partially collapsed by a gradual measurement. Weak measurement allows *quantum feedback* as the state can be measured before it fully collapses and modified by applying controls. It has been shown by Kurt Jacobs that for a generic qubit model the purification rate can be accelerated thought the use of quantum feedback, in this thesis we provide feedback protocols that operate within the constraints of a superconducting charge qubit system.

Papers:

E. J. Griffith, C. D. Hill, J. F. Ralph, H. M. Wiseman and Kurt Jacobs, *Rapid-state purification protocols for a Cooper pair box*, Phys. Rev. B **75**, 014511 (2007)

E. J. Griffith, J. F. Ralph, Andrew D. Greentree and T. D. Clark, *Spectroscopy of a Cooper-pair box in the Autler-Townes configuration*, Phys. Rev. B **74**, 094510 (2006)

E. J. Griffith, C. D. Hill, J. F. Ralph, H. M. Wiseman and Kurt Jacobs, *Rapid state purification in a superconducting charge qubit*, Proceedings of Photon06 (2006)

C. Hill, J. F. Ralph, E. Griffith, *Guidance Applied to Quantum Operations in Josephson Charge Qubits*, Proceedings of Photon06 (2006)

Jason F. Ralph, Elias J. Griffith, Charles D. Hill, and Terence D. Clark, *Rapid purification of a solid state charge qubit*, Proceedings of SPIE, Volume **6244** Quantum Information and Computation IV, 624403 (2006)

Jason F. Ralph, Elias J. Griffith, Terence D. Clark and Mark J. Everitt, *A proportional guidance law for quantum information processing*, Proceedings of SPIE, Volume **5815** Quantum Information and Computation III, pp. 32-39 (2005)

E. J. Griffith, J. F. Ralph and T. D. Clark, *Superconducting Qubits and Environmental Noise*, AIP Conference Proceedings, Volume **734**, pp. 401-404 (2004)

Jason F. Ralph, Elias J. Griffith, Terence D. Clark, Mark J. Everitt and Peter Stiffell, *Characterizing a superconducting charge qubit via environmental noise*, Proceedings of SPIE, Volume **5436** Quantum Information and Computation II, pp. 242-249 (2004)

Chapter 2

Quantum mechanics and weak measurement

This chapter explains the essentials of quantum mechanics pictorially and mathematically by using the Dirac formalism, which is more suited for simulation purposes than using a wavefunction approach. It is intended as an engineers approach to quantum mechanics. Firstly, quantum states and their various representations are examined, together with the operators needed to manipulate and measure these states. The chapter is concluded by examining the concept and mathematics of weak measurement theory, with the intention of expressing this theory in terms of the evolution of Bloch sphere coordinates rather than the usual master equation evolution of a density matrix. This geometric approach will aid understanding of the main topic of this thesis found in chapter 5, 'Rapid state purification'.

2.1 Quantum mechanics basics

Reference [42] by Isham, provides a short and readable introduction to the fundamentals of 'Quantum Theory', whilst the the well known book by Nielsen and Chuang [15] develops this somewhat further.

2.1.1 Pure states, mixed states and probability

Numerous physics textbooks introduce the foundations of quantum mechanics using the concept of continuous wavefunctions [43, 44, 45], as the imagery of interfering waveforms intuitively describes electron scattering effects and the structure of atoms. However, it may be preferred for the purposes of quantum computation and simulation to use the Dirac formalism where the mathematical objects called *state vectors* are now discrete containers rather than continuous functions.

In the Dirac formalism, the *state* of a quantum system is represented by an $[n\times 1]$ vector, where the elements of the vector c_0,c_1 and c_n are **complex** valued numbers. The angular brackets of the Dirac notation $|\psi\rangle$ is called a *ket*, $|\psi\rangle$ comprises of a number of basis states $|0\rangle$ to $|n\rangle$ each 'weighted' by a complex number c_n.

$$|\psi\rangle = c_0|0\rangle + c_1|1\rangle + c_2|2\rangle + \cdots + c_n|n\rangle \tag{2.1}$$

These complex numbers define the state and can be written as a column vector, which assumes the same set of basis states are used throughout.

$$|\psi\rangle = \begin{pmatrix} c_0 \\ c_1 \\ c_2 \\ \vdots \\ c_n \end{pmatrix} \equiv \begin{pmatrix} A_0 e^{i\theta_0} \\ A_1 e^{i\theta_1} \\ A_2 e^{i\theta_2} \\ \vdots \\ A_n e^{i\theta_n} \end{pmatrix} \tag{2.2}$$

The corresponding *bra* $\langle\psi|$ is the *Hermitian conjugate* of the ket $|\psi\rangle$, denoted by a dagger the Hermitian conjugate is a transpose followed by a conjugate of the vector.

$$\begin{aligned} \langle\psi| &= |\psi\rangle^\dagger \\ &= \begin{pmatrix} c_0^*, & c_1^*, & c_2^*, & \ldots & c_n^* \end{pmatrix} \\ &= \begin{pmatrix} A_0 e^{-i\theta_0}, & A_1 e^{-i\theta_1}, & A_2 e^{-i\theta_2}, & \ldots & A_n e^{-i\theta_n} \end{pmatrix} \end{aligned} \tag{2.3}$$

The simplest useful quantum system is a two-level system, so the system state is a vector that has only two complex valued elements, *polarisation* is an introductory example found in many texts [46, 47]. For a two state system the vector (Eq. 2.2) is constrained to the first two elements:

$$|\psi\rangle = \begin{pmatrix} c_0 \\ c_1 \end{pmatrix} \equiv \begin{pmatrix} A_0 e^{i\theta_0} \\ A_1 e^{i\theta_1} \end{pmatrix} \tag{2.4}$$

The state vector $|\psi\rangle$ is formed from two component vectors, these are called the *basis states* as other states are built from these states. These vectors are generally

selected to be an *orthonormal* set, meaning every axis in the set should have unit length and does not overlap the other axes. The example state vector can be expressed as a superposition of two basis states:

$$|\psi\rangle = \begin{pmatrix} c_0 \\ c_1 \end{pmatrix} \equiv c_0 \begin{pmatrix} 1 \\ 0 \end{pmatrix} + c_1 \begin{pmatrix} 0 \\ 1 \end{pmatrix} \tag{2.5}$$

$$|\psi\rangle = c_0|0\rangle + c_1|1\rangle \tag{2.6}$$

In this case the orthonormal set of basis states is given by:

$$|0\rangle = \begin{pmatrix} 1 \\ 0 \end{pmatrix} \qquad |1\rangle = \begin{pmatrix} 0 \\ 1 \end{pmatrix} \tag{2.7}$$

The basis states are denoted by $|0\rangle$ and $|1\rangle$ as when $|\psi\rangle = |0\rangle$ the measured outcome will always be 0, likewise when $|\psi\rangle = |1\rangle$ the measured outcome will always be 1. However, when $|\psi\rangle = c_0|0\rangle + c_1|1\rangle$ the measurement outcome may be either 0 or 1 dependent on the values of c_0 and c_1. The axes defined by equation 2.7 can be rotated to form a different but valid computational basis where c_0 and c_1 are adjusted to compensate, often the computational basis will be defined by the *eigenvectors* of an operator rather than equation 2.7, as these are the states linked to the possible measured outcomes (Refer to section 2.1.3).

The probabilistic nature of the measurement *outcome* means any experiment needs to be repeated many times, but the computational benefit of a quantum algorithm should outweigh this cost. The probability of being in one of the basis states is calculated by multiplying each vector element of equation 2.2 by the complex conjugate of the element.

$$P\left(|\psi\rangle = |x\rangle\right) = |c_x|^2 = c_x^* c_x \tag{2.8}$$

It is key to understand that the state vector defining the probabilities is deterministic (unless modified by a stochastic process) and it is the measurement result that is random [42, 15, 48]. As the state vector is a complete description of the system it should contain all possible outcomes, therefore all the probabilities should sum to one [42]. Despite the outwardly pointing brackets $\langle\psi|\psi\rangle$ is known as the *inner product* of two states, it is similar to the *dot product* of classical geometry, but with a complex conjugate.

$$c_0^* c_0 + c_1^* c_1 + c_2^* c_2 + \ldots + c_n^* c_n = \langle\psi|\psi\rangle = 1 \tag{2.9}$$

Any state can be renormalised to satisfy equation 2.9 by dividing $|\psi\rangle$ by the length of $|\psi\rangle$ given by $\sqrt{\langle\psi|\psi\rangle}$.

$$|\psi\rangle_n = \frac{|\psi\rangle}{\sqrt{\langle\psi|\psi\rangle}} \tag{2.10}$$

The column vector $|\psi\rangle$ (Eq. 2.2) is also known a *pure state*, meaning the values of the vector elements are known to be the actual true values. An example of when this is true is after a projective or strong measurement, the state will collapse into an eigenstate defined by the measured outcome. However, as any real world system evolves it experiences *decoherence*, the environment will affect the system in ways we can not measure, effectively the system can be thought of as being 'measured' by the environment and the result is unknown to the experimentalist. Thus decoherence can be understood as the reduction of the *confidence* in our knowledge of the *true* value of state vector. To model this lack of information, *mixed states* are used [15, 48]. A mixed state is a classical probabilistic mixture of more than one pure state, the probabilities p_i represent the confidence of each pure state $|\psi_i\rangle$ being the true pure state.

$$\rho_{mixed} = \sum_i p_i |\psi_i\rangle \langle\psi_i| \tag{2.11}$$

$$\rho_{mixed} = \sum_i p_i \rho_i \tag{2.12}$$

The two inwardly pointing brackets are the *outer product* of two pure state vectors, forming a square matrix known as a *density matrix*, (ρ_i).

$$\rho_{pure} = |\psi\rangle\langle\psi| = \begin{pmatrix} c_0 \\ c_1 \end{pmatrix} \begin{pmatrix} c_0^* & c_1^* \end{pmatrix} = \begin{pmatrix} c_0^* c_0 & c_1^* c_0 \\ c_0^* c_1 & c_1^* c_1 \end{pmatrix} \tag{2.13}$$

$$\rho_{pure} = |\psi\rangle\langle\psi| = \begin{pmatrix} P(0) & c_1^* c_0 \\ c_0^* c_1 & P(1) \end{pmatrix} \tag{2.14}$$

Note that the terms on the leading diagonal are the **measurement** probabilities (Eq. 2.8), and the off-diagonal terms are referred to as the *coherences*. As a decoherence process is applied to the system, these off-diagonal terms will gradually reduce to zero, it is the off diagonal terms that indicate the amount of uncertainty in the actual system state.

The uncertainty is quantified by calculating the state *purity* (Eq. 2.15). Chapter 5 investigates the use of *weak measurement theory* for *purification* (increasing the purity or confidence in the true state) via a series of small measurements and proposes a means of implementing a feedback protocol for increasing the rate information is extracted from a superconducting charge qubit.

$$P = Tr\left\{\hat{\rho}^2\right\} \tag{2.15}$$

Where the purity of a pure state is $P = 1$ and given a mixed state $P < 1$ where $P = 0.5$ for the completely mixed state.

2.1.2 The Bloch sphere

The Bloch sphere is a simple method of representing a two level quantum system visually inclusive of the real and imaginary parts of a state [15]. The four variables that define a state (two real and two imaginary) are reduced to a three dimensional coordinate system where all possible pure states are mapped onto a unit sphere called the *Bloch sphere*, and the $[x, y, z]$ position of the state is called the *Bloch vector*, $\vec{v}$.

The Bloch vector coordinates can be calculated from the density matrix ρ, by multiplying the density matrix with the corresponding Pauli matrix and taking the trace of the result (sum along the leading diagonal of the matrix).

$$x = Tr\{\sigma_x \rho\} \tag{2.16}$$

$$y = Tr\{\sigma_y \rho\} \tag{2.17}$$

$$z = Tr\{\sigma_z \rho\} \tag{2.18}$$

where the Pauli matrices σ_x, σ_y and σ_z are a set of well known matrices that correspond to 180^o rotations about the x, y and z axes of the Bloch sphere.

$$\sigma_x = \begin{pmatrix} 0 & +1 \\ +1 & 0 \end{pmatrix} \tag{2.19}$$

$$\sigma_y = \begin{pmatrix} 0 & -i \\ +i & 0 \end{pmatrix} \tag{2.20}$$

$$\sigma_z = \begin{pmatrix} +1 & 0 \\ 0 & -1 \end{pmatrix} \tag{2.21}$$

It can be seen from figure 2.1 that the poles of each axis are the states after projective measurements using σ_x, σ_y or σ_z operators. For example taking z as the observable, the z-axis poles are the cases where the state $|\psi\rangle$ is either in the state $|0\rangle$ or $|1\rangle$ but not in both. The equatorial plane contains the so called *superposition states* where the two outcomes are in an equally likely superposition of $|0\rangle$ and $|1\rangle$, but differ in phase as the Bloch vector proceeds around the equator. The x-axis poles are the positive and negative *real* superpositions, and the y-axis poles are the positive and negative *imaginary* superpositions of $|0\rangle$ and $|1\rangle$.

The set of pure states map on to the surface of the Bloch sphere, however the mixed states exist within the sphere becoming more mixed when approaching the centre. The very centre of the sphere is referred to as the *completely mixed state* at this point nothing is known about the actual value of the system state and the true pure state of the system could be any state potentially. The act of measurement draws the Bloch vector from the centre to the surface of the sphere as information

is extracted from the system, if the measurement is strong/projective then the system purifies the vector instantly into either of the z-axis poles. In the case of projective measurement, the true pure state is known from the measured outcome so the observer knows with absolute confidence where the Bloch vector is, as the state will have collapsed into the corresponding eigenstate.

The Bloch sphere allows the rotations created by a non-zero Hamiltonian to be visualised, whereas the evolution of a density matrix is not so intuitive. Therefore the Bloch sphere is of great importance to designing quantum feedback protocols (Chapter 5), however the Bloch sphere representation becomes much more complicated when two qubits (four level system) are considered [49], as there will be **15** axes.

2.1.3 Operators and expectation values

Operators are used to perform a variety of tasks such as measuring the state of the system and manipulating the system state, which can include purposeful control and implementing environmental effects.

Operators are square matrices that describe how to transform one state to another [50]. The operators are classified according to particular properties; *Unitary* operators which preserve the normalisation of a state (Eq. 2.9) and have unit eigenvalues, whilst *Hermitian* operators have real eigenvalues that correspond to experimentally measurable values [46]. The eigenvalues of operators form the set of possible values taken by the outcome of a measurement using said operator. After a measurement of the current state is performed, the new state becomes the eigenvector that corresponds to the eigenvalue result.
Operators are said to be unitary if they satisfy the following conditions

$$U^\dagger U \;=\; UU^\dagger \;=\; I \tag{2.22}$$

Hermitian operators are invariant to the Hermitian conjugate:

$$H \;=\; H^\dagger \tag{2.23}$$

Updating the quantum state

To apply an operator to a state vector $|\psi\rangle$, the vector is simply premultiplied by the operator matrix (Eq. 2.24) [50]. However for a density matrix ρ, which as a product of a *bra* and a *ket*, the matrix is premultiplied by the operator matrix and postmultiplied by the Hermitian conjugate of the operator (Eq. 2.25).

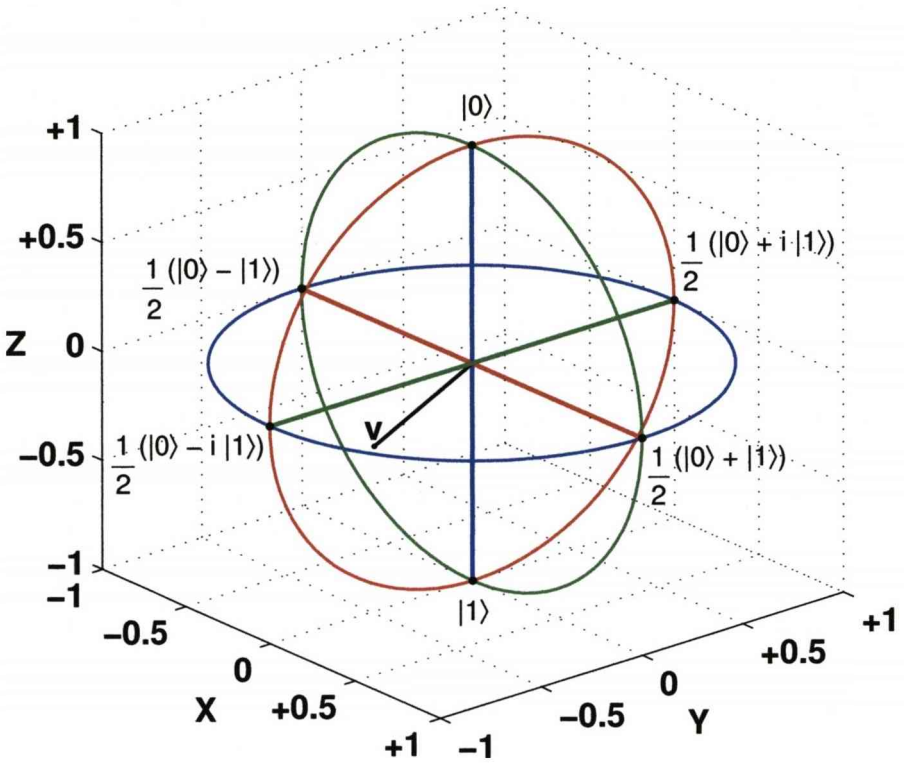

Figure 2.1: The Bloch sphere. Where the density matrix ρ is represented geometrically by the position of a vector $\vec{v}$ in a unit sphere.

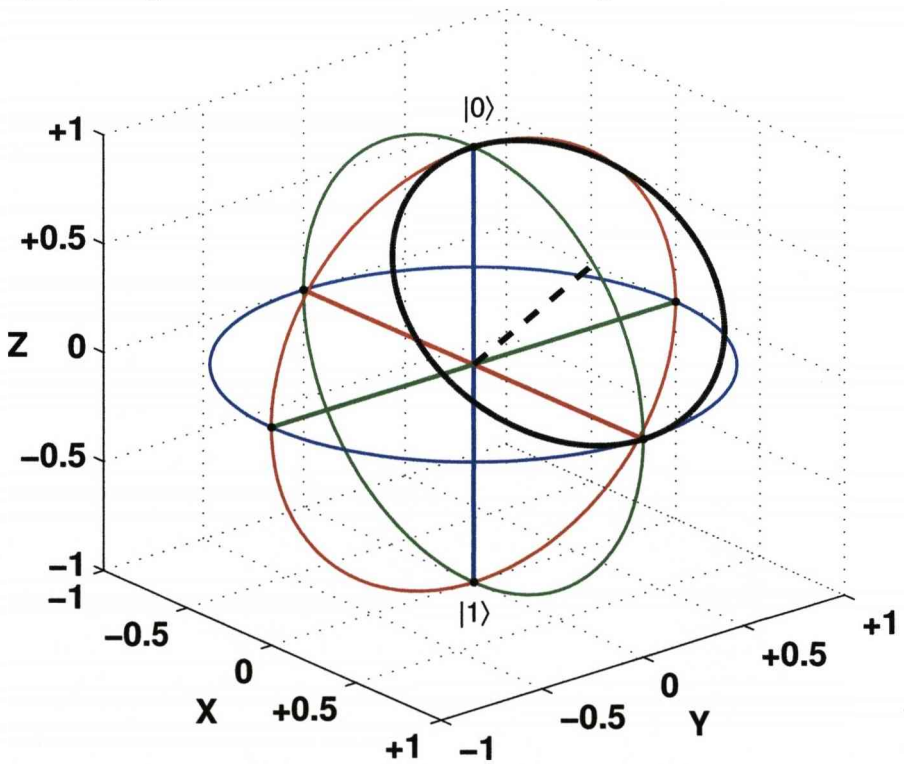

Figure 2.2: Path of the Bloch vector starting from $|0\rangle$, rotating about an axis defined by the Hamiltonian matrix $\hat{H}$. (Section 2.1.4)

$$|\psi\rangle' = A\,|\psi\rangle \tag{2.24}$$

$$\rho' = A\,|\psi\rangle\langle\psi|\,A^\dagger \tag{2.25}$$

$$\rho' = A\,\rho\,A^\dagger$$

The expectation value

The average value of the *observable* (measurement outcome) is given by the *expectation value*, which is the mean outcome of the operator obtained after a large number of repeated measurements given the same state vector. The expectation value calculation is the sum of all the outcome values of an operator weighted by the probabilities of each outcome.

$$\langle A\rangle = \langle\psi|\,A\,|\psi\rangle \tag{2.26}$$

The expectation value of a density matrix is calculated somewhat differently, instead a trace is taken over the product of the operator and density matrix.

$$\langle A\rangle = \mathrm{Tr}\,\{\mathrm{A}\rho\} \tag{2.27}$$

The commutator and anticommutator

If the order that two operators are multiplied does not matter, then the operators are said to *commute*. Operators which do commute have the same eigenvectors and are therefore said to be *compatible* and behave in a classical sense, thus no uncertainty relationship exists between them [46]. Else if the two operators do not commute then the operators are said be a *conjugate pair* and one observable can not be measured without affecting the other, so that the Heisenberg uncertainty relationship applies [51]. Indeed, the generalised uncertainty relation (Eq. 2.32) is defined with commutator brackets, which take a non-zero value.

The commutator is a convenient notation for describing if two operators do or do not commute. Equation (2.28) is the commutator and equation (2.29) is the anticommutator:

$$\left[\hat{A},\hat{B}\right] \equiv \hat{A}\hat{B} - \hat{B}\hat{A} \tag{2.28}$$

$$\left\{\hat{A},\hat{B}\right\} \equiv \hat{A}\hat{B} + \hat{B}\hat{A} \tag{2.29}$$

Taking the charge and magnetic flux variables for two quantum systems as an example. The charge of one system can be measured without disturbing the other

charge, as the two charge operators $\hat{x}_1$ and $\hat{x}_2$ commute with each other. The same is true for the two flux operators $\hat{\Phi}_1$ and $\hat{\Phi}_2$.

$$\begin{aligned}\left[\hat{Q}_1, \hat{Q}_2\right] &= 0 \\ \left[\hat{\Phi}_1, \hat{\Phi}_2\right] &= 0\end{aligned} \tag{2.30}$$

However one cannot measure the charge *and* flux of the *same* system as the act of measuring one variable disturbs the other. This relationship is expressed by a non-zero commutator that indicates a finite uncertainty [52].

$$\begin{aligned}\left[\hat{Q}_1, \hat{\Phi}_1\right] &= i\hbar \\ \left[\hat{Q}_2, \hat{\Phi}_2\right] &= i\hbar\end{aligned} \tag{2.31}$$

Substituting equation 2.31 shows that the product of the two standard deviations $\Delta\hat{Q}$ and $\Delta\hat{\Phi}$ can not be zero, so the individual deviations can never be zero. Therefore as the uncertainty of one variable is reduced, the uncertainty in the other is increased by the very act of measurement to compensate.

$$\Delta\hat{A}\Delta\hat{B} \geq \frac{1}{2}\left|\left\langle\left[\hat{A}, \hat{B}\right]\right\rangle\right| \tag{2.32}$$

$$\Delta\hat{Q}\Delta\hat{\Phi} \geq \frac{1}{2}\hbar \tag{2.33}$$

2.1.4 The Hamiltonian and time evolution

The energy contained within a quantum system will drive the time evolution of a quantum state, this is stated by a *postulate* of quantum mechanics.

Postulate IV - taken from reference [46]
Let $|\psi(t)\rangle$ be the state of the system at time t. Then as long as the system is not disturbed by any experiments, $|\psi(t)\rangle$ satisfies:

$$i\hbar\frac{d}{dt}|\psi(t)\rangle = \hat{H}|\psi(t)\rangle \tag{2.34}$$

where $\hat{H}$ is the operator describing the total energy of the system.

Equation 2.34 is called the Time Dependent Schrödinger Equation (TDSE) and is a first order differential equation governing the evolution of the state vector. The evolution is defined by the operator $\hat{H}$ called the *Hamiltonian* of the system, the expectation value of the Hamiltonian corresponds to the current total energy of the quantum system.

The solution of the TDSE is a unitary operator $\hat{U}(t)$:

$$\hat{U}(t_0) = \exp\left(-\frac{i}{\hbar}\hat{H}\ t_0\right) \tag{2.35}$$

Applying this operator will immediately evolve the state $|\psi(0)\rangle$ at $t = 0$ to the state $|\psi(t_0)\rangle$. However, as the energy of the system ($\hat{H}$) may not be constant between $t = 0$ and $t = t_0$, we use a small time step and incrementally change $|\psi(t)\rangle$ to $|\psi(t + dt)\rangle$ calculating a new $\hat{U}(dt)$ with the current Hamiltonian $\hat{H}(t)$ for each time step.

$$\hat{U}(dt) = \exp\left(-\frac{i}{\hbar}\hat{H}(t)\ dt\right) \tag{2.36}$$

$$|\psi(t + dt)\rangle = \hat{U}(dt)\ |\psi(t)\rangle \tag{2.37}$$

Understanding the behaviour of the Bloch vector whilst undergoing Schrödinger evolution is of considerable importance for designing quantum feedback protocols, as the experimentalist will have some control over the Hamiltonian $\hat{H}$. Under continuous Schrödinger evolution a Bloch vector will rotate around an axis defined by the Hamiltonian. The Hamiltonian matrix can be formed from the weighted sum of three Pauli matrices (Eqs. 2.19, 2.20 and 2.21) where the weights α, β and γ define the x, y and z-axis rotational speeds (dependent on dt).

$$\hat{H} = \alpha\sigma_x + \beta\sigma_y + \gamma\sigma_z + \delta I \tag{2.38}$$

The values of α, β and γ can be extracted by using the equations for the Bloch vector coordinates (Eq. 2.16, 2.17 and 2.18) the resultant vector $[\alpha, \beta, \gamma]$ can then be normalised to obtain the axis of rotation. In addition, when designing for a particular speed and axis of rotation, suitable values of α, β and γ can be calculated by scaling the axis of rotation by the desired rotational velocity.

The incremental angles given timestep dt for rotation about a desired axis $[\alpha, \beta, \gamma]$ can then be calculated:

$$d\theta_x = \frac{\alpha}{\hbar}dt \tag{2.39}$$

$$d\theta_y = \frac{\beta}{\hbar}dt \tag{2.40}$$

$$d\theta_z = \frac{\gamma}{\hbar}dt \tag{2.41}$$

Equation 2.42 is the transformation matrix for rotating a Bloch vector around the x, y and z-axes of a Bloch sphere by $d\theta_x$, $d\theta_y$ and $d\theta_z$

$$\mathbf{R} = \tag{2.42}$$

$$\begin{pmatrix} Cd\theta_y Cd\theta_z & -Cd\theta_x Sd\theta_z + Sd\theta_x Sd\theta_y Cd\theta_z & Sd\theta_x Sd\theta_z + Cd\theta_x Sd\theta_y Cd\theta_z \\ Cd\ Sd\theta_z & Cd\theta_x Cd\theta_z + Sd\theta_x Sd\theta_y Sd\theta_z & -Sd\theta_x Cd\theta_z + Cd\theta_x Sd\theta_y Sd\theta_z \\ -Sd\theta_y & Sd\theta_x Cd\theta_y & Cd\theta_x Cd\theta_y \end{pmatrix}$$

where $Cd\theta_x \equiv \cos d\theta_x$ and $Sd\theta_x \equiv \sin d\theta_x$

2.1.5 Composite systems

When modelling two or more systems that could potentially interact, the state vectors of the individual systems need to be combined using the *tensor product* (denoted by $\otimes$) to form a composite state vector, this is equally true when using density matrices. Consider a three state system $|\psi\rangle$ and a two state system $|\phi\rangle$ which are to be simulated together as composite state $|\Psi\rangle$. Equation 2.43 shows that the tensor product created three copies of $|\phi\rangle$ weighted by the elements of $|\psi\rangle$, such that the composite system is represented by a single vector with six elements. It is very important to note that the length of a composite quantum state is given by the product of the individual systems dimensions ($3 \times 2 = 6$), whereas combining classical systems (through concatenation of the vectors) creates a composite state of length equal to the sum of the individual vector dimensions ($3 + 2 = 5$). As the number of systems that can interact increases, the dimensions of the quantum state vector increases rapidly (For example five coupled two-state systems $2 \times 2 \times 2 \times 2 \times 2 = 32$ elements) whereas for the equivalent number of classical systems the state has much smaller dimensions (E.g. $2+2+2+2+2 = 10$ elements), it is this ability to create a larger number of state variables with the same physical resources which gives quantum computing the advantage [9, 53].

$$|\Psi\rangle = |\psi\rangle \otimes |\phi\rangle = \begin{pmatrix} a_0 \\ a_1 \\ a_2 \end{pmatrix} \otimes \begin{pmatrix} b_0 \\ b_1 \end{pmatrix} \equiv \begin{pmatrix} a_0 \begin{bmatrix} b_0 \\ b_1 \end{bmatrix} \\ a_1 \begin{bmatrix} b_0 \\ b_1 \end{bmatrix} \\ a_2 \begin{bmatrix} b_0 \\ b_1 \end{bmatrix} \end{pmatrix} \tag{2.43}$$

$$|\Psi\rangle = |\psi\rangle \otimes |\phi\rangle = \begin{pmatrix} a_0 b_0 \\ a_0 b_1 \\ a_1 b_0 \\ a_1 b_1 \\ a_2 b_0 \\ a_2 b_1 \end{pmatrix} = \begin{pmatrix} c_0 \\ c_1 \\ c_2 \\ c_3 \\ c_4 \\ c_5 \end{pmatrix} \tag{2.44}$$

Operators are applied to the entire vector $|\Psi\rangle$, however the individual systems within the composite state can be manipulated separately by tensoring the operator for the individual system with an identity matrix of dimensions equal to the

other system. The method of expansion illustrated by equation 2.43 is equally valid for matrices.

$$\hat{U} = I_{3\times 3} \otimes \hat{U}_{\phi} \tag{2.45}$$

To separate the two individual systems it is necessary to apply the *partial trace* to remove a system, producing what are termed the *reduced density matrices* which are the density matrices of the individual systems [48]. The partial trace for obtaining $|\phi\rangle$ is performed by summing three $[2 \times 2]$ density matrices obtained using particular parts of the composite vector as shown by equation 2.46.

$$\begin{aligned}
\hat{\rho}_{\phi} &= \begin{pmatrix} c_0^2 + c_1^2 + c_2^2 & c_0 c_1^* + c_2 c_3^* + c_4 c_5^* \\ c_0^* c_1 + c_2^* c_3 + c_4^* c_5 & c_0^2 + c_1^2 + c_2^2 \end{pmatrix} \\
\hat{\rho}_{\phi} &= \begin{pmatrix} (a_0^2 + a_1^2 + a_2^2)\, b_0^2 & (a_0^2 + a_1^2 + a_2^2)\, b_0 b_1^* \\ (a_0^2 + a_1^2 + a_2^2)\, b_0^* b_1 & (a_0^2 + a_1^2 + a_2^2)\, b_1^2 \end{pmatrix} \\
\hat{\rho}_{\phi} &= \begin{pmatrix} b_0^2 & b_0 b_1^* \\ b_0^* b_1 & b_1^2 \end{pmatrix} = |\phi\rangle\langle\phi|
\end{aligned} \tag{2.46}$$

By substituting $c = ab$ from equation 2.44 it can be seen that the term $a_0^2 + a_1^2 + a_2^2$ is common to all elements of equation 2.46, however this is removed when renormalising the denisty matrix as it is known that $b_0^2 + b_1^2 = 1$, the correct scale factor can be calculated.

Likewise, the reduced density matrix of system $|\psi\rangle$ is recovered by summing two $[3 \times 3]$ density matrices, using specific elements of the composite vector $|\Psi\rangle$ as per equation 2.47.

$$\begin{aligned}
\hat{\rho}_{\psi} &= \begin{pmatrix} c_0^2 + c_1^2 & c_0 c_2^* + c_1 c_3^* & c_0 c_4^* + c_1 c_5^* \\ c_0^* c_2 + c_1^* c_3 & c_2^2 + c_3^2 & c_2 c_4^* + c_3 c_5^* \\ c_0^* c_4 + c_1^* c_5 & c_2^* c_4 + c_3^* c_5 & c_4^2 + c_5^2 \end{pmatrix} \\
\hat{\rho}_{\psi} &= \begin{pmatrix} (b_0^2 + b_1^2)\, a_0^2 & (b_0^2 + b_1^2)\, a_0 a_1^* & (b_0^2 + b_1^2)\, a_0 a_2^* \\ (b_0^2 + b_1^2)\, a_1^* a_2 & (b_0^2 + b_1^2)\, a_1^2 & (b_0^2 + b_1^2)\, a_1 a_2^* \\ (b_0^2 + b_1^2)\, a_0^2 a_2 & (b_0^2 + b_1^2)\, a_0^* a_1 & (b_0^2 + b_1^2)\, a_2^2 \end{pmatrix} \\
\hat{\rho}_{\psi} &= \begin{pmatrix} a_0^2 & a_0 a_1^* & a_0 a_2^* \\ a_1^* a_2 & a_1^2 & a_1 a_2^* \\ a_0^2 a_2 & a_0^* a_1 & a_2^2 \end{pmatrix} = |\psi\rangle\langle\psi|
\end{aligned} \tag{2.47}$$

Similarly, the common term $b_0^2 + b_1^2$ if not already equal to one, is removed when the density matrix is renormalised.

2.2 Weak measurement theory

The early work on weak measurement theory was started in the 1980's [54, 55, 56]. A weak measurement process assumes the qubit is coupled weakly to an environment that can be measured with projective measurements, the weak coupling allows indirect measurements of the qubit state without completely collapsing the qubit. Unlike projective measurements, which is the standard measurement scheme of quantum systems where the qubit is measured directly by an apparatus that collapses the state.

The main advantage of using a weak measurement setup is that it allows the measurement device to be coupled to the qubit at all times, whereas a projective measurement device would require an adjustable coupling system to allow the qubit to evolve freely. It would be beneficial to integrate such a measurement device next to a qubit using the existing manufacturing techniques, engineering a constant coupling without having to rely on controlling a variable coupling.

The main disadvantage of weak measurement is additional stochastic noise continually modifying the qubit state, this *measurement noise* arises from the random results of the projective measurements made on the coupled environment. Unfortunately the measurement noise can be significant, and may disturb the qubit state to an extent that computation can not be performed, however this is beyond the scope of this thesis.

This section describes the mathematics of the weak measurement theory, and derives equations that describe the effect of a weak measurement process on the Bloch vector.

2.2.1 The master equation and the conditioned master equation

A quantum system which is in some way coupled to an external environment (or a measurement device) that is not modelled explicitly as a composite state vector is termed an open quantum system. Originally derived by Carmichael, the *master equation* describes the time evolution of a density matrix ρ for an open quantum system, expressed as a differential equation $d\rho/dt$. Equation 2.48 shows the most common form of master equation, the Lindblad form [57], as per quantum optics literature [58, 59] $\hbar$ is set to one for clarity.

$$\hbar d\hat{\rho} = -i\left[\hat{H},\hat{\rho}\right]dt + \sum_m \left(\hat{L}_m\hat{\rho}\hat{L}_m^\dagger - \frac{1}{2}\left\{\hat{L}_m^\dagger\hat{L}_m,\hat{\rho}\right\}\right) \tag{2.48}$$

Where the standard Schrödinger evolution is modified by a series of Lindblad operators $L_1, L_2, ...L_m$ that defined the effect of the external environment on the quantum system. For example L_1 may be defined as a raising operator with L_2 cast as a lowering operator whose transition rate is weighted more heavily to create the effect of dissipation.

When using projective measurements on the qubit, the qubit state is always collapsed and the result averaged, therefore the effect of the environment **E** on the qubit **Q** is an average. In this case, the qubit density matrix ρ evolves deterministically, governed by a master equation akin to equation 2.48. The Calderia-Leggett model [60, 61] for dissipation is such an example. Alternatively,

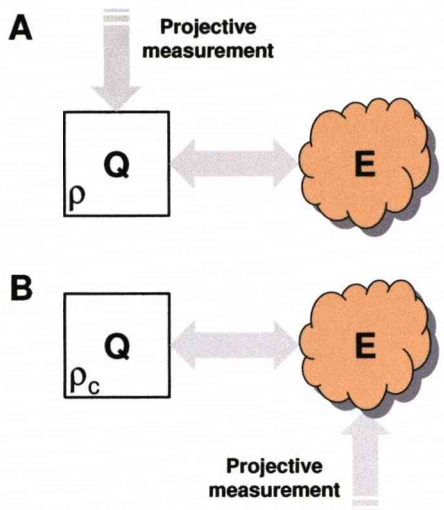

Figure 2.3: **(A)** If projective measurements of the the qubit are made, ρ is modified by the average effect of environment (Eq. 2.48). **(B)** Weak measurement of a qubit is made indirectly by performing a projective measurement on the coupled environment, recording the stochastic measurement result equates to partially measuring the qubit and so ρ_c is said to be the density matrix *conditioned on the measurement result.*

it is possible to weakly measure the qubit state by performing projective measurements on the environment coupled to the qubit, where the state of the qubit is imparted to the environment due to the coupling. However, the qubit state does not completely collapse and quantum operations (Hamiltonians) can still be applied whilst measuring. As information about the qubit state is now being extracted *during the time evolution*, the qubit density matrix is updated by the stochastic results of the projective measurements on the environment. Hence, the *conditioned density matrix* for the qubit is so named because the density matrix evolution is conditioned on the past history of the measurement record [62, 63].

The evolution of a density matrix undergoing Shrödinger evolution with con-

tinuous weak measurement of an observable A is governed by the following *conditioned master equation* [64].

$$d\hat{\rho}_c = -i\left[\hat{H}, \hat{\rho}_c\right] dt - \gamma\left[\hat{A}, \left[\hat{A}, \hat{\rho}_c\right]\right] dt + \sqrt{2\gamma}\left(\hat{A}\hat{\rho}_c + \hat{\rho}_c\hat{A} - 2\left\langle\hat{A}\right\rangle\hat{\rho}_c\right) dW \quad (2.49)$$

where γ is the measurement strength, $\hat{A}$ is the operator corresponding to observable and dW is a Weiner increment. The Weiner increment [1, 65] is a stochastic variable drawn from a Gaussian distribution with variance dt. The first term is the familiar Hamiltonian evolution, the second term continuously decoheres the qubit and the last term represents the stochastic modification of the density matrix by the random result of the projective measurement. Interestingly, if the measurement result is ignored the last term is removed and the stochastic conditioned master equation reduces to the deterministic unconditioned master equation:

$$d\hat{\rho} = -i\left[\hat{H}, \hat{\rho}\right] dt - \gamma\left[\hat{A}, \left[\hat{A}, \hat{\rho}\right]\right] dt \quad (2.50)$$

This is because the conditioned master equation describes the evolution of the state of knowledge of the system and ignoring the measurement record means that the state of knowledge can not be updated based on the actual measurement record.

2.2.2 Weak measurement in the Bloch sphere representation

Working with density matrices is computationally expensive due to the matrix exponential of the Schrödinger evolution and eight matrix multiplications required for each weak measurement time step. For a two state system this can be reduced to three scalar equations by working entirely with Bloch coordinates, in this section we derive the positional updates of the Bloch vector dx, dy and dy.

Starting with the conditioned master equation for weak measurement and removing the Hamiltonian term for clarity, the z-axis corresponds to measurement of the qubit charge hence $\hat{A} = \sigma_z$ is the measurement operator:

$$d\hat{\rho}_c = -\gamma\left[\sigma_z, \left[\sigma_z, \hat{\rho}_c\right]\right] dt + \sqrt{2\gamma}\left(\sigma_z\hat{\rho}_c + \hat{\rho}_c\sigma_z - 2\left\langle\sigma_z\right\rangle\hat{\rho}_c\right) dW \quad (2.51)$$

The density matrix ρ can be written in terms of the Bloch vector coordinates and their respective Pauli matrices:

$$\hat{\rho}_c = \frac{1}{2}\left(I + \vec{v}\cdot\vec{\sigma}\right) \quad (2.52)$$

$$d\hat{\rho}_c = \frac{1}{2}\left(I + \vec{dv}\cdot\vec{\sigma}\right) \quad (2.53)$$

where $\vec{\sigma}$ is a vector of matrices.

$$\vec{v}=\begin{pmatrix} x \\ y \\ z \end{pmatrix}, \qquad \vec{dv}=\begin{pmatrix} dx \\ dy \\ dz \end{pmatrix}, \qquad \vec{\sigma}=\begin{pmatrix} \sigma_x \\ \sigma_y \\ \sigma_z \end{pmatrix} \tag{2.54}$$

$$\Rightarrow \quad \hat{\rho}_c = \frac{1}{2}(I + x\sigma_x + y\sigma_y + z\sigma_z) \tag{2.55}$$

$$\Rightarrow \quad d\hat{\rho}_c = \frac{1}{2}(I + dx\sigma_x + dy\sigma_y + dz\sigma_z) \tag{2.56}$$

In addition, the following Pauli identities are key to simplifying the derivations:

$$\begin{aligned} \sigma_x\sigma_y &= i\sigma_z, \quad & \sigma_y\sigma_x &= -i\sigma_z \\ \sigma_y\sigma_z &= i\sigma_x, \quad & \sigma_z\sigma_y &= -i\sigma_x \\ \sigma_z\sigma_x &= i\sigma_y, \quad & \sigma_x\sigma_z &= -i\sigma_y \end{aligned} \tag{2.57}$$

$$\sigma_x^2 = \sigma_y^2 = \sigma_z^2 = I$$

Starting with the deterministic term of equation 2.51.

$$-\gamma\left[\sigma_z,[\sigma_z,\hat{\rho}_c]\right]\,dt \;=\; -2\gamma\left(\hat{\rho}_c - 2\sigma_z\hat{\rho}_c\sigma_z\right)\,dt \tag{2.58}$$

Substitute equation 2.55 for $\hat{\rho}_c$ and apply the Pauli identities to simplify the expression:

$$-\gamma\left[\sigma_z,[\sigma_z,\hat{\rho}_c]\right]\,dt \;=\; -2\gamma\left(x\sigma_x + y\sigma_y\right)\,dt \tag{2.59}$$

The stochastic term in dW is expanded and then simplified in the same manner as equation 2.59 but is somewhat complicated by the expectation value $\langle\sigma_z\rangle$

$$\begin{aligned} &\sqrt{2\gamma}\left(\sigma_z\hat{\rho}_c + \hat{\rho}_c\sigma_z - 2\langle\sigma_z\rangle\hat{\rho}_c\right)\,dW \\ =\;& \sqrt{2\gamma}\left(\sigma_z + z - \frac{\langle\sigma_z\rangle}{2}(I + x\sigma_x + y\sigma_y + z\sigma_z)\right)\,dW \end{aligned} \tag{2.60}$$

However, the expectation value $\langle\sigma_z\rangle = \mathrm{Tr}\{\sigma_z\hat{\rho}_c\}$ simplifies well to $\langle\sigma_z\rangle = 2z$ as the trace of the matrix is all that is needed.

$$\begin{aligned} &\sqrt{2\gamma}\left(\sigma_z\hat{\rho}_c + \hat{\rho}_c\sigma_z - 2\langle\sigma_z\rangle\hat{\rho}_c\right)\,dW \\ =\;& \sqrt{2\gamma}\left(-xz\sigma_x - yz\sigma_y + \left(1 - z^2\right)\sigma_z\right)\,dW \end{aligned} \tag{2.61}$$

Combining both the deterministic and stochastic parts yields an expression for the incremental change of the conditioned density matrix as a function of the Bloch vector position prior to measurement.

$$d\hat{\rho}_c = -2\gamma\left(x\sigma_x + y\sigma_y\right)\,dt \;+\; \sqrt{2\gamma}\left(-xz\sigma_x - yz\sigma_y + \left(1 - z^2\right)\sigma_z\right)\,dW \tag{2.62}$$

Collecting the Pauli matrix terms:

$$\begin{aligned} d\hat{\rho}_c = & - (2\gamma dtx + xz\sqrt{2\gamma}dW)\ \sigma_x \\ & - (2\gamma dty + yz\sqrt{2\gamma}dW)\ \sigma_y \\ & + (1-z^2)\sqrt{2\gamma}dW\ \sigma_z \end{aligned} \tag{2.63}$$

Equating the coefficients of the σ_x, σ_y and σ_z terms of equations 2.63 and 2.56 will result in a system of three equations for dx, dy and dz purely in terms of the Bloch vector coordinates x, y and z prior to measurement. This is in agreement with Jacobs' reference [66].

$$dx = -(4\gamma dt + z\sqrt{8\gamma}dW)\ x \tag{2.64}$$

$$dy = -(4\gamma dt + z\sqrt{8\gamma}dW)\ y \tag{2.65}$$

$$dz = +(1-z^2)\sqrt{8\gamma}dW \tag{2.66}$$

These three simple equations (approximately equivalent to a single matrix multiplication) are much more computationally efficient than the original density matrix formulation. It must be remembered that for these equations $\hbar = 1$, so the measurement strength is scaled by $\hbar$ when the Hamiltonian evolution is reintroduced.

It can be seen from equations 2.64 and 2.65 whenever the Bloch vector is displaced from the measurement axis (z-axis) so that $x \neq 0$ and/or $y \neq 0$ there is a constant drift term $-4\gamma dt$ that draws the Bloch vector back to the measurement axis ($x = y = 0$). As this drift occurs perpendicular to the measurement axis, the length of the Bloch vector will shorten and the state $\hat{\rho}$ will become more mixed.

However, the action of storing the weak measurement introduces the stochastic terms in dW which implies that the z coordinate of the now conditioned density matrix $\hat{\rho}_c$ may be non-zero. As the Bloch vector is drawn along the z-axis the Bloch vector may lengthen and the measurement will fractionally purify the state, indeed given time the Bloch vector will gradually purify into one of the two measurement outcomes $|0\rangle$ or $|1\rangle$ (the z-axis poles) due to the non-linearity $1-z^2$.

The work of chapter 5 considers how to implement a remarkable discovery by Jacobs [1] that the rate of qubit purification can be accelerated and indeed made deterministic by exploiting quantum mechanical effects, positioning the Bloch vector on the xy-plane of the Bloch sphere though the use of quantum feedback.

Chapter 3

Modelling the Cooper pair box

In this chapter we focus on superconducting quantum devices that exploit the phenomenon of macroscopic quantum coherence, whereby the quantum effects normally associated with microscopic particles are present in large objects, so that an artificial atom can be created but on a scale measurable by probes. To introduce this a non-mathematical description of superconductivity is provided which leads to macroscopic quantum objects. This is followed by a description of the Josephson junction, a tunnel junction that allows the coherent tunnelling of the many Cooper pairs that form the macroscopic quantum object and provides the conjugate variables of charge and superconductor phase difference. The superconducting charge qubit, also known as the Cooper pair box, is explained and a loop analysis technique developed by Burkard [67] is used as a straightforward and reliable means of obtaining the Hamiltonian of the two superconducting circuits discussed in this thesis.

3.1 Superconducting quantum device physics

Initially, superconducting devices were proposed as fast switching devices for classical computers as an alternative to silicon transistors [68], it was only in the late 1980's that quantum information processing applications were suggested [34].

3.1.1 Superconductivity and macroscopic quantum objects

Superconductivity was discovered in 1911 by Kammerlingh-Onnes [69] whilst measuring the resistivity of mercury at low temperatures. It was found that the resistivity dropped suddenly as the temperature of the mercury fell below a transition temperature, T_C. Furthermore it was later discovered by Meissner in 1933 [70] that all magnetic flux is excluded from the superconductor when cooled

below the transition temperature, this is called the Meissner effect.

Determining the cause of superconductivity proved problematic until a now accepted theory appeared in 1957 by Bardeen, Cooper and Schreiffer, the so called BCS theory [71]. When a metal is cooled, the vibrations of the atomic lattice become smaller as the thermal energy is removed. In a superconductor, the energy is sufficiently small that the vibrations caused by the electrons are transfered to other electrons, these electrons pair up to form *Cooper pairs.* The wavefunction of a pair of bound electrons extends over a longer range than the distance between neighbouring pairs, so that all the Cooper pairs tend to be in the same state, and if one pair moves they all move in the same manner. Therefore, the probability of collisions between the atomic lattice and other scattered electrons is small, therefore the resistance, which is caused by electron collisions, is extremely low.

The collection of many microscopic objects behaving quantum mechanically as one is called a Bose-Einstein condensate, as system cools, many individual Cooper pairs merge together becoming an indistinguishable mass. The Cooper pairs behave as bosons and therefore do not obey the Pauli exclusion principle and can merge together indistinctly into the ground state. Hence, superconductors are *macroscopic quantum objects* which, with a suitable design, could be used to encode microscopic quantum states in a system which yields large measurable results, an artificial atom.

Each superconductor segment X has a phase value θ_X associated with the wavefunction ψ_X that is supported within the segment. This phase value is called the *superconducting phase* and is akin to a voltage potential for normal conductors, as the phase difference between two segments regulates the flow of electrons (current). Electrons can tunnel between two separated superconductors either singly (quasi-particle) or in Cooper pairs, the majority mechanism depends on the temperature of the superconductors. For very low temperatures the majority of charge carriers will be Cooper pairs, the tunnelling distance for Cooper pairs outside of a superconductor is very short (1nm), so is only possible through a thin gap such as a *Josephson junction.* Therefore, Cooper pairs are necessary for Josephson tunnelling currents. For higher temperatures the Cooper pairs break apart and conventional single electron tunnelling starts to occur, the tunnelling distance of a single electron is much larger (10nm) than for a Cooper pair and therefore is generally easier to observe.

3.1.2 The Josephson junction

In 1962 Josephson predicted the tunnelling of a supercurrent between two superconductors separated by an insulator, and derived the equations that describe this process [72]. An excellent introduction to the theory can be found in reference [73]. This result was difficult to verify experimentally as a very fine conducting link between the two superconductors can yield similar effects. The insulator need not necessarily be an oxide type insulator as commonly used in classical electronics, but instead can be a semiconductor or normal metal that is not superconductive, however the analysis becomes more complex as a conductance term is added to fundamental equation 3.1 [74] (*see below*).

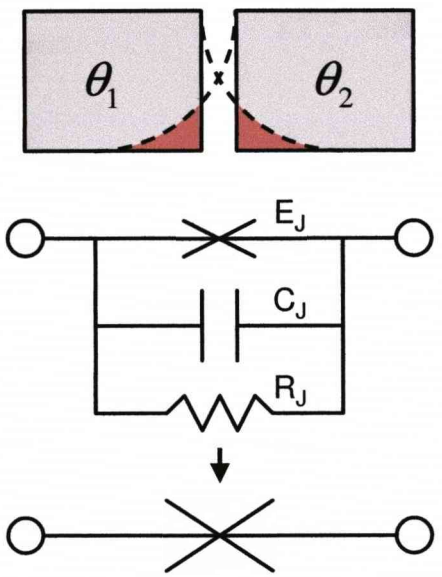

Figure 3.1: Whenever two superconductors are placed close together such that the Cooper pair wavefunctions can overlap (red areas), tunneling of Cooper pairs will occur, this is the Josephson effect. The supercurrent that flows is governed by the phase difference $\theta = \theta_1 - \theta_2$ across the junction. The Josephson junction (cross symbol) can be modelled with a resistor and capacitor in parallel with an ideal junction.

There have been many implementations of Josephson junctions since Josephson first proposed his theory. For early experiments point contact devices [75] were used, where the junction is formed by bringing a sharpened point together with a flat contact (Fig. 3.2A). An advantage of this is that the junction can be adjusted by mechanical means, but unfortunately can suffer from mechanical vibration. Alternatively, a single strip can be narrowed by cutting notches to form the necessary weak link or an insulated break [76] (Fig. 3.2B), although cutting the notch mechanically posed problems in the past which modern micromachin-

ing may now consider trivial. In addition, an unusual solder drop junction was designed by Clarke [77] which fixes the separation of the junction electrodes by joining them using a non-superconductive solder drop (Fig. 3.2C). These implementations would not be considered for use in a future quantum computer as they do not scale well, most modern implementations use photo-lithography to create many junctions where the overlaps formed between the evaporated layers form the Josephson junctions, (Nakamura uses an Al-SiN-Al 'sandwich' where Aluminium is the superconductor and Silicon Nitride is the insulator barrier of the Josephson junction [37]) in addition complex circuits can be created including islands and measurement/control probes (Fig. 3.2D).

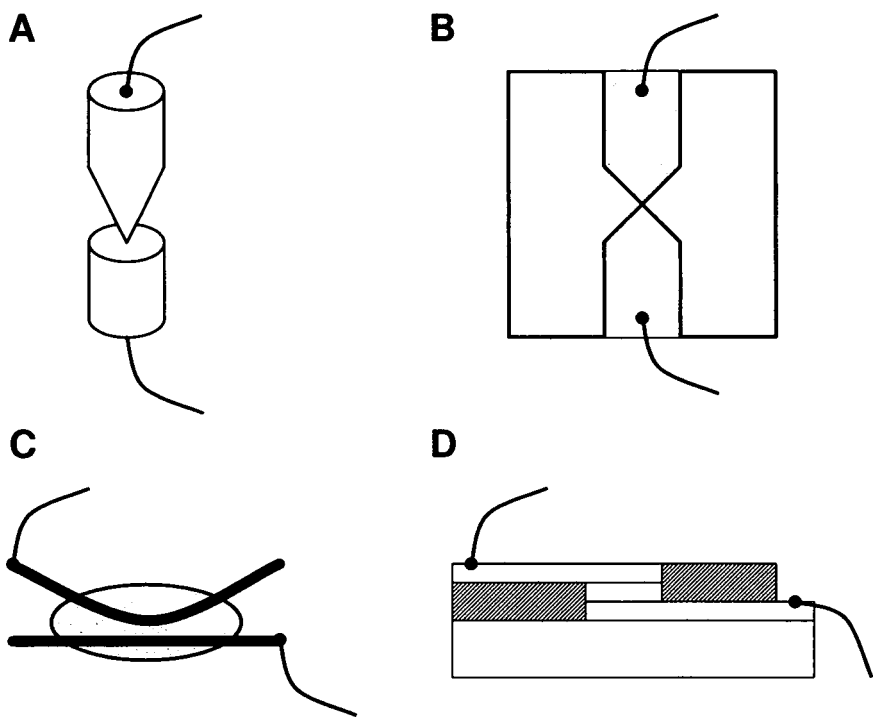

Figure 3.2: (**A**) The point-contact device allows mechanical adjustment of the junction. (**B**) A weak-link device is a planar implementation of the point-contact device. (**C**) Solder-drop junctions encapsulate two superconducting wires within non-superconducting solder keeping the device mechanically stable. (**D**) Modern lithographic techniques form junctions at the overlaps of superconductor-insulator-superconductor regions.

The current through a Josephson junction is dependent on the superconducting phase difference across the junction $\theta = \theta_1 - \theta_2$. A derivation of the Josephson relations (Eqs. 3.1 and 3.2) can be found in reference [78].

$$I = I_C \sin\theta \tag{3.1}$$

$$\frac{\partial\theta}{\partial t} = \frac{2e}{\hbar}V \tag{3.2}$$

where I_C is the critical current, the maximum Cooper pair based current that the superconductor can support before a voltage appears across the junction as the superconductor returns to the normal conduction state.

$$E = E_J \cos\theta = \frac{\hbar}{2e} I_C \cos\theta \tag{3.3}$$

Applying equation 3.2 to 3.1 yields the energy of the Josephson junction, which will be necessary for deriving qubit Hamiltonians. Equation 3.3 can be quantised to a matrix form by expressing the cosine term as the sum of a raising and lowering operator:

$$E = E_J \frac{1}{2}\left(e^{+i\theta} + e^{-i\theta}\right) \tag{3.4}$$

where $\exp(+i\theta)$ is a lowering operator and $\exp(-i\theta)$ is the corresponding raising operator:

$$\hat{H} = E_J \frac{1}{2}\left(\hat{b}^\dagger + \hat{b}\right) \tag{3.5}$$

Constraining the system to two states, the matrix forms of raising and lowering operators are:

$$\hat{b} = \begin{pmatrix} 0 & 1 \\ 0 & 0 \end{pmatrix}, \qquad \hat{b}^\dagger = \begin{pmatrix} 0 & 0 \\ 1 & 0 \end{pmatrix}, \tag{3.6}$$

Hence, by referring to the Pauli matrices σ_x, σ_y and σ_z (Eqs. 2.19, 2.20 and 2.21), the matrix form of a Josephson junction Hamiltonian becomes:

$$\hat{H}_{JJ} = \frac{E_J}{2}\begin{pmatrix} 0 & 1 \\ 1 & 0 \end{pmatrix} = \frac{E_J}{2}\sigma_x \tag{3.7}$$

This Hamiltonian will rotate a Bloch vector around the x-axis at angular frequency $\omega = E_J/\hbar$

Combining two Josephson junctions in parallel allows the critical current I_C to be modified by the magnetic flux flowing between the loop formed by the two junctions.

Given identical junctions, the current applied is assumed to split evenly:

$$I = I_1 + I_2 = I_0(\sin\theta_1 + \sin\theta_2) \tag{3.8}$$

The superconducting phase differences and the flux applied to the loop should sum to zero.

$$\theta_1 - \theta_2 + 2\pi\frac{\Phi}{\Phi_0} = 0 \tag{3.9}$$

$$\Rightarrow \qquad \theta_1 = \theta_2 - 2\pi\frac{\Phi}{\Phi_0}, \qquad \theta_2 = \theta_1 + 2\pi\frac{\Phi}{\Phi_0}$$

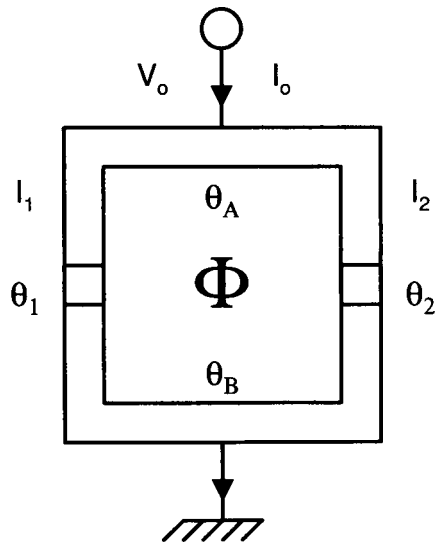

Figure 3.3: The flux threading two parallel connected Josephson junction modulates the critical current of the pair, and thus the junction energy E_J. This potentially allows control of the σ_x rotations for a qubit.

where Φ_0 is the flux quantum:

$$\Phi_0 = \frac{h}{2e} \approx 2.07 \times 10^{-15} Wb \tag{3.10}$$

Subsituting for θ_2 and then subtracting a relative phase in $\pi\Phi/\Phi_0$ yields:

$$\begin{aligned} I &= I_0 \left(\sin(\theta_1) + \sin\left(\theta_1 + 2\pi \frac{\Phi}{\Phi_0}\right)\right) \\ I &= I_0 \left(\sin\left(\theta_1 - \pi \frac{\Phi}{\Phi_0}\right) + \sin\left(\theta_1 + \pi \frac{\Phi}{\Phi_0}\right)\right) \end{aligned} \tag{3.11}$$

which allows a trigonometric identity to be used, that reveals on comparison with equation 3.1 that the flux Φ passing through the ring modulates the critical current I_C:

$$I = 2I_0 \cos\left(\pi \frac{\Phi}{\Phi_0}\right) \sin(\theta) \tag{3.12}$$

$$I_C(\Phi) = 2I_0 \cos\left(\pi \frac{\Phi}{\Phi_0}\right) \tag{3.13}$$

This allows the tunnelling frequency $\omega = E_J/\hbar$ to be controllable, which proves useful for developing the quantum feedback protocols of Chapter 5.

As an aside, this circuit has led to perhaps the most common use of Josephson junctions, as magnetometers [79]. A constant current I_0 flows into the parallel junctions, if it exceeds the combined critical current of the pair I_C a voltage forms across the circuit V_0. As the critical current I_C has a cosinusoidal dependence

on the applied magnetic flux Φ, this threshold I_C will reduce toward zero as Φ tends to $\Phi_0/2$ and a detectable voltage start to form ($I_0 > I_C$), with each cycle corresponding to one flux quantum.

3.1.3 Superconducting charge qubits

The Cooper pair box designed by Buttiker in 1987 [34], is named because of the tunnelling of Cooper pairs in to and out of a box-like island. As it is a superconducting implementation of a qubit that uses charge as the observable, it is also known as a superconducting charge qubit [80].

The qubit is essentially a small segment of superconductor called the 'island' or 'box' coupled to a bulk superconductor called the 'reservoir' or 'tank' via one or more Josephson junctions. The island is small enough to warrant a large charging energy such that the tunnelling experiences the Coulomb blockade effect [81, 35], so that the island can only support one excess Cooper pair at any one time and likewise only a single Cooper pair can tunnel on to and off this island.

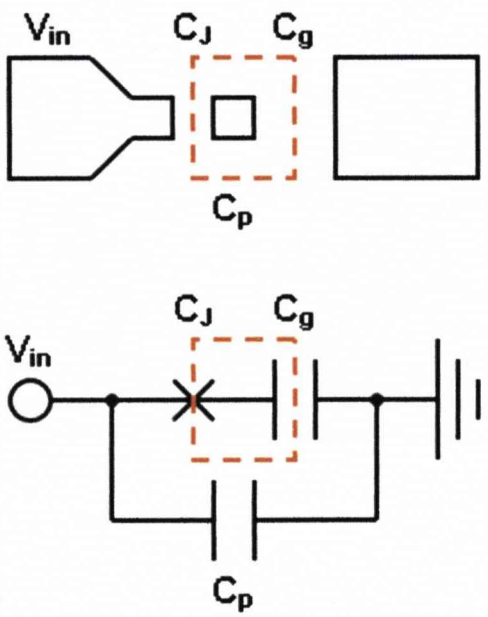

Figure 3.4: The single junction Cooper pair box can be modelled by an equivalent electrical circuit model. The three most significant capacitances are: C_J - The capacitance of the Josephson junction. C_g - The capacitance between the island and the bulk superconductor. C_P - The parasitic capacitance formed between the biasing and ground electrodes. The bias is applied using voltage V_{in}.

The quantum state information is encoded as the presence or absence of a Cooper pair charge on the island, for example $2e \equiv |1\rangle$ and $0e \equiv |0\rangle$. The

quantum mechanical nature of such a qubit arises from the macroscopic wave-function within the superconductor. The conjugate variables are charge q and superconducting phase difference θ, and so a commutator relation is allowed by introducing the Josephson junction.

$$[\hat{n}, \hat{\theta}] = i \tag{3.14}$$

This non zero commutator implies that the island charge and phase can not be measured simultaneously, identical to that of the position and momentum relation found in atomic physics. The qubit is biased by applying a voltage V across the device using a *gate* electrode which induces the biasing charge n_g (expressed as a number of Cooper pairs), where:

$$n_g = \frac{C_g}{2e} V \tag{3.15}$$

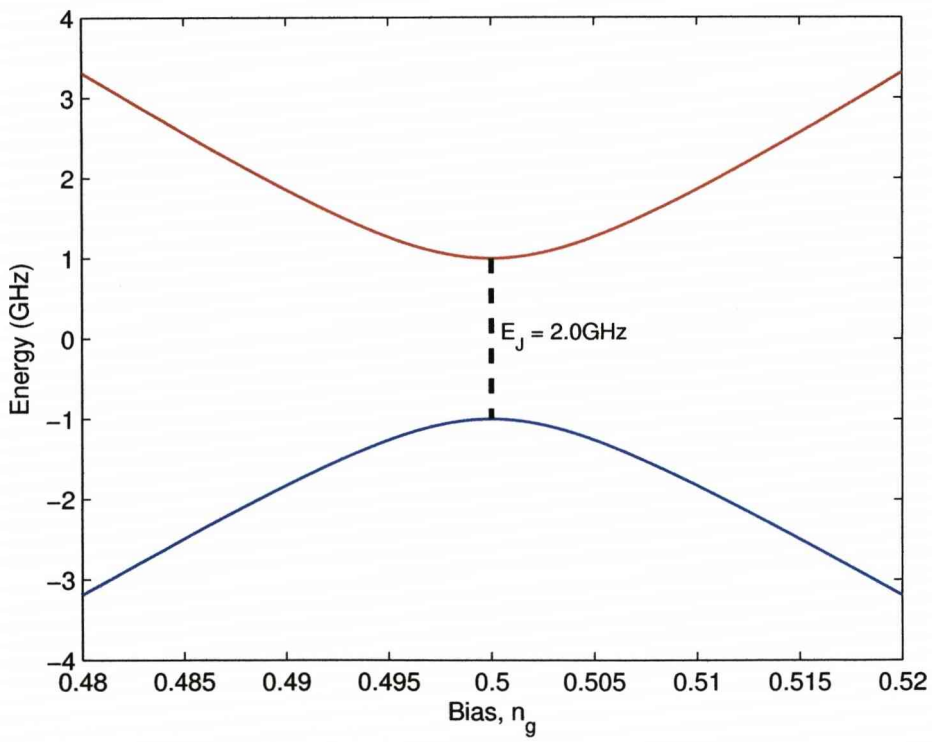

Figure 3.5: The charge qubit energylevel structure where the energy is expressed in GHz, $E = hf$. A Josephson junction causes an avoided crossing at what would otherwise be the degeneracy point $n_g = 0.5$)

The charge qubit energy level separation varies as a function of the applied bias charge n_g (Fig. 3.5). Without a Josephson junction present the energy states would simply cross at $n_g = 0.5$, however when a finite frequency Josephson

junction is included an avoided crossing occurs with an energy splitting equal to the junction frequency when biased at $n_g = 0.5$. This avoided crossing creates two different energy eigenvalues instead of the expected degeneracy.

It can be seen from Figure 3.6 that the energy states are formed from many overlapping parabolas with minimas at integer values of n_g, each parabola corresponds to a different charge state, i.e. the number of extra Cooper pairs on the island. It is of considerable importance to note that whenever the bias is near $n_g = 0.0$ or $n_g = 1.0$ the energy gap between the $|1\rangle$ and $|2\rangle$ states becomes small, and so there is an increased risk of accessing the unwanted $|2\rangle$ state via thermal or driven excitation.

When working near $n_g \approx 0.5$ the energy required to access the $|2\rangle$ state is considerable (Fig.3.6) and so the *two state approximation* should be valid, whereby the single qubit Hilbert space is constrained to two dimensions, and therefore the matrices that represent qubit operators need only have dimensions of [2x2] elements.

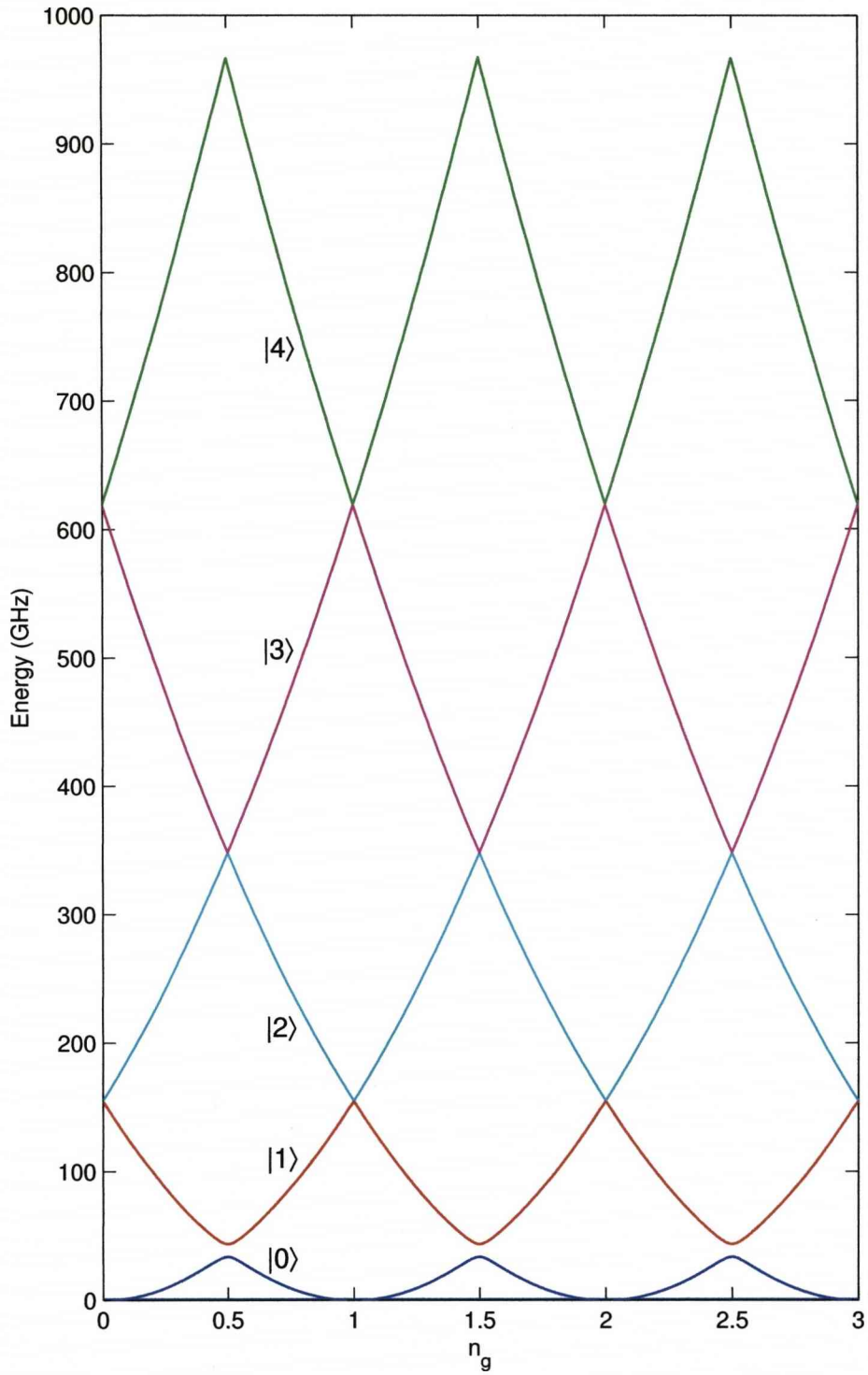

Figure 3.6: Parabolic shaped energy level structure of a qubit with more than two energy states, it can be seen that when the the bias n_g is set to a half integer value the energy separation between state $|1\rangle$ and state $|2\rangle$ is very large and so the two state approximation should hold. However, whenever n_g approaches an integer value these energy separations become small and the qubit may easily access the unwanted $|2\rangle$ state. (E_J=10GHz to show visible splitting, E_C=160GHz.)

3.2 Superconducting circuits

Modern electronic engineering literature [82, 83, 84] teaches electrical circuit analysis by solution of simultaneous equations to calculate the necessary voltage and currents as this allows the circuit to be solved in a clear manner, however an alternative technique considers the total energy in the system, the Hamiltonian. The Hamiltonian (H) is more commonly found in physics and mechanical engineering literature [85] and completely describes the system in terms of the energy stored in the components, the circuit voltages and currents derive from the charges (Q) and fluxes (Φ) within the circuit are given by Hamilton's equations.

$$\dot{x} = \frac{\partial H}{\partial p}, \qquad \dot{p} = \frac{\partial H}{\partial x} \tag{3.16}$$

$$\dot{Q} = \frac{\partial H}{\partial \Phi}, \qquad \dot{\Phi} = \frac{\partial H}{\partial Q} \tag{3.17}$$

Like their classical counterparts, quantum superconducting circuits can be modelled through equivalent circuit analysis, although the Josephson junction has no exact classical analogue it exhibits behaviour similar to an inductor. The layout of the physical superconducting segments can be mapped to a circuit diagram, however there will also be parasitic capacitances between the segments that need to be identified and added to the network.

3.2.1 Loop analysis for superconducting circuits

Deriving a circuit Hamiltonian can be a cumbersome task, however work by Burkard has yielded a set of rules for determining the Hamiltonian of any superconducting circuit [67], focusing on charge and flux qubits. Burkard's technique uses matrices to define the topology of a circuit.

1. Simplify graph

The circuit diagram is reduced to a graph where each circuit component forms a branch. The Josephson junction is always assumed to have a small capacitance in parallel with the junction.

2. Assign directions

Every branch of the circuit graph is assigned a direction, which would be typically in line with the expected current flow.

3. Extract network tree

The network tree is constructed by removing **capacitor branches only** so that there are no loops in the graph but every node is still connected. The branches that have been removed are termed *chords*.

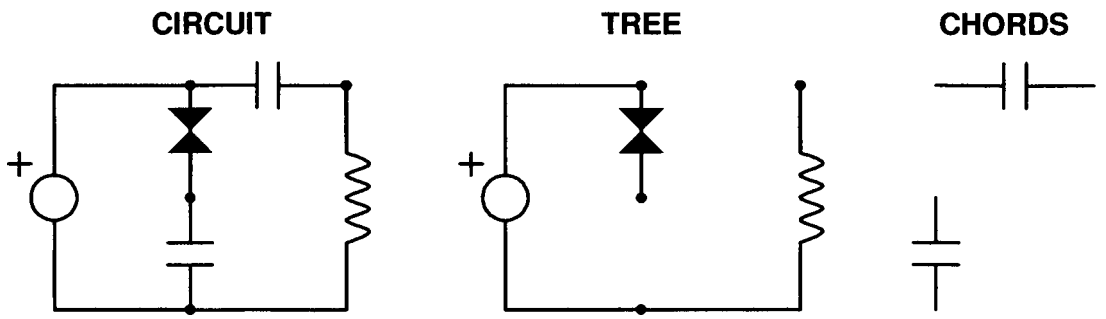

Figure 3.7: Capacitors are removed to form the 'Tree' (a loopless graph), each removed branch is called a 'Chord'. Replacing each chord creates a 'Fundamental loop'.

4. Fundamental loop matrix

Each fundamental loop F_i is created by replacing one chord, to reform a unique loop. The loop is encoded in a matrix by comparing the flow of the loop with the direction of each component branch in the original network graph.

$$\mathbf{F}_{\mathbf{ij}}^{(\mathbf{L})} = \begin{cases} +1, & \text{if } \mathrm{b_j} \in \mathrm{F_i} \text{ and same direction} \\ -1, & \text{if } \mathrm{b_j} \in \mathrm{F_i} \text{ and opposite direction} \\ 0, & \text{if } \mathrm{b_j} \notin \mathrm{F_i} \end{cases} \tag{3.18}$$

where i = 1, ... M and j = 1, ... N as there are M loops and N branches.

5. Current and voltage vectors and loop matrix detail

The individual currents and voltages in and across each branch, are represented by vectors.

$$\mathbf{I} = \left(\mathbf{I_{tr}}, \mathbf{I_{ch}} \right), \qquad \mathbf{V} = \left(\mathbf{V_{tr}}, \mathbf{V_{ch}} \right) \tag{3.19}$$

With this ordering of the tree and chord variables, the fundamental loop matrix $\mathbf{F^{(L)}}$ will have the following form if equation 3.18 is followed correctly:

$$\mathbf{F^L} = \left(-\mathbf{F^T}, \mathbf{1} \right) \tag{3.20}$$

where $\mathbf{F}$ is now the loop matrix of interest and $\mathbf{1}$ is just a matrix of ones.

Furthermore the current and voltage vectors can be subdivided into groups pertaining to the **type** of circuit component:

$$\begin{aligned} \mathbf{I_{tr}} &= \left(\mathbf{I_J}, \mathbf{I_L}, \mathbf{I_V}, \mathbf{I_Z} \right), & \mathbf{I_{ch}} &= \left(\mathbf{I_{C_J}}, \mathbf{I_C}, \mathbf{I_K} \right) \\ \mathbf{V_{tr}} &= \left(\mathbf{V_J}, \mathbf{V_L}, \mathbf{V_V}, \mathbf{V_Z} \right), & \mathbf{V_{ch}} &= \left(\mathbf{V_{C_J}}, \mathbf{V_C}, \mathbf{V_K} \right) \end{aligned} \tag{3.21}$$

where for the tree: $\mathbf{J} \Rightarrow$ Josephson junctions, $\mathbf{L} \Rightarrow$ inductors, $\mathbf{V} \Rightarrow$ voltage sources and $\mathbf{Z} \Rightarrow$ impedances. Likewise for the chord branches, $\mathbf{C_J} \Rightarrow$ capacitances associated with Josephson junctions, $\mathbf{C} \Rightarrow$ capacitors and $\mathbf{K} \Rightarrow$ chord inductors (inductances of the capacitors and wires - which can be optional). Thus the loop matrix should have the following structure, from which particular parts will be extracted for further use:

$$\mathbf{F} = \begin{pmatrix} \mathbf{1} & \mathbf{F_{JC}} & \mathbf{F_{JK}} \\ \mathbf{0} & \mathbf{F_{LC}} & \mathbf{F_{LK}} \\ \mathbf{0} & \mathbf{F_{VC}} & \mathbf{F_{VK}} \\ \mathbf{0} & \mathbf{F_{ZC}} & \mathbf{F_{ZK}} \end{pmatrix} \tag{3.22}$$

The third column with the chord inductor terms ($\mathbf{K}$) can be omitted if the inductance of the capacitances (and wires) can be ignored, from this point on the chord inductances will be ignored as it somewhat simplifies the analysis and is suggested by Burkard that is only necessary for circuits such as the quantronium [33].

6. Calculate the capacitance matrix C

It is necessary to calculate a capacitance matrix which will be used in the final equation for the Hamiltonian.

$$C = \begin{pmatrix} \mathbf{C_J} & \mathbf{0} \\ \mathbf{0} & \mathbf{0} \end{pmatrix} + F_C \, \mathbf{C} \, F_C^T \equiv \begin{pmatrix} \mathbf{C_{tot}} & \mathbf{C_{JL}} \\ \mathbf{C_{JL}^T} & \mathbf{C_L} \end{pmatrix} \tag{3.23}$$

where F_C is a new notation introduced to represent a vector of parts from equation 3.22.

$$F_C = \begin{pmatrix} \mathbf{F_{JC}} \\ \mathbf{F_{LC}} \end{pmatrix} \tag{3.24}$$

The matrix $\mathbf{C}$ is a diagonal matrix with the capacitances listed on the diagonal in the order that the loop chords were removed to be consistent with the loop matrix $\mathbf{F}$, similarly matrix $\mathbf{C_J}$ stores the Josephson junction capacitances and should be listed in the order that they were analysed to be consistent with loop matrix $\mathbf{F}$.

$$\mathbf{C} = \begin{pmatrix} C_1 & 0 & 0 & 0 \\ 0 & C_2 & 0 & 0 \\ 0 & 0 & \ddots & 0 \\ 0 & 0 & 0 & C_M \end{pmatrix}, \quad \mathbf{C_J} = \begin{pmatrix} C_{J1} & 0 & 0 & 0 \\ 0 & C_{J2} & 0 & 0 \\ 0 & 0 & \ddots & 0 \\ 0 & 0 & 0 & C_{JX} \end{pmatrix} \tag{3.25}$$

Next the capacitance as seen by the voltage sources needs to be determined, referring back to equation 3.22 for the relevant parts:

$$\mathbf{C_V} = F_C \, \mathbf{F_{VC}^T} \, F_C^T \equiv \begin{pmatrix} \mathbf{C_{JV}} \\ \mathbf{C_{LV}} \end{pmatrix} \tag{3.26}$$

7. The potential U(Φ)

At this point, the cosinusoidal terms characteristic of Josephson junctions are added in addition to the potential caused by the magnetic flux in the circuit inductors. Burkard defines the potential to be (in the absence of chord inductors):

$$\mathbf{U}(\Phi) \;=\; -\mathbf{E_J}\cos\theta + \frac{1}{2}\Phi^{\mathrm{T}}\mathbf{L}^{-1}\Phi \tag{3.27}$$

where like before (Eq. 3.25), the matrices $\mathbf{E_J}$ and $\mathbf{L}$ are diagonal matrices with the component values listed along the diagonal in an order consistent with the loop analysis.

$$\mathbf{E_J} = \begin{pmatrix} E_{J1} & 0 & 0 & 0 \\ 0 & E_{J2} & 0 & 0 \\ 0 & 0 & \ddots & 0 \\ 0 & 0 & 0 & E_{JX} \end{pmatrix}, \qquad \mathbf{L} = \begin{pmatrix} L_1 & 0 & 0 & 0 \\ 0 & L_2 & 0 & 0 \\ 0 & 0 & \ddots & 0 \\ 0 & 0 & 0 & L_Y \end{pmatrix} \tag{3.28}$$

8. Define the charge variables

The charges present in the system can be divided into two groups: $\mathbf{Q_J}$ which are the island charges and $\mathbf{Q_L}$ which are the tank circuit charges.

$$\mathbf{Q} = \begin{pmatrix} \mathbf{Q_J} \\ \mathbf{Q_L} \end{pmatrix} \tag{3.29}$$

9. Substitute to determine the Hamiltonian

The Hamiltonian H is defined by the following matrix equation which should yield a scalar expression for the energy when the results of the previous stages have been substituted.

$$H \;=\; \frac{1}{2}\left(\mathbf{Q} - \mathbf{C_V}\,\mathbf{V}\right)^T C^{-1}\left(\mathbf{Q} - \mathbf{C_V}\,\mathbf{V}\right) + \mathbf{U}(\Phi) \tag{3.30}$$

3.2.2 Simple Cooper pair box Hamiltonian

This is the simplest Cooper pair box circuit, as it does not take into account the dynamics associated with the biasing circuitry. It is the circuit used for the purification work of chapter 5 as the bias charge n_g does not depend on the value of a dynamically changing system and can instead be held constant.

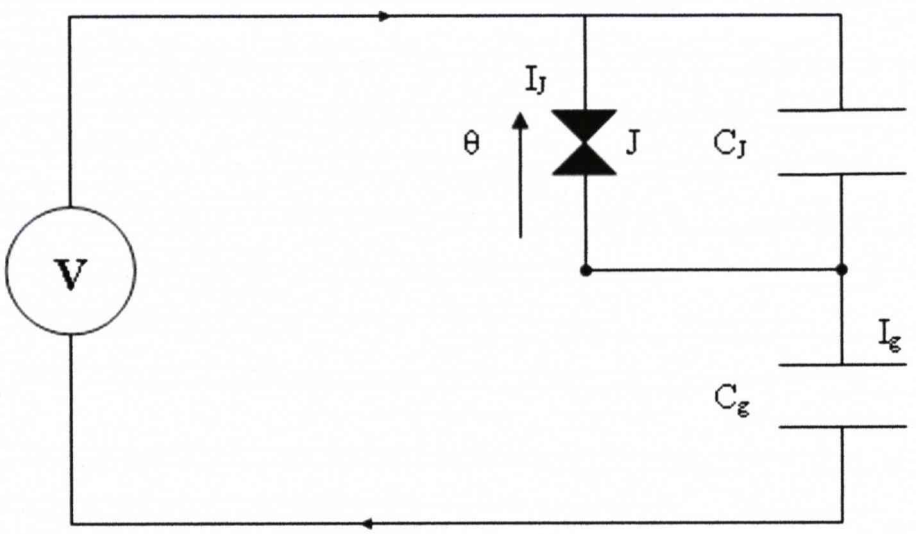

Figure 3.8: Directions added to graph

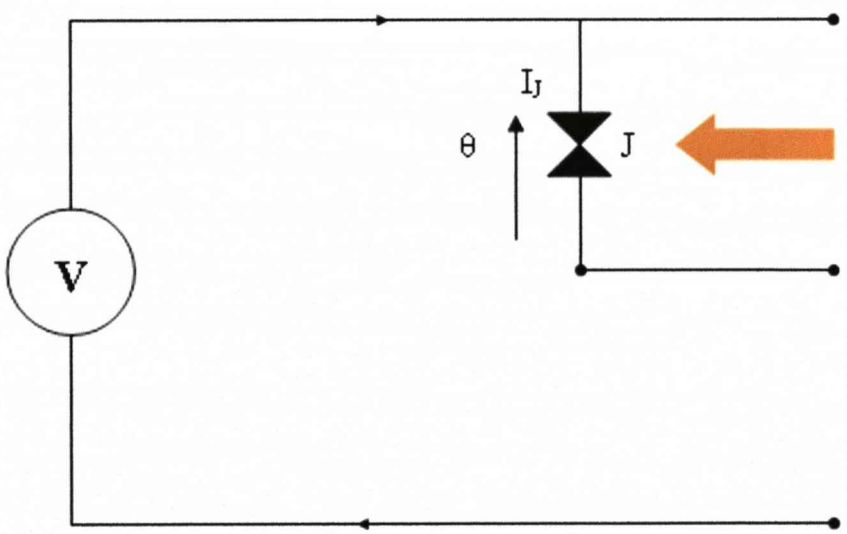

Figure 3.9: Graph is reduced to a tree, where the capacitance of the Josephson is lumped with the junction symbol and remaining capacitors are removed.

The tree is easily obtained by removing capacitor C_g. The capacitance of the Josephson junction C_J is always assumed to be in parallel with the junction and

no other components are in the loop, therefore it is combined with the junction symbol.

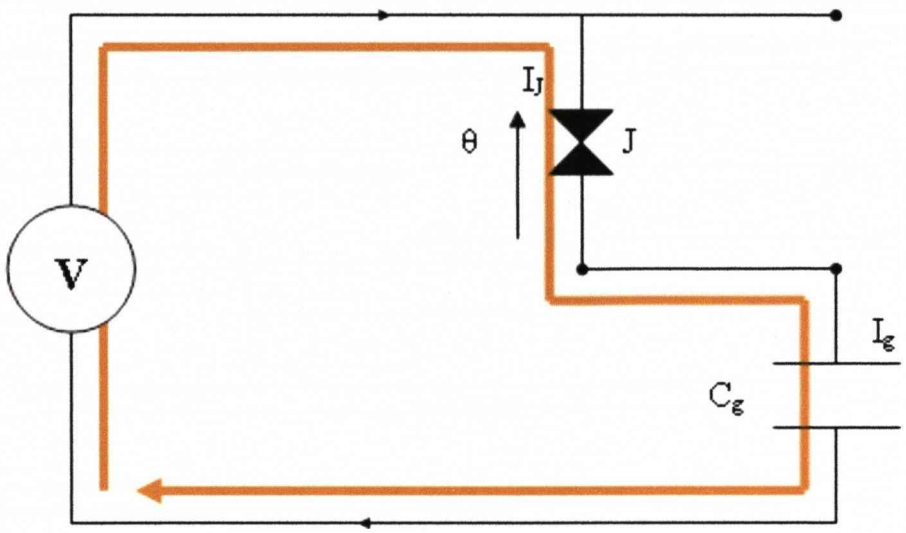

Figure 3.10: Fundamental loop created by replacing chord capacitor C_g

We have assumed that no components are inductively shunted because the inductance of capacitors should be very small, and as there are no inductors or resistive components, the loop matrix (Eq. 3.22) reduces to:

$$\mathbf{F} = \begin{pmatrix} \mathbf{1} & \mathbf{F_{JC}} \\ \mathbf{0} & \mathbf{F_{VC}} \end{pmatrix} \tag{3.31}$$

As replacing the chord capacitor yields the only fundamental loop, the submatrices $\mathbf{F_{JC}}$ and $\mathbf{F_{VC}}$ are scalar:

$$\mathbf{F_{JC}} = 1, \qquad \mathbf{F_{VC}} = 1, \tag{3.32}$$

Similarly, the capacitance matrices are simply $\mathbf{C} = C_g$ and $\mathbf{C_J} = C_J$. In addition, the charge matrix $\mathbf{Q}$ only contains a single variable, the island charge $q \equiv Q_J$. As there is no inductance, the potential $U(\Phi)$ (Eq. 3.27) reduces to the cosinusoidal Josephson energy term:

$$U(\Phi) \;=\; -E_J \cos\theta \tag{3.33}$$

Substituting into equation 3.30 yields the Hamiltonian:

$$\hat{H} \;=\; \frac{1}{2}\frac{(\hat{q} + C_g V)^2}{C_J + C_g} \;-\; E_J \cos\hat{\theta} \tag{3.34}$$

where $C_g V = n_g$ is the biasing charge induced by the voltage source that controls the qubit behaviour (Sec. 3.3).

The matrix form of the Hamiltonian operator $\hat{H}$ is required to solve the time dependent Schrödinger equation (Eq 2.34) numerically. We have constrained the qubit to two states and therefore defined the excited state as the existence of a single Cooper pair on the island, and the ground state to be an absence of island charge. The co-sinusoidal Josephson energy-phase relation is replaced by a tunnelling matrix which is the combination of a raising and lowering operator as derived in section 3.1.2.

$$\hat{q} = \begin{pmatrix} 0 & 0 \\ 0 & +2e \end{pmatrix}, \qquad \cos\hat{\theta} = \frac{1}{2}\begin{pmatrix} 0 & 1 \\ 1 & 0 \end{pmatrix} \tag{3.35}$$

The voltage term $C_g V$ is a biasing charge, which is usually expressed as a biasing value n_g that has units of 'Number of Cooper pairs'. The tunnelling frequency of the Josephson junction ν is related to the junction energy E_J through Planck's constant. The effective qubit capacitance C_q is the capacitance that defined the energy of qubit charge q in equation 3.34.

$$C_g V = 2e\, n_g, \qquad E_J = \hbar\nu, \qquad C_q = C_g + C_J \tag{3.36}$$

Subsituting equations 3.35 and 3.36 into equation 3.34, working with the charge expressed as the number of Cooper pairs rather than in Coulombs yields:

$$\hat{H} = \frac{(2e)^2}{2C_q}\begin{pmatrix} 0-n_g & 0 \\ 0 & 1-n_g \end{pmatrix}^2 - \frac{\hbar\nu}{2}\begin{pmatrix} 0 & 1 \\ 1 & 0 \end{pmatrix} \tag{3.37}$$

Multiplying the diagonal charge matrix:

$$\hat{H} = \frac{2e^2}{C_q}\begin{pmatrix} n_g^2 & 0 \\ 0 & 1-2n_g+n_g^2 \end{pmatrix} - \frac{\hbar\nu}{2}\begin{pmatrix} 0 & 1 \\ 1 & 0 \end{pmatrix} \tag{3.38}$$

The charge matrix is separated into an identity matrix which will not affect the dynamics, and a remainder that will:

$$\hat{H} = \frac{2e^2}{C_q}\left(\begin{pmatrix} n_g^2 & 0 \\ 0 & n_g^2 \end{pmatrix} + \begin{pmatrix} 0 & 0 \\ 0 & 1-2n_g \end{pmatrix}\right) - \frac{\hbar\nu}{2}\begin{pmatrix} 0 & 1 \\ 1 & 0 \end{pmatrix} \tag{3.39}$$

It can be shown that the matrix which defines the dynamical behavior of the system, only creates z-axis rotations of the Bloch vector, as it can be decomposed into a σ_z Pauli matrix and an identity matrix.

$$\hat{H} = \frac{2e^2}{C_q}\left(\begin{pmatrix} n_g^2 & 0 \\ 0 & n_g^2 \end{pmatrix} + \begin{pmatrix} -0.5+n_g & 0 \\ 0 & 0.5-n_g \end{pmatrix} + \begin{pmatrix} 0.5-n_g & 0 \\ 0 & 0.5-n_g \end{pmatrix}\right) - \frac{\hbar\nu}{2}\begin{pmatrix} 0 & 1 \\ 1 & 0 \end{pmatrix} \tag{3.40}$$

$$\hat{H} = \frac{2e^2}{C_q}\left(\frac{1}{2} - n_g + n_g^2\right) I + \frac{2e^2}{C_q}\left(\frac{1}{2} - n_g\right)\sigma_z - \frac{\hbar\nu}{2}\sigma_x \tag{3.41}$$

3.2.3 Cooper pair box Hamiltonian including parasitic capacitance and oscillator dynamics

This is the circuit used for the work of Chapter 4. We now include the parasitic capacitance C_P connected across the entire qubit as it is formed between the biasing electrodes that surround the qubit island. In addition, the inductance L of the wire connecting the bias is included. For this circuit the tree (Fig. 3.12) is formed by removing the two capacitances C_P and C_g, the Josephson junction capacitance is combined with the junction symbol.

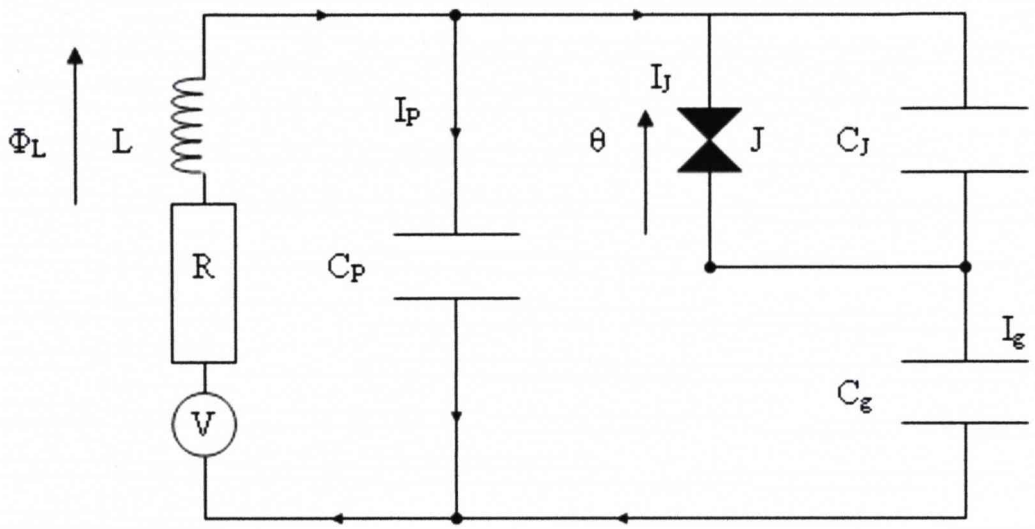

Figure 3.11: Directions added to graph

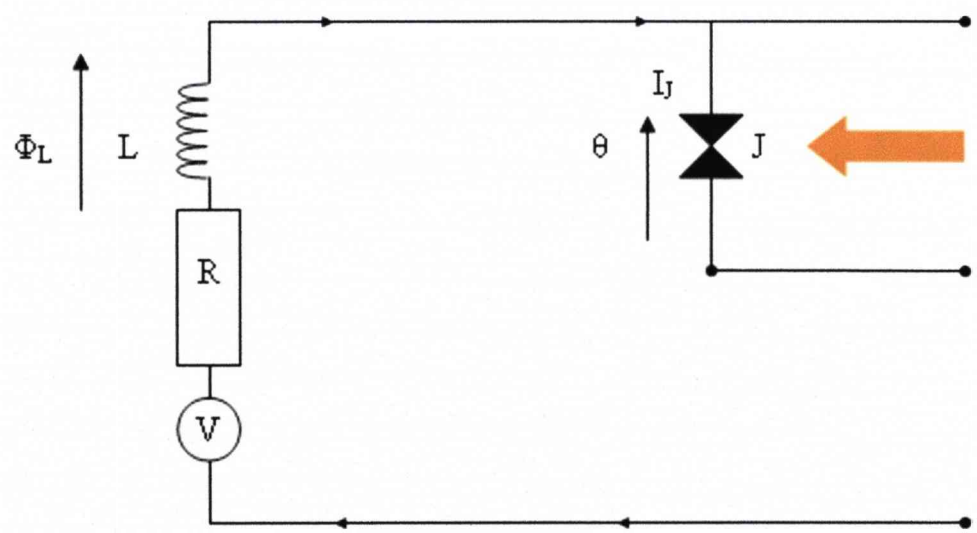

Figure 3.12: Graph is reduced to a tree, where the capacitance of the Josephson is lumped with the junction symbol and remaining capacitors are removed.

The two chords that were removed from figure 3.11 to form the tree are replaced to form the two fundamental loops shown by figure 3.13.

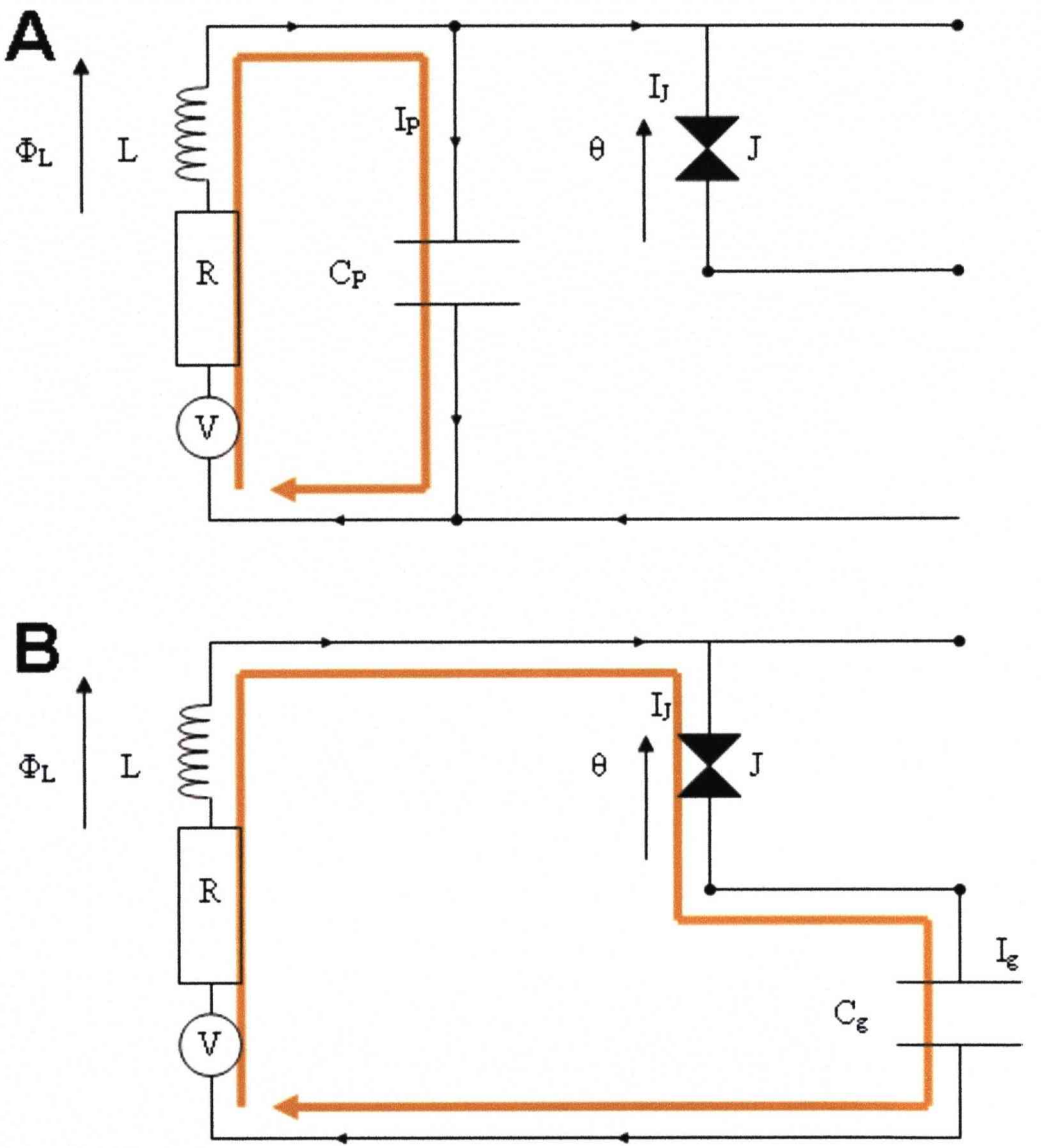

Figure 3.13: Fundamental loops obtained by replacing a chord capacitor, C_P generates Loop **A**, likewise C_g creates Loop **B**.

As in section 3.2.2, we have assumed that no components are inductively shunted so that $K = 0$ and the loop matrix (Eq. 3.22) reduces to:

$$\mathbf{F} = \begin{pmatrix} \mathbf{1} & \mathbf{F_{JC}} \\ \mathbf{0} & \mathbf{F_{LC}} \\ \mathbf{0} & \mathbf{F_{VC}} \\ \mathbf{0} & \mathbf{F_{ZC}} \end{pmatrix} \tag{3.42}$$

where the sub-matrices $\mathbf{F_{JC}}$, $\mathbf{F_{LC}}$, $\mathbf{F_{VC}}$ and $\mathbf{F_{ZC}}$ are found by applying the rules

defined in equation 3.18. Note that $\mathbf{F_{JC}}$ is different because the Josephson junction only exists in Loop **B**, whereas all other component types are present in both loops, and defined in the same direction.

$$\begin{array}{c} \qquad\qquad\quad Loop\ A \quad Loop\ B \\ Component\ 1 \quad (\ X \qquad Y\ ) \end{array} \tag{3.43}$$
$$\mathbf{F_{JC}} = \begin{pmatrix} 0 & 1 \end{pmatrix}, \qquad \mathbf{F_{LC}} = \begin{pmatrix} 1 & 1 \end{pmatrix}$$
$$\mathbf{F_{VC}} = \begin{pmatrix} 1 & 1 \end{pmatrix}, \qquad \mathbf{F_{ZC}} = \begin{pmatrix} 1 & 1 \end{pmatrix}$$

There is only one Josephson junction hence matrix $\mathbf{C_J}$ is actually scalar. As Loop **A** was formed by replacing capacitor C_g and likewise Loop **B** formed by replacing C_P, the capacitance matrix **C** is:

$$\mathbf{C_J} = C_J, \qquad \mathbf{C} = \begin{pmatrix} C_g & 0 \\ 0 & C_P \end{pmatrix} \tag{3.44}$$

For this circuit there is a single junction energy E_J and one inductance L and flux variable Φ, hence the expression for the potential $U(\Phi)$ is purely scalar.

$$U(\Phi) \;=\; -E_J \cos\theta + \frac{\Phi^2}{2L} \tag{3.45}$$

However we define two charge variables, the island charge $q \equiv \mathbf{Q_J}$ and the tank circuit (bias circuit) charge $Q \equiv \mathbf{Q_L}$ which forms the vector **Q**:

$$\mathbf{Q} = \begin{pmatrix} q \\ Q \end{pmatrix} \tag{3.46}$$

Subsituting the above into equation 3.30 yields a rather lengthy expression, however it is possible to collect the energy terms in q, Q and the cross coupling term qQ and replace the physical capacitances C_J,C_g and C_P with capacitances C_q,C_Q and C_{qQ} which define the energies associated with charges q, Q and qQ.

$$H = \frac{1}{2}\frac{q^2}{C_q} + \frac{1}{2}\frac{qQ^2}{C_{qQ}} + \frac{1}{2}\frac{Q^2}{C_Q} + QV + \frac{1}{2}\frac{\Phi^2}{L} - E_J \cos\theta \tag{3.47}$$

where:

$$C_q \;=\; \frac{C_J C_P + C_g C_P + C_J C_g}{C_g + C_P} \tag{3.48}$$
$$C_{qQ} \;=\; \frac{C_J C_P + C_g C_P + C_J C_g}{2C_g} \tag{3.49}$$
$$C_Q \;=\; \frac{C_J C_P + C_g C_P + C_J C_g}{C_J + C_g} \tag{3.50}$$

Through the introduction of a 'coupling constant' it is possible to recover the simple qubit model from the previous section (Eq. 3.34) plus additional terms regarding the oscillator and qubit coupling. This process is described as part of section 4.2.1.

3.3 Qubit behaviour

On comparing the value of the effective qubit capacitance C_q from section 3.2.2 with section 3.2.3 it can be seen that when C_g and C_P are small compared with C_J, the capacitance of the Josephson junction tends to dominate in both circuits. Therefore the qubit behaviour may not be affected greatly by the presence of the parasitic capacitance *per se*, but is instead much more dependent on the applied bias n_g which for the work of chapter 4 *is* affected by the capacitance C_P as it forms part of a coupled oscillator circuit. However, if the oscillator dynamics are ignored and a perfect bias can be applied, either model (and value of C_q) would be acceptable. The circuit used for the purification work of chapter 5 includes a parasitic capacitance C_P but ignores the oscillator dynamics caused by the inductor L_{osc} and so simplifies to equation 3.41.

3.3.1 Qubit rotations

The qubit Hamiltonian (Eq. 3.41) is formed from the sum of an identity matrix that does not affect the Bloch vector, a σ_z Pauli matrix that creates z-axis rotations controlled by biasing charge n_g and a σ_x Pauli matrix that generates rotations around the x-axis at an angular frequency ν defined by the Josephson energy E_J. Whilst there is no σ_y matrix present, any required rotation about the y-axis can be created from combinations of the other two rotational axes, although the path of rotation may differ.

It is important to note that whilst the z-axis rotations of the Bloch vector can be stopped by setting $n_g = 0.5$, the x-axis rotations can only be halted by setting the tunnelling energy to $E_J = 0$ which may not be possible or desirable as this makes the energy eigenstates degenerate where the separation between the energy levels becomes zero at $n_g = 0$. Ideally we would like the energy separation to be quite large as this prevents unwanted transitions between states caused by thermal excitation. It is the key problem of 'halting' the Bloch vector of a qubit with non-zero tunnelling energy that we address within Chapter 5, indeed we find that an engineered constant (non-zero) value of E_J can be beneficial to some purification protocols [86, 1].

3.3.2 Microwave drive and Rabi oscillations

The qubit may also be driven by exposure to microwave radiation (Chapter 4). The microwave drive can be modelled by adding a sinusoidal varying bias at the microwave frequency in addition to the dc voltage bias n_g, such that the

Hamiltonian becomes time varying [87, 88]:

$$\hat{H}(t) = \frac{2e^2}{C_q}\left(\frac{1}{2} - n_g(t) + n_g(t)^2\right) I + \frac{2e^2}{C_q}\left(\frac{1}{2} - n_g(t)\right)\sigma_z - \frac{\hbar\nu}{2}\sigma_x \quad (3.51)$$

where $n_g(t) = n_g + A_{mw}\cos(\omega_{mw}t)$

As the Hamiltonian is changing as a function of time, it is necessary to calculate the time averaged energies or Floquet energies to obtain a stationary result that can be plotted. The microwave drive creates transitions between the energy levels whenever the energy gap is equal to the microwave frequency $E_{mw} = \hbar\omega_{mw}$ (Black lines). There are also weaker multi-photon transitions at the higher harmonics, as illustrated by the 3.0GHz microwave drive and 6.0GHz harmonic. The width of these transitions increase with the amplitude of the driving microwave: Large microwave fields can distort the energy structure far from the intended bias point, especially when applied close to the avoided crossing as this region is locally flat.

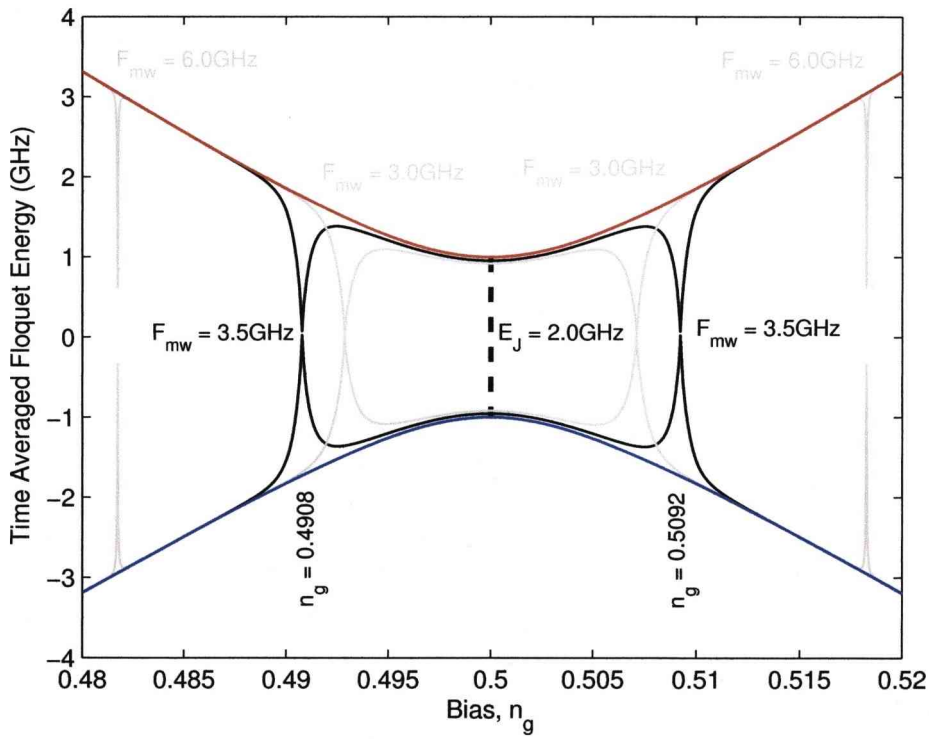

Figure 3.14: The microwave drive creates transitions between the energy levels. The transitions occur where the energy gap is equal to the microwave energy (frequency). The width of the transition is proportional to the microwave amplitude.

Whenever the qubit is biased near a microwave transition, Rabi oscillations occur such that the qubit state is driven in a sinusoidal fashion between two computational states, for example if F_{mw}=3.5GHz then n_g=0.5092 as per figure 3.14.

The 'amplitude' of the Rabi (state) oscillations is dependent on the biasing, with maximum amplitude when the qubit energy gap is biased at the microwave drive frequency. Whereas, the frequency of the Rabi oscillation is directly proportional to the microwave amplitude [89].

Changing the state of a microwave driven qubit can be achieved through manipulating either the microwave or bias. Note that to demonstrate the change of qubit state, figures 3.15 and 3.16 do not include decoherence so the state does not relax back to the ground state. Figure 3.15 shows one such method that involves pulsing the microwave drive to momentarily create a Rabi oscillation that changes the qubit state, by holding the qubit on a constant bias the oscillation has constant frequency and therefore the qubit rotation is defined by the duration of the microwave pulse [88]. Unfortunately the constant bias is difficult to achieve due to a backreaction effect proportional to the gradient of the energy structure that moves the bias away from the steep microwave transition (Fig. 3.14). An alternative scheme uses a 'continuous' microwave to create a constant transition between the energy levels, through which the biasing point is transferred by ramping the bias value from one side of the transition to the other (the microwave can be pulsed but should be continuous over the duration of the ramping). Whilst the bias point is being ramped, a partial Rabi oscillation occurs that changes the state, a slower ramp results in a larger qubit rotation.

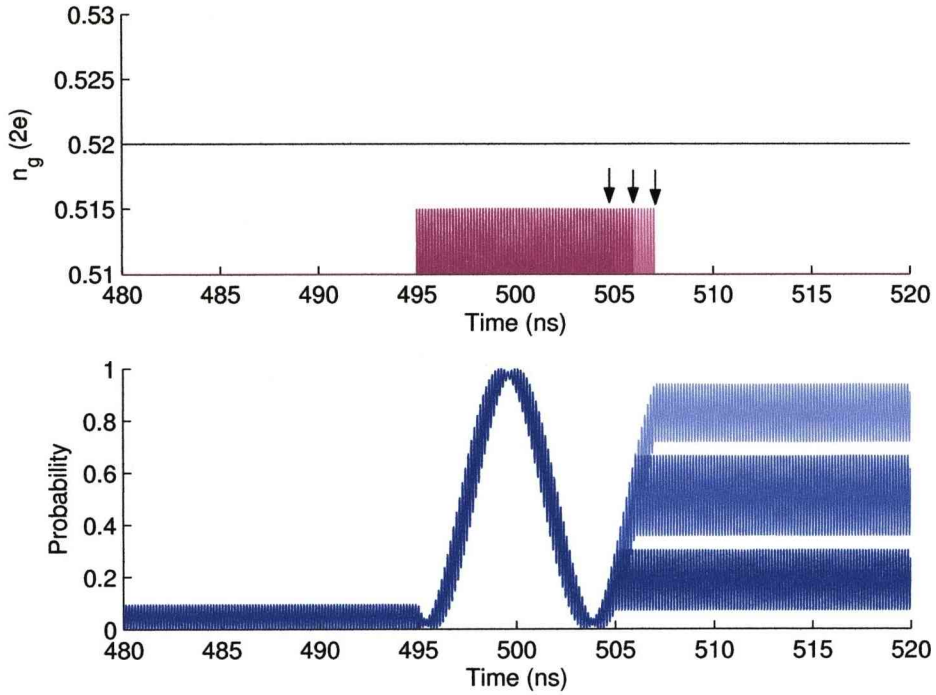

Figure 3.15: Qubit is held at a constant bias on the microwave transition and irradiated by a microwave pulse. The probability of being in the excited state can be set by stopping the microwave pulse mid-cycle. (the three arrows)

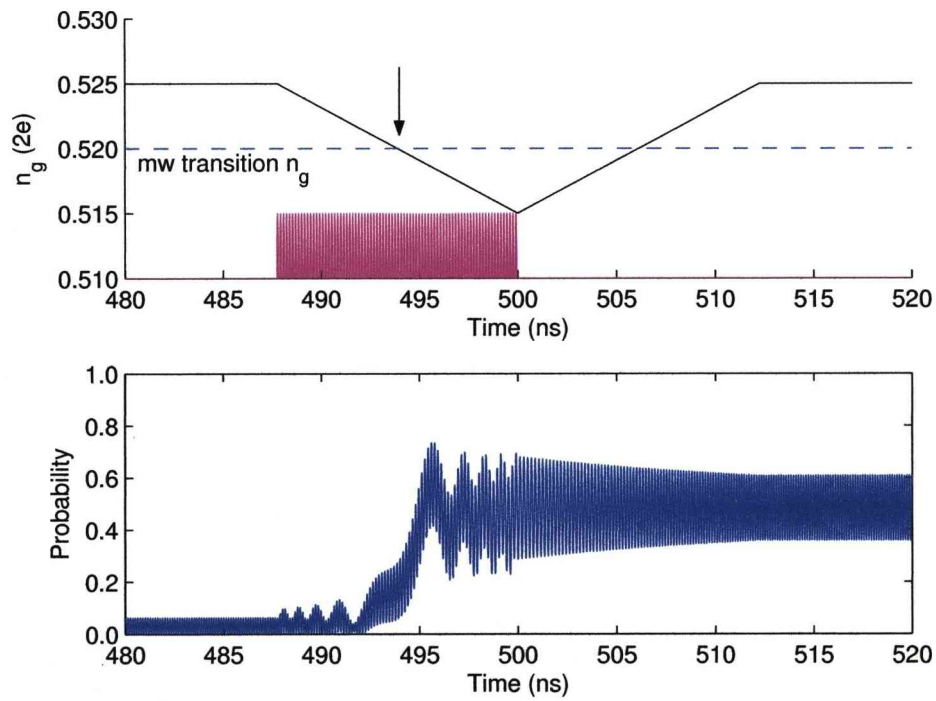

Figure 3.16: The qubit bias is ramped from $n_g = 0.525$ to $n_g = 0.515$ through a microwave transition at $n_g = 0.520$, the duration of the ramp at the point indicated by the arrow sets the final qubit state. Note that the microwave drive is not applied if the bias point is to be moved back to the start $n_g = 0.525$.

Chapter 4

Qubit spectroscopy

This chapter focuses on the problem of characterising the actual controls applied to a superconducting charge qubit. This is usually not considered a significant problem for quantum computing architectures such as quantum optics or ion trapping, however the solid state architectures exhibit strong coupling to external devices which includes lengthy measurement and control probes [90]. To enable superconduction and reduce thermal noise, it is necessary to cool a Niobium qubit down to the order of 10-30mK, and therefore the qubit has to be very well insulated and isolated from the 300K temperature of the typical laboratory workroom [91, 92]. This isolation is a key problem as the control fields must be applied through a complicated series of amplifiers and filters to reach the qubit [8], which can not be easily characterised and thus the actual value of the control can be difficult to ascertain. The following work investigates spectroscopy as a possible means of charactersing a microwave driven qubit, whilst a classical model is used for the microwave we also consider classical and quantised models for bias control field. We will show that particular features found within a frequency spectrum can be useful, and in addition by operating the qubit in an unusual frequency regime a greater number of features can be obtained.

4.1 The external world

Solid state implementations of quantum computing exploit macroscopic quantum coherence to allow quantum effects to be reproduced using large devices 3.1.1, indeed these device are even considered large (1μm [8] and 700nm [37]) when compared with contemporary classical integrated circuit technology (90nm [93]). However, there is a key difference, quantum effects are extremely sensitive to noise and so the solid state quantum devices need to operate at very low temperatures (regardless of superconductor or semiconductor implementations) within a *cryo-*

stat to suppress thermal transitions between states and to ensure that there are only two computational states in use (usually the two lowest states). As the device needs to be well isolated from the external environment this naturally makes the qubit environment inaccessible, therefore experimentalists use long chains of finite bandwidth amplifiers and filters to take well defined signals produced by a signal generator on the 'laboratory bench' to the isolated qubit without coupling too much noise. Unfortunately, to achieve control of a qubit the experimentalist needs to know the *actual* value of the control reaching the qubit after the effects of dissipation and noise.

In this chapter we investigate the use of the qubit backreaction on the biasing field to extract information regarding the qubit behaviour caused by the actual controls, this backreaction effect arises from the capacitive coupling between the qubit island and biasing probe. Thereby opening the possibility that the actual control received at the qubit can be estimated through distinct changes in the qubit behaviour but observed in the biasing field.

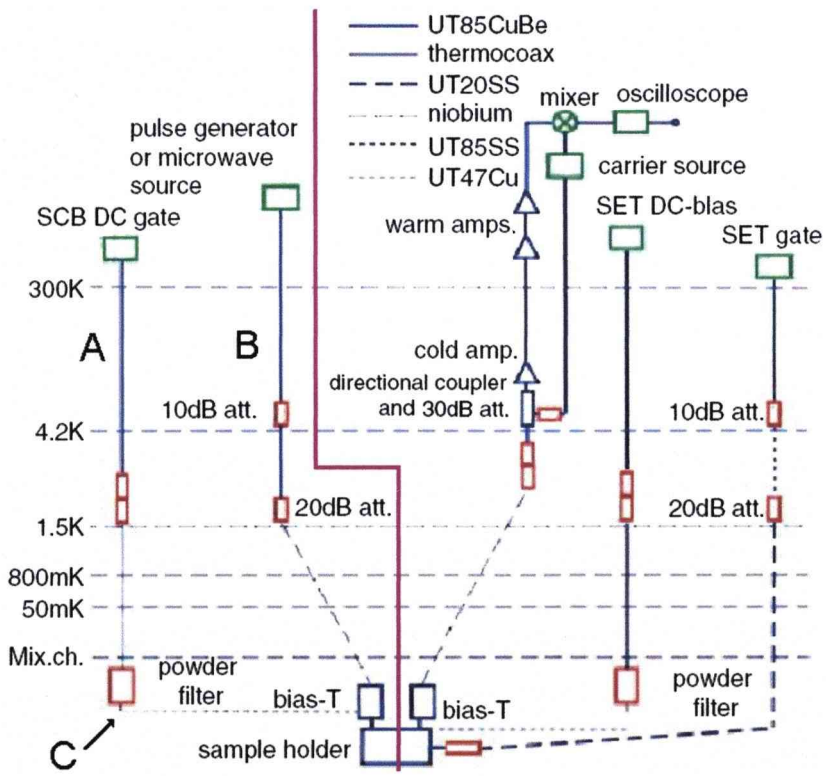

Figure 4.1: A typical cryostat setup showing the attenuation and filter stages for each temperature range. The work of this chapter focuses on the qubit-bias control interaction and does not consider the SET device on the right hand side of the dividing line. The original image can be found in figure 8 of reference [8], K Bladh *et al.* (2005)

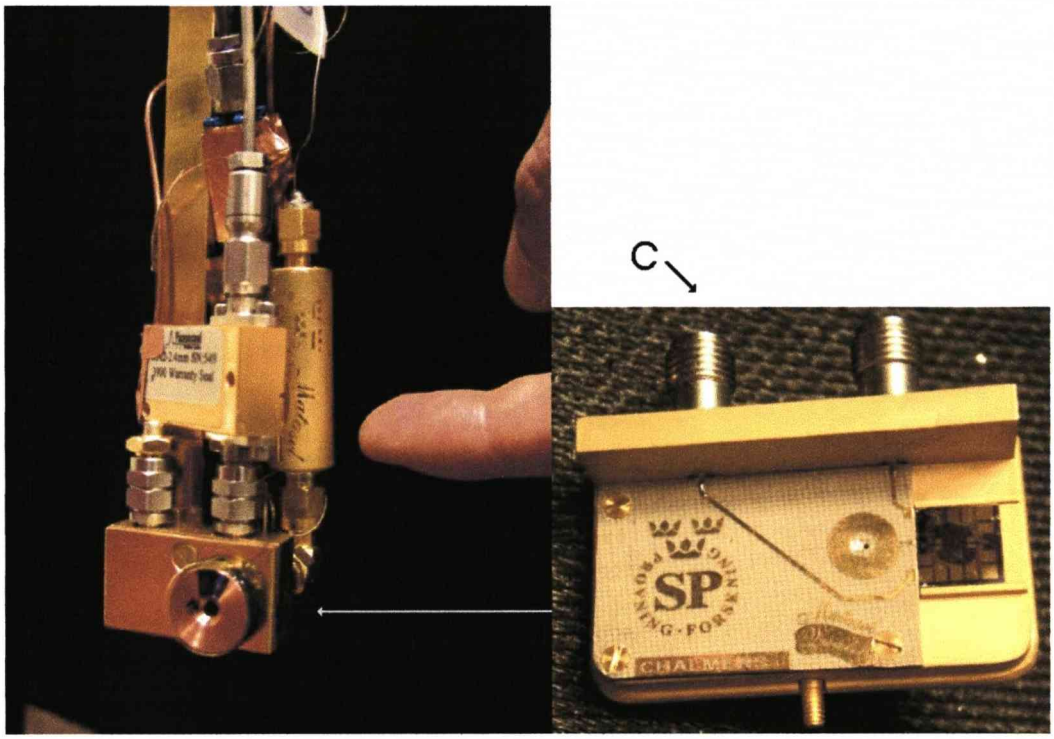

Figure 4.2: Photographs of the cold end of the cryostat (left) and sample holder (right) used by experimentalists at Chalmers University, Sweden. Our model is limited to the 'sample holder' region, where the bias is applied through point C. The original images can be found in reference [8], K Bladh *et al.* (2005)

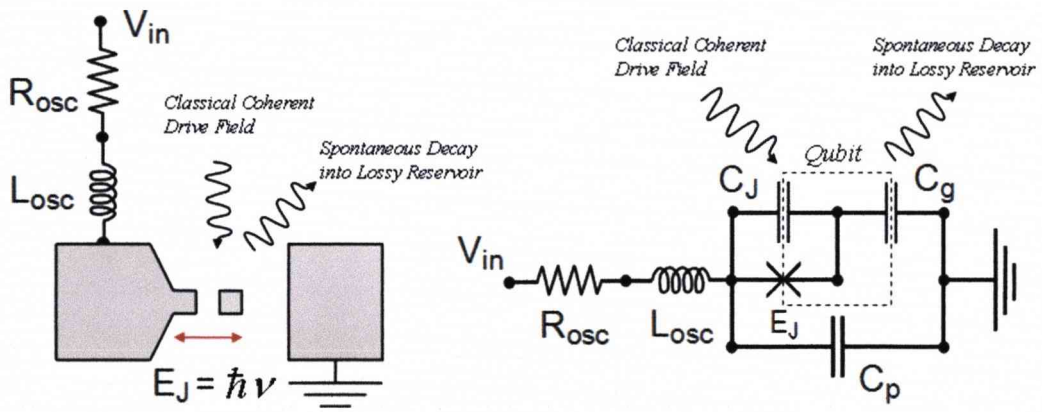

Figure 4.3: An abstract layout of a simple single junction Cooper pair box, with the biasing voltage connection to the first filter stage modelled by a resistor and inductor. The Cooper pair box is modeled by an equivalent circuit network, consisting of three capacitors: C_J - the capacitance of the Josephson junction, C_g - The capacitance of the island gate, and C_p - the parasitic capacitance formed between the biasing electrodes. These capacitors, together with the resistor and inductor form an RLC oscillator circuit. The qubit also undergoes spontaneous emission which is modelled by a two-level atom quantum jump model.

This work focuses on the interaction between the qubit and the coupled control probe at the end of the amplifier chain (as indicated by the arrow **C** of figure 4.1, for simplicity the dynamics of the full amplifier and filter chain are not included. The dissipative control probe (immediately coupled to the qubit) is modelled by the series inductor and resistor found in the cable, together with the parasitic and device capacitances associated with the qubit this forms a series RLC oscillator as shown in figure 4.3. The values for each component in this chapter can be found in table 4.1, note that the work of section 4.4 uses a higher frequency 3.00GHz oscillator, otherwise all other sections assume $F_{osc} = 1.33$GHz.

Table 4.1: Components

	Description	Typ.
$\nu/2\pi$	Josephson junction energy	2.00GHz
C_J	Josephson junction capacitance	500aF
C_g	Qubit-Grounded Bulk capacitance	0.5aF
C_p	Electrodes parasitic capacitance	1.0aF
Q_{osc}	Oscillator quality factor	300
γ	Qubit jump rate parameter	65×10^6
	(Low frequency)	
F_{osc}	Resonant frequency of biasing circuit	1.33GHz
R_{osc}	RLC circuit resistance	265kΩ
L_{osc}	RLC circuit inductance	95mH
	(High frequency)	
F_{osc}	Resonant frequency of biasing circuit	3.00GHz
R_{osc}	RLC circuit resistance	118kΩ
L_{osc}	RLC circuit inductance	19mH

In section 4.2 the bias oscillator circuit is modelled by a dampened second order classical system which interacts with the two level qubit. However in section 4.3.3 this oscillator is modelled as a many level simple harmonic oscillator coupled to the two level qubit.

4.2 Classical dynamics coupled to a quantum system

Initially, it is a reasonable simplification to assume that the qubit is coupled to a control probe that behaves classically, hence the RLC oscillator is governed by a second order differential equation.

4.2.1 Deriving the classical equations of motion

Starting from the Hamiltonian of the coupled system as derived in section 3.2.3 it is possible to rewrite this Hamiltonian so that the product of the qubit and oscillator charges are separated. In addition, a coupling constant κ is introduced by which the coupling capacitance C_{qQ} is expressed as a ratio of C_q.

$$H_{system} = \frac{\hat{q}^2}{2C_q} + \frac{\hat{q}Q}{2C_{qQ}} + \frac{Q^2}{2C_Q} + \frac{\Phi^2}{2L_{osc}} + VQ - \hbar\nu\cos\left(\frac{2\pi}{\Phi_0}\hat{\theta}\right) \tag{4.1}$$

Collect the classical terms (Q, Φ) and quantum terms $(\hat{q}, \hat{\theta})$ together:

$$H_{system} = \frac{Q^2}{2C_Q} + \frac{\Phi^2}{2L_{osc}} + VQ + \frac{\hat{q}^2}{2C_q} + \frac{\hat{q}Q}{2C_{qQ}} - \hbar\nu\cos\left(\frac{2\pi}{\Phi_0}\hat{\theta}\right) \tag{4.2}$$

Introduce the coupling term κ:

$$\kappa = \frac{C_q}{2C_{qQ}} \tag{4.3}$$

$$H_{system} = \frac{Q^2}{2C_Q} + \frac{\Phi^2}{2L_{osc}} + VQ + \frac{\hat{q}^2}{2C_q} + \frac{2\kappa\hat{q}Q}{2C_q} - \hbar\nu\cos\left(\frac{2\pi}{\Phi_0}\hat{\theta}\right) \tag{4.4}$$

It is now possible to factor the qubit charge term $\hat{q}^2$ and cross-product charge term $2\kappa\hat{q}Q$, in to $(\hat{q}+\kappa Q)^2$ with the introduction of a subtractive term to compensate for the expansion of $(\hat{q}+\kappa Q)^2$.

$$H_{system} = \frac{Q^2}{2C_Q} + \frac{\Phi^2}{2L_{osc}} + VQ + \underbrace{\frac{(\hat{q}+\kappa Q)^2}{2C_q} - \frac{\kappa^2 Q^2}{2C_q}} - \hbar\nu\cos\left(\frac{2\pi}{\Phi_0}\hat{\theta}\right) \tag{4.5}$$

Collecting the two classical and two quantum variables together as best possible yields an equation which can be somewhat divided into classical and quantum parts, although still coupled through the classical variable Q:

$$H_{system} = \underbrace{\frac{Q^2}{2C_Q}\left(1 - \kappa^2\frac{C_Q}{C_q}\right) + \frac{\Phi^2}{2L_{osc}} + VQ}_{H_{oscillator}(\Phi,Q;\ V)} + \underbrace{\frac{(\hat{q}+\kappa Q)^2}{2C_q} - \hbar\nu\cos\left(\frac{2\pi}{\Phi_0}\hat{\theta}\right)}_{H_{qubit}(\hat{q},\hat{\theta};\ Q)} \tag{4.6}$$

The qubit Hamiltonian will eventually be quantised to a matrix form whilst the oscillator Hamiltonian evolves separately as a scalar classical evolution. To simulate the entire system, at each time step the qubit Hamiltonian is evolved as a Time Dependent Schrödinger Equation (TDSE) and the energy expectation value is taken, thus the energy contribution of the qubit is assumed to be $\langle E \rangle$:

$$\langle E \rangle = \langle \psi(t) | \, H_{qubit}(\hat{q}, \hat{\theta};\ Q) \, | \psi(t) \rangle \tag{4.7}$$

$$\langle E \rangle = E(Q) \tag{4.8}$$

$$H = H_{system} = \frac{1}{2C_Q}\left(1 - \kappa^2 \frac{C_Q}{C_q}\right) Q^2 + \frac{1}{2L_{osc}} \Phi^2 + VQ + E(Q) \tag{4.9}$$

Hamilton's equations, which describe the relationship between position, momentum and energy are employed to derive the classical equations of motion that govern the evolution of the oscillator charge Q. The oscillator charge Q is taken to be analogous to the position x and likewise the oscillator flux Φ is the conjugate momentum p.

$$\dot{x} = \frac{\partial H}{\partial p}, \qquad \dot{p} = \frac{\partial H}{\partial x} \tag{4.10}$$

$$\dot{Q} = \frac{\partial H}{\partial \Phi}, \qquad \dot{\Phi} = \frac{\partial H}{\partial Q} \tag{4.11}$$

Applying Hamilton's equations (Eq. 4.11) to the system Hamiltonian (Eq. 4.9):

$$\dot{Q} = -\frac{1}{L_{osc}} \Phi \tag{4.12}$$

$$\dot{\Phi} = \frac{1}{C_Q}\left(1 - \kappa^2 \frac{C_Q}{C_q}\right) Q + V + \frac{\partial E}{\partial Q} \tag{4.13}$$

Equation 4.12 would imply that the second order time derivative of the oscillator charge is now conveniently given by equation 4.13 as:

$$\ddot{Q} = -\frac{1}{L_{osc}} \dot{\Phi} \quad \ldots\ldots \quad = -\frac{1}{L_{osc}}\left(\frac{1}{C_Q}\left(1 - \kappa^2 \frac{C_Q}{C_q}\right) Q + V + \frac{\partial E}{\partial Q}\right) \tag{4.14}$$

The contribution of the qubit to the evolution of the oscillator charge by the backreaction effect is obtained by differentiating $E(Q)$ with respect to Q, which is equivalent to differentiating $\langle H_{qubit} \rangle$.

$$\langle H_{qubit} \rangle = \frac{1}{2C_q}(\langle \hat{q} \rangle + \kappa Q)^2 - \hbar\nu \cos\left(\frac{2\pi}{\Phi_0}\langle \hat{\theta} \rangle\right) \tag{4.15}$$

$$\langle H_{qubit} \rangle = \frac{1}{2C_q}(\langle \hat{q} \rangle^2 + 2\kappa \langle \hat{q} \rangle Q + \kappa^2 Q^2) - \hbar\nu \cos\left(\frac{2\pi}{\Phi_0}\langle \hat{\theta} \rangle\right) \tag{4.16}$$

$$\frac{\partial E}{\partial Q} = \frac{\partial \langle H_{qubit} \rangle}{\partial Q} = \frac{\kappa \langle \hat{q} \rangle + \kappa^2 Q}{C_q} \tag{4.17}$$

Therefore completing equation 4.14 which can be numerically solved at each simulation step to obtain the time evolution of the oscillator charge. A resistive term is added to model dissipation losses in the biasing circuitry, as the Hamiltonian itself is generally assumed to model non-dissipative processes.

$$\ddot{Q} = -\frac{1}{L_{osc}} \left(\frac{1}{C_Q} Q - R_{osc} \dot{Q} + V + \frac{\kappa}{C_q} \langle \hat{q} \rangle \right) \tag{4.18}$$

We have used Euler's method to solve the differential equation numerically and reduce the complexity and computational time of the model:

$$Q = Q + \dot{Q} dt \tag{4.19}$$

$$\dot{Q} = \dot{Q} + \ddot{Q} dt \tag{4.20}$$

It is of vital importance to remember that the classical equation to be solved is also a function of the qubit island charge, and likewise the qubit behaviour is partly governed by the biasing charge of the oscillator. Therefore it is necessary to update the classical oscillator and evolve the qubit state simultaneously, for each time step dt.

4.2.2 Qubit evolution

As the qubit is a quantised system it is simulated quite differently. It is necessary to quantise the qubit Hamiltonian (H_{qubit}) to a matrix form, by quantising the two operators $\hat{q}$ and $\hat{\theta}$.

$$H_{qubit} = \frac{1}{2C_q} (\hat{q} + \kappa Q)^2 - \hbar \nu \cos \left(\frac{2\pi}{\Phi_0} \hat{\theta} \right) \tag{4.21}$$

We assume a two level approximation for the qubit, where the qubit state is represented by a $[2 \times 1]$ element vector $|\psi\rangle$. The two level approximation constrains the qubit charge operator $\hat{q}$ to a $[2 \times 2]$ element matrix, where the two possible outcomes on the diagonal are either an uncharged island (0) to represent $|0\rangle$, or the island is charged with a Cooper pair ($2e$) to represent $|1\rangle$.

$$\hat{q} = \begin{pmatrix} 0 & 0 \\ 0 & 2e \end{pmatrix} \tag{4.22}$$

The classical variable Q is simply introduced by using the identity matrix $\hat{Q} \equiv Q\hat{I}$, so that Q affects the qubit regardless of the current state of the qubit.

The cosine term containing the superconducting phase variable $\hat{\theta}$ across the Josephson junction is quantised to a σ_x Pauli matrix (See section 3.1.2) which permits tunnelling between the two outcomes at a frequency defined by ν. Substituting the operators for the matrix forms yields:

$$\hat{H}_{qubit} = \frac{1}{2C_q}\begin{pmatrix} \kappa Q & 0 \\ 0 & 2e+\kappa Q \end{pmatrix}^2 - \frac{\hbar\nu}{2}\begin{pmatrix} 0 & 1 \\ 1 & 0 \end{pmatrix} \tag{4.23}$$

The qubit is driven by a classical microwave field at frequency F_{mw} and amplitude A_{mw}, the microwave is applied as a time dependent bias field [87, 88] at the microwave frequency. The now time dependent Hamiltonian is:

$$\begin{aligned} \hat{H}_{qubit}(t) &= \frac{1}{2C_q}\begin{pmatrix} \kappa Q + Q_{mw}(t) & 0 \\ 0 & 2e+\kappa Q + Q_{mw}(t) \end{pmatrix}^2 \\ &\quad -\frac{\hbar\nu}{2}\begin{pmatrix} 0 & 1 \\ 1 & 0 \end{pmatrix} \end{aligned} \tag{4.24}$$

$$Q_{mw}(t) = A_{mw}\sin(\omega_{mw}(t)) \tag{4.25}$$

The qubit Hamiltonian can also be expressed with Pauli matrices as per section 3.2.2, where $n_g = \kappa Q + Q_{mw}(t)$:

$$\begin{aligned} \hat{H}_{qubit}(t) &= \frac{(2e)^2}{2C_q}\left(n_g^2 - n_g + \frac{1}{2}\right) I \\ &\quad + \frac{(2e)^2}{2C_q}\left(\frac{1}{2} - n_g\right)\sigma_z - \frac{\hbar\nu}{2}\,\sigma_x \end{aligned} \tag{4.26}$$

The state $|\psi(t)\rangle$ of a closed (not disturbed) quantum system evolves deterministically as per the Schrödinger Equation. However, to model spontaneous emission of photons in the qubit we introduce a quantum jump unravelling [94], which is a stochastic process called a *quantum trajectory* [95] that modifies a pure state, if we assume that all emitted photons are measured without loss then the state vector should remain pure [94]. Each trajectory can be interpreted as an example of a *single qubit* evolution undergoing stochastic changes. The quantum jump model has been adapted from a two-level atom model, by which the atom either emits a photon that is measured and collapses the qubit state or proceeds with a modified Schrödinger evolution. The decision to emit a photon is governed by two jump operators, Ω_0 and Ω_1, and the jump rate parameter γ where the probability of emission increases as the current qubit state nears the excited state.

$$\text{NO JUMP} \qquad \Omega_0 = \hat{H}_{qubit} - \frac{\gamma}{2}\,\sigma^\dagger\sigma dt \tag{4.27}$$

$$\text{JUMP} \qquad \Omega_1 = \sqrt{\gamma dt}\,\sigma \tag{4.28}$$

Ω_1 is the detection operator and Ω_0 is the Schrödinger evolution as per the qubit Hamiltonian, however it is modified as it is known that a photon was **not** emitted. The qubit will collapse into the ground state $|g\rangle$ (lower energy eigenstate) with probability $P = \langle\psi|\,\Omega_1\,|\psi\rangle$, which is most likely to occur when the state is close to the excited state $|e\rangle$ (upper energy eigenstate). This is implemented through the operator $\sigma = |g\rangle\langle e|$.

For each time step, the probability of a jump $P = \langle\psi|\,\Omega_1\,|\psi\rangle$ is calculated and on comparison with a random number chosen from a uniform distribution between 0 and 1, the relevant jump operator Ω_0 or Ω_0 is chosen. If a jump occurs, equation 4.30 is used to replace the state vector, otherwise equation 4.29 is used to evolve the state with the Hamiltonian (Eq. 4.24).

$$\text{NO JUMP} \qquad |\psi(\mathrm{t}+\mathrm{dt})\rangle = \Omega_0\,|\psi(t)\rangle \tag{4.29}$$

$$\text{JUMP} \qquad |\psi(\mathrm{t}+\mathrm{dt})\rangle = \Omega_1\,|\psi(t)\rangle \tag{4.30}$$

The expectation value of the qubit charge must be obtained to solve the second order differential equation for the classical oscillator charge (Eq. 4.18). In addition both the time evolutions of qubit and oscillator charges are recorded for analysis:

$$\langle\hat{q}\rangle = \langle\psi(t)|\,\hat{q}\,|\psi(t)\rangle \tag{4.31}$$

4.2.3 Qubit and oscillator power spectra

The separate qubit and oscillator power spectra are obtained from simulating the transient response of the combined system, as the behaviour of each component affects the other. The capacitative coupling of the qubit island and the oscillator circuit allows the bias field to be applied to the qubit, however this coupling is bidirectional and hence the qubit charge will also have an effect on the bias charge within the oscillator circuit known as the 'backreaction effect' or 'backaction' [91, 96, 97]. It is this reactive effect of the qubit on the externally connected biasing circuit that we intend to exploit for measurement purposes.

Rather than use an analytical solution, the time evolutions of the island charge $\langle\hat{q}\rangle$ and the oscillator charge Q was numerically simulated due to the stochastic nature of the quantum jump process. The observable charges $\langle\hat{q}\rangle$ and Q are converted to voltages through the capacitor voltage relations (Eq. 4.32), then the Fourier transform [98] is applied to calculate the power spectra plotted in decibels.

$$V_{qubit}(t) = \frac{\langle\hat{q}\rangle}{C_q}, \qquad V_{osc}(t) = \frac{Q}{C_Q} \tag{4.32}$$

$$P = 20\log_{10}\left(F\{V(t)\}\right) \tag{4.33}$$

Figure 4.4A shows the qubit power spectrum for the case when the qubit is correctly biased such that the qubit energy gap set by the bias $n_g = 0.5092$ is equal to the transition created by the $F_{mw} = 3.5$GHz microwave of amplitude $A_{mw} = 2.5\times10^{-3}$. In this case the Rabi oscillations (microwave driven oscillations of the qubit state) are of minimum frequency and so the qubit state is more easily controlled. In addition, these Rabi oscillations mix with the microwave to generate two sidebands to the microwave drive. In the case of a correctly biased qubit the Rabi oscillations occur at maximum amplitude, sinusoidally changing the qubit state from $|0\rangle$ to $|1\rangle$ and back. The increased amplitude of the Rabi oscillations can be seen as a large +12dB peak at the Rabi frequency, F_{Rabi} compared with biasing off the microwave transition. In turn, the large amplitude oscillations increase the jump probability as the qubit state is taken closer to the excited state thereby creating a large number of quantum jumps in a given time. These discontinuities in the time domain caused by the quantum jumping results in an increase of broadband noise, which is readily apparent when comparing the background noise level and characteristics of figures 4.4A and 4.4B. The off transition bias setting of $n_g = 0.5075$ is shown by figure 4.4B, at which point the amplitude of the Rabi oscillations is severely attenuated by -20dB.

This attenuation of the Rabi amplitude implies the qubit cannot reach the excited state, and hence the jump probability is reduced to the point that there are few jumps, if any. The reduction of broadband noise results in a cleaner power spectrum, to the point that the bias oscillator resonator can be observed within the lowered noise floor.

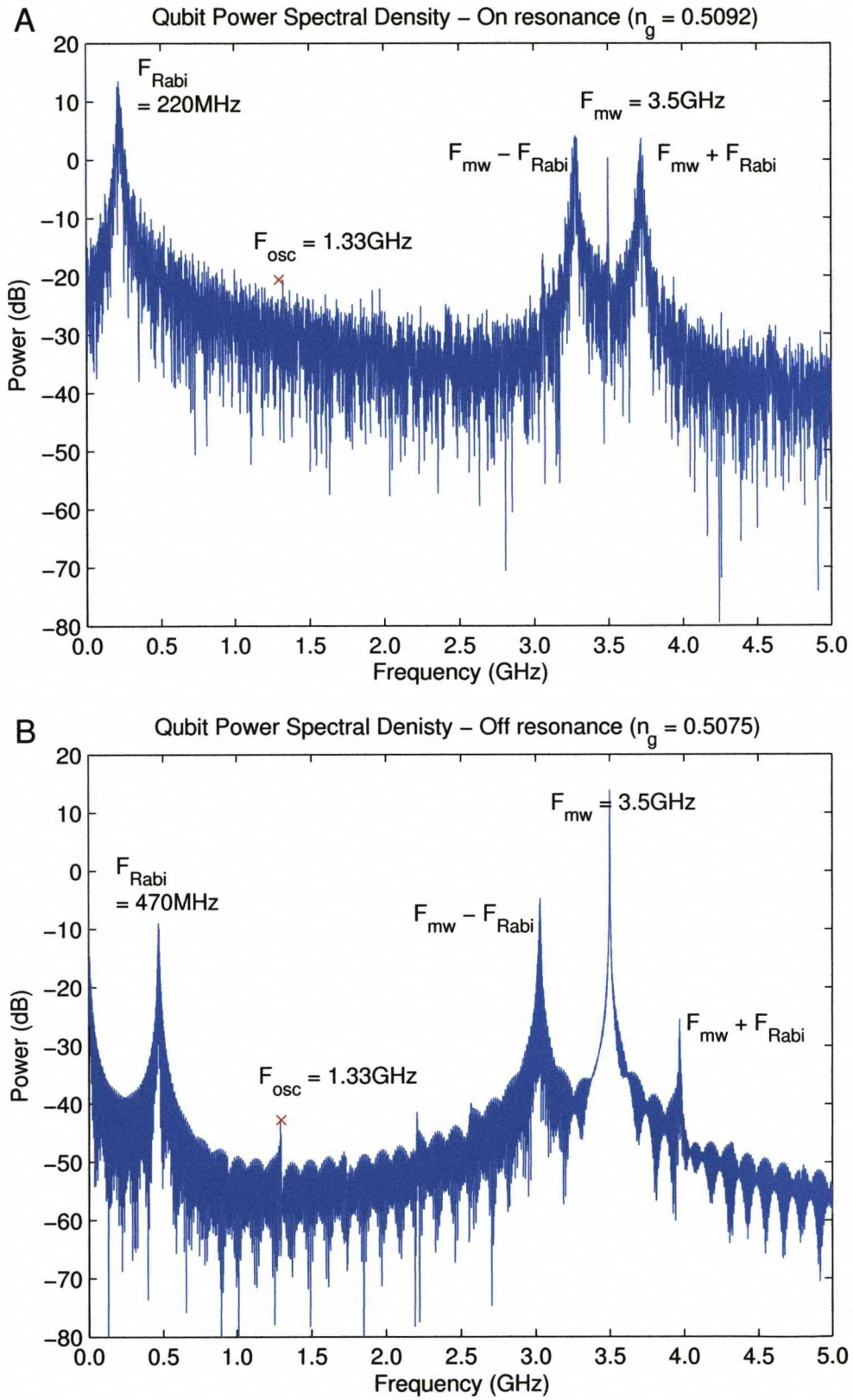

Figure 4.4: Qubit power spectral density (PSD) for the cases when the qubit is biased on (**A**) and off (**B**) the microwave driven transition. There is less broadband noise due to reduced quantum jumping when off resonance.

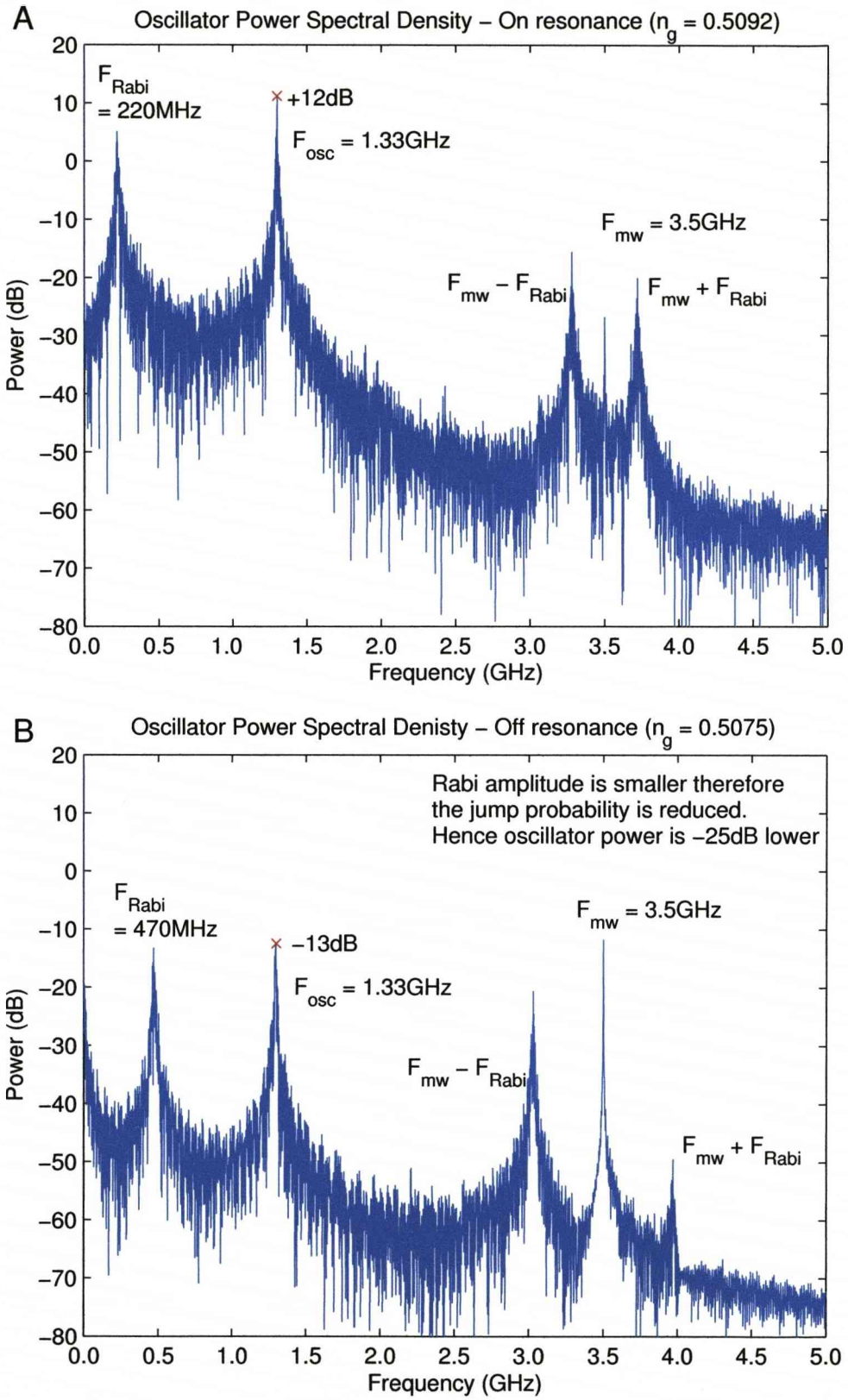

Figure 4.5: Oscillator power spectral density (PSD) for the cases when the qubit is biased on (**A**) and off (**B**) the microwave driven transition. Most noteworthy is the reduction of the oscillator noise power by approximately 25dB when the qubit is off resonance.

The oscillator power spectrum, given a correctly biased qubit, is shown in figure 4.5A, immediately it can be seen that all the qubit features can be found within the oscillator spectrum. The feature of most interest is the resonant peak found at the bias oscillator frequency $F_{osc} = 1.33$GHz, marked by the red 'x'. The signal power at this peak is a maximum whenever the qubit is somehow excited, as the excitations increase the number of quantum jumps occurring, and therefore the aforementioned discontinuities in the time domain creates broadband noise in the qubit. However, as this is a coupled system, the jumps (broadband noise) couple through to the resonant oscillator circuit driving the oscillator peak higher. The difference between on and off transition is shown in figures 4.5A and 4.5B, with a measurable difference of approximately -25dB. This response only occurs when the qubit is able to access the excited state of the two level approximation, **this should occur when a correctly biased qubit energy gap is resonant with a drive of equal frequency**. Therefore it suggests that a mapping of the qubit energy level diagram could be achievable through the biasing circuitry, rather than a single electron transistor (SET) measurement device normally used.

4.2.4 The classical oscillator as a probe

Typically, the result of a spectroscopy experiment on a Cooper pair box is 'read-out' using a single electron transistor (SET) [36, 91], however this requires an extra measurement device coupled to the qubit. This coupling will introduce additional noise to the qubit from the external environment coupled to the SET, which will decohere the qubit. An alternative solution is to make better use of the resources already present, namely the qubit control fields connecting the qubit with the experimentalist.

Using the main result from section 4.2.3 that the noise power present in the oscillator increases when the qubit is correctly biased, we intend to show that the energy level separation can be measured using only the changes observed in the oscillator circuit [99]. A similar analysis has been performed for a flux qubit [100] and in this work we show that the technique can also be applied to charge qubits. It is important to remember there is no qubit measurement device used, or included in the model.

The energy level separation of a charge biased Cooper pair box varies as a function of bias charge, given a fixed tunneling energy, it is therefore necessary to somehow associate each bias point with the correct energy separation. To do this, the qubit is excited by a continuous microwave drive field of amplitude $A_{mw} = 2.5\times10^{-3}$ at a fixed frequency F_{mw} which is set to the energy separation of interest.

Whilst measuring the resulting changes in the oscillator power (amplitude) over a fixed period of time, the bias field is stepped through producing figure 4.6. The largest peak found in figures 4.6A-F occurs whenever the qubit energy separation (set by the bias) is correctly matched with the applied microwave drive, thus producing many quantum jumps (Fig. 4.6G-L), which as previously described creates the broadband noise in the qubit that drives oscillator circuit strongly.

Caution should be taken as there are a number of minor power peaks that are a result of the qubit being driven by a mixture of the microwave field and the oscillator circuit. Figure 4.6A is of particular interest, as the applied microwave frequency is $F_{mw} = 3.0\text{GHz}$ the second harmonic $2F_{mw} = 6.0\text{GHz}$ is resonant within the range of bias values explored ($0.5 \leq n_g \leq 0.52$). The second harmonic still drives the qubit strongly, however it should be sufficiently far from the fundamental frequency to avoid confusion. More subtle is the drive at $F_{mw} - F_{osc}$ when the oscillator frequency is small, as the energy diagram will be shifted along the bias axis by detecting this 'trailing' peak.

Figure 4.7 shows how the energy level diagram is constructed by associating each microwave frequency (F_{mw}) with a bias value (n_g) as the microwave frequency is equal to the energy gap when the qubit is correctly biased at the peak oscillator power. The figure shows the energy diagram from figures 3.5 and 3.14 combined with the oscillator power plots from figure 4.6 plotted on the same bias axis, the peaks clearly coincide with the energy separation at the correct microwave frequencies. In addition, the narrow peak caused by the 6.0GHz second harmonic of $F_{mw} = 3.0\text{GHz}$, (Fig. 4.6A) is consistent with the position of the 6.0GHz energy gap, this narrower peak suggests that a finer energy digram could be best constructed using the second harmonics of the microwave drive.

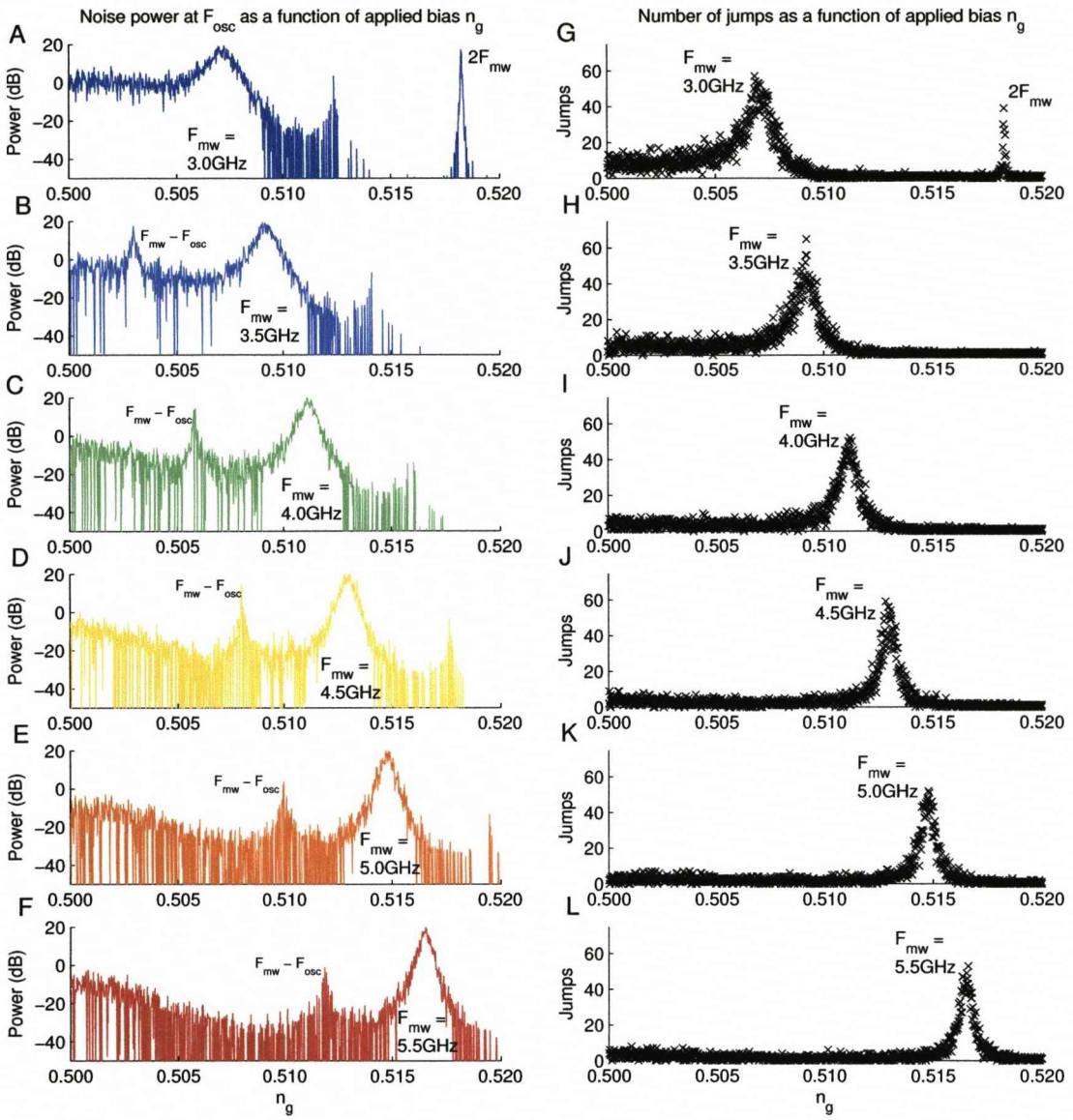

Figure 4.6: (**A-F**) Record of the oscillator power (power at the frequency F_{osc}) as a function of the applied bias (n_g) for different microwave drive frequencies (F_{mw}). The largest peak occurs whenever the qubit is correctly biased, such that the qubit energy gap is equal to the microwave energy. (**G-L**) When correctly biased, the Rabi oscillations have maximum amplitude therefore more quantum jumps will occur. As the qubit state collapses, these large discontinuities generate broadband noise which drives the oscillator circuit creating the aforementioned peaks in oscillator power.

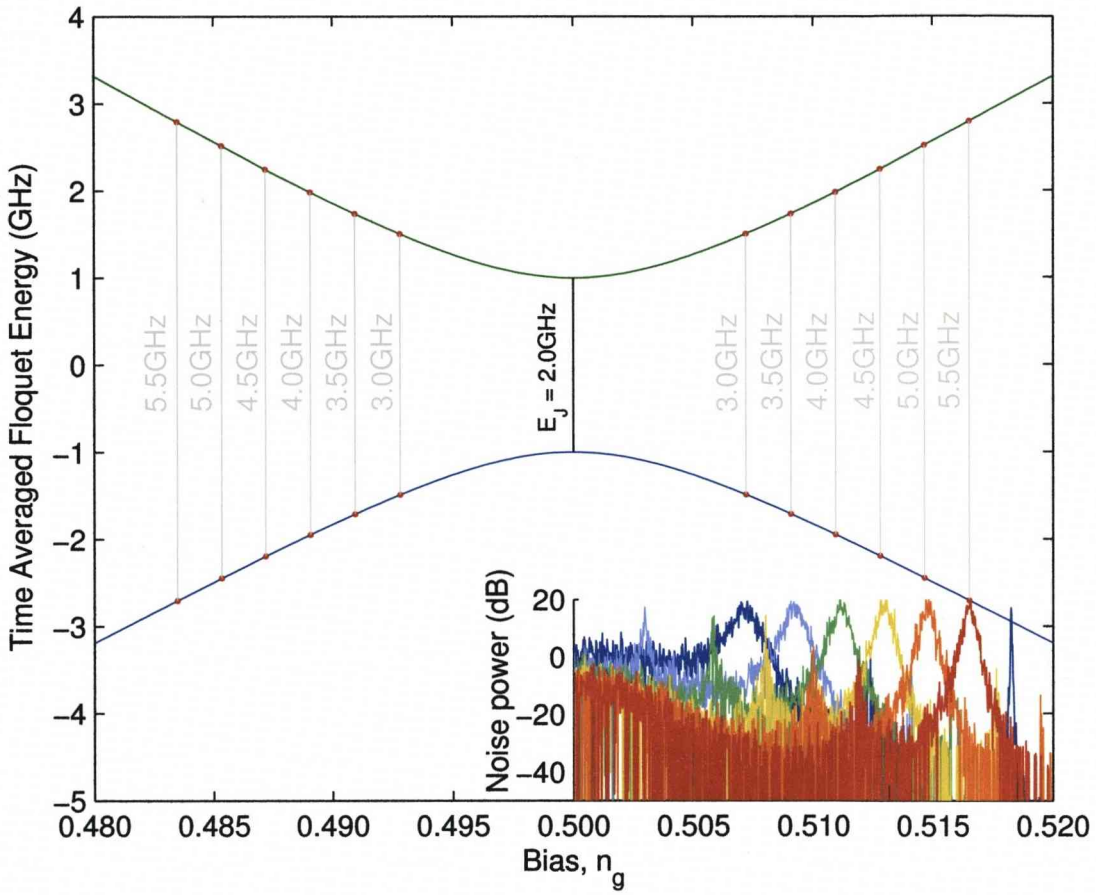

Figure 4.7: The energy level diagram can be constructed by using a sudden rise in oscillator power to associate a microwave drive frequency with a bias point. It is known that there is a measurable change in oscillator power whenever the qubit is correctly biased, which is whenever the energy gap (set by the known bias) is equal to the microwave energy (which is also known). This 'feature' is used to pair off energy separations and bias points such that the energy level diagram can be constructed.

4.3 Quantum dynamics coupled to a quantum system

Whilst the classical model may be a reasonable approximation for the bias circuit, a more accurate model is to quantise an oscillator with an infinite number of states, although in practice a limited number of the lowest states are occupied due to the low temperatures involved [101, 102]. This model is more appropriate due the nature of the coupling objects with a two state system, it would be unreasonable to expect the highly constrained two level system to be directly coupled to a classical system.

4.3.1 The Simple Harmonic Oscillator (SHO)

It can be shown by comparing the system Hamiltonian with the standard form of a simple harmonic oscillator Hamiltonian, that the biasing circuitry can be modelled as a quantised simple harmonic oscillator. Rearranging equation 3.47 to collect the conjugate variables of the oscillator (capacitor charge $\hat{Q}$ and inductor flux $\hat{\Phi}$), and the conjugate variables of the qubit (island charge $\hat{q}$ and superconducting phase $\hat{\theta}$).

$$H_{system} = \underbrace{\frac{\hat{Q}^2}{2C_Q} + \frac{\hat{\Phi}^2}{2L_{osc}}}_{\text{Harmonic oscillator}} + \kappa\frac{\hat{Q}\hat{q}}{C_q} + \frac{\hat{q}^2}{2C_q} - \hbar\nu\cos\left(\frac{2\pi}{\Phi_0}\,\hat{\theta}\right) + V\hat{Q} \quad (4.34)$$

As the oscillator charge $\hat{Q}$ and flux $\hat{\Phi}$ are conjugate variables, there is an equivalence to the momentum $\hat{\rho}$ and position $\hat{x}$ variables by which the Simple Harmonic Oscillator is typically defined. Equating the standard form of the simple harmonic oscillator in momentum and position, with the quadratic oscillator charge and flux terms found in the system Hamiltonian (Eq. 4.34) yields:

$$H_{system} = \frac{\hat{\rho}^2}{2m} + \frac{1}{2}\,k\,\hat{x}^2 \equiv \frac{\hat{Q}^2}{2C_Q} + \frac{\hat{\Phi}^2}{2L_{osc}} \quad (4.35)$$

This equivalence extends to the mass (m) and spring constant (k) of the standard simple harmonic oscillator model and the RLC oscillator capacitance (C_Q) and inductance (L_{osc}).
Given the conjugate variables:

$$\hat{\rho} \equiv \hat{Q}, \qquad \hat{x} \equiv \hat{\Phi} \quad (4.36)$$

Then by equivalence, the component values are:

$$m \equiv C_Q, \qquad k \equiv \frac{1}{L_{osc}} \quad (4.37)$$

The values of m and k defines the resonant frequency of the oscillator, ω_{osc}.

$$\omega_{osc} = \sqrt{\frac{k}{m}} \equiv \sqrt{\frac{1}{L_{osc}C_Q}} \tag{4.38}$$

Rather than use Hermite polynomials to analyse a simple harmonic oscillator [43], it is easier to quantise the Hamiltonian to a matrix form through the use of raising and lowering operators [103], a process known a *second quantisation.* When these operators act on the oscillator state vector they shift the elements in the vector one step in either direction, a raising operator will shift the state upwards increasing the energy in the system by one quanta, and a lowering operator will cause a downwards shift corresponding to the release of one quanta of energy ($E = \hbar\omega_{osc}$).

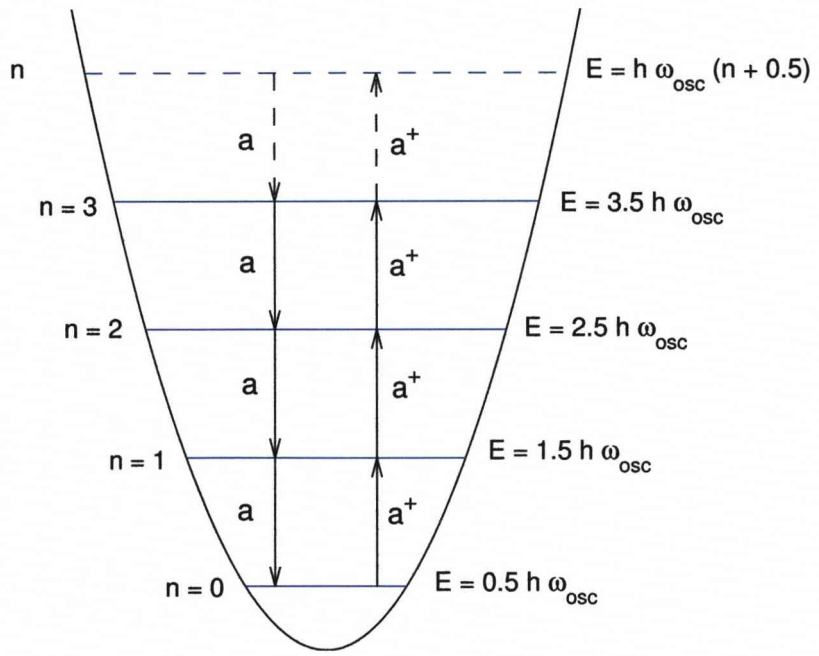

Figure 4.8: Quadratic potential of the simple harmonic oscillator is quantised into energy levels separated by the energy quanta $E = \hbar\omega_{osc}$. Note the offset of $E_0 = 0.5\hbar\omega_{osc}$ which is the vacuum energy where there are no photons present, this arises from a non-zero commutator relation. When lowering operator $\hat{a}$ is applied the energy of the oscillator is reduced by one quanta, through emission of a photon of frequency ω_{osc}. Likewise, the raising operator $\hat{a}^\dagger$ increases the oscillator energy through absorption of a photon.

The raising and lowering operators are of a standard form and can be obtained from reference [103] (Equations 4.60a and 4.60b, page 150).

Lowering operator:

$$\hat{a} = \sqrt{\frac{m\omega}{2\hbar}}\left(\hat{x} + i\frac{\hat{\rho}}{m\omega}\right) \tag{4.39}$$

Raising operator:

$$\hat{a}^\dagger = \sqrt{\frac{m\omega}{2\hbar}}\left(\hat{x} - i\frac{\hat{\rho}}{m\omega}\right) \tag{4.40}$$

We rearrange equations 4.39 and 4.40 to obtain the position and momentum operators in terms of the raising and lowering operators, the form of $\hat{Q}$ will be important for implementing the cross coupling term $\hat{Q}\hat{q}$.

Flux/Position operator:

$$\hat{\Phi} \equiv \hat{x} = \sqrt{\frac{\hbar m\omega}{2}}\left(\hat{a} + \hat{a}^\dagger\right) \tag{4.41}$$

Charge/Momentum operator:

$$\hat{Q} \equiv \hat{\rho} = -i\sqrt{\frac{\hbar m\omega}{2}}\left(\hat{a} - \hat{a}^\dagger\right) \tag{4.42}$$

Rather than subsituting the charge and flux operators in to the quadratic terms of the Hamiltonian (Eq.4.35), a simplification can be made. A useful result of using a raising and lowering operator approach is the number operator, $\hat{N} = \hat{a}^\dagger\hat{a}$, the expectation value of which reveals the average oscillator state number $n = \langle N \rangle$, the number of photons in the oscillator.

$$\hat{N} = \hat{a}^\dagger\hat{a} = \frac{m\omega}{2\hbar}\left(\hat{x} - i\frac{\hat{\rho}}{m\omega}\right)\left(\hat{x} + i\frac{\hat{\rho}}{m\omega}\right) \tag{4.43}$$

As the position $\hat{x}$ and momentum $\hat{\rho}$ cannot be measured simultaneously, there must exist a commutator relation between the conjugate variables. Using the commutator $[\hat{x}, \hat{\rho}] = i\hbar$ creates a half quanta term which would not normally arise in the classical harmonic oscillator, this is called the *vacuum energy* as there is still a non-zero energy when there are zero photons in the oscillator ($n = 0$).

$$\hat{N} = \frac{1}{\hbar\omega}\left(\frac{\hat{\rho}^2}{2m} + \frac{1}{2}\,k\,\hat{x}^2\right) - \frac{1}{2} \tag{4.44}$$

$$\hat{N} = \frac{1}{\hbar\omega}\hat{H} - \frac{1}{2} \tag{4.45}$$

Rearranging to obtain the simplified Hamiltonian:

$$\hat{H} = \frac{\hat{Q}^2}{2C_Q} + \frac{\hat{\Phi}^2}{2L_{osc}} = \hbar\omega_{osc}\left(\hat{N} + \frac{1}{2}\right) \tag{4.46}$$

The matrix form of these operators is of vital importance for simulation purposes, unfortunately as this is not the typical goal of textbooks, the matrix structure of operators are not usually defined, therefore the information is provided here. The raising and lowering operators are off diagonal, which allows transfer of state coefficients to the neighbouring element of the state vector, the magnitude of each matrix element is chosen such that the number matrix (Eq. 4.49) is correctly formed.

$$\hat{a} = \begin{pmatrix} 0 & \sqrt{1} & 0 & 0 & 0 \\ 0 & 0 & \sqrt{2} & 0 & 0 \\ 0 & 0 & 0 & \ddots & 0 \\ 0 & 0 & 0 & 0 & \sqrt{n-1} \\ 0 & 0 & 0 & 0 & 0 \end{pmatrix} \tag{4.47}$$

$$\hat{a}^\dagger = \begin{pmatrix} 0 & 0 & 0 & 0 & 0 \\ \sqrt{1} & 0 & 0 & 0 & 0 \\ 0 & \sqrt{2} & 0 & 0 & 0 \\ 0 & 0 & \ddots & 0 & 0 \\ 0 & 0 & 0 & \sqrt{n-1} & 0 \end{pmatrix} \tag{4.48}$$

The number operator maps the oscillator state to the oscillator occupancy $\{0, 1, 2, \ldots\ n\}$, the occupancy may also be fractional when the state coefficients are spread throughout the state vector.

$$\hat{N} = \hat{a}^\dagger \hat{a} = \begin{pmatrix} 0 & 0 & 0 & 0 & 0 \\ 0 & 1 & 0 & 0 & 0 \\ 0 & 0 & 2 & 0 & 0 \\ 0 & 0 & 0 & \ddots & 0 \\ 0 & 0 & 0 & 0 & n \end{pmatrix} \tag{4.49}$$

Thus the two quadratic terms in $\hat{Q}$ and $\hat{\Phi}$ in equation 4.34, is simulated by the matrix:

$$\hat{H}_{osc} = \begin{pmatrix} 0.5\,\hbar\omega_{osc} & 0 & 0 & 0 & 0 \\ 0 & 1.5\,\hbar\omega_{osc} & 0 & 0 & 0 \\ 0 & 0 & 2.5\,\hbar\omega_{osc} & 0 & 0 \\ 0 & 0 & 0 & \ddots & 0 \\ 0 & 0 & 0 & 0 & (n+0.5)\,\hbar\omega_{osc} \end{pmatrix} \tag{4.50}$$

For computational efficiency we limit the number of oscillator states to $n = 10$, as the low temperature of $T = 10\text{mK}$ constrained the oscillator state to low values. This is a valid assumption provided the state probabilities are not overflowing the size of the state vector.

4.3.2 Modelling dissipation in a quantised system

The standard Schrödinger evolution assumes the energy is conserved within the system and not transferred to an external environment, and therefore it is not easy to include the effect of dissipation. Modelling dissipation in a quantised system is an area open to debate, and there are a number of different approaches. For superconducting devices, the 'Calderia-Leggett model' is the most popular, however there also exists techniques known as 'Unravellings' which use a Stochastic Schrödinger Equation (SSE) to simulate the stochastic noise processes associated with dissipation. It is these unravellings that we focus on in this work, most notably 'Quantum State Diffusion'. A significant feature of using an unraveling approach is that the individual trajectories appear similar to experimental results [104, 105], through which the stochastic evolution can be thought of as a weak measurement process made by the *environment* on the system of interest.

The Caldeira-Leggett model - Bath of oscillators

The Calderia-Leggett model is perhaps the most popular means of modelling ohmic dissipation within a harmonic oscillator [60]. The quantum system of interest is assumed to be coupled to a bath of many other harmonic oscillators, whose spectrum is chosen to be representative of a resistive component. The spectrum is bandlimited from $\omega = 0$ to $\omega = \Lambda$ rads^{-1}. In the long time limit ($t >> \Lambda^{-1}$) and given high temperatures ($kT >> \Lambda$) the equations simplify to a deterministic master equation.

$$d\hat{\rho} \;=\; -i\left[\hat{H},\hat{\rho}\right]dt \;-\; i\frac{\eta}{2}\left[\hat{x},\{\hat{p},\hat{\rho}\}\right]dt \;-\; \eta kT\left[\hat{x},[\hat{x},\hat{\rho}]\right]dt \qquad (4.51)$$

where η is a friction coefficient. The two additional terms decay the non-dissipative Schrödinger evolution.

Unfortunately, due to the constant dissipation terms, the Caldeira-Leggett model is said to violate the state positivity [106], meaning for a set of initial conditions the system can evolve to have negative probabilities, which is not possible in real systems.

Quantum state diffusion unravelling - Stochastic Schrödinger Equation

Quantum state diffusion (QSD) proposed by Gisin and Percival [105] models the random drift and fluctuations in the quantum state, these are dependent on the temperature of the thermal bath, oscillator resonant frequency (energy quanta) and the quality factor of the oscillator circuit. We will be using Spiller's analysis

of QSD with a finite temperature to model the dissipative effects of a thermal environment on the quantised oscillator [104].

The quality factor, in a classical context is governed by the resistance R_{osc} and inductance L_{osc} in an RLC oscillator, however it is the effect of this dissipative element R_{osc} that needs to be modelled. As the theoretical nature of the QSD literature does not make an explicit reference to a practical resistive circuit, we make the reasonable assumption that the quality factors (Q_{osc}) of a classical and quantised oscillator are equal. The quality factor for a classical RLC oscillator is defined by the following equation [83]:

$$Q_{osc} = \omega_0 \frac{L_{osc}}{R_{osc}} \tag{4.52}$$

where the resonant frequency ω_0 is a function of L_{osc} and C_Q.

QSD is applied through modification of the normal Schrödinger evolution by using the incremental state vector update $|d\psi\rangle$ defined by equation 4.53 [104].

$$\begin{aligned} |d\psi\rangle &= -\frac{i}{\hbar}\hat{H}\,|\psi\rangle\,dt \\ &\quad + \sum_{m=1}^{2}\left(\langle\hat{L}_m^\dagger\rangle\hat{L}_m - \frac{1}{2}\hat{L}_m^\dagger\hat{L}_m - \frac{1}{2}\langle\hat{L}_m^\dagger\rangle\langle\hat{L}_m\rangle\right)|\psi\rangle\,dt \\ &\quad + \sum_{m=1}^{2}\left(\hat{L}_m - \langle\hat{L}_m\rangle\right)|\psi\rangle\,d\xi_m \end{aligned} \tag{4.53}$$

where the first term is the usual Schrödinger evolution, the second term defines the drift of the quantum state and the third term includes the effects of stochastic fluctuations. The random variables $d\xi_m$ driving the state fluctuations are complex valued independent random variables satisfying:

$$E\langle d\xi_m\rangle = 0 \tag{4.54}$$

$$E\langle d\xi_n d\xi_m\rangle = 0 \tag{4.55}$$

$$E\langle d\xi_n^* d\xi_m\rangle = \delta_{mn}dt \tag{4.56}$$

The Lindblad operators L_m determine the effect of the environment on the quantum oscillator, it is through these operators that the noise effects of temperature and the dissipative effects of the oscillator quality factor are applied.

$$\hat{L}_1 = \sqrt{\frac{(\bar{n}+1)\,\omega_0}{Q_{osc}}}\,\hat{a} \tag{4.57}$$

$$\hat{L}_2 = \sqrt{\frac{\bar{n}\,\omega_0}{Q_{osc}}}\,\hat{a}^\dagger \tag{4.58}$$

$\hat{L}_1$ is a lowering operator (due to $\hat{a}$) and it can be seen that it is more heavily weighted in comparison with the corresponding raising operator $\hat{L}_2$ as ($\bar{n}+1 > \bar{n}$), this means the oscillator state will tend to drift downwards dissipating energy.

The average oscillator occupancy $\bar{n}$ is the average oscillator number state $\langle \hat{N} \rangle$ at temperature T, the oscillator occupancy will settle at this value over long time scales.

$$\bar{n} = \frac{1}{\exp\left(\frac{\hbar\omega_0}{kT}\right) - 1} \tag{4.59}$$

When implemented, QSD creates the effects of dissipation in a quantum system and also includes quantum fluctuations about $\bar{n}$. For the remainder of this work, the quality factor is taken to be $Q_{osc} = 300$ and the environmental temperature experienced by the oscillator is $T = 10\text{mK}$. For a 1.33GHz oscillator $\bar{n} = 0.0017$.

Quantum jump unravelling - Stochastic Schrödinger Equation

There are many possible unravellings of the master equation, and the difference between the two unravellings presented here can be interpreted as two differing measurements on the environment, the key constraint is that the average behaviour of the system should be the same for all unravellings.

An alternative, but equally valid, unravelling of the master equation is the Quantum Jump unravelling [107], whereby the dissipation is modelled by changing the state using a series of discrete steps, or jumps, rather than a continuous process such as quantum state diffusion. With QSD, the incremental change of the state vector (Eq. 4.53) included the effects of drift and fluctuations using random increments calculated every time step drawn from a continuous distribution (Eq. 4.54). As per QSD, the Quantum Jump unravelling is also applied by incrementally changing the state vector, however the stochastic term is calculated differently using a discrete random distribution.

The state of the oscillator is updated via equation 4.60.

$$\begin{aligned} |d\psi\rangle = & -\frac{i}{\hbar}\hat{H}\,|\psi\rangle\,dt \\ & -\frac{1}{2}\sum_{m=1}^{2}\left(\hat{L}_m^\dagger\hat{L}_m - \langle\hat{L}_m^\dagger\hat{L}_m\rangle\right)|\psi\rangle\,dt \\ & +\sum_{m=1}^{2}\left(\frac{\hat{L}_m}{\sqrt{\langle\hat{L}_m^\dagger\hat{L}_m\rangle}} - 1\right)|\psi\rangle\,dN_m \end{aligned} \tag{4.60}$$

As before, the first term of equation 4.60 is the standard Schrödinger evolution and the second term creates a dissipative drift towards the lower energy states.

However the third term is significantly different, here the jump process is implemented by two independent discrete random variables dN_1 and dN_2 each of which can only take the values 0 or 1. The jump probabilities of each stochastic variable depends on the current state through:

$$P(dN_1 = 1) = \sqrt{dt}\left\langle \hat{L}_1^\dagger \hat{L}_1 \right\rangle \tag{4.61}$$

$$P(dN_2 = 1) = \sqrt{dt}\left\langle \hat{L}_2^\dagger \hat{L}_2 \right\rangle \tag{4.62}$$

For the majority of the evolution $dN_1 = 0$ and $dN_2 = 0$, so the third term of equation 4.60 is removed and the state merely experiences Schrödinger evolution and a continuous decay. However, if $dN_1 = 1$ then the lowering operator L_1 is effectively applied by forcing the state $|\psi\rangle$ to:

$$|\psi\rangle \rightarrow \frac{\hat{L}_1}{\sqrt{\left\langle \hat{L}_1^\dagger \hat{L}_1 \right\rangle}} |\psi\rangle \tag{4.63}$$

Equation 4.60 sets $|d\psi\rangle$ equal to the negative difference between the current state and that of equation 4.63, effectively lowering the state of the system when the state is updated. Likewise when $dN_2 = 1$, the raising operator L_2 is applied in the same manner. The triggering of these two stochastic variables creates stepping up and down the energy levels of the oscillator.

On comparing the QSD and QJ unravellings, the different evolutions are immediately apparent. However, despite the fundamental differences between a continuous (QSD) and discrete (QJ) evolution, on average they are equivalent.

We have selected Quantum State Diffusion as our preferred method for implementing dissipation within the quantised harmonic oscillator, as the single evolutions appear to be more similar to the average behaviour of the system compared with a Quantum Jump unravelling.

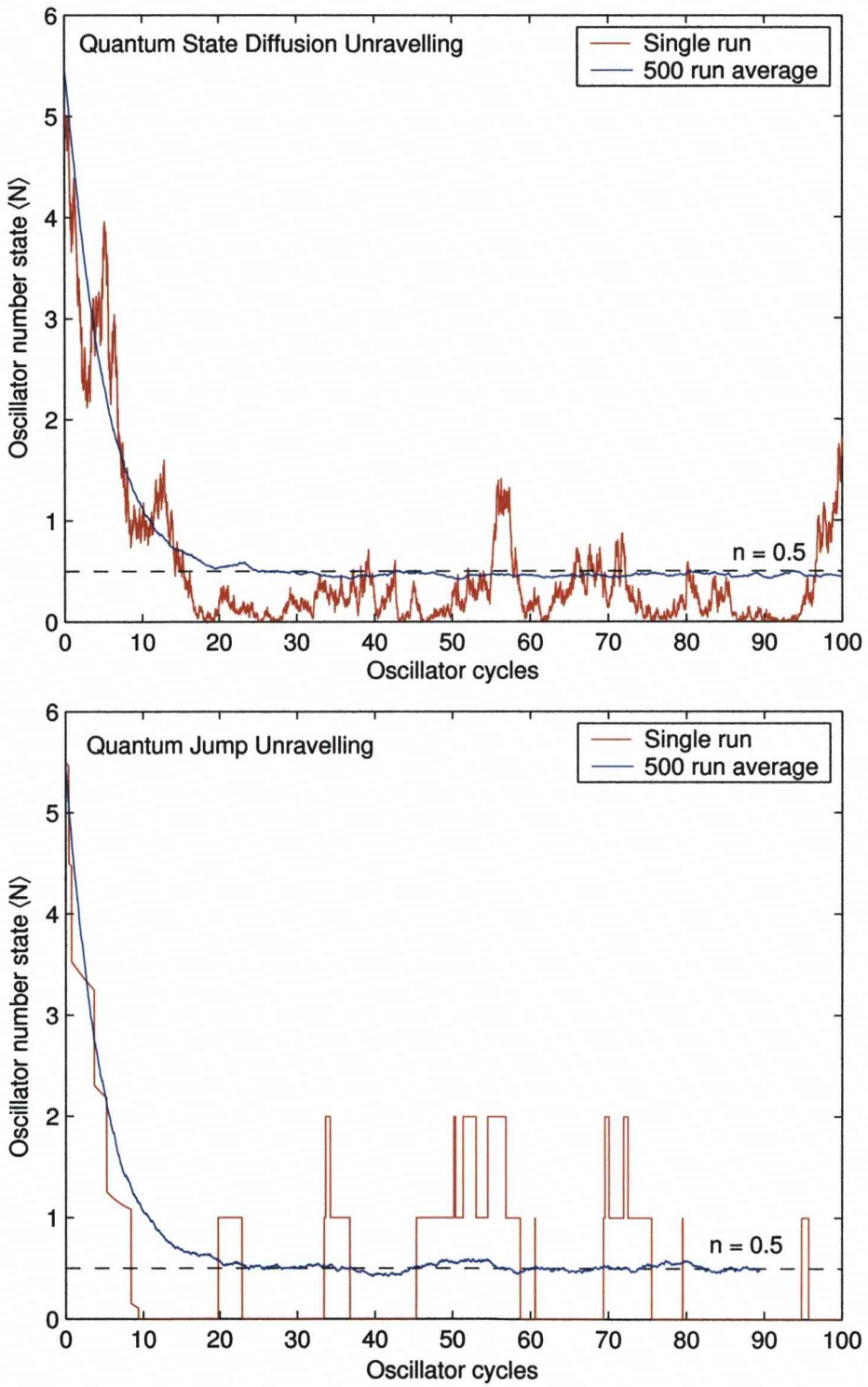

Figure 4.9: Number state as a function of time, for the Quantum state diffusion (QSD) and Quantum jump (QJ) unravellings. In this example the oscillator quality factor is taken to be $Q_{osc} = 30$ and $\bar{n} = 0.5$. The evolution of the two unravellings is vastly different, however the average evolution is quite similar, an indication that they are indeed valid unravellings of the master equation.

4.3.3 Coupling the qubit and oscillator

It is important to note that the harmonic oscillator is an n-level quantum system and the qubit is a two level quantum system, and are therefore modeled using state vectors of different dimensions, $[n \times 1]$ and $[2 \times 1]$ respectively. When two or more quantum systems are combined, a *composite state vector* is formed using the *tensor product* (Sec. 2.1.5), whereby the entire system is analysed using a single large Hilbert space represented by a single state vector, in this case $[2n \times 1]$.

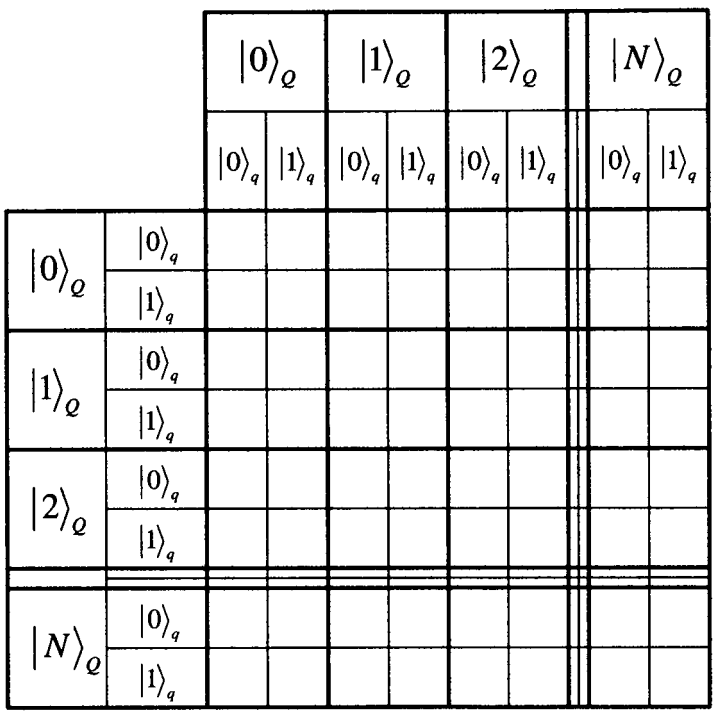

Figure 4.10: The coupled system Hamiltonian is formed from several tensor products, in this work we have always taken the oscillator basis to be the right-hand side operator of any tensor product and the qubit basis is on the left-hand side, which defines the grid like structure shown.

Figure 4.10 clearly shows that the number of elements within a tensored matrix increases as the product of the component matrices, unfortunately the size of the dataset rapidly increases to the point that a quantum system can not be easily simulated on a classical computer, the simulation of quantum systems on a quantum computer is one of potential uses of a quantum computer. For this work we have taken the oscillator basis to be the left-hand variable of the tensor product and the qubit basis is always on the right, $|\psi_{system}\rangle = |\psi_{osc}\rangle \otimes |\psi_{qubit}\rangle$.

With regard to the example system Hamiltonian H_{system}, there exists a cross-coupling term between the oscillator charge $\hat{Q}$ and qubit charge $\hat{q}$, the strength of the coupling is set by coupling constant κ, which was defined in section 4.2.1

as a function of the capacitances within the system (Eq. 4.3).

$$H_{system} = \frac{\hat{Q}^2}{2C_Q} + \frac{\hat{\Phi}^2}{2L_{osc}} + \underbrace{\kappa\frac{\hat{Q}\hat{q}}{C_q}}_{\text{Coupling}} + \frac{\hat{q}^2}{2C_q} - \hbar\nu\cos\left(\frac{2\pi}{\Phi_0}\hat{\theta}\right) + V\hat{Q} \quad (4.64)$$

As $\hat{Q}$ and $\hat{q}$ are both operators, the product $\hat{Q}\hat{q}$ is taken as a tensor product of the two operators:

$$\hat{H'}_{coupling} = \kappa\frac{\hat{Q}\hat{q}}{C_q} \equiv \kappa\frac{\hat{Q}\otimes\hat{q}}{C_q} \quad (4.65)$$

To determine the structure of the coupling matrix, the qubit charge $\hat{q}$ and oscillator charge $\hat{Q}$ operator matrices are required, where the raising and lowering operators $\hat{a}^\dagger$ and $\hat{a}$ are defined in equations 4.48 and 4.47.

$$\hat{q} = \begin{pmatrix} 0 & 0 \\ 0 & 2e \end{pmatrix} \quad (4.66)$$

$$\begin{aligned} \hat{Q} &= -i\sqrt{\frac{\hbar m\omega}{2}}\left(\hat{a}-\hat{a}^\dagger\right) \\ &= -i\sqrt{\frac{\hbar m\omega}{2}}\begin{pmatrix} 0 & \sqrt{1} & 0 & 0 & 0 \\ -\sqrt{1} & 0 & \sqrt{2} & 0 & 0 \\ 0 & -\sqrt{2} & 0 & \ddots & 0 \\ 0 & 0 & \ddots & 0 & \sqrt{n-1} \\ 0 & 0 & 0 & -\sqrt{n-1} & 0 \end{pmatrix} \end{aligned} \quad (4.67)$$

It should be remembered that equation 4.66 uses the qubit basis, and equation 4.67 is described using the oscillator basis and these are incompatible until tensored into a new composite basis that is representative of all possible degrees of freedom. Hence using equation 4.65 the expanded coupling Hamiltonian matrix is:

$$\kappa\frac{\hat{Q}\hat{q}}{C_q} = -i\kappa\frac{2e}{C_q}\sqrt{\frac{\hbar\omega C_Q}{2}} \times \quad (4.68)$$

$$\begin{pmatrix} 0 & 0 & 0 & 0 & 0 & 0 & 0 & 0 & 0 & 0 \\ 0 & 0 & 0 & 1 & 0 & 0 & 0 & 0 & 0 & 0 \\ 0 & 0 & 0 & 0 & 0 & 0 & 0 & 0 & 0 & 0 \\ 0 & -1 & 0 & 0 & 0 & \sqrt{2} & 0 & 0 & 0 & 0 \\ 0 & 0 & 0 & 0 & 0 & 0 & \ddots & \ddots & 0 & 0 \\ 0 & 0 & 0 & -\sqrt{2} & 0 & 0 & \ddots & \ddots & 0 & 0 \\ 0 & 0 & 0 & 0 & \ddots & \ddots & 0 & 0 & 0 & 0 \\ 0 & 0 & 0 & 0 & \ddots & \ddots & 0 & 0 & 0 & \sqrt{n-1} \\ 0 & 0 & 0 & 0 & 0 & 0 & 0 & 0 & 0 & 0 \\ 0 & 0 & 0 & 0 & 0 & 0 & 0 & -\sqrt{n-1} & 0 & 0 \end{pmatrix}$$

The above matrix describes the coupling between the qubit and oscillator, but in a new basis that comprises of all the $2n$ states. The positions of the off-diagonal terms allows the qubit to affect the oscillator state and vice versa.

Likewise, the qubit Hamiltonian matrix is to be expanded in the composite basis. Equation 4.69 is similar to equation 4.23, however as the Hamiltonian has not been separated into a classical and quantum part, the cross-coupling term is already accounted for by equation 4.68 and has been thusly removed from equation 4.23. Although the classical microwave drive is still added as a time-dependent charge bias $Q_{mw}(t) = A_{mw}\sin(\omega_{mw}(t))$.

$$\begin{aligned}\hat{H}_{qubit} &= \frac{(2e)^2}{2C_q}\begin{pmatrix} 0+Q_{mw} & 0 \\ 0 & 1+Q_{mw}\end{pmatrix}^2 - \frac{\hbar\nu}{2}\begin{pmatrix} 0 & 1 \\ 1 & 0\end{pmatrix} \\ &= \begin{pmatrix} \frac{(2e)^2}{2C_q}Q_{mw}^2 & -\frac{\hbar\nu}{2} \\ -\frac{\hbar\nu}{2} & \frac{(2e)^2}{2C_q}(1+Q_{mw})^2\end{pmatrix} \equiv \begin{pmatrix} a & -c \\ -c & b\end{pmatrix}\end{aligned} \tag{4.69}$$

To change the qubit basis to the composite basis it is necessary to tensor the qubit Hamiltonian with an identity matrix of the same dimensionality as the oscillator matrix. This ensures that the only possible means for the oscillator and qubit to interact is through the coupling matrix (Eq. 4.68).

$$\hat{H'}_{qubit} = \hat{I}_{(n\times n)} \otimes \hat{H}_{qubit} \tag{4.70}$$

As equation (4.70) is unweildly to expand, the matrix elements of equation (4.69) have been labeled a,b and c. Hence the expanded qubit Hamiltonian matrix is:

$$\hat{H'}_{qubit} = \begin{pmatrix} a & -c & 0 & 0 & 0 & 0 & 0 & 0 & 0 & 0 \\ -c & b & 0 & 0 & 0 & 0 & 0 & 0 & 0 & 0 \\ 0 & 0 & a & -c & 0 & 0 & 0 & 0 & 0 & 0 \\ 0 & 0 & -c & b & 0 & 0 & 0 & 0 & 0 & 0 \\ 0 & 0 & 0 & 0 & a & -c & 0 & 0 & 0 & 0 \\ 0 & 0 & 0 & 0 & -c & b & 0 & 0 & 0 & 0 \\ 0 & 0 & 0 & 0 & 0 & 0 & \ddots & \ddots & 0 & 0 \\ 0 & 0 & 0 & 0 & 0 & 0 & \ddots & \ddots & 0 & 0 \\ 0 & 0 & 0 & 0 & 0 & 0 & 0 & 0 & a & -c \\ 0 & 0 & 0 & 0 & 0 & 0 & 0 & 0 & -c & b \end{pmatrix} \tag{4.71}$$

The qubit matrix is tiled along the leading diagonal of the expanded matrix, this implies the qubit behaviour is unchanged no matter the current oscillator state.

The oscillator Hamiltonian matrix (Eq. 4.50 derived in section 4.3.1) is expanded to the composite basis in a similar fashion, however in this case the

identity matrix has dimensions equal to the 2-level qubit matrix.

$$\hat{H'}_{osc} = \hat{H}_{osc} \otimes \hat{I}_{(2\times 2)} \tag{4.72}$$

Hence the expanded oscillator Hamiltonian matrix is:

$$\hat{H'}_{osc} = \tag{4.73}$$

$$\begin{pmatrix}
\frac{1}{2}\hbar\omega & 0 & 0 & 0 & 0 & 0 & 0 & 0 & 0 & 0 \\
0 & \frac{1}{2}\hbar\omega & 0 & 0 & 0 & 0 & 0 & 0 & 0 & 0 \\
0 & 0 & \frac{3}{2}\hbar\omega & 0 & 0 & 0 & 0 & 0 & 0 & 0 \\
0 & 0 & 0 & \frac{3}{2}\hbar\omega & 0 & 0 & 0 & 0 & 0 & 0 \\
0 & 0 & 0 & 0 & \frac{5}{2}\hbar\omega & 0 & 0 & 0 & 0 & 0 \\
0 & 0 & 0 & 0 & 0 & \frac{5}{2}\hbar\omega & 0 & 0 & 0 & 0 \\
0 & 0 & 0 & 0 & 0 & 0 & \ddots & 0 & 0 & 0 \\
0 & 0 & 0 & 0 & 0 & 0 & 0 & \ddots & 0 & 0 \\
0 & 0 & 0 & 0 & 0 & 0 & 0 & 0 & (n+\frac{1}{2})\hbar\omega & 0 \\
0 & 0 & 0 & 0 & 0 & 0 & 0 & 0 & 0 & (n+\frac{1}{2})\hbar\omega
\end{pmatrix}$$

The oscillator control term $\hat{H}_{control} = V\hat{Q}$ which sets the qubit bias, is added in the same manner.

$$\hat{H'}_{control} = \hat{H}_{control} \otimes \hat{I}_{(2\times 2)} \tag{4.74}$$

$$\hat{H'}_{control} = -i\sqrt{\frac{\hbar\omega C_Q}{2}}\ V\ \times \tag{4.75}$$

$$\begin{pmatrix}
0 & 0 & 1 & 0 & 0 & 0 & 0 & 0 & 0 & 0 \\
0 & 0 & 0 & 1 & 0 & 0 & 0 & 0 & 0 & 0 \\
-1 & 0 & 0 & 0 & \sqrt{2} & 0 & 0 & 0 & 0 & 0 \\
0 & -1 & 0 & 0 & 0 & \sqrt{2} & 0 & 0 & 0 & 0 \\
0 & 0 & -\sqrt{2} & 0 & 0 & 0 & \ddots & 0 & 0 & 0 \\
0 & 0 & 0 & -\sqrt{2} & 0 & 0 & 0 & \ddots & 0 & 0 \\
0 & 0 & 0 & 0 & \ddots & 0 & 0 & 0 & \sqrt{n-1} & 0 \\
0 & 0 & 0 & 0 & 0 & \ddots & 0 & 0 & 0 & \sqrt{n-1} \\
0 & 0 & 0 & 0 & 0 & 0 & -\sqrt{n-1} & 0 & 0 & 0 \\
0 & 0 & 0 & 0 & 0 & 0 & 0 & -\sqrt{n-1} & 0 & 0
\end{pmatrix}$$

The applied voltage V controls the off-diagonal terms that allows access to new oscillator energy states when $V \neq 0$ regardless of the qubit state. The complete system Hamiltonian, expanded in the composite basis $|\psi_{system}\rangle$, is then simply the sum of equations 4.73, 4.68, 4.71 and 4.75.

$$\hat{H'}_{system} = \hat{H}_{osc} \otimes \hat{I}_{(2\times 2)} + \kappa\frac{\hat{Q} \otimes \hat{q}}{C_q} + \hat{I}_{(n\times n)} \otimes \hat{H}_{qubit} + \hat{H}_{control} \otimes \hat{I}_{(2\times 2)} \tag{4.76}$$

The composite system state is evolved as per the Schrödinger equation 2.35 to model the Hamiltonian dynamics and couplings. In addition, the state vector is also modfied by the stochastic quantum state diffusion process to model dissipation in the oscillator (Sec. 4.3.2), furthermore the qubit quantum jump process described in section 4.2.2 is implemented whereby every operator associated with these processes is tensored to the correct dimensions using the appropriate sized identity matrix.

4.3.4 Qubit and oscillator power spectra

At each time step, the expectation values of the oscillator and qubit charge operators are obtained by using the *partial trace* of the system density matrix to trace out one system to obtain the other.

$$\rho_{qubit} = \mathrm{Tr}_{\mathrm{osc}}\left\{\rho_{\mathrm{system}}\right\} \tag{4.77}$$

$$\langle\hat{q}\rangle = \mathrm{Tr}\left\{\hat{\mathrm{q}}\rho_{\mathrm{qub}}\right\} \tag{4.78}$$

$$\rho_{osc} = \mathrm{Tr}_{\mathrm{qubit}}\left\{\rho_{\mathrm{system}}\right\} \tag{4.79}$$

$$\langle\hat{Q}\rangle = \mathrm{Tr}\left\{\hat{\mathrm{Q}}\rho_{\mathrm{osc}}\right\} \tag{4.80}$$

The power spectral density is calculated as before by taking the Fourier transform of the expectation values and expressing the power in decibels. The qubit and oscillator model described in this section uses identical parameters to the classical model (described in section 4.2) with component values listed in Table 4.1, the qubit is driven by a continuous 3.5GHz microwave drive with amplitude 2.5×10^{-3} as per section 4.2.3.

The spectra of the quantised oscillator model (Figs. 4.11 and 4.12) are similar to their classical counterparts (Figs. 4.4 and 4.5), however in all four plots there is a considerable amount of broadband noise even when the qubit is off transition and therefore not quantum jumping. This can be attributed to the stochastic quantum state diffusion process acting on the oscillator component of the composite state vector. Interestingly despite the noise, the mixing of the 1.33GHz biasing oscillator and 3.50GHz microwave drive can be clearly seen in the qubit spectra at $F_{mw} - F_{osc}$=2.17GHz (Fig. 4.11), although these signals are too weak to be coupled through to the oscillator spectra (Fig. 4.12). We believe that by treating the oscillator as a quantum object there appears to be stronger interactions between the two systems despite the identical coupling strength of $\kappa = 0.333$.

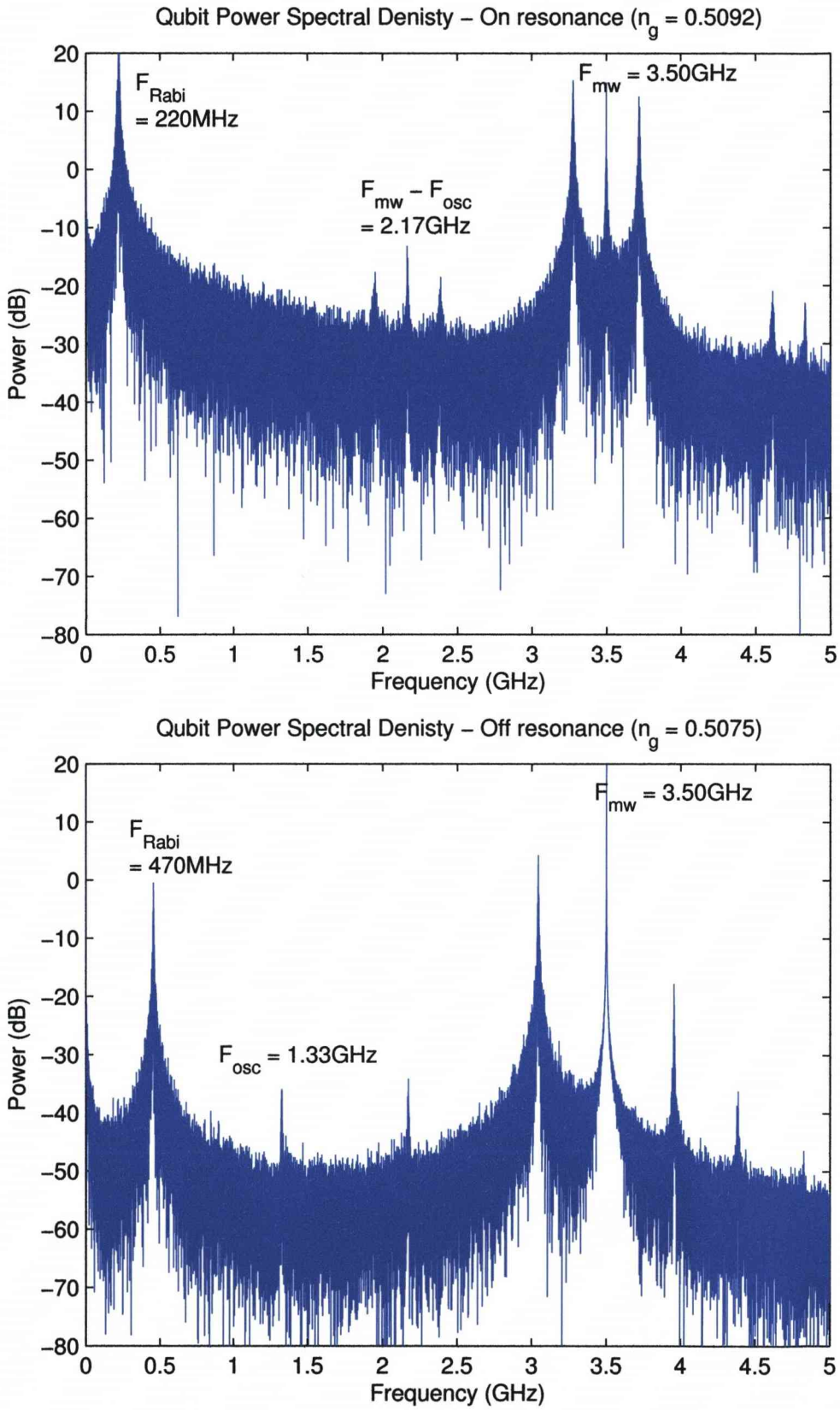

Figure 4.11: Qubit power spectral density (PSD) for the cases when the qubit is biased on (**A**) and off (**B**) the microwave driven transition. There is less broadband noise due to reduced quantum jumping when off resonance.

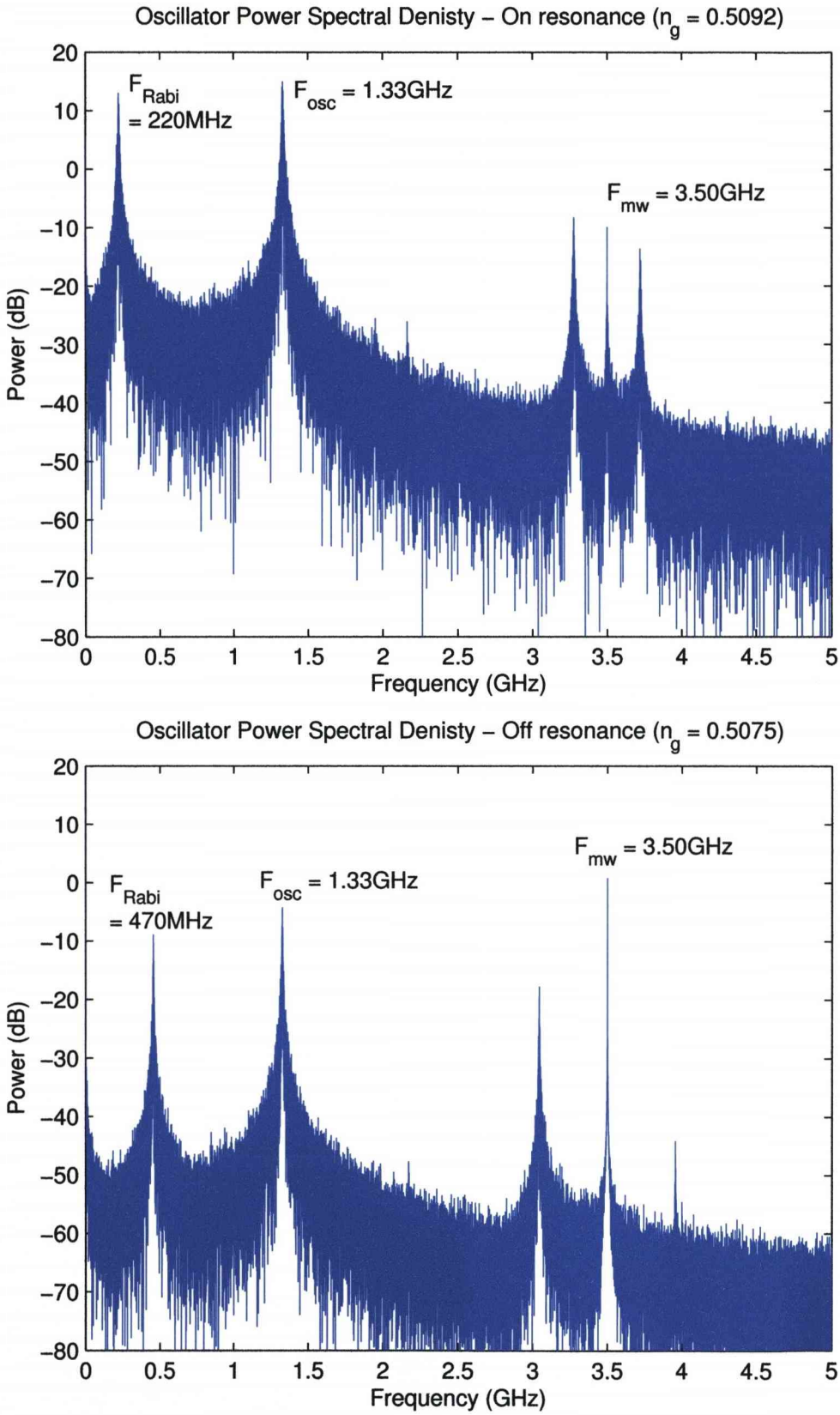

Figure 4.12: Oscillator power spectral density (PSD) for the cases when the qubit is biased on (**A**) and off (**B**) the microwave driven transition. Most noteworthy is the reduction of the oscillator noise power by approximately 25dB when the qubit is off resonance.

4.3.5 Using the quantised oscillator as a probe

Using a quantised simple harmonic oscillator to model the biasing circuitry yields a similar result as the classical oscillator model found in section 4.2.4. However, the system appears to be somewhat noisier than a classical equivalent, this can in part be attributed to the quantum state diffusion (QSD) which is a stochastic process within the oscillator. The oscillator is also more sensitive to quantum jumps within the qubit compared with a classical system, which adds a considerable amount of noise to the bias power measurements that makes the characteristic peaks of figure 4.6 more difficult to find. Therefore it was necessary to average the bias power plots over 10 simulations, such that the stochastic noise is reduced and the fixed peaks become detectable.

Figure 4.13 **G-L** show a similar result as before, a cluster of jumps whilst the biasing point is moved through the microwave transition. However it can be seen that for low microwave drive frequencies and bias values i.e. the region near the minimum splitting energy, there are a number of jumps occurring off the expected resonance. These jumps are caused by a distortion to the energy level diagram created by the microwave transition, the curvature between the minimum splitting and the microwave drive becomes almost constant such that the qubit effectively becomes weakly driven over a wider range of n_g than one would expect. The quantised oscillator coupled to the qubit accentuates this, so that there is little difference between the noise power peak and the background noise (Fig. 4.13 **A-B**) unless averaging is performed. As the microwave drive frequency is increased further away from the minimum splitting the peak noise power caused by the microwave drive become more distinct. Indeed, the rectanglar shape of the peak response is indicative of the sensitivity of the quantised oscillator to a relatively small number of jumps, the width of the peak power response is very similar to that of the peak jump response in the neighbouring plot axis (Compare figures 4.13 **D-F** with figures 4.13**J-L**). Thus the peak noise power in the oscillator could be used to directly characterise the microwave transition width, but spurious jumps will cause problems hence the need to average the power plots over 10 runs.

The qubit is also driven by the microwave-oscillator mixture and indeed as the qubit is weakly driven by $F_{mw} - F_{osc}$ the narrow transition produced may be more suited for finely probing the qubit energy level structure, or at least check previous results whilst working with F_{mw}.

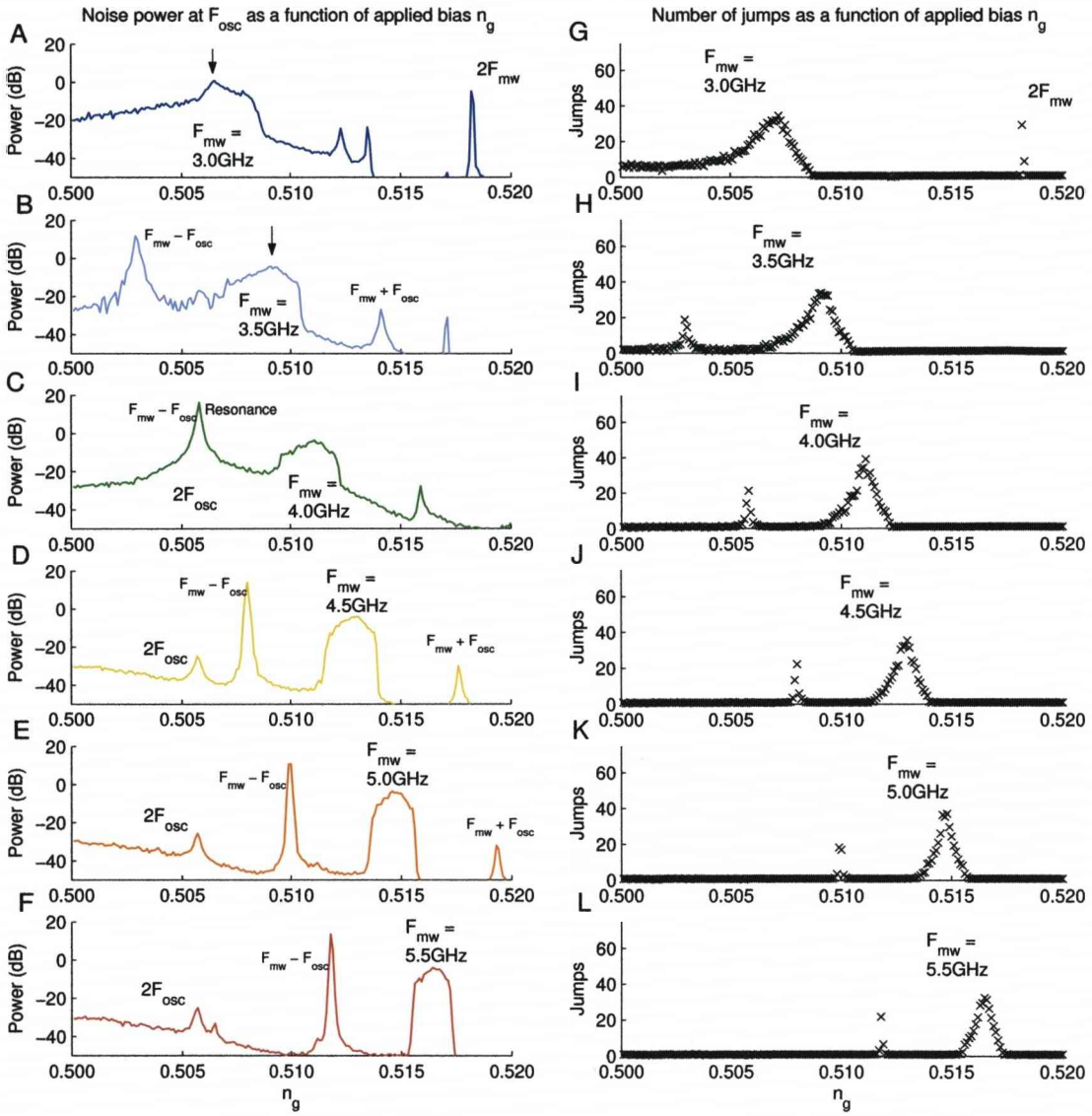

Figure 4.13: (**A-F**) Record of the oscillator power (power at the frequency F_{osc}) as a function of the applied bias (n_g) for different microwave drive frequencies (F_{mw}). With a quantised oscillator model the peaks can be difficult to observe within the large amounts of noise caused by the quantum state diffusion unravelling, hence the power has been averaged over 10 runs. (**G-L**) As with the classical oscillator model, when the qubit is correctly biased, the Rabi oscillations have maximum amplitude therefore more quantum jumps will occur. As the qubit state collapses, these large discontinuities generate broadband noise which drives the oscillator circuit creating the aforementioned peaks in oscillator power. The quantised oscillator model appears to be more sensitive to the qubit jumps as the composite state of the system is directly affected, the rectangular shaped peaks suggest a significant response can be observed even for a small number of jumps.

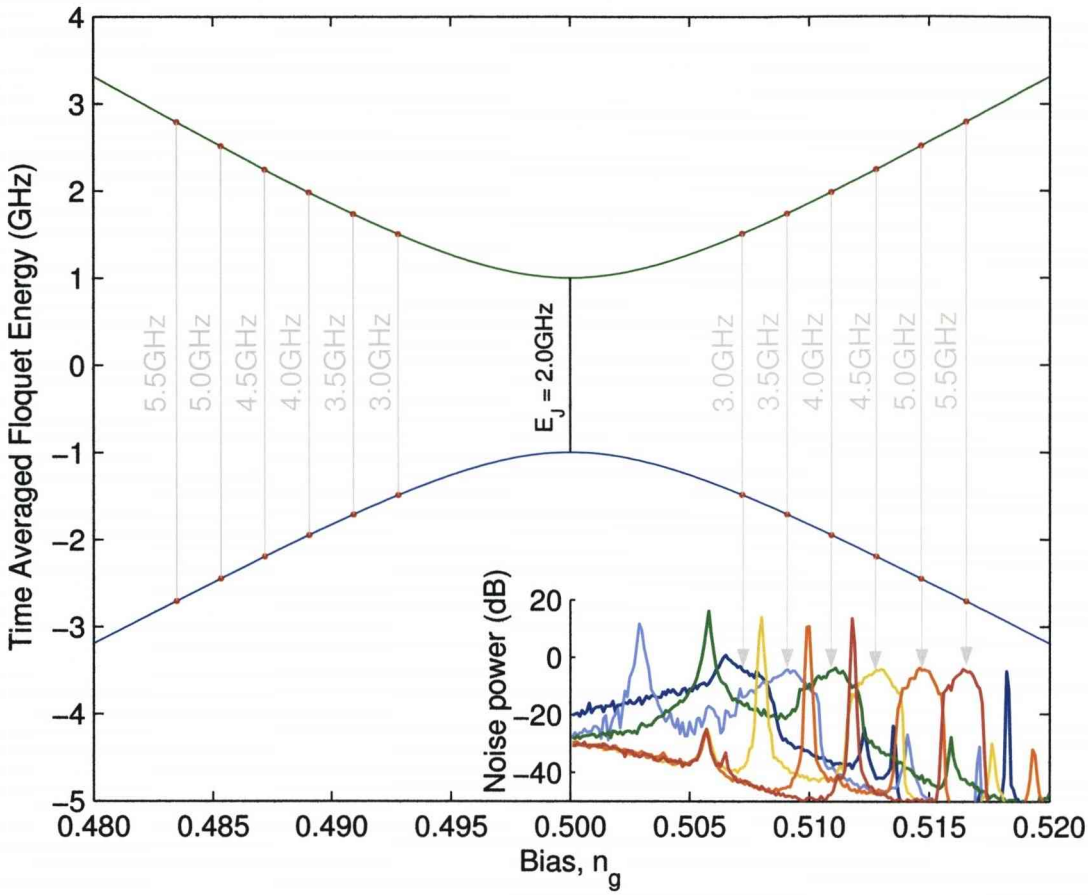

Figure 4.14: The energy level diagram can be constructed by using a sudden rise in oscillator power to associate a microwave drive frequency with a bias point. As per section 4.2.4, it is known that there is a measurable change in oscillator power whenever the qubit energy gap (set by the known bias) is equal to the microwave energy (which is also known). This 'feature' is used to pair off energy separations and bias points such that the energy level diagram can be constructed.

4.4 System behaviour in unusual frequency regimes

The resonant frequency of the biasing field is usually much lower than the Josephson junction frequency, however we are interested in discovering if there are any advantages to biasing the qubit with a high frequency resonator that can itself drive excitations within the qubit. As in previous sections the work focuses on spectroscopy, although in this section only the oscillator response is of interest for different resonant frequencies and microwave amplitudes. The resonant frequency of the 'low frequency' oscillator is always taken to be 1.33GHz and likewise a 'high frequency' resonator is assumed to be 3.00GHz, this value is chosen as to exceed the 2.00GHz Josephson junction frequency whilst not being a harmonic of the low frequency oscillator. The overall aim to determine if there are any additional features in the oscillator which may be of help characterising the qubit behaviour through the backreaction effect.

4.4.1 Bias field sweep

To determine how the oscillator frequency spectrum changes as a function of the bias field applied to the qubit, the DC bias n_g is maintained at a constant value whilst the stochastic oscillator-qubit system is continually driven by a microwave, the spectrum is then extracted from a lengthy time evolution. The system is then reinitialised and the qubit bias n_g is incremented. The resulting spectra are collated as a two-dimensional plot of frequency and bias, with the spectral power density (in decibels) represented by the plot colour.

Figures 4.15A and 4.15B shows plots of the power spectral density (PSD) for two different microwave amplitudes $A_{mw} = 1.5 \times 10^{-3}$ (A) and $A_{mw} = 3.0 \times 10^{-3}$ (B) driving at 3.5GHz with a low frequency bias oscillator of 1.33GHz. In this configuration all frequencies are well separated and so do not interfere in a complex fashion. The Rabi frequency is clearly present and also the sidebands around the fixed microwave drive frequency. When correctly biased on the microwave transition, the Rabi frequency doubles in line with the microwave amplitude, confirming this linear relation [89]. However, figures 4.15C and 4.15D show rather more complex behaviour, in this case the biasing oscillator is taken to be 3.00GHz. The high resonant frequency of the biasing circuitry is of interest as the qubit becomes doubly driven, but with a noise driven drive field that is always coupled to the qubit. When the microwave field is removed there are still some effects due to the 3.0GHz high-frequency oscillator causing excitations and a splitting in the qubit. This is possible as the oscillator exceeds the Josephson junction frequency

(2.0GHz) and so drives the qubit as per an injected microwave field. Alternatively, when the low frequency oscillator (1.33GHz) was used (Figs. 4.15A and 4.15B) there were no excitations, however if the qubit is biased on a harmonic of the oscillator, this would exceed the Josephson frequency and start driving the qubit.

When the microwave is applied, we notice interesting effects, arising from the additional interference of the 'side bands' created by the 3.0GHz oscillator drive signal, which is now in close proximity to the 3.5GHz microwave field. This relatively small detuning causes a multitude of splittings, similar to that of the Autler-Townes effect [108]. However, this is a benefit as it creates many more features in the frequency spectrum, which in turn increases the available frequency bands in which useful information can be obtained [109]. Although the features obtained are clearly related, the presence of multiple frequencies (mixtures, splittings and harmonics) in different regions of frequency provides different experimental 'windows' within which to explore the behaviour of Josephson charge devices.

The mixing of the Rabi oscillations with the microwave field causes 'side bands' surrounding the drive signal. It is important to note that the high frequency behaviour surrounding the drive signals is replicated at $F_{mw} - F_{osc} =$ 500MHz, and this area of interest has been enlarged for each of figures 4.15C and 4.15D, indeed, this should be an easily accessible frequency range. Of most importance is that this frequency regime can be adjusted on to an experimentally accessible bandwidth by changing the oscillator frequency, and hence the aforementioned separation $(F_{mw} - F_{osc})$.

In addition, within the power spectral density there exists a point of interest ($\diamondsuit$) where the microwave and oscillator excitations intersect (Figs. 4.15C and 4.15D). As the hyperbolic shape of the oscillator excitations remains relatively constant for low amplitude microwaves, the intersection point will mainly be governed by the amplitude and frequency of the microwave. If the microwave amplitude is too large then the microwave transition width eventually increases to enclose the oscillator transition and the two transitions are no longer distinct, then the features merge. It can be seen in plot 4.15D, when the microwave is driving at a similar amplitude to the oscillator signal ($A_{mw} = 1.5 \times 10^{-3}$), the intersection occurs roughly halfway between the two signals. This is potentially a useful feature that may be of benefit to experimentalists. The application of microwaves is normally via a frequency dependent coupling, if multiple frequencies are to be used in an experiment, each will need to be characterised.

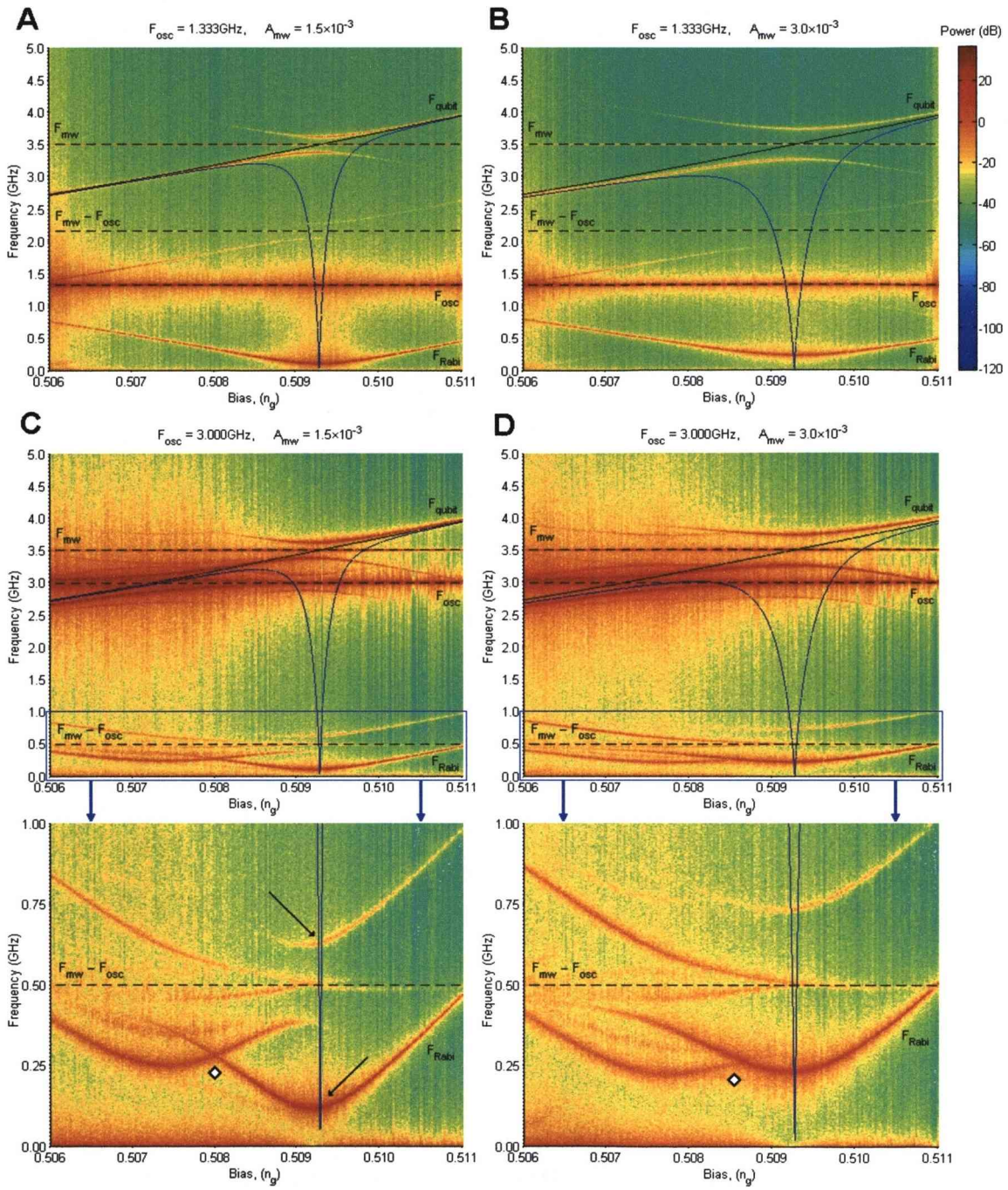

Figure 4.15: PSD plots for the *oscillator* as a function of the qubit bias n_g. Plots **(A-B)** assume a low frequency (1.33GHz) oscillator coupled to a qubit driven by a constant 3.5GHz microwave, these two plots show the effect on the Rabi frequency of doubling the microwave amplitude A_{mw}. **(C-D)** More interestingly, if the oscillator is replaced by a high frequency (3.00GHz) alternative, a number of interactions occur which shifts the qubit Rabi frequency into a new frequency regime centered on the oscillator-microwave frequency separation. This upward shift is indicated by the two black arrows in the magnifed section of **C**. The lowest plots show a magnified region from 0 to 1 GHz indicated by the blue box in the corresponding upper plot.

This feature may provide an independent measure for the amplitude of the microwaves which actually couple to the device at different frequencies. This should allow the amplitude of the microwaves actually reaching the device to be kept constant even though the coupling changes with frequency. In addition, it may be possible to characterise the oscillator in terms of microwave properties, and furthermore estimate the effects or significance of the oscillator energy transition.

4.4.2 Microwave frequency sweep

Fig. 4.16 is presented in a similar manner as Fig. 4.15. However there are now two frequency axes: the horizontal axis represents the frequency of the applied microwave drive field, and the vertical axis is the frequency response. It should be remembered that the microwave frequency axis is focused near the qubit transition frequency ($F_{qubit} = 3.50$GHz) and the diagonally increasing line is now the *microwave frequency.*

The most interesting features in question are secondary splittings, which occur only when the lower Rabi side-band passes through the oscillator peak, splitting it. The oscillator frequency split is somewhat obscured by the large oscillator peak, however the low frequency splitting centred on $F_{mw} - F_{osc} = 500$MHz is clearly visible in the magnified section, as indicated by the arrows.

We find the particular combination required to cause maximum splitting only occurs when $F_{Rabi} = F_{mw} - F_{osc}$ **and** the Rabi oscillations have maximum amplitude, (i.e. when the microwave is in resonance with the bias setting). Hence the microwave amplitude and a feature in frequency space can be related. The traces created by these splittings can be observed at a given applied microwave frequency, the traces expand and contract dependant on the proximity to the splitting. Tracking the expansion of these traces it may be possible to tune the microwave amplitude for the desired Rabi frequency.

This could be applied to calibrate the microwave waveguide, in which one could determine the effective microwave applied to the qubit in terms of the microwave amplitude applied at the external end of the waveguide. This is important as the characteristics of the waveguide, such as impedance, are frequency dependant. If the separation of the two known frequencies is fixed, (the oscillator and the microwave), we know by maximising the secondary splitting using the microwave amplitude that the Rabi side-band must now be equal to the well defined oscillator-microwave frequency separation, and therefore the external microwave amplitude that caused it. In addition, the maximum splitting solution should indicate a correctly biased system. If the oscillator were of a much lower

frequency (1.36GHz) then only the Rabi oscillations and Rabi side-bands would appear (Fig. 4.15A), and none of these additional interactions would exist. The extra features caused by this small detuning is an important point to reinforce as it links the microwave, oscillator, Rabi oscillations and bias field together at a single location.

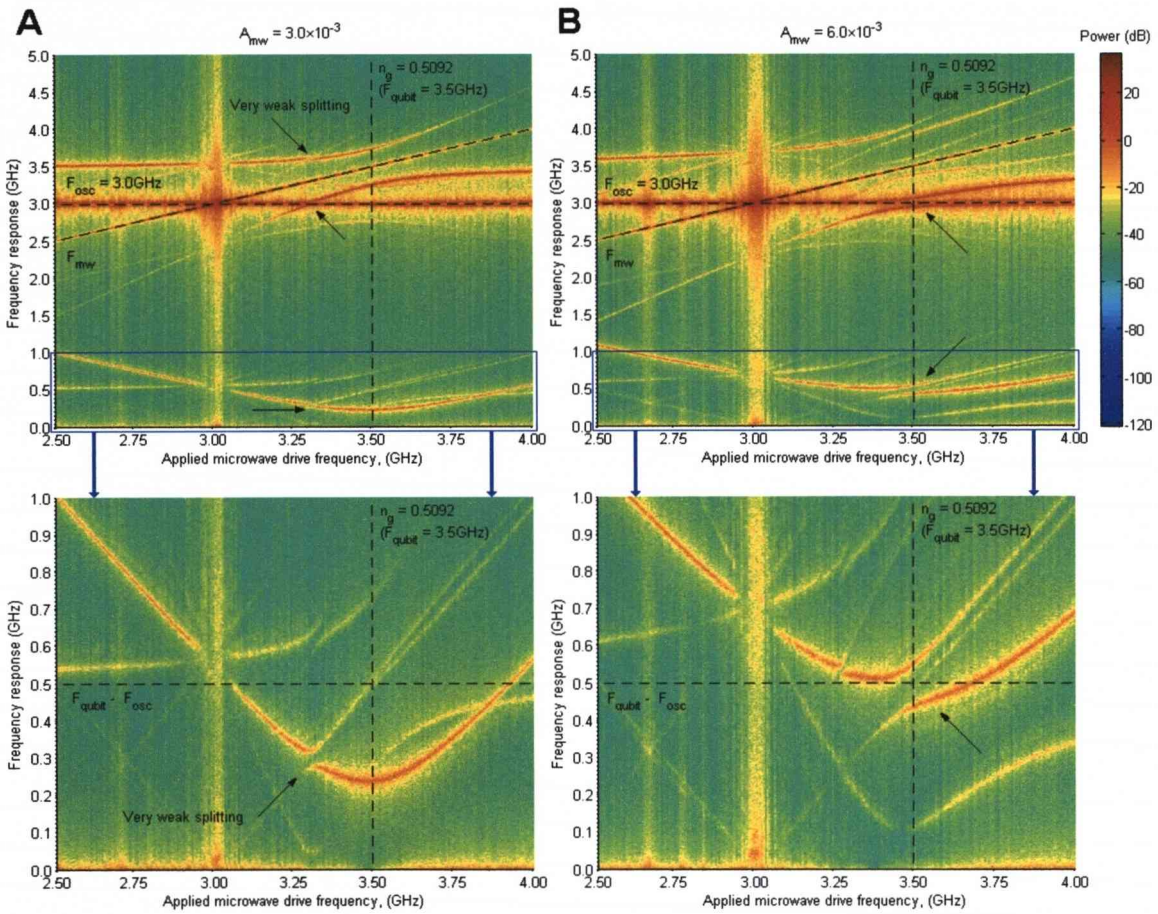

Figure 4.16: PSD plots for the *oscillator* as a function of the applied microwave drive frequency assuming a constant bias $n_g = 0.5092$ corresponding to an energy level separation of 3.5GHz. The small splitting links a number of known and potentially unknown frequencies when the splitting separation is maximised. The lower plots show a magnified region from 0 to 1 GHz indicated by the blue box in the corresponding upper plot.

4.5 Summary

In this chapter we have presented a spectroscopic analysis of a two level qubit coupled to an RLC oscillator circuit. Initially, a classical oscillator was considered where the dynamics of the oscillator were modelled by a second order differential equation modified by the qubit evolution. However, as it is unlikely that such a constrained quantum system such as a qubit will interact directly with a classical system, a similar set of analysis was performed using a quantised simple harmonic oscillator with many levels coupled to the two level qubit as a fully quantised composite system. We investigated what information or characteristics of the qubit can be obtained through measurement of the oscillator voltage (charge). It would be advantageous to reduce the number of systems interacting with the qubit, whereas the conventional measurement schemes employ separate measurement devices such a single electron transistors, the biasing circuitry is already in place.

A quantum trajectory approach has been used as individual trajectories are somewhat similar to the average measurement record. The quantum state diffusion unravelling of the master equation simulates a dissipative oscillator in the fully quantised model, and a quantum jumps unravelling simulates spontaneous emissions from the qubit to a lossy reservoir for both the classical and quantised oscillator models.

We have shown that the qubit energy level structure could be constructed through measurement of the peak power in the oscillator circuitry as the dc qubit bias n_g is swept through a fixed frequency microwave transition F_{mw}. The peak power is a result of increased quantum jumping as Rabi oscillations are created when the qubit is biased on the microwave transition, allowing the energy gap equal to F_{mw} to be associated with a horizontal position n_g in the structure. However care should be taken to avoid detecting the higher oscillator harmonics and sidebands. This holds for both the classical and quantised oscillator, however we note that the quantised oscillator generates a significant response even for single jumps, this perhaps due to the entanglement in composite state vector.

We have also presented features that exist within the power spectra of a charge qubit that are copied into the oscillator spectra through the coupling defined by κ. The qubit is coupled via a single Josephson junction and capacitance to a (fully quantised) oscillator circuit, which provides a bias voltage and a means of measurement. However of most interest is the choice of a high frequency oscillator circuit that can create additional features in the power spectrum of the qubit

and the coupled oscillator when the oscillator resonant frequency and microwave frequency are similar (3.0GHz and 3.5GHz respectively). These features are predominantly discontinuous frequency splittings akin to the Autler-Townes effect in quantum optics, in addition to intersections of frequency peaks. We find that the low frequency Rabi oscillations can be moved into a different (experimental) bandwidth centered on $F_{mw} - F_{osc}$ by adjusting the oscillator frequency.

In addition, figure 4.16 shows a small frequency splitting centred on $F_{qubit} - F_{osc}$ that occurs whenever the lower Rabi sideband of the microwave mixes with the high frequency oscillator ($F_{Rabi} = F_{mw} - F_{osc}$). This splitting is widest when the qubit is properly bias as the Rabi oscillations will have maximum amplitude, and so a single point-like feature links F_{qubit} set by the bias, with F_{mw}, F_{osc} and F_{Rabi}. So the microwave frequency can be adjusted to maximise the splitting and hence aid in placing the microwave transition accurately on the bias point. Note that this small splitting feature will only occur when using a relatively high frequency oscillator close to the microwave frequency, else the Rabi sideband would have to be unfeasibly large.

Chapter 5

Rapid purification techniques

The following work discussed in this chapter investigates the problems associated with the application of rapid purification techniques to superconducting charge qubits. These techniques were derived for the case of a general qubit, assuming a stationary system and perfect control over the feedback Hamiltonian. Whereas for the charge qubit, the non-zero Hamiltonian means the Bloch vector [Chapter 3] can not be held in an optimal location. In addition, the finite and often inaccurately applied Hamiltonian resources implies that not all the necessary qubit rotations may be available. However, we propose a set of purification protocols to overcome these limitations, whilst maintaining near optimal performance.

5.1 The purity of a state

Decoherence can be interpreted as the loss of information known about a system, this can occur naturally due to an interaction between the qubit and it's environment or purposefully by discarding accumulated measurement results. Regardless of the decoherence mechanism, the loss of information corresponds to an uncertainty of the actual pure state of the system.

This uncertainty is represented by a probabilistic mixture of *pure states*, where many potential states have an assigned probability. The resulting accumulation of these weighted pure states is referred to as the *mixed state* of an ensemble.

$$\rho = \sum_i p_i |\psi_i\rangle \langle\psi_i| \tag{5.1}$$

$$\rho = \sum_i p_i \rho_i \tag{5.2}$$

Whereas pure states are known with complete confidence, the mixed state with most uncertainty is called the *completely mixed state*, in this case the distribution of probabilities p_i is uniform. For a completely mixed state, every pure state is

equally likely to be the true pure state, thus no useful information is known and therefore quantum computation from an unknown starting point is meaningless.

To prepare a known state for useful quantum computation requires the observer to obtain knowledge of the true state of the system by some form of measurement, this process is also known as purifying the qubit state (as the process involves taking a mixed state toward a pure state). To gauge the purity of a qubit state, we have defined the purity P and impurity L to be:

$$P = Tr\left\{\hat{\rho}^2\right\} \tag{5.3}$$

$$L = 1 - P \tag{5.4}$$

The purity P, ranges from 0.5 (the completely mixed state) to 1.0 (a pure state). Whilst the remaining impurity L, tends to zero as the mixed state is purified to a pure state (Figure 5.1). It is often more convenient to refer to the remaining impurity L of the qubit state, as logarithmic scales can be used with more ease for small numbers.

The purification of a two-state system is best visualised in the Bloch sphere representation, where the state of the system is described by the position of a vector, $\vec{v}$. In addition, there is a direct relation between the purity and the length of the Bloch vector, $R = \mid \vec{v} \mid$. By expressing the mixed state or density matrix as a function of the Bloch vector components x,y and z:

$$\hat{\rho} = \frac{1}{2}\left(I + \vec{v} \cdot \vec{\sigma}\right) \tag{5.5}$$

$$\hat{\rho} = \frac{1}{2}\left(I + x\sigma_x + y\sigma_y + z\sigma_z\right) \tag{5.6}$$

Applying the relevant Pauli matrix identities (Eqs. 2.19, 2.20 and 2.21) and tracing out the result yields the purity (or impurity) as a function of Bloch vector position in Cartesian coordinates.

$$P = \frac{1}{2}\left(1 + x^2 + y^2 + z^2\right) \tag{5.7}$$

$$P = \frac{1}{2}\left(1 + R^2\right) \tag{5.8}$$

$$L = \frac{1}{2}\left(1 - x^2 - y^2 - z^2\right) \tag{5.9}$$

$$L = \frac{1}{2}\left(1 - R^2\right) \tag{5.10}$$

It can immediately be seen that the pure states indeed exist on the surface of the sphere, when the spherical radius R is equal to one. Therefore to purify a qubit as quickly as possible, it is perhaps best understood as moving from the

centre of the sphere to a point on the surface. Decoherence processes reduce the length of the Bloch vector as information on the actual state is destroyed, and measurement attracts the vector towards the surface as knowledge is gained.

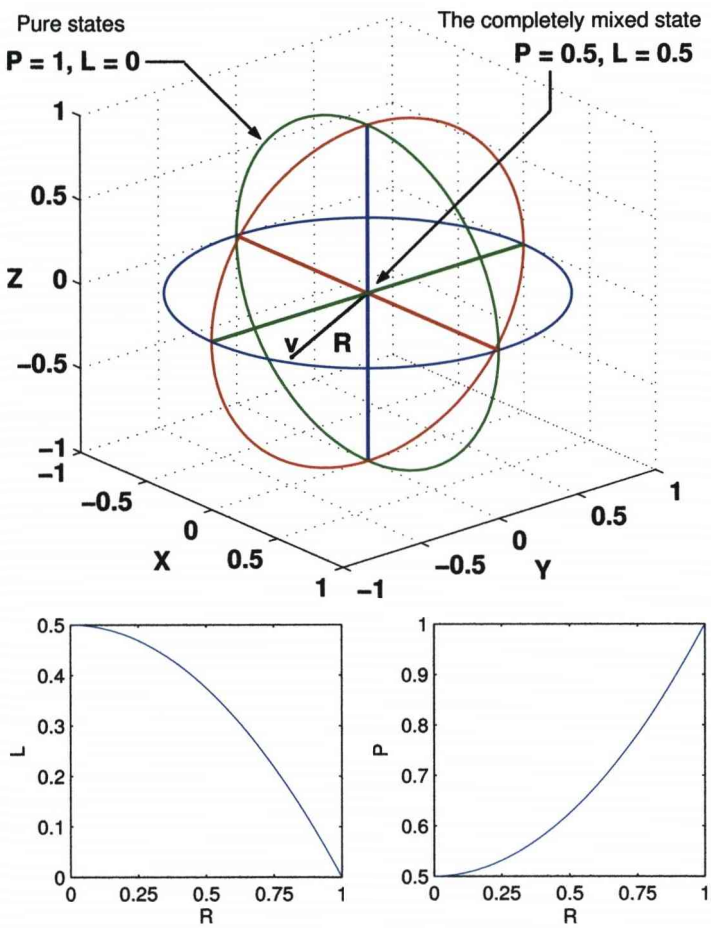

Figure 5.1: Pure states are located on the surface of the Bloch sphere, mixed states exist inside the sphere

5.2 Purification by using weak measurements of a state

Projective or infinitely strong measurements will instantly purify a qubit, as the state of the system will collapse into a known state, one of the two measurement basis, dependent on the actual measurement outcome. This allows the qubit state to be prepared in a known state, and furthermore any pure state can then be created as rotations can be applied starting from this known state. However, such projective type measurements require a strong interaction between the fragile

qubit state and the environment though the large couplings of the qubit island and the measurement device. It is difficult to remove the influence of the measurement device from the qubit as it is often integrated on the same substrate. Therefore these couplings can not be easily adjusted in an experimental apparatus.

One possible solution is to utilise a weakly coupled device to perform all the required measurements at a constant strength γ sufficiently weak to also allow conventional quantum computation when the need arises, whereas the projective type measurements purified the qubits instantaneously, the weak measurements gradually purify the qubit over a finite amount of time, indeed this *purification time* can be considerable, so the need for efficiently purifying a qubit is great.

The weak measurements create stochastic changes in the purity, which on average tends to move the Bloch vector to the surface of the Bloch sphere. However, due to this stochastic nature there exists the possibility that the Bloch vector recedes back to the towards centre of the sphere and so the qubit does not fully purify, and it can be problematic if the purification randomly fails.

Starting from the set of simultaneous stochastic differential equations for the weak measurement evolution in Bloch sphere coordinates [66], the incremental change of impurity dL for each point within the Bloch sphere can be derived:

$$dr = -\left(4\gamma dt + z\sqrt{8\gamma}dW\right) r \tag{5.11}$$

$$dz = \left(1 - z^2\right)\sqrt{8\gamma}dW \tag{5.12}$$

where γ is the measurement strength, dW is the Weiner increment (Zero mean Gaussian noise source with variance dt) and $r = \sqrt{x^2 + y^2}$ is the radial distance the Bloch vector projects on to the xy-plane. Rewriting equation (5.9) in terms of r and z, the incremental change of impurity dL is given by:

$$L = \frac{1}{2}\left(1 - r^2 - z^2\right) \tag{5.13}$$

$$L + dL = \frac{1}{2}\left(1 - (r + dr)^2 - (z + dz)^2\right) \tag{5.14}$$

$$dL = -\frac{1}{2}\left(2rdr + dr^2 + 2zdz + dz^2\right) \tag{5.15}$$

Substituting the equations for the positional increments dr and dz yields:

$$\begin{aligned} dL = \quad & -\frac{1}{2}(-2(4\gamma dt + z\sqrt{8\gamma}dW)r^2 \\ & +(4\gamma dt + z\sqrt{8\gamma}dW)^2 r^2 \\ & +2z(1 - z^2)\sqrt{8\gamma}dW \\ & +(1 - z^2)^2 8\gamma dW^2) \end{aligned} \tag{5.16}$$

The time increment and Weiner increment terms are collected, the terms in dt causes a drift towards the measurement axis (z-axis) and the stochastic terms in dW models the noise due to the random measurement results.

$$\begin{aligned} dL = \quad & -\frac{1}{2}(-8\gamma dt r^2 + 16 g^2 dt^2 r^2 \\ & +4\gamma\sqrt{8\gamma}dt z r^2 dW - 2\sqrt{8\gamma} z r^2 dW + 2z(1-z^2)\sqrt{8\gamma}dW \\ & +8\gamma r^2 z^2 dW^2 + (1-z^2)^2 8\gamma dW^2) \end{aligned} \tag{5.17}$$

$$\begin{aligned} dL = \quad & -\frac{1}{2}(8\gamma dt r^2(2\gamma dt - 1) \\ & +2\sqrt{8\gamma} z(4\gamma dt r^2 - r^2 + (1-z^2))dW \\ & +8\gamma(r^2 z^2 + (1-z^2)^2)dW^2) \end{aligned} \tag{5.18}$$

Terms in γdt are assumed to be small for weak measurements and so can be removed. The resulting equation is the incremental change of impurity dL given the Bloch vector (r, z), where r is the radial distance from the z-axis. Page seven of reference [110], which is an introduction to weak measurement, shows that when using Ito Calculus, the ensemble average $E(dW^2) = dt$ also holds for the single case. Hence $dW^2 = dt$ which greatly simplifies the above equations, however due to non-linearity $E(\sqrt{8\gamma}z(1-r^2-z^2)dW) \neq 0$ and must be retained.

$$dL = \quad -4\gamma dt(1-z^2)(1-r^2-z^2) - \sqrt{8\gamma} z(1-r^2-z^2)dW \tag{5.19}$$

It is extremely important to note that the dW term needs to be included for calculating $L(t)$. As the magnitude of the measurement noise term depends on the current value of the impurity, we find merely assuming $E(dW) = 0$ is incorrect due to the wide variety of iteration histories caused by the non-linearities present. A more complex analysis is required and is explained further in references [2, 66, 111].

It would be preferential to express the incremental change of impurity as a function of the remaining impurity. Due to the rotational symmetry about the measurement axis (z-axis), the Bloch vector can be sufficiently defined in terms of the angle the vector forms with the z-axis [1].

$$R = \sqrt{1-2L} = \sqrt{r^2+z^2} \tag{5.20}$$

$$r = R\sin\theta, \quad z = R\cos\theta \tag{5.21}$$

There are two valid substitutions for $(1-z^2)$, in terms of either sine or cosine:

$$dL = -8\gamma dt L(2L + (1-2L)\sin^2\theta) - 2L\sqrt{8\gamma(1-2L)}\cos\theta\, dW \tag{5.22}$$

alternatively

$$dL = -8\gamma dt L(1-(1-2L)\cos^2\theta) - 2L\sqrt{8\gamma(1-2L)}\cos\theta\, dW \quad (5.23)$$

It can now be clearly understood that the magnitude of change in impurity varies as a function of the angle the Bloch vector makes with the measurement axis.

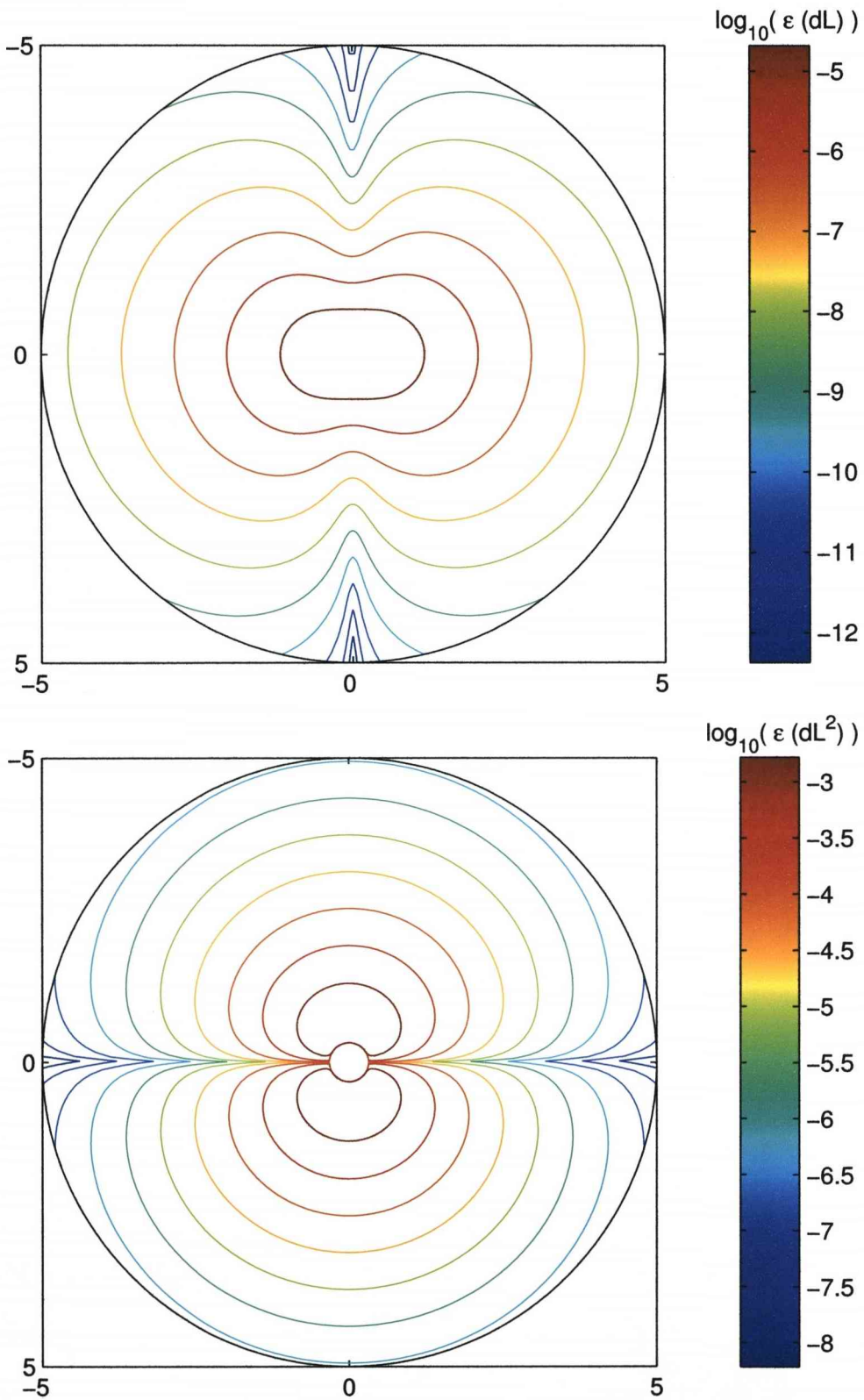

Figure 5.2: Diagram showing the variation of the mean change of impurity and variance within a cross-section of the Bloch sphere, plotted with logarithmic radial distance $\log_{10}(R)$. (Eqns. 5.22 and 5.23)

5.3 Charge qubit model - Purification

A superconducting charge qubit (Cooper pair box), illustrated in Fig. 5.3, consists of a small island of superconducting material connected via a single Josephson junction to a bulk superconducting electrode. The weak link caused by the Josephson junction allows Cooper pairs to tunnel to and from the small island, and is assumed to be suitably engineered to have a fixed tunnelling frequency ν. The Josephson junction is sufficiently weak and the total capacitance of the island sufficiently small that the energy associated with charging the island is large compared to the tunnelling energy of the junction ($E_J = \hbar\nu/2\pi$), this is normally called the Coulomb blockade regime [35]. In the Coulomb blockade regime only one Cooper pair can occupy the island, the presence or absence of this electron forms a two-state system. The electrode supplies a voltage bias, which can be expressed as an effective charge q_g. The island is also capacitively coupled to a grounded electrode to supply a common reference. For simplicity, in this section we ignore the dynamics of the biasing circuitry, as the lack of direct control of the qubit bias and the two way interaction between the qubit and external components examined in chapter 4 detracts from the key issue of designing feedback pulses.

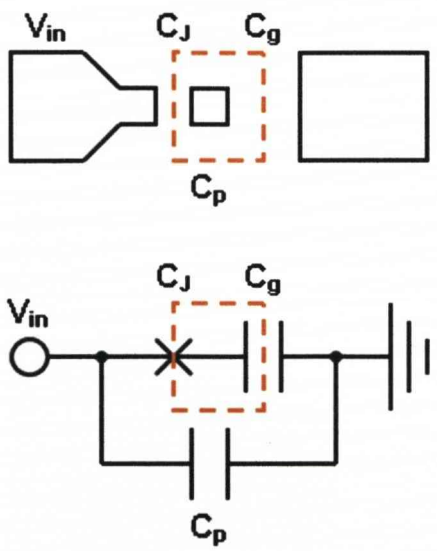

Figure 5.3: The simple charge qubit model is an island (orange box) coupled to a bulk bias electrode via a single Josephson junction whose frequency is known. The qubit is controlled via a bias voltage applied across the device. There are three major capacitances, C_J is the capacitance of the Josephson junction, C_g couples the island to a grounded electrode, and C_p is the parasitic capacitance observed between the bulk electrodes.

The Hamiltonian of this system was derived in section 3.2.2.

$$H = \frac{(q-q_g)^2}{2C_q} - \hbar\nu \sin\left(2\pi\frac{\theta}{\Phi_0}\right) \tag{5.24}$$

Here θ is the superconducting phase difference across the Josephson junction expressed in units of the flux quantum $\Phi_0 = h/2e$. The capacitance C_q is the effective qubit capacitance calculated from the three physical capacitances [67], C_J, C_g and C_p.

$$C_q = \frac{C_gC_J + C_JC_p + C_pC_g}{C_g + C_p} \approx C_J + C_g \tag{5.25}$$

where the component values are constant and consistent for all simulations, in line with experimental values quoted in reference [38].

Table 5.1: Components

	Description	Typ.
$\nu/2\pi$	Josephson junction energy	10GHz
C_J	Josephson junction capacitance	500aF
C_g	Qubit-Grounded Bulk capacitance	0.5aF
C_p	Electrodes parasitic capacitance	1.0aF
γ	Measurement strength constant	75×10^6

At low energies, this Hamiltonian can be approximated with just two states. Using $n_g = q_g/2e$ for the effective number of Cooper pairs induced by the bias voltage, the modified Hamiltonian is [112, 113].

$$\begin{aligned} H = & \frac{(2e)^2}{2C_q}\left(n_g^2 - n_g + \frac{1}{2}\right) I \\ & + \frac{(2e)^2}{2C_q}\left(\frac{1}{2} - n_g\right)\sigma_z \\ & - \frac{\hbar\nu}{2}\sigma_x \end{aligned} \tag{5.26}$$

The first term (I) may be discarded as the identity matrix does not affect the dynamics of the system, however it is included for completeness. The second term (σ_z) shows that the applied voltage bias field controls the rotations about the z-axis. When $n_g = 0.5$ the rotations are halted; when $n_g > 0.5$ the qubit rotates in one direction, and when $n_g < 0.5$ the direction is reversed. The third

and final term (σ_x) is caused by the Josephson junction, it should be clearly noted that this specific qubit model does not permit the σ_x contribution to be removed, therefore the qubit undergoes constant rotations about the x-axis. However, a different qubit topology can be employed (section 3.1.2) for which the σ_x term can be modulated by applying magnetic flux between a pair of Josephson junctions.

In addition, the qubit is assumed to be weakly coupled to a charge measurement device such as a Single Electron Transistor (SET), the charge measurement corresponds to measurements along the z-axis of the Bloch sphere. The effect of the weak coupling is modeled using a generic weak measurement model [62, 1] (Section 2.2), with a constant measurement strength of $\gamma = 75 \times 10^6$. This value allows significant purification to be observed over 20ns, which is a timescale similar to the decoherence times for solid state qubits.

5.3.1 Specific system constraints

I) The frequency of rotation around the x-axis is fixed by manufacture — this frequency is taken to be 10GHz, in line with experimental values [38]. This frequency is equal to the minimum splitting ($n_g = 0.5$) shown by Figure 5.4 and it is vital that a sizeable separation is maintained to preserve the two distinct states and suppress the effect of thermal fluctuations.

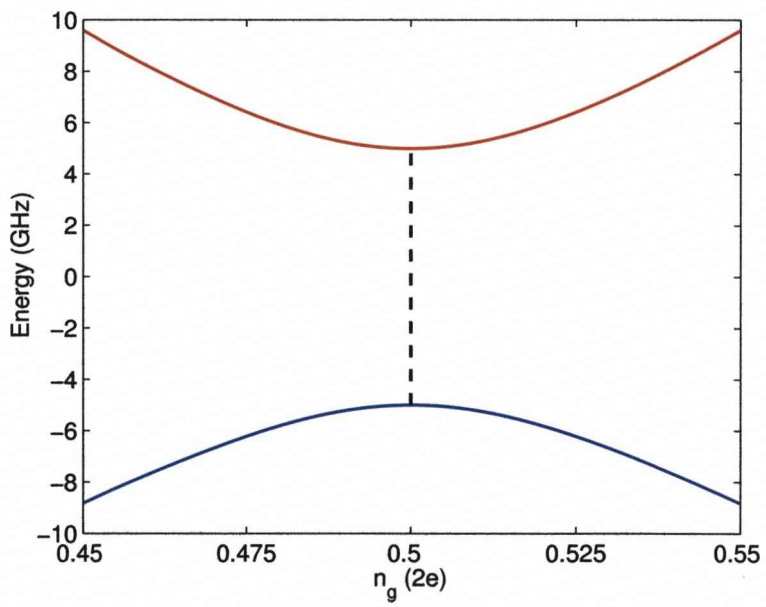

Figure 5.4: Energy level structure of the qubit. The avoided crossing caused by the 10GHz Josephson junction creates an energy gap between the energy states. This separation is kept relatively large to reduce problems caused by thermal excitations or other extraneous noise.

Figure 5.4 and equation 5.26 clearly shows the minimum energy of the system can not be zero for any n_g operating point. The Bloch vector is constantly orbiting the x-axis and so can not be halted. This inability to hold the Bloch vector in any given position is the **critical problem** we seek to address in this chapter.
II) The voltage bias n_g is assumed to be the only means of control permitted, and the magnitude of n_g must be limited to avoid accessing the neighbouring charge state ($0.25 < n_g < 0.75$). Although the Josephson tunnelling frequency can be adjusted, with the introduction of a magnetic flux, it is preferable to use a single control field as it would not then be necessary to implement extra hardware that may couple the environment to the system. In addition, there would be problems associated with synchronising multiple control pulses and monitoring the stability of the controls when not in use. The significant disadvantage is limiting control of the Bloch vector to rotations about a single axis, the z-axis.
III) Weak measurements are taken along the z-axis of the Bloch sphere, as this corresponds to measurement of the charge observable. Measurements along other axes are not permitted as these are not physically realisable for a charge qubit.

5.4 Qubit evolution in the absence of feedback

By way of constraint **II**, all feedback is applied using a single control field, the charge n_g induced by the bias voltage V_g. The biasing charge is set to $n_g = 0.5$, the operating point at which the feedback control has zero effect and the Hamiltonian of the system with no feedback reduces to equation 5.27. Under this condition, the Bloch vector experiences only the x-axis rotations caused by tunnelling across the Josephson junction, and the random fluctuation effects due to weak measurement [114].

$$H = \frac{(2e)^2}{4C_q} I - \frac{\hbar\nu}{2} \sigma_x \tag{5.27}$$

For computational efficiency the system was simulated as three simultaneous difference equations (the three Bloch vector components: x, y and z), which combines the weak measurement evolution with an incremental angular change about the x-axis, $d\theta_x = \nu\ dt$.

$$R_x(d\theta_x) = \begin{pmatrix} 1 & 0 & 0 \\ 0 & \cos(d\theta_x) & -\sin(d\theta_x) \\ 0 & \sin(d\theta_x) & \cos(d\theta_x) \end{pmatrix} \tag{5.28}$$

$$\begin{pmatrix} dx(d\theta_x) \\ dy(d\theta_x) \\ dz(d\theta_x) \end{pmatrix} = \begin{pmatrix} 0 \\ y\cos(d\theta_x) - z\sin(d\theta_x) - y \\ y\sin(d\theta_x) + z\cos(d\theta_x) - z \end{pmatrix} \tag{5.29}$$

Adding the weak measurement evolution yields:

$$\begin{pmatrix} dx \\ dy \\ dz \end{pmatrix} = \begin{pmatrix} -(4\gamma dt + z\sqrt{8\gamma}dW)x \\ y\cos(d\theta_x) - z\sin(d\theta_x) - y - (4\gamma dt + z\sqrt{8\gamma}dW)y \\ y\sin(d\theta_x) + z\cos(d\theta_x) - z + (1-z^2)\sqrt{8\gamma}dW \end{pmatrix} \tag{5.30}$$

Equation 5.30 highlights an important result that the Bloch vector is constrained to only rotate in the yz-plane at $x = 0$, when no feedback is applied. The dx increment will only be non-zero if $x \neq 0$, given that the Bloch vector is initiated in the completely mixed state ($[x, y, z] = [0, 0, 0]$) then x will remain at zero throughout the entire purification process. The weak measurement process increases the length of the Bloch vector on average and hence the vector follows a spiral path formed in the yz-plane at $x = 0$:

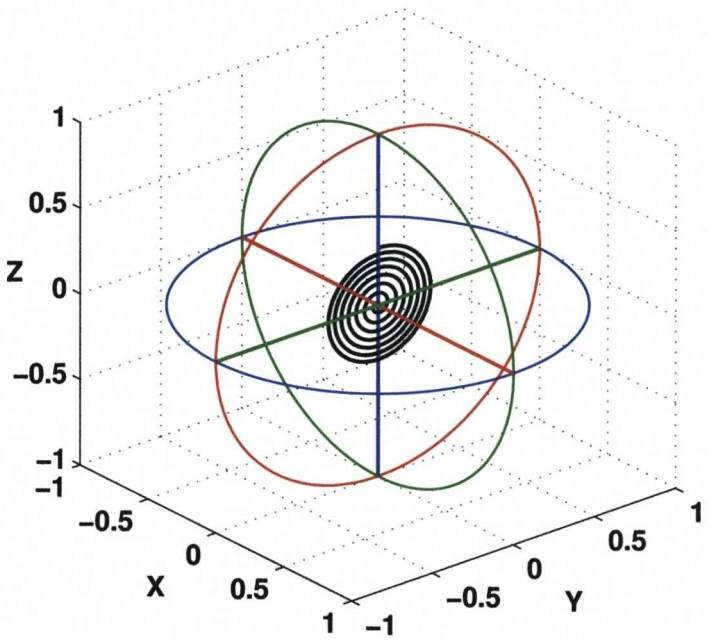

Figure 5.5: Averaged path of the Bloch vector, the length of the vector has been extracted from the impurity transient and the rotational frequency is fixed at 10GHz.

Using figures 5.2 and 5.5, it can be seen that the spiralling path of the 'no-feedback' evolution causes the average change of impurity (dL) to decrease in magnitude by several orders as the Bloch vector is swept through the z-axis. However as the Bloch vector also passes through the xy-plane, the average change of impurity is momentarily maximised, thus a naturally evolving a charge qubit under weak measurement purifies faster than one would expect. Although it is important to note that due to passage of the measurement axis (z-axis) the overall purification rate is only moderate and it will be demonstrated in the following

sections that using quantum feedback to manipulate the path of the Bloch vector can significantly improve the average purification rate [1, 66, 115, 114, 86].

5.5 Optimal purification rate for the ensemble average - Ideal Protocol I

It has been suggested by Jacobs [1], that quantum mechanical effects can be used to accelerate the purification process.

By using quantum feedback it is possible to rotate the Bloch vector on to a set of states that maximises the average rate of purification. Starting from equation 5.23 it is possible to prove that these states form the plane orthogonal to the measurement axis, this will be furthermore referred to as Ideal Protocol **I**. In the case of charge measurement along the z-axis, this optimal region is the xy-plane.

$$dL = -8\gamma dt L(1-(1-2L)\cos^2\theta) - 2L\sqrt{8\gamma(1-2L)}\cos\theta\, dW \quad (5.31)$$

$$\overline{dL} = -8\gamma dt L(1-(1-2L)\cos^2\theta) \quad (5.32)$$

The average decrease of impurity is maximised when $\theta = 90^o$, as setting $\cos\theta = 0$ removes the term $(1-2L)$ which due to $0 \leq L \leq 0.5$ must always be positive. Due to the cylindrical symmetry around the measurement axis (z-axis) the entire orthogonal plane (equatorial xy-plane) is a valid set of solutions [1].

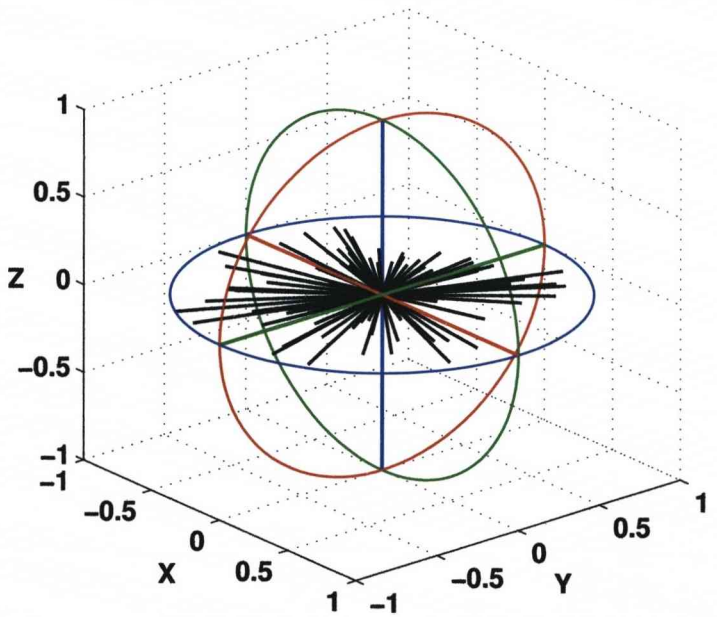

Figure 5.6: Prior to measurement, returning the Bloch vector to the plane orthogonal to the measurement axis yields the largest change of impurity [1].

It can be shown that the evolution of the impurity transient is **deterministic** under this feedback protocol. By setting $\theta = 90^o$ for the equation of instantaneous impurity change (5.23), the stochastic term in dW is removed. In which case the impurity equals the average impurity, integrating the impurity increment with the initial condition $L = 0.5$ yields an exponential decay:

$$dL_{xy} = \overline{dL}_{xy} = -8\gamma dt L \tag{5.33}$$

$$L_{xy}(t) = \overline{L}_{xy}(t) = \frac{1}{2}\, e^{-8\gamma t} \tag{5.34}$$

Due to the removal of the stochastic terms in dW by setting $\theta = 90^o$, the distribution of L_{xy} is an impulse function:

$$\Lambda_{xy}(L,t) = \delta\left(\frac{1}{2}\, e^{-8\gamma t}\right) \tag{5.35}$$

From this, the time taken to reach impurity L_{xy} under this protocol is:

$$t_{xy} = \frac{1}{8\gamma} \ln\left(\frac{1}{2L_{xy}}\right) \tag{5.36}$$

As equation (5.32) is now maximised, this is an optimal protocol, and the time t_{xy} is the fastest **average** purification time for the measurement strength γ.

Jacobs proposed that the perturbed measured Bloch vector can be returned to the xy-plane by rotating about an axis in the xy-plane which is orthogonal to the measured Bloch vector. Hamiltonian evolution is then applied to perform a minimum angle rotation α_1 on to the xy-plane, within a single time step.

$$\phi = \tan^{-1}\left(\frac{y}{x}\right) \tag{5.37}$$

$$\overline{\mathbf{n}}_1 = (-\cos(\phi),\ \sin(\phi),\ 0) \tag{5.38}$$

$$\alpha_1 = \tan^{-1}\left(\frac{\pm dz}{\sqrt{1-2L-dz^2}}\right) \tag{5.39}$$

Jacobs' minimum angle rotation requires measurement of the x, y and z axes to obtain the axis of rotation $\overline{\mathbf{n}}_1$ and angle of rotation α_1. Furthermore, two control fields (both σ_x and σ_y) are required to apply the protocol by creating $\overline{\mathbf{n}}_1$.

An alternative scheme is to rotate the measured Bloch vector about either the x or y axes, on to the xy-plane. As each of these rotational planes intersects with the xy-plane, any Bloch vector can be instantly returned to the xy-plane given infinite Hamiltonian resources. Reducing the number of qubit controls from two fields to a single control is advantageous, avoiding stability and synchronisation problems associated with the two controls required to create axis $\overline{\mathbf{n}}_1$.

$$\overline{\mathbf{n}}_2 = (1,\ 0,\ 0) \tag{5.40}$$

$$\alpha_2 = \tan^{-1}\left(\frac{\pm dz}{y}\right) \tag{5.41}$$

However, it would be extremely difficult to apply the instant and perfect control fields for either scheme to a practical qubit, as this would require infinite Hamiltonian resources and no errors in measurement and application. In addition, for the superconducting charge qubit there is also the continual motion of the state vector due to the non-zero Josephson junction energy. The protocols discussed within the next section address these issues.

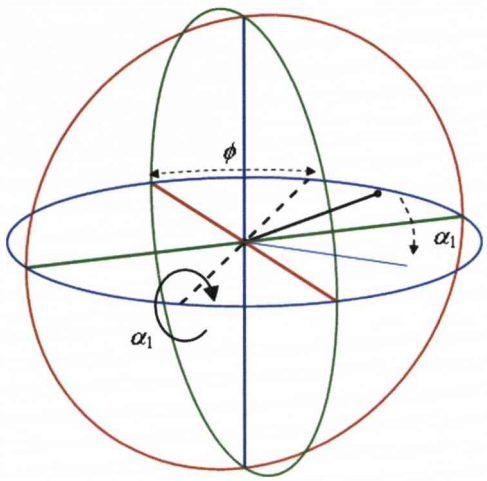

Figure 5.7: Jacobs' seminal paper proposed a minimum angle rotation of the measured Bloch vector to the xy-plane. This would be the optimal solution for limited Hamiltonian resources, but requires perfect measurements of all axis and perfect application of the control fields.

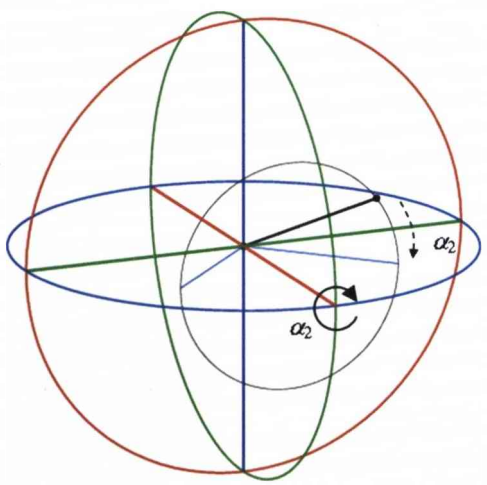

Figure 5.8: Performing the rotation about a Bloch axis would somewhat simplify the feedback process at the expense of more Hamiltonian resources. However, this still requires perfect measurement of the two axes orthogonal to the axis of rotation, in addition to the perfect application of the single control field.

5.6 Practical means of increasing the average purification rate

In this section we propose two methods for increasing the average purification rate which could be considered to be more practical than Jacobs' protocol described in the previous section, but using only one control field and one measurement axis (z). Firstly, we consider a charge qubit that has a tunable Josephson energy $E_J(\Phi)$ that is controlled by threading a magnetic flux Φ through the loop formed by two parallel connected Josephson junctions. This flux control protocol slows the passage of the Bloch vector through the desireable xy-plane and speeds the vector through the z-axis poles, which achieves a moderate increase in the average purification rate. Secondly, a different qubit is examined which has a fixed Josephson energy but is controlled by the biasing charge n_g induced by a control voltage. The resulting protocol aims to return the Bloch vector to the x-axis via a quick corrective rotation about the z-axis caused by a control pulse, this protocol yields near optimal results as the Bloch vector is constrained for a large amount of time in a region close to the xy-plane.

5.6.1 Flux controlled Hamiltonian feedback

As stated previously in section 5.4, the constant x-axis rotations in the yz-plane, due to the Josephson tunnelling, passes the Bloch vector momentarily through the xy-plane, thus permitting a temporary increase in the average purification rate. However, the same rotation also takes the vector out of the xy-plane, creating a sub-optimal purification, although with the application of quantum feedback it is possible to modulate the Josephson tunnelling energy to slow the passage of the vector through the xy-plane and hasten it through the z-axis poles. Hence, the Bloch vector experiences the accelerated purification for a greater proportion of the time evolution, as the vector remains near the optimal region for longer.

It has been previously shown in section 3.1.2 that it is possible to change the Josephson tunnelling energy by threading magnetic flux through the ring formed by a pair of parallel connected Josephson junctions. The pair of junctions is equivalent to a single device with a junction energy that varies as the cosine of the flux inside the loop.

$$E_J(\Phi_x) = 2E_{J0}\cos\left(\pi\frac{\Phi_x}{\Phi_0}\right)\cos\left(2\pi\frac{\Theta}{\Phi_0}\right) \tag{5.42}$$

This modulation of the Josephson energy by the flux closes the energy separation between the two energy levels as the cosine approaches zero (when $\Phi_x = 0.5\Phi_0$).

Indeed, in order for the direction of rotation to reverse, it is necessary to cross the zero point and momentarily close the energy levels. This would imply a brief degeneracy between the two computational states as the energy levels are no longer distinct, it is preferable to avoid this by confining the flux control to operate on one side of the sinusoid, away from the zero point.

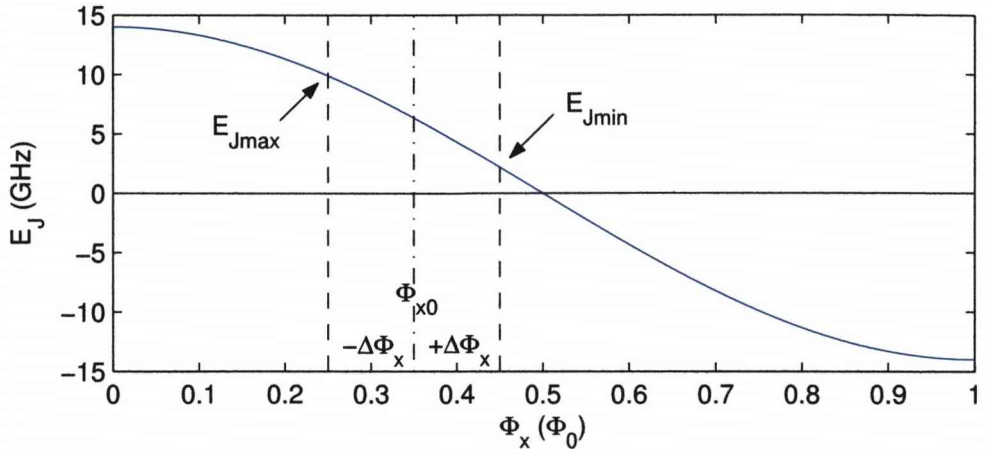

Figure 5.9: For a flux tuned Josephson junction the tunnelling energy varies as a function of the flux threading the two junction ring. To maintain two distinct states at all times, the flux values are constrained to either the positive or negative half of the cycle. ($E_{Jmax} \approx 10$GHz and $E_{Jmin} \approx 2$GHz)

An operating point is chosen on the linear regime of the sinusoid, the range of flux values is chosen to be:

$$\Phi_x = \Phi_{x0} \pm \Delta\Phi_x \tag{5.43}$$

Where $\Phi_{x0} = 0.35\Phi_0$ and $\Delta\Phi_x = 0.1\Phi_0$ with the Josephson energy $E_{J0} = 7$GHz. At the extremes, these flux values corresponds to energies $E_{Jmax} \approx 10$GHz and $E_{Jmin} \approx 2$GHz. This limited range of flux values only permits rotation in a single direction around the x-axis, unfortunately once the Bloch vector has moved away from the xy-plane, it can only return by rotating through the sub-optimal polar regions. A simple protocol proposed by Ralph *et al* [114] minimises the time moving through the z-poles and maximises the time occupied near the xy-plane by using a 'Bang-Bang' control, found in classical control theory [116].

Bang-Bang control techniques alternate between two control values dependent on comparing a threshold value against the input, for the problem specified this 'decision boundary' is a fixed angle α in the yz-plane of rotation. The 'switch angle' α is constantly compared against the angle θ formed between the Bloch

vector and the x-axis in the yz-plane (Figure 5.11).

$$\theta = \tan^{-1}\left(\frac{z}{y}\right) \tag{5.44}$$

whenever

$$not\{(180 - \alpha) > \mid \theta \mid > +\alpha\} \tag{5.45}$$

is true, the purification is considered to be benefiting from the Bloch vector's proximity to xy-plane, hence the tunnelling energy is slowed to E_{Jmin}, elsewhere E_{Jmax} is used for the quicker passage (Figure 5.11). Given a pair of tunnelling energies, the size of the switch angle α can be adjusted for best performance. As an approximation for the optimum switching angle α to use, an accumulation of the incremental changes in the average impurity (Eq. 5.32) is obtained for a circular path of fixed impurity ($L = 0.01$) over a fixed period of time. In figure 5.10 these summations are plotted as a function of α, and the range of values normalised. For $E_{Jmax} \approx$ 10GHz and $E_{Jmin} \approx$ 2GHz the optimum switching angle is $\alpha = 31.2^o$. It is found that a simple straight line boundary should perform exceedingly well, as the optimum switching angle is independent of the current impurity and therefore the radial distance.

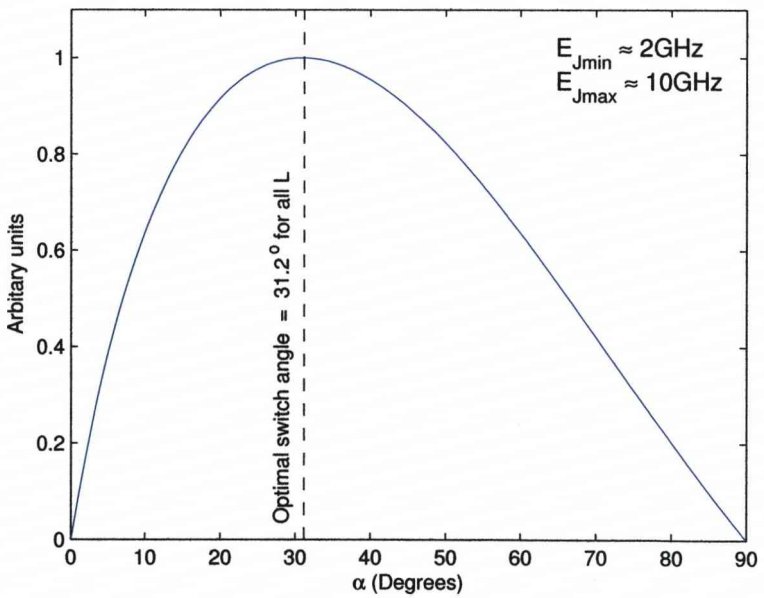

Figure 5.10: Summing the incremental changes of impurity experienced by a Bloch vector following circular path with changing angular frequency at boundary α, allows the optimal value of α to be approximately determined. The optimal switching angle α is constant regardless of the remaining impurity, L.

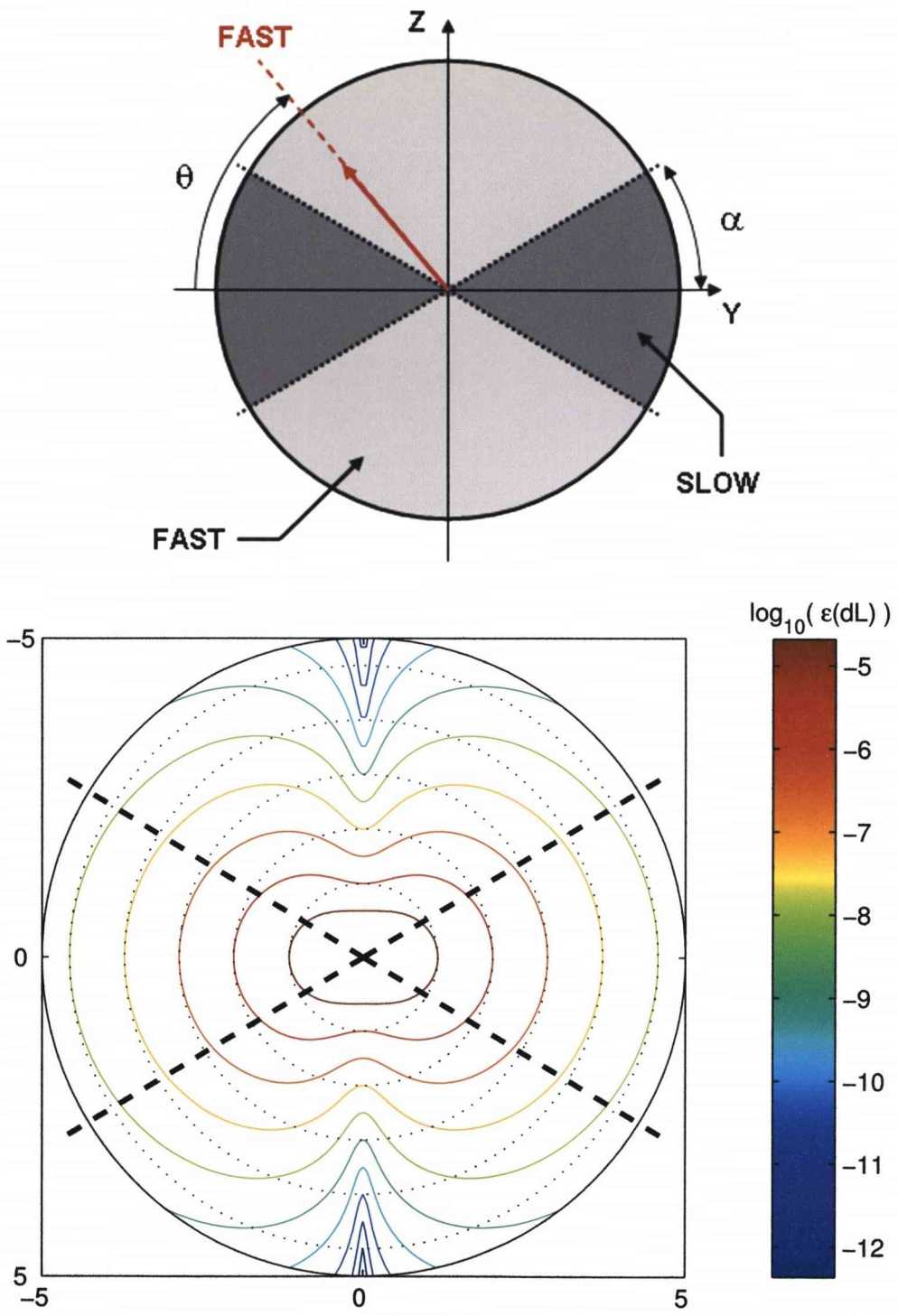

Figure 5.11: The 'Bang-Bang' flux feedback control alternates between high and low tunnelling energies, switching whenever the Bloch vector crosses a predetermined threshold at angle α. The lower graph shows that this feedback protocol holds the Bloch vector close to the optimal xy-plane for a longer duration. Indeed it can be seen that a straight line decision boundary separates the optimal and sub-optimal areas exceedingly well.

A possible implementation of this flux controlled protocol would only require measurement of the z-axis, and extraction of the current impurity from the measurement record to determine the angle θ.

$$\theta = \sin^{-1}\left(\frac{z}{\sqrt{1-2L}}\right) \tag{5.46}$$

These are all experimentally accessible variables for a superconducting charge qubit, therefore this protocol for enhancing the average purification rate can be said to be more practical and viable than those considered in section 5.5. Although, a considerable disadvantage is the rapid application of the flux control to change the tunnelling frequency four times per cycle, for a 2–10GHz rotational frequency this would require extremely fast processing of data from measurement to application. In addition, the transient response of the external circuitry is not considered, and this would certainly add delay.

5.6.2 Charge controlled Hamiltonian feedback

This algorithm solely uses the bias charge n_g induced by the applied bias voltage to control the qubit, the single Josephson junction tunnelling energy is engineered to be a fixed value of 10GHz. These severe constraints limit the control over the Bloch vector to rotations about the z-axis, which corresponds to the charge variable (Eq. 5.24). However, it should be stressed that this proposed feedback protocol does indeed take particular advantage of the constant x-axis rotations, despite the lack of a flux control field.

The feedback protocol attempts to use finite duration voltage bias pulses to constrain the Bloch vector to a small cylindrical volume close to and indeed enclosing part of the xy-plane. To achieve this, the feedback protocol fully specifies the pulse amplitude, duration and timing requirements to rotate the Bloch vector repeatedly on to the x-axis, taking a screw-like path (Fig. 5.12a). By definition the x-axis forms part of the xy-plane hence the average purification rate is increased. The x-axis is of particular interest as it is invariant under x-rotation caused by the Josephson junction.

The combined effect of the x and z-axis rotations is to tilt the Bloch vector's plane of rotation about the y-axis (Fig. 5.12b), the angle of the tilt is set by the relative magnitudes of the x and z rotational frequencies. Therefore if the σ_z control can somehow be used to position the Bloch vector close to the x-axis, it should remain close to the xy-plane, even in the absence of further control pulses. This is why the x-axis is such an attractive target in the presence of continuous

x-axis rotation. However, the effect of the weak measurement is to pull the Bloch vector towards the poles, so the Bloch vector will be gradually pulled away from the x-axis in a growing spiral path, as per section 5.4.

Therefore, to successfully return the Bloch vector to the x-axis, a simple control scheme has been devised which utilises a finite duration Hamiltonian proportional to σ_z to return the vector to the x-axis within a half cycle:

1. Initially, the qubit is allowed to precess naturally about the x-axis under constant weak measurement, as per section 5.4. The spiralling path of the Bloch vector increases in radius as the qubit purifies.

2. The feedback process triggers when the Bloch vector is at the topmost point of the x-axis orbit, **and** first exceeds the positive valued threshold z_{Limit} on the measurement axis (Figure 5.12). This information can be obtained by detecting the maximum peak values in the z measurement record.

On triggering, the controller applies a single π-pulse to the bias control (n_g), the amplitude of which is carefully selected to rotate the Bloch vector 180^o about the **tilted axis**. π-pulses are commonly used by contemporary quantum information processing devices [117], and therefore these bias pulses should be feasible to generate.

The tilt angle α is selected such that the Bloch vector starts at the uppermost point of a tilted circular path and the lowest point of the path coincides with the x-axis as illustrated by figure 5.12. The π rotation moves the vector from the trigger point to the x-axis.

$$\begin{pmatrix} x \\ y \\ z \end{pmatrix} \xrightarrow{\pi} \begin{pmatrix} R \\ 0 \\ 0 \end{pmatrix} \tag{5.47}$$

once the feedback pulse amplitude n_g and duration τ has been calculated, it is blindly applied without further changes until the duration has finished.

3. After the pulse has finished it is *assumed* that the Bloch vector has reached the x-axis, and the qubit once again only experiences the constant x-rotation. The x component of the Bloch vector is no longer zero (Eq. 5.47) and so the previously planar spiral of figure 5.5 is now distorted. Nethertheless, this spiral will once again expand to exceed z_{Limit}, where upon the feedback will re-trigger. The overall effect is to constrain the magnitude of z to z_{Limit}, so that the Bloch vector remains relatively near the x-axis (xy-plane).

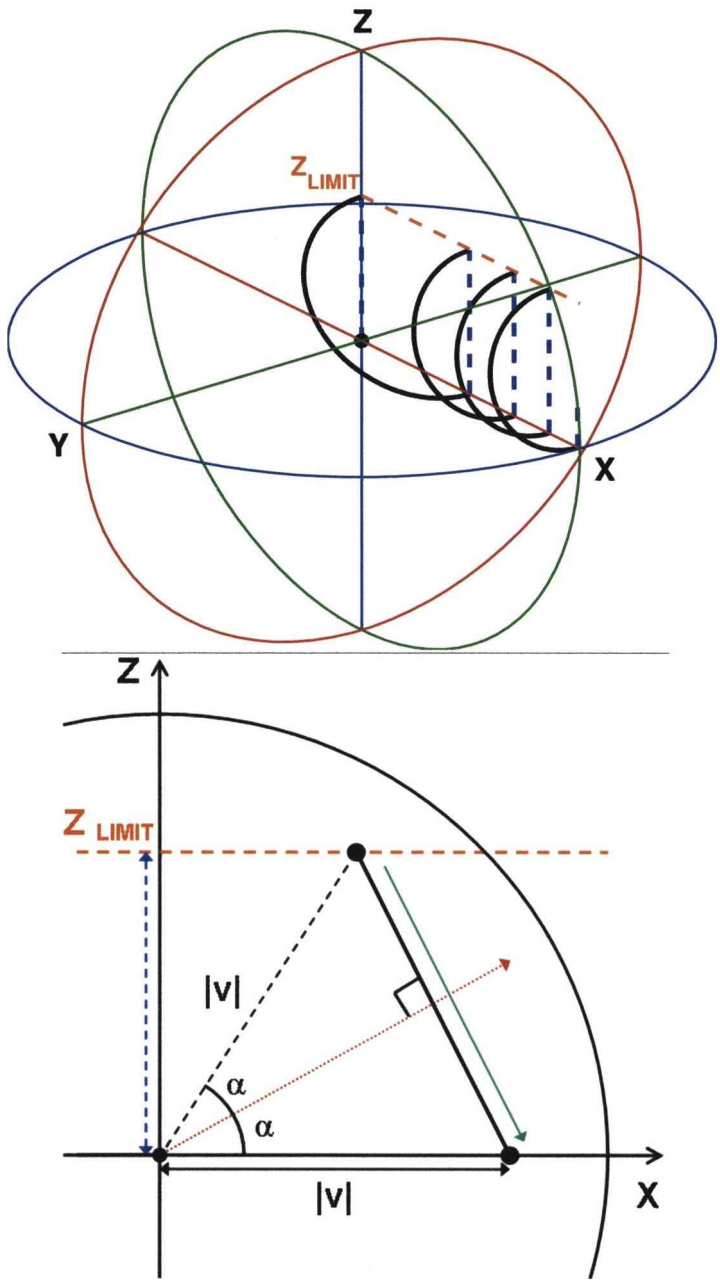

Figure 5.12: (**A**) Path of the Bloch vector under the charge controlled feedback. The Bloch vector is repeatedly returned to lie on the x-axis. This is achieved using pulsed rotations around the z-axis, the combined rotational frequencies of the x and z rotations define a plane of rotation about an arbitrary axis. The timing and duration is selected to move the vector from the top of the circular path to the bottom (x-axis). This quick corrective feedback is performed whenever the weak measurement process pulls the vector past a predetermined threshold z_{Limit}, creating a screw-like path. The dashed vertical lines represent the gradual spiralling observed in Figure 5.5. (**B**) The applied feedback creates a rotation about the axis (dotted arrow) defined by α, this angle can be calculated through a measurement, or estimate, of z and either the purity, P or impurity, L. The z rotation frequency is adjusted and pulsed to ideally take the Bloch vector to ($\mid \vec{v} \mid$,0,0) within a half cycle.

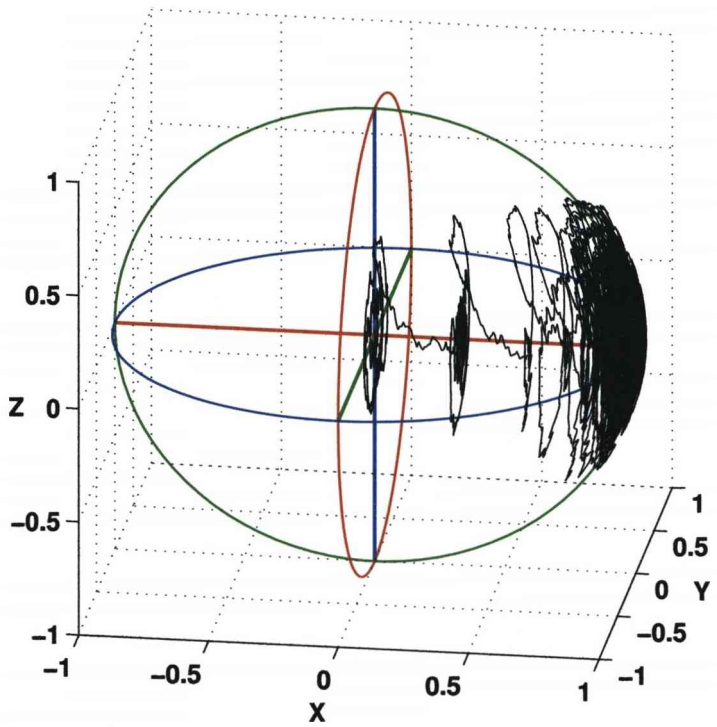

Figure 5.13: A single simulation of the proposed protocol including the effects of weak measurement on the qubit state. It can be clearly seen that the weak measurement noise severely disrupts the intended path of the Bloch vector. For weak measurement strength this is minimised but larger measurement strengths eventually destroy the structure in this figure with random diffusion. However, the presence of the **complete** spirals about the x-axis suggest that the feedback protocol is successfully returning the Bloch vector to very near the x-axis.

The measurement process distorts the path of a Bloch vector undergoing Hamiltonian evolution, such is the effect of the stochastic measurement noise and persistent drift toward the measurement axis. If the measurement strength γ is sufficiently small then the distortion of the ideal path of the Bloch vector is minimal. However, for stronger measurement strengths the larger stochastic increments causes the Bloch vector to merely diffuse into the Bloch sphere, therefore the true path and ideal path become divergent. To prevent the Bloch vector diffusing too far away from the target x-axis the feedback must be applied quickly. To minimise the duration of the feedback pulse τ (Eq. 5.55), equations 5.54 and 5.53 show the underlying limiting factor is E_J which should be large. Indeed, increasing the tunnelling energy E_J will also further reduce the possibility of thermal excitations. Ignoring the effects of weak measurement during the application of the feedback pulse, it is possible to simplify the procedure to determine the π-pulse amplitude and duration analytically.

Consider a point on the xz-plane (Fig. 5.12) with $z = z_{\text{Limit}}$ and use a π-rotation about an axis (dotted arrow) to rotate out of xz-plane and finish exactly on the x-axis, by rotating from the very top to the very bottom of the circular path about this axis. Using figure 5.12b, the angle α of the axis can be calculated using elementary geometry from z_{Limit} and the distance from the centre of the Bloch sphere ($\mid \vec{v} \mid = 1 - 2L$). The latter can be obtained from the conditional density matrix ρ_c (which represents the current state of knowledge of the system). The angle of the tilted plane caused by the feedback pulse is:

$$z_{\text{Limit}} = \left|\vec{v}\right| \sin(2\alpha) \tag{5.48}$$

$$\alpha = \frac{1}{2} \sin^{-1}\left(\frac{z_{\text{Limit}}}{\mid \vec{v} \mid}\right) \tag{5.49}$$

As $0 \leq \mid \vec{v} \mid \leq 1$ the angle α is bounded as follows:

$$\alpha_{\text{max}} = \frac{1}{2} \sin^{-1}(1) = 45^\circ \qquad (x = 0) \tag{5.50}$$

$$\alpha_{\text{min}} = \frac{1}{2} \sin^{-1}(z_{\text{Limit}}) \qquad (\mid \vec{v} \mid = 1) \tag{5.51}$$

To implement this control strategy it is necessary to determine the x and z angular velocity components. To simplify matters we assume that the Josephson junction angular frequency is fixed, $\omega_x = \nu$ where $E_J = \hbar\nu = \hbar\omega_x$. Then the two angular components are defined by the following relationship:

$$\frac{\omega_z}{\omega_x} = \tan\alpha \tag{5.52}$$

$$\omega_z = \omega_x \tan\alpha \tag{5.53}$$

the required bias value n_g to create ω_z can then be obtained from equation (5.56). The angular frequency about the tilted axis is found by combining the x and z components:

$$\omega_\alpha = \sqrt{{\omega_x}^2 + {\omega_z}^2} \tag{5.54}$$

therefore the bias pulse duration τ, required to perform the necessary π-rotation about the α axis is:

$$\tau = \frac{1}{2}\frac{2\pi}{\omega_\alpha} \tag{5.55}$$

The relation between the z-axis rotational frequency ω_z and bias n_g is depicted in figure 5.14, for $n_g > 0.5$. It is a linear relationship described by the following equation:

$$\omega_z = \frac{(2e)^2}{\hbar C_q}\left(\frac{1}{2} - n_g\right) \tag{5.56}$$

which can be derived through examination of the σ_z terms in the Hamiltonian (Eq. 5.26):

$$H_z = +\frac{(2e)^2}{2C_q}\left(\frac{1}{2} - n_g\right)\sigma_z \tag{5.57}$$

the rotational frequency is equal to the separation of the two energy levels which are given by the eigenvalues of the Hamiltonian:

$$\lambda = eig\{H_z\} = eig\{\sigma_z\}\frac{(2e)^2}{2C_q}\left(\frac{1}{2} - n_g\right) \tag{5.58}$$

$$\lambda_1 = -1\,\frac{(2e)^2}{2C_q}\left(\frac{1}{2} - n_g\right), \quad \lambda_2 = +1\,\frac{(2e)^2}{2C_q}\left(\frac{1}{2} - n_g\right) \tag{5.59}$$

$$\omega_z = \frac{\lambda_1 - \lambda_2}{\hbar} \tag{5.60}$$

which yields equation 5.56

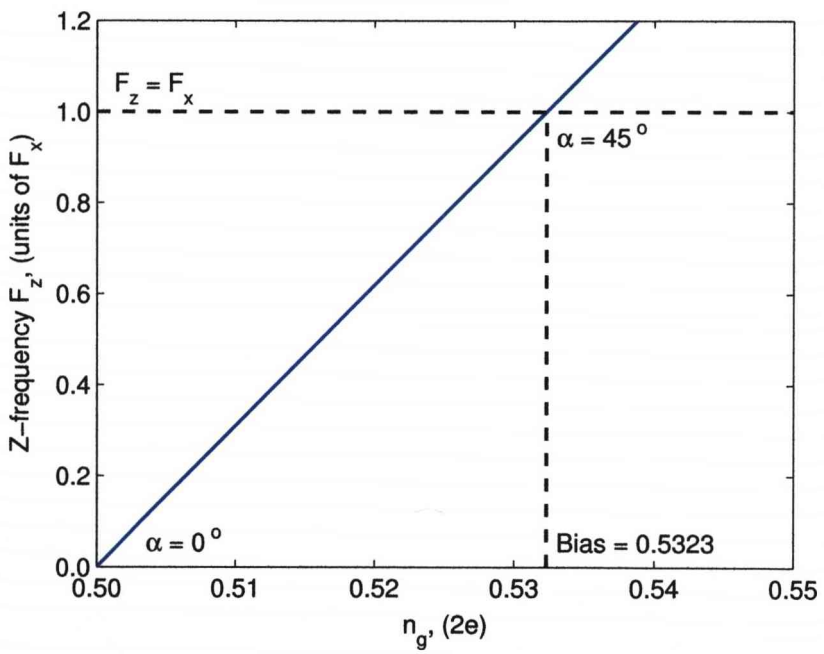

Figure 5.14: z-axis rotational frequency as a function of applied bias. The maximum required angle α is 45^o, (to be applied when $x = 0$), this sets an intrinsic upper limit for the bias as the x and z rotational frequencies must be equal and, the later, lesser angles are achieved by reducing the z-rotational frequency. (F_x=10GHz)

For our feedback mechanism presented we find that the maximum ω_z is equal to the Josephson junction frequency, which means there is a limit on the size of

bias which should be applied. The maximum occurs at $x = 0$ and reduces as the Bloch vector is displaced along the x-axis by the feedback protocol. This maximum $w_z(n_g) = w_x$ is actually a favourable constraint as applying a bias field substantially larger than $n_g > 0.75$ would increase the risk of accessing an unwanted third charge state [113, 117]. Another requirement of the control system is being able to halt the z-rotations or at least slow the rotations significantly by setting the n_g close to 0.5. It is expected that both of these requirements should be achievable. The bias control range to compensate for a system with a constant 10 GHz x-axis rotation and the capacitances provided in table 5.1 is:

$$0.5000 \leq n_g \leq 0.5323. \tag{5.61}$$

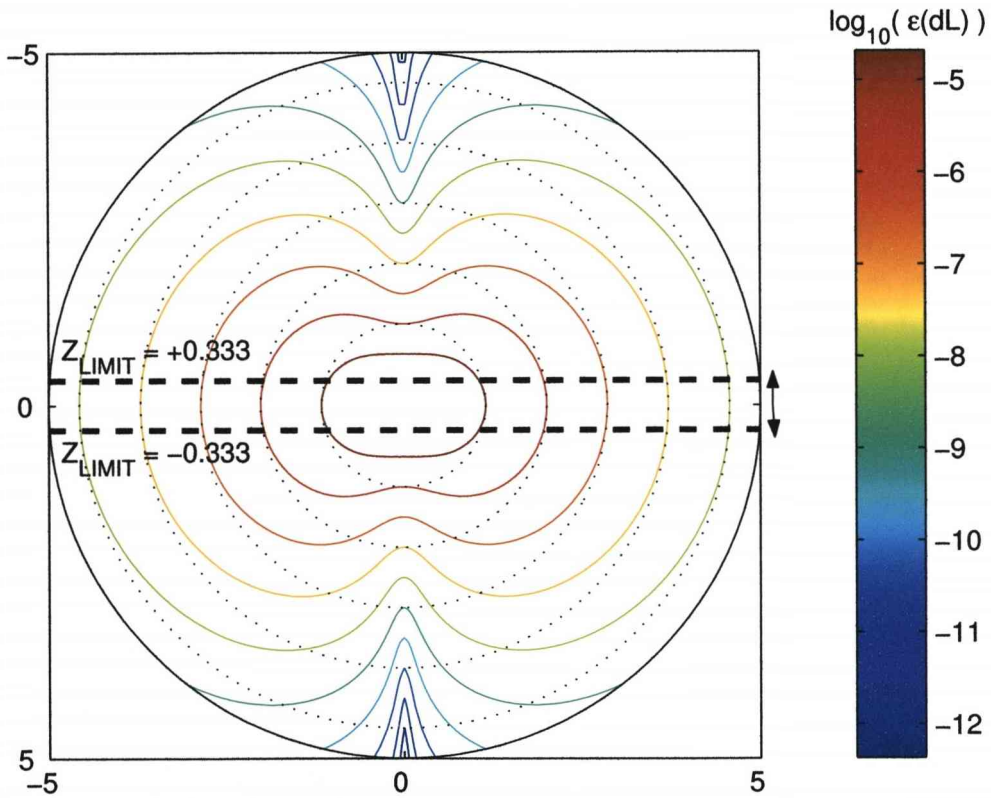

Figure 5.15: The Bloch vector is constrained to a narrow region with very large dL of approximately uniform distribution within the proximity of the xy-plane, which accounts for the near optimal performance of this feedback protocol. The two dashed lines represent $z = +z_{\text{Limit}} = 0.333$ and $z = -z_{\text{Limit}} = -0.333$. For the impurity axes used in this figure, $z_{\text{Limit}} = 0.333$ equates to $L = 0.4446$ when $x = y = 0$. The independence of dL as a function of the angular displacement θ above or below the xy-plane within this region suggests significant robustness.

On repeated application of these carefully constructed π-pulses, the Bloch vector is returned downwards to the $z = 0$ plane whenever the z component of

the vector exceeds $+z_{\text{Limit}}$. As the continuous x-axis rotations will eventually rotate the Bloch vector into the lower hemisphere, the vector can be said to be constrained within a cylindrical volume between two z-planes:

$$-z_{\text{Limit}} \leq z \leq +z_{\text{Limit}}. \tag{5.62}$$

Figure 5.16 shows the relation between the measured z value and the application of feedback as a realsitic function of time for the first two applications of the feedback protocol with the Bloch vector starting from $\vec{v} = [x, y, z]^T = [0, 0, 0]^T$. For this example $z_{\text{Limit}} = 0.333$ and all other values can be found in section 5.3.

The blue dashed sinusoids represent the average behaviour of the Bloch vector whilst there is **no** feedback, the amplitude (orbital radius from the x-axis) grows under the attractive influence from the poles of the measurement axis (z-axis), as the qubit purifies. The application of the feedback rapidly returns the vector to the $z = 0$ plane as indicated by the solid black lines. The required bias pulse width and inter-pulse spacing shown in the second set of axes clearly illustrates the brief and occasional controls required for the protocol, this should reduce the complexity of implementing the pulse generator. Although the Bloch vector is returned to the $z = 0$ plane it is important to note that the impurity is preserved by the unitary rotation about the α-axis such that as $z \to 0$ the length of the vector is transfered along the x-axis. It is the unitary nature of rotations that allows the purity gained through the 'no feedback' stage to be kept and accumulated.

The pulse train featured in figure 5.16 shows a decreasing trend in the voltage bias amplitude (n_g) and an increase in the pulse duration (τ). This increase is due to the slower z-axis angular velocity at the latter stages, the horizontal component of the α-axis tilt reduces as the Bloch vector is displaced further from the z-axis. Indeed, the values of n_g and τ tend to steady state values defined by α_{min}, (5.51).

Unfortunately, under the noisy conditions imposed by the weak measurement system, there are practical considerations. Indeed, determining the peak value of the z measurement can be extremely difficult, however the simulation results in section 5.9.2 show the overall performance of the system is not severely degraded if a basic threshold is used instead. It is sufficient to merely return the Bloch vector to the vicinity of the x-axis. In addition, as previously indicated the stochastic nature of the noise will distort the ideal path regardless.

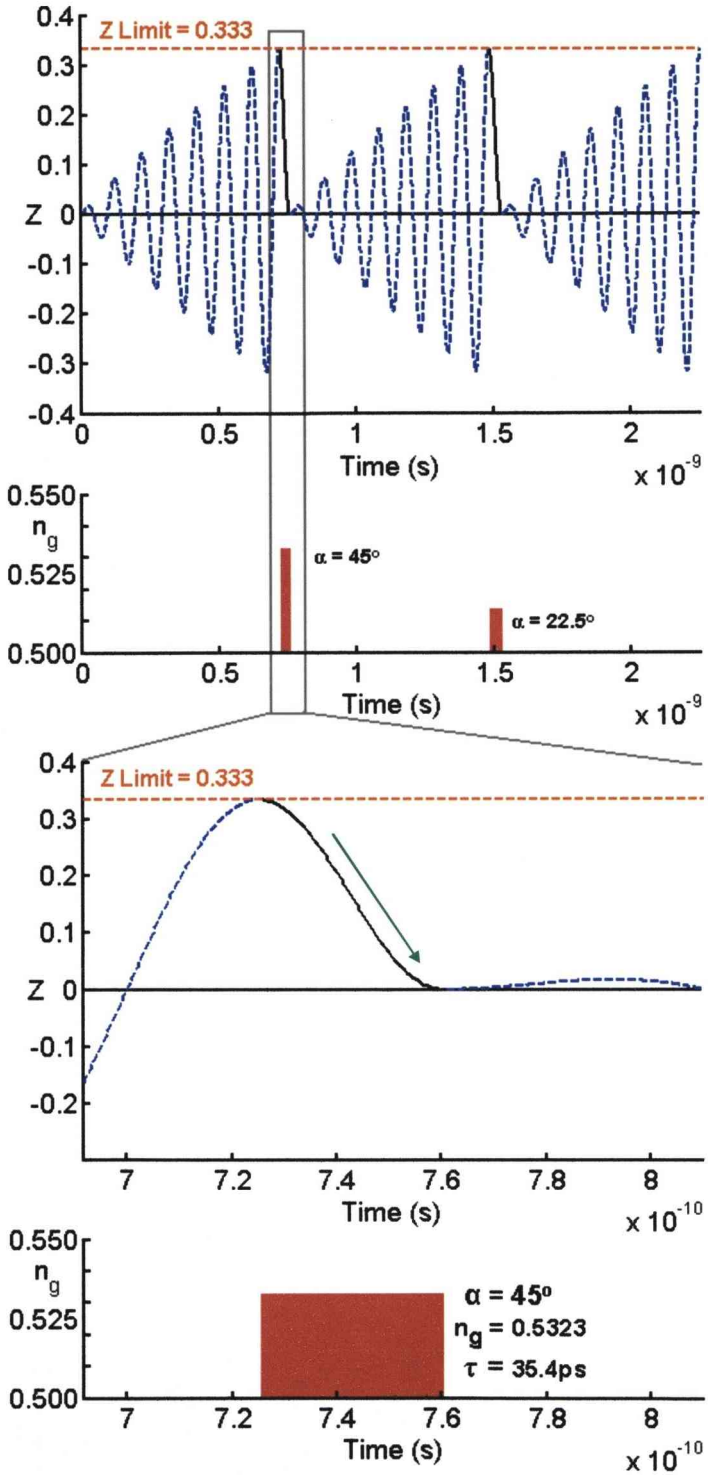

Figure 5.16: Idealised timing diagram for the feedback pulses with $z_{\text{Limit}} = 0.333$. The topmost graph shows the ideal evolution of z as a function of time, with the dashed and solid line segments corresponding to those found in figure 5.12. The dashed lines indicates no feedback ($n_g = 0.5$), the sinusoids are rotations about the x-axis (Fig. 5.5). When $z_{\text{Limit}} = 0.333$ is exceeded, the feedback is applied, and the Bloch vector is π-rotated from the top of the tilted plane to the bottom such that $z = 0$. The process is repeated when z again exceeds z_{Limit}.

5.7 Optimal purification rate for individual qubits - Ideal Protocol II

By using a similar analysis to Jacobs [1], it has been determined by Wiseman and Ralph [2] that *rotating the Bloch vector instantaneously to the measurement axis prior to taking the measurement* yields the largest number of highly purified qubits, for a given amount of time. However, whereas Jacobs' protocol minimises the stochastic terms to produce deterministic purifications, the protocol described in this section maximises the stochasticity, consequently there is a small but significant probability that a number of qubits may not purify at all. It will be shown in section 5.9 that the existence of these remaining mixed qubits reduces the average purity of the ensemble, indeed it can be shown that the **average** purification rate of an ensemble under Ideal Protocol **II** is the mimimum.

To compare the average purification performance against Jacobs' Ideal Protocol **I**, the application of Ideal Protocol **II** sets the angle θ from the measurement axis to $\theta = 0^o$, where the measurement axis is taken to be the z-axis.

$$dL = -8\gamma dtL(1-(1-2L)\cos^2\theta) - 2L\sqrt{8\gamma(1-2L)}\cos\theta\, dW \quad (5.63)$$

$$dL_z = -8\gamma dtL(1-(1-2L)) - 2L\sqrt{8\gamma(1-2L)}\, dW \quad (5.64)$$

$$\overline{dL_z} = -16\gamma dtL^2 \quad (5.65)$$

L is small and is defined by equation 5.10 to be less than one ($0.5 \geq L \geq 0$). Thus when comparing $\overline{dL_z}$ against $\overline{dL_{xy}}$ (Ideal Protocol **I**), placing the Bloch vector on the xy plane always yields a larger change in impurity than returning the vector to the $z$axis:

$$\left|\, \overline{dL_{xy}} = -8\gamma dtL \,\right| \quad \geq \quad \left|\, \overline{dL_z} = -16\gamma dtL^2 \,\right| \quad \forall\, L \quad (5.66)$$

An important result is the magnitude of the average change of impurity is significantly reduced whenever the Bloch vector is returned to the measurement axis ($\overline{dL_z}$), indeed it can be shown that this yields the **minimum** average purification rate, as the subtractive term $(1-2L)\cos^2(\theta)$ is now maximised as $\cos^2(0) = 1$.

Unfortunately, as the stochastic term in equation 5.64 is not removed by setting $\theta = 0^o$, determining an equation for the average time evolution $\bar{L}_z(t)$ is non-trival, considering the nonlinearities in L. The complication arises from averaging over the wide variety of iteration histories for L, caused by the variance of dL_z being dependent on the current value of L. Jacobs uses a linear quantum trajectory approach [111] to redefine the set of nonlinear weak measurement

equations for the Bloch vector coordinates $[r, z]$ (Eqs.5.11 and 5.12) in a linear form that can be solved [66].

The average purity transient $\bar{L}_z(t)$ over an infinite number of evolutions, for ideal feedback to the measurement axis is given by:

$$\bar{L}_z(t) = \frac{e^{-4\gamma t}}{\sqrt{8\pi t}} \int_{-\infty}^{+\infty} \frac{e^{-x^2/(2t)}}{\cosh\left(\sqrt{8\gamma}x\right)} dx \tag{5.67}$$

The integral appears to have no analytical solution [1]. To show the significant advantage of Wiseman and Ralph's protocol it is necessary to examine the evolution of the impurity distribution. Work performed by Wiseman and Ralph has yielded an expression for the distribution of impurity at any given time whilst Ideal Protocol **II** has been employed [2]:

$$\Lambda_z(L,t) = \frac{e^{-4\gamma t}}{\pi\sqrt{2\gamma t}} \frac{\exp\left(-\frac{1}{16\gamma t}\,\mathrm{atanh}^2\sqrt{1-2L}\right)}{\sqrt{L(1-2L)}} \tag{5.68}$$

This equation is a modified form of equation (24) from reference [2], Wiseman and Ralph have used purity ($P = 1 - L$) and arbitrary time units for this work, wheras equation 5.68 is expressed in terms of the impurity ($L = 1 - P$) and also includes the measurement strength γ that suitably scales the time axis.

Figure 5.18 compares the evolving distributions of Ideal Protocols **I** and **II** over 20ns with measurement strength $\gamma = 75 \times 10^6$. The blue dashed line is the deterministic distribution of Ideal Protocol **I** (Eq. 5.35), which divides the impurity in to two regions of relative "high" and "low" impurity (red and green respectively). The advantage of Ideal Protocol **II** is readily apparent when the skewed distribution of equation (5.68) is overlaid, as this clearly shows that the *majority* of purified qubits will have a much smaller remaining impurity (L). Unfortunately, the spread of impurity values is considerable, as it can be seen that L can vary over ten orders of magnitude after purifying for $t = 20$ns, indeed for $t < 10$ns a substantial amount of the probability distribution is still concentrated in the under-performing region, suggesting there will be many impure qubits remaining near the centre of the Bloch sphere after 10ns. These largely impure qubits skew the average impurity such that protocol **II** appears to perform poorly when comparing the *average* performance of protocol **I**, as shown in figure 5.17.

To sumerise, Wiseman and Ralph's Ideal Protocol **II** maximises the number of highly purified qubits in a given amount of time, balanced against the risk of some qubits failing to purify. Whereas using Jacobs' Ideal Protocol **I**, the experimentalist is guaranteed that all the qubits in the quantum computer will achieve a level of purity albeit at a slower rate.

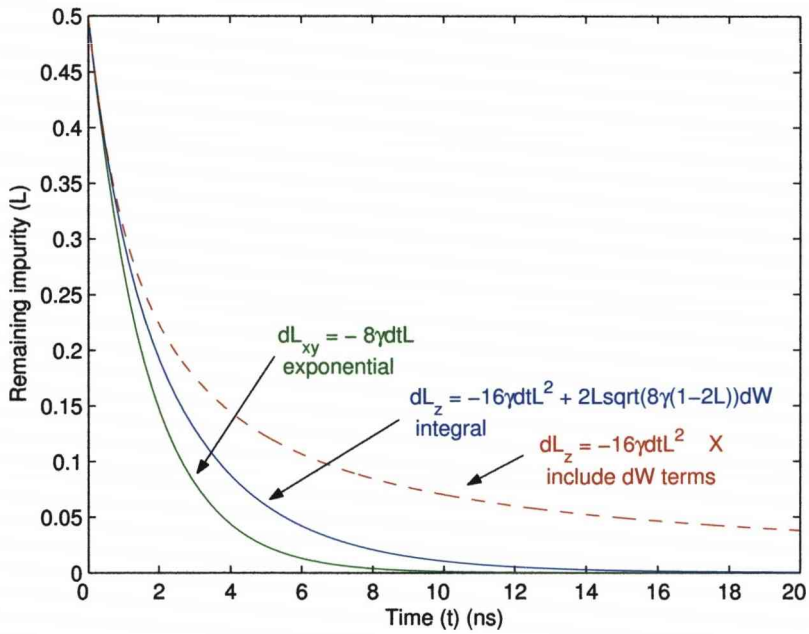

Figure 5.17: Transient evolution of the average remaining impurity, comparing the two forms of ideal feedback for the same measurement strength γ. The green line is the evolution under Ideal Protocol **I** (Eq.5.34), and the blue line represents the slower average evolution under Ideal Protocol **II** (Eq.5.67)

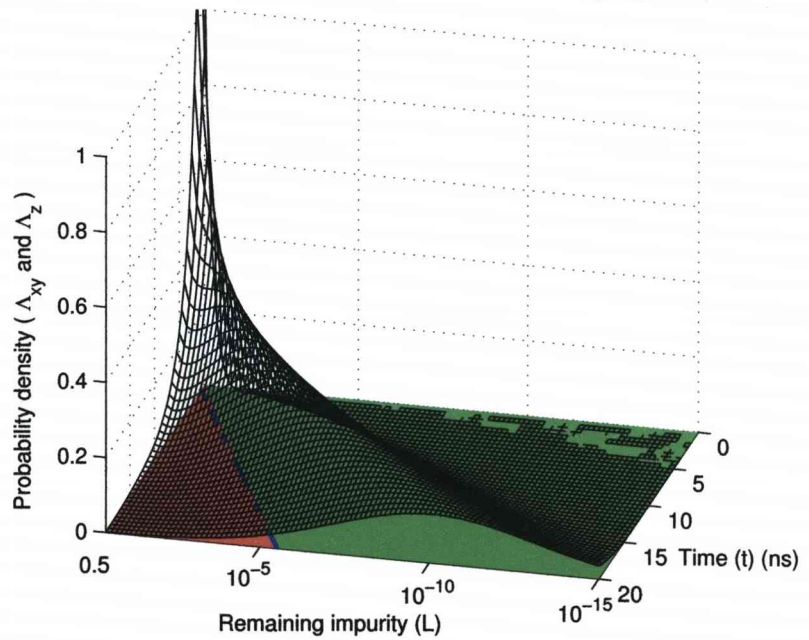

Figure 5.18: Time evolution of the probability distributions for both the deterministic Ideal Protocol **I** (dashed line) (Eq. 5.35) and the skewed Ideal Protocol **II** (mesh plot) (Eq. 5.68). A substantial proportion of the protocol **II** probability is weighted in the "low" impurity area indicating better performance than protocol **I**, although there is extreme variability in the final impurity (L).

5.8 Practical means of increasing the number of high purity qubits

Keeping the Bloch vector inline with the measurement axis, to implement Wiseman and Ralph's protocol for a superconducting charge qubit presents certain difficulties when considering the constant rotations about the x-axis caused by the Josephson tunnelling. As the axis of rotation (x-axis) is orthogonal to the measurement axis (z-axis), the resulting rotations in the yz-plane continually takes the Bloch vector away from the measurement axis, and the feedback must compensate for this. Given the limited controls, in terms of magnitude and rate of application of either charge (σ_z) or flux (σ_x), this section proposes two practical protocols for achieving near optimal performance.

The flux controlled protocol assumes the charge control is set to the neutral position and so the Bloch vector can only be manipulated in the yz-plane, which contains both optimal and non-optimal regions. Although it provides an improvement over using no feedback, more favorable results can be obtained by tightly confining the Bloch vector using only charge control (Section 5.9.4).

5.8.1 Flux controlled Hamiltonian feedback

The flux controlled feedback described in section 5.6.1 can be modified to keep the Bloch vector near the measurement axis (z-axis), in the presence of a continuous but controllable x-axis rotation. The 'Bang-Bang' control logic illustrated by figure 5.11 for the feedback protocol in section 5.6.1 is now reversed, such that the passage of the Bloch vector is now slowed near the z-axis and swiftly moved through the xy-plane. Where the switch angle α is still measured from the xy-plane, and to preserve the two state system the previous flux control values are used (Fig. 5.9), however due to the different control logic, the roles are reversed. In this work, the fast and slow rotational frequencies are 10GHz and 2GHz respectively.

It is known that Ideal Protocol **II** (perfect rotations of the Bloch vector to the measurement axis) yields the smallest average purification rate ($\overline{dL}$), therefore to gain the best approximation to Ideal Protocol **II** we can attempt to minimise $\overline{dL}$. By repeating a similar analysis as featured in section 5.6.1, it is possible to estimate the optimum switch angle α for the aforementioned rotational frequencies. The accumulated $\overline{dL}$ is normalised between 0 and 1, thus the optimum value of α is located at the minimum, $\Sigma\overline{dL} = 0$.

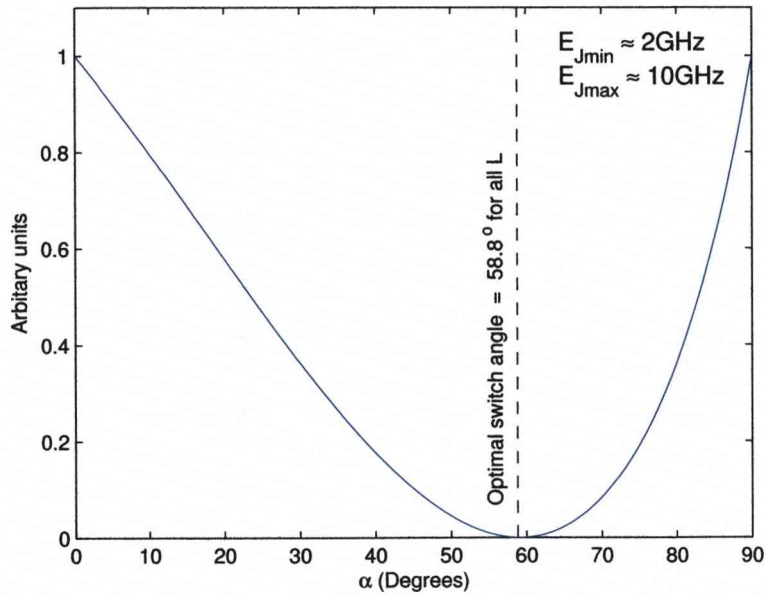

Figure 5.19: Summing the incremental changes of impurity experienced by a Bloch vector following circular path with changing angular frequency at boundary α, allows the optimal value of α to be approximately determined. The optimal switching angle α is constant regardless of the remaining impurity, L.

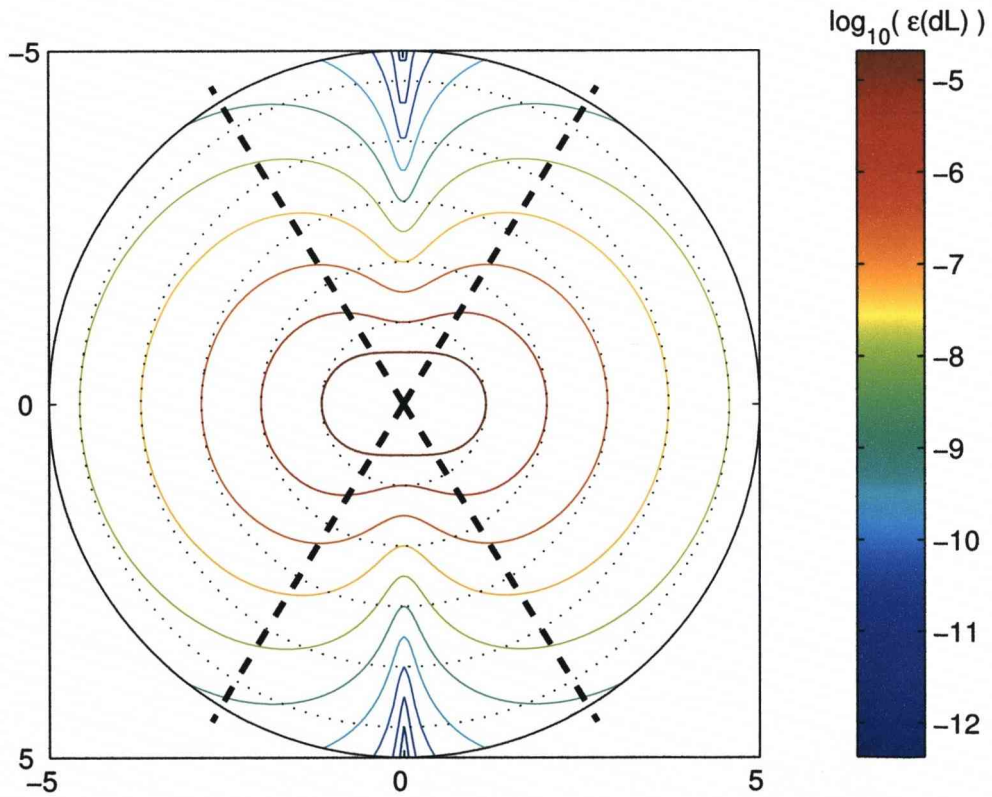

Figure 5.20: Exchanging the fast and slow speeds of the Bang-Bang control proposed in section 5.6.1 effectively exchanges the segments defined by switch angle α, when compared with figure 5.11.

5.8.2 Charge controlled Hamiltonian feedback

Using the biasing charge as the sole means of feedback control, it is anticipated that there would be difficulties in adapting the previously described method of section 5.6.2 for rotating to the x-axis, to rotate to the z-axis instead. Due to the constant fixed frequency x-axis rotations, the controllable z-axis rotations and the z-axis measurement, the nature of the problem is not symmetrical. Whenever the z-axis rotations are removed by setting $n_g = 0.5$, the Bloch vector will still rotate about the x-axis therefore taking the vector away from the required z-axis. Unless the experimental apparatus can measure, process and apply a correcting control field within a fraction of a cycle, the application of feedback will be futile as a complete cycle about the x-axis will have been made anyhow, with identical behaviour described by section 5.4.

To solve this, a very simple feedback protocol is proposed where the Bloch vector rotates about a tilted axis almost parallel to the measurement axis, locking the vector in a tight spiraling path close to the actual measurement axis (Fig. 5.21).

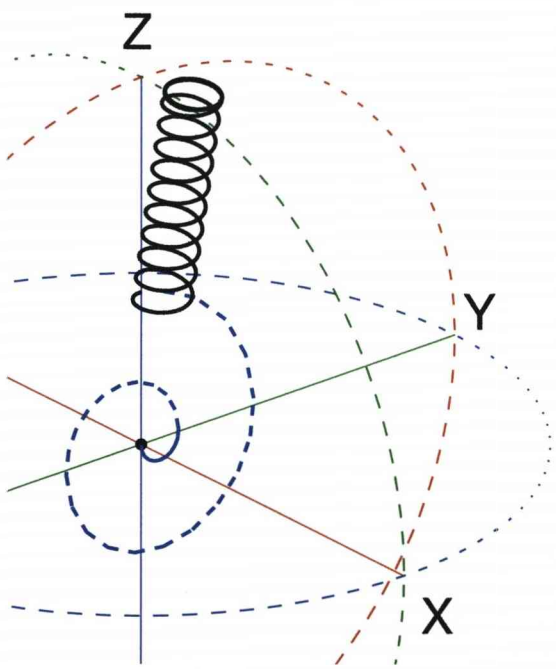

Figure 5.21: Diagram showing the ideal path of the Bloch vector. The feedback control is initially off, so that the Bloch vector continually rotates and grows around the x-axis, this is to allow the peak value of z to become more distinct. Once the Bloch vector has exceeded a threshold and is at a maximum or minimum, the high frequency z-rotations are applied which locks the Bloch vector to the measurement axis.

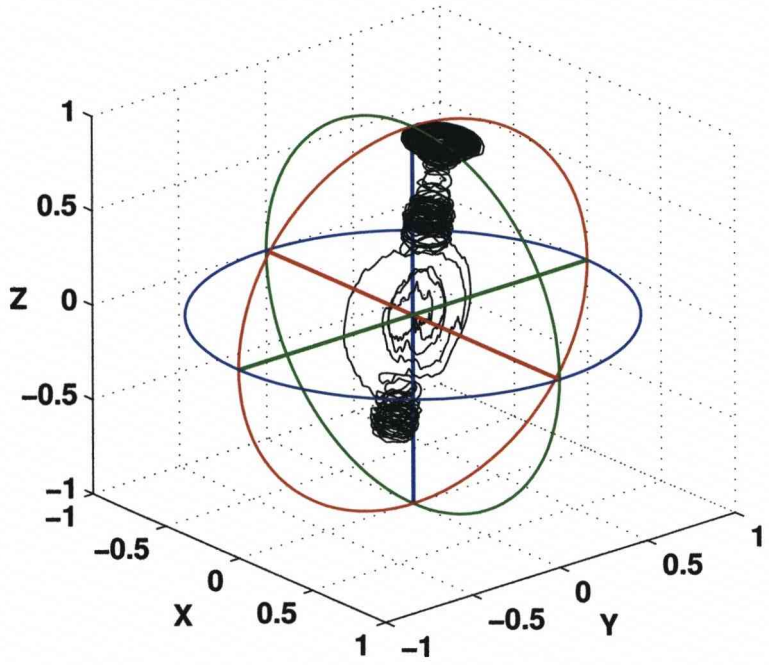

Figure 5.22: A single simulated trajectory, the Bloch vector starts to spiral then is locked to the lower z-axis, however the stochastic measurement process pulls the vector upwards where it eventually reaches the surface creating an 'end cap' effect as it cannot settle exactly on the z-pole.

Initially, no z control is applied and the Bloch vector is allowed to rotate about the x-axis. The effect of the weak measurement is to pull the Bloch vector towards the poles, and a spiral growth results. This initial period allows an experimentalist to detect a sizeable peak or trough in the z measurement record corresponding to the phase of the oscillation in z, indicating when the Bloch vector is near to the z-axis. When at this point, if the threshold value ($z_{\text{Limit}} = 0.33$) is exceeded, the strong z control is applied, creating a rotation about an axis that should be almost parallel to the z-axis. If the initial detection is completed successfully, the Bloch vector should be near the z-axis and will now travel in a tight spiral close to the z-axis (Fig. 5.21). Alternatively, if the Bloch vector was somewhere near the y-axis, for example due to an initial delay, the orbital path about this tilted axis would be much wider and fail to coincide with the actual z-axis. Applying the σ_z control very early in the purification process has the same effect. As long as the length of the Bloch vector is small when the σ_z is initially applied, then the spiral should be small and close to the z-axis. However, their is little benefit in doing this initially because the performance gain close to the centre of the Bloch sphere is small and - as a general rule - control systems tend to be designed to react to a detected signal rather than a null signal.

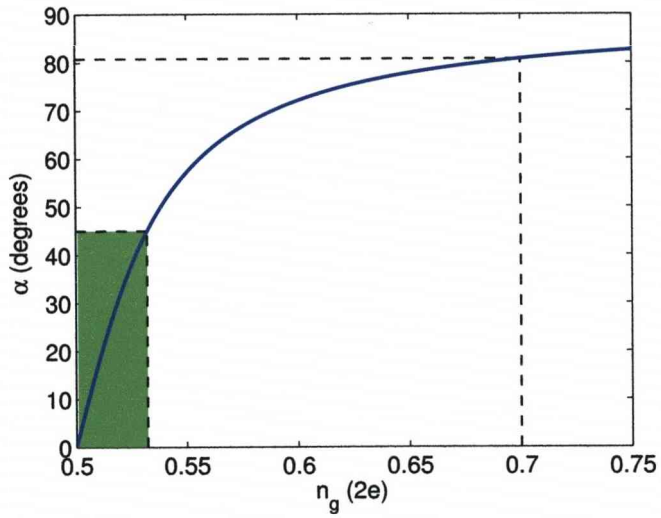

Figure 5.23: Angle α as a function of bias, n_g. The green region indicates the necessary angles and biases for Charge Protocol **I**, the range of which is intrinsically constrained by the maximum value of $\alpha = 45°$, $(0° \leq \alpha \leq 45°)$. The solitary dashed line illustrates a possible bias value for generating the tilted axis of Charge Protocol **II**. Notice that only one value is required. We require α to be as close to 90° as possible, however for large bias values the gains in α are actually quite minimal.

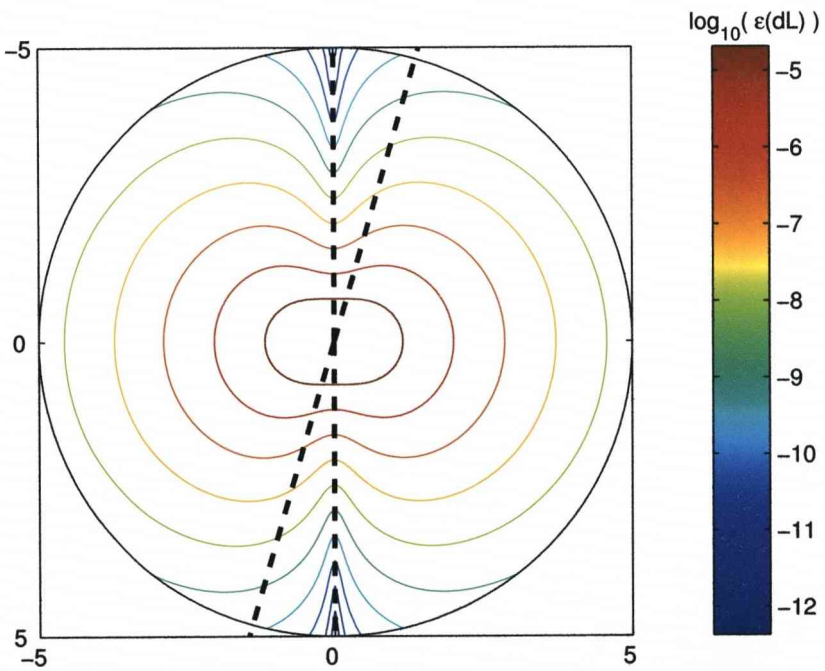

Figure 5.24: The protocol described in this section constrains the Bloch vector within two cone shaped regions next to the measurement axis. There are two cones as both poles are equally likely outcomes of the random diffusion of the Bloch vector along the z-axis.

The definition of α as the angle of the axis of rotation between the x and z axes, still holds for this method. Equation (5.69) defines α as a function of Bloch sphere coordinates. Here we express it in terms of the system frequencies: the constant Josephson junction frequency $\omega_x = 2\pi E_J$ and bias control frequency ω_z (Eq. 5.53):

$$\alpha = \frac{1}{2}\sin^{-1}\left(\frac{\omega_z}{\omega_x}\right). \tag{5.69}$$

The magnitude of the bias field should not be too large or the next charge state may be accessed and the two state approximation would be violated. Figure 5.23 shows how α varies as a function of the bias control, plotted until $n_g = 0.75$ as this is halfway between the charge states. A bias value of $n_g = 0.70$ is chosen in the simulations below to reduce the possibility of accessing a new state. This gives $\alpha = 82°$ (see Fig. 5.23). Increasing n_g gives minimal gain in α as the angle asymptotes to 90°. Ideally we would have $\alpha = 90°$ but we find an angle of 82° gives acceptable performance.

5.9 Analysis of feedback performance

A variety of feedback protocols can be applied to control the positioning of the Bloch vector in relation to the measurement axis. To quantify the performance of these protocols, the statistics for an ensemble of identical qubits are examined due to the stochastic nature of the measurement process. All seven feedback strategies are presented with optimised control parameters as previously discussed.

5.9.1 Average evolution of the ensemble

The average evolution of the ensemble impurity is quite simply the mean impurity at any given time. It has been calculated through numerical simulation of a large number of impurity transients, or trajectories. Each averaged evolution is

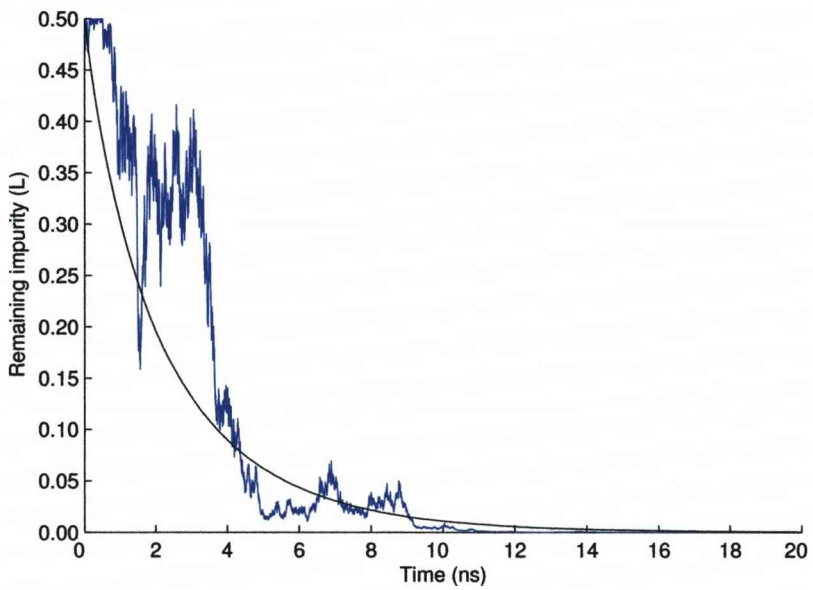

Figure 5.25: Numerous stochastic trajectories are averaged to allow meaningful comparisons between the examined and proposed protocols

compared against the slowest performing protocol: Ideal Protocol **II** - *Perfect feedback of the Bloch vector to the measurement axis.* The average improvement S, also referred to as 'Speedup' [1], is a ratio of two purification times and is a convenient figure of merit.

$$S_{average}(\overline{L}) = \frac{T_{ideal\ \mathbf{II}}(\overline{L})}{T_{test}(\overline{L})} \tag{5.70}$$

where it is necessary to invert the following equation **numerically** to obtain a purification time reference to form comparisons.

$$\overline{L}_{ideal\ \mathrm{II}}(t) = \frac{e^{-4\gamma t}}{\sqrt{8\pi t}} \int_{-\infty}^{+\infty} \frac{e^{-x^2/(2t)}}{\cosh\left(\sqrt{8\gamma}x\right)}\, dx \tag{5.71}$$

Equation 5.71 is derived in reference [2].

The ratio $S_{average}$ is plotted in figure 5.26 and is found to vary as a function of the remaining impurity, with maximum gains (for all forms of feedback) being obtained when the remaining impurity is small. It should be noted that as $S_{average}$ is a ratio of two purification times, the performance increase is independent of measurement strength, γ. The results are presented in a manner consistent with the initial papers by Jacobs and Combes, [1, 66, 115].

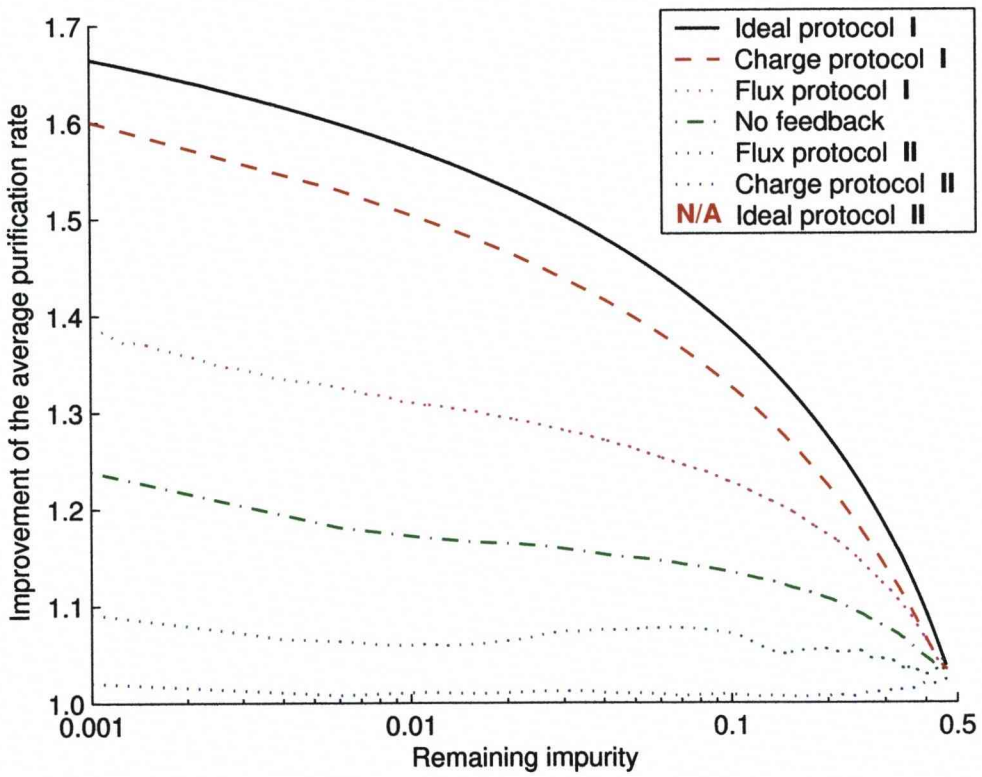

Figure 5.26: The improvement of the average purification rate as a function of the remaining impurity.

Ideal Protocol **I** (rotating perfectly on to the xy-plane prior to each measurement) forms an envelope of solutions, gaining a 67% advantage over Ideal Protocol **II** within the limited scales of figure 5.26, however this improvement increases to 100% as the impurity tends to zero [1]. Charge Protocol **I** yields near optimal performance, this can be explained by examining figure 5.15 where

the incremental change in the remaining impurity (dL) is almost independent of the vertical displacement from the xy-plane, for $z \leq 0.333$. This suggests a great degree of tolerance in the value of z, and therefore it not neccessary to feedback the Bloch vector to regions very close to xy-plane. Indeed, Charge Protocol **I** attempts to constrain the Bloch vector within this regime at all times.

Flux Protocol **I** does not appear to reach similar levels of performance as it is necessary to transfer the Bloch vector through the z-axis poles to once again reach the xy-plane, momentarily creating sub-optimal conditions for the average purification. However, a significant improvement can still be achieved by switching between two σ_x rotational frequencies compared with a constant frequency x-axis rotation (which is the case when using no feedback).

It is very important to note that the two '**II**' practical protocols *should* satisfy $S_{average} \approx 1$ for all L, as this is an indication that the flux and charge controlled feedback mimics Ideal Protocol **II** correctly. Therefore, although the average evolution Flux Protocol **II** performs somewhat less well than using no feedback, this is actually desirable. As before, the limiting factor of Flux Protocol **II** is the necessary passage of the Bloch vector through non-optimal regions. Whereas Charge Protocol **II** approximates $S_{average} = 1$ throughout the purification process, figure 5.24 shows the Bloch vector is constrained within two conical regions near to the measurement axis (z-axis) and within these regions the average incremental change of impurity is still reduced by several orders of magnitude.

5.9.2 Distribution of remaining impurities

An alternative method for measuring the success of stochastic purification processes is to determine the spread of remaining impurities after a given amount of time. Certainly, when the Bloch vector is close to the centre of the Bloch sphere there exists a significant possibility that the vector will remain near the centre, equally attracted to both measurement outcomes. Therefore the qubit may fail to sufficiently purify within the alloted time. This would present a significant risk for the successful operation of a practical quantum computer. Figure 5.28 shows the distribution of impurities at $t = 7.5$ns, which is the time at which the impurity under Ideal Protocol **I** reaches 5×10^{-3}. The probability density is calculated from 50,000 qubit evolutions separated into 50 logarithmically spaced bins.

Comparing figures 5.28A and 5.28F we see a dramatic difference in the spread of values by many orders of magnitude. The deterministic natures of both Ideal Protocol **I** and the reduced stochasticity of the two more practical **I** protocols

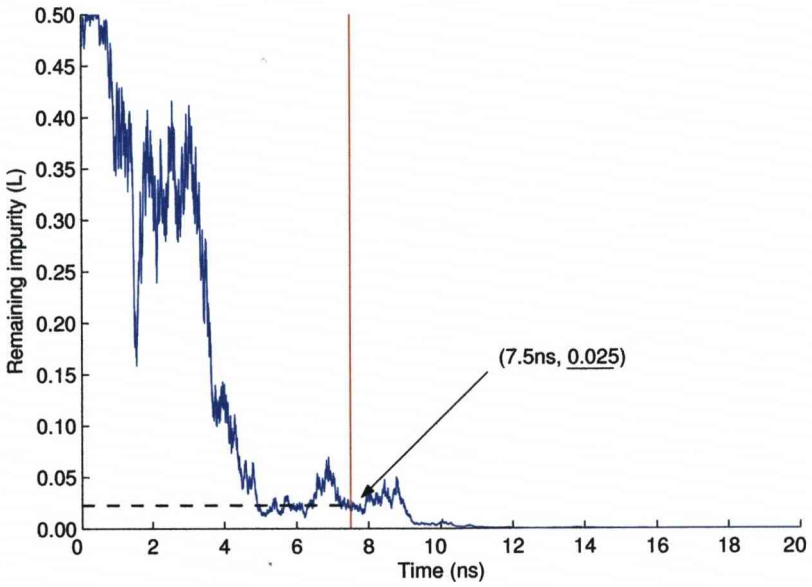

Figure 5.27: The purity at any given time is of considerable interest as the stochastic evolution yields the possibility of failure to purify.

can easily be observed. Of particular interest is the area corresponding to high impurity indicated by the arrow. In figure 5.28D this region is mostly unoccupied, but the other three histograms which do not employ protocol **I** have high occupancy. This implies that although these three methods can potentially reach very low impurities, it is done at the risk of ending with a high impurity.

Interestingly, figure 5.28B follows a similar profile to figure 5.28A until the impurity is of the order 10^{-4}, when smaller impurities become inaccessible. This is due to a *mushrooming* effect which creates an end-cap to the expected path of the Bloch vector (Figure 5.22 shows two such end-caps). The end-cap occurs whenever the Bloch vector is near a pole at the surface of the Bloch sphere and is due to the weak measurement noise not shown in the expected path (Fig. 5.21). This can be further explained by examining the equation for the radial displacement of the Bloch vector due to weak measurement 5.11. Applying the case when the Bloch vector is near a z-axis pole, it can be seen that as $|z|$ approaches one, the random contribution of the Weiner increment becomes much larger, but if $r = 0$ this has no effect. However, as the radial distance from the z-axis is now non-zero (due to the off-axis rotations removing the Bloch vector from the z-axis), the 'large' random changes in dr combined with the constant rotation due to Hamiltonian evolution makes it naturally improbable that the Bloch vector will again settle exactly on the z-axis. Hence, in practice access to the smallest impurities may be difficult without increasing the measurement strength γ.

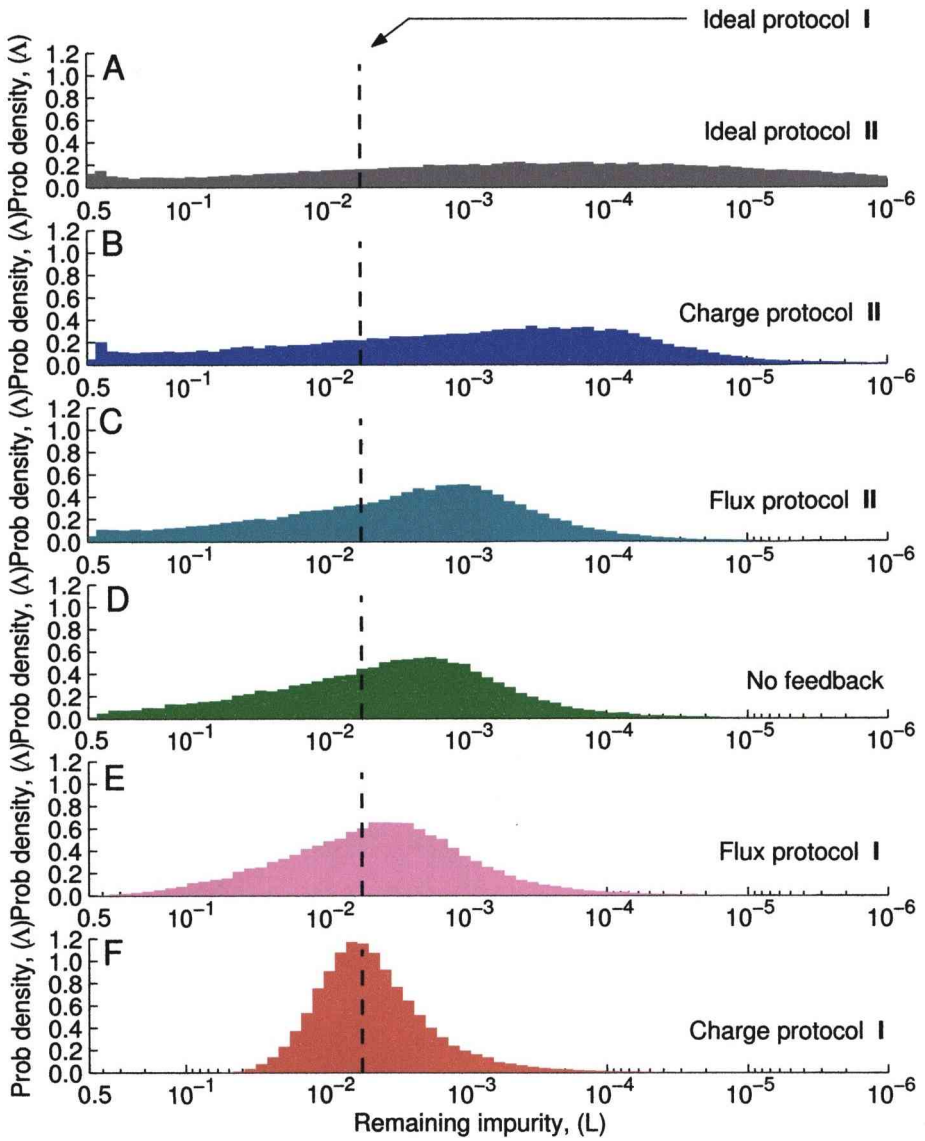

Figure 5.28: Distribution of times to purify to $L = 1 \times 10^{-3}$. The majority of the qubits in an ensemble are quickly purified under the version **II** protocols. However it is most important to understand (for A,B,C and D) that a significant number are not purified at all after 20ns of purification, as indicated by '$>$ 20ns'.

As stated in the previous section, the case of no feedback combines the long tailed property of Ideal Protocol **II** with the peaked response of the deterministic Ideal Protocol **I**, due to the momentary passage of the Bloch vector through both the z-axis and the xy-plane.

5.9.3 Numerical simulation issue

The measurement strength γ and simulation time step dt, are limiting factors concerning the numerical simulation of very small impurities whenever the Bloch vector is away from the z-axis poles. Assuming the Bloch vector is at $[x, y, z] = [1, 0, 0]$, as z=0 the familiar equations reduce to:

$$dz = \sqrt{(8g)}dW \tag{5.72}$$

$$dL = -\frac{1}{2}(dz)^2 = L \tag{5.73}$$

it can be seen that the changes in dz (and therefore dL) can only be made smaller by reducing the size of the simulation timestep dt, or the measurement strength γ. However, reducing either of these variables would increase the number of simulation steps required to reach the simulation end-time. The computational resources available limit the number of simulation steps to approximately 400000 steps per evolution and therefore with a total simulation time of 20ns, $dt = 5 \times 10^{-14}$. Numerical simulations show that this limits the resolution of the remaining impurity to the order of 10^{-5}. The gains obtained by using $dt = 5 \times 10^{-20}$ appears minimal.

The exception to this problem is Ideal Protocol **II**, as by equation 5.12 the stochastic changes in dz decrease as z tends to 1. Therefore this protocol can be successfully simulated to extremely low impurity values, and as shown in figure 5.29 the analytical expression for the probability density (Eq. 5.68) fits the numerically calculated distribution.

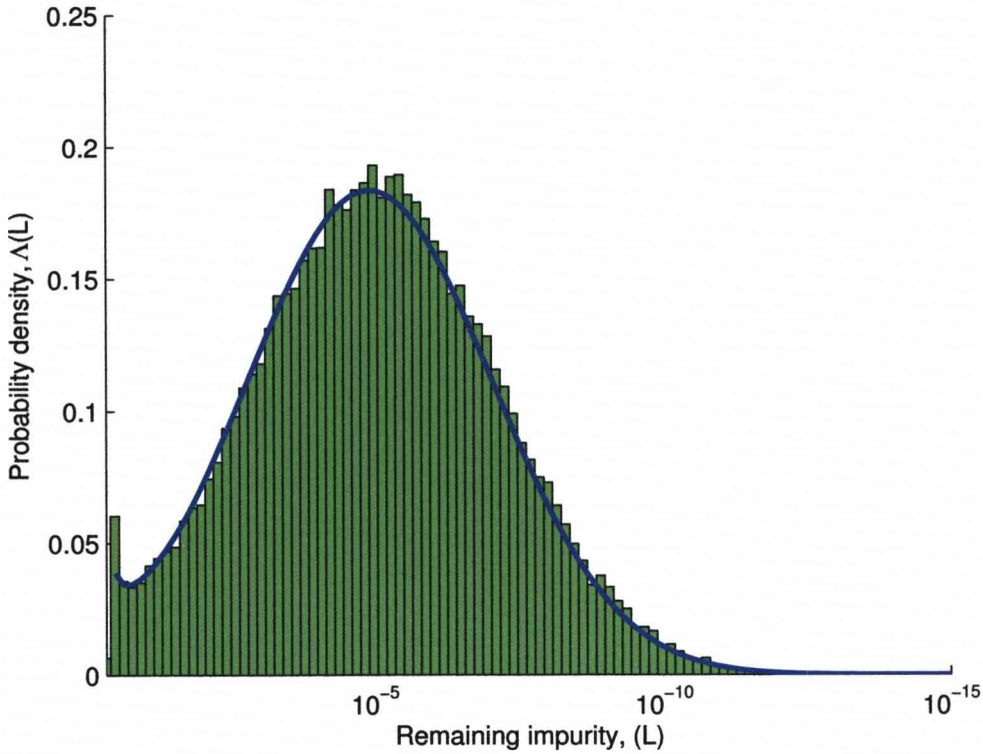

Figure 5.29: The analytical solution (Blue line) as determined by Wiseman and Ralph, fits the numerical simulation of Ideal Protocol **II** well. It was found that numerical simulation of the other protocols proved difficult for small impurities due to the nature of the weak measurement model.

5.9.4 Distribution of final purification times

To determine the spread of purification times, and thereby providing one estimate of the reliability of the feedback protocol, the time of first passage is used as a measure. The time of first passage is defined to be the time at which the measured quantity first crosses a predefined boundary (Fig. 5.30), in this case when the impurity first falls below a set threshold of $L = 1 \times 10^{-3}$. I.e. the time at which the qubit has been purified to 99.9%. Depending on the measurement outcome, the impurity of the qubit may *increase* above the threshold again, however any subsequent purification through the threshold is ignored. Due to the measurement noise, threshold crossing occurs stochastically, and for the many qubits used in the ensemble, a distribution of purification times can be constructed.

Figure 5.31A shows the widest range of purification times is only possible under Ideal Protocol **II**, in complete contrast to the deterministic result of Ideal Protocol **I** (Dark dashed line). It can be clearly seen from the skewed distribution, that the majority of qubits in the ensemble purify faster than the average, this

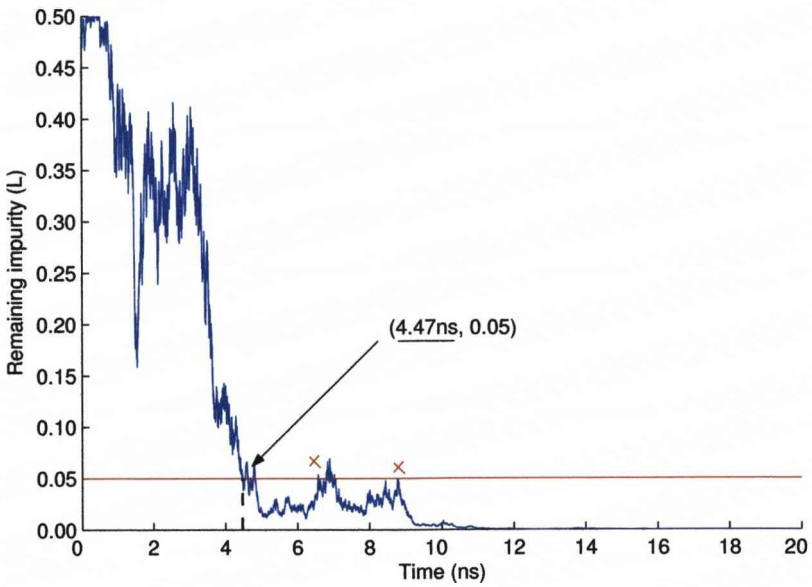

Figure 5.30: The time of first passage is the time to first reach a predetermined level of purity (Horizontal line). Subsequent increases and decreases of impurity are ignored.

is the main result from Wiseman and Ralph. Whereas Jacobs' considered only average values, it was determined that the average purification time for Ideal Protocol **II** is distorted by the existence of a significant number of qubits which do not purify [2], as indicated in figure 5.31 by '> 20ns' (exceeded the total simulation time).

Charge Protocol **II** appears to perform with near optimal results, as the distribution is very similar to the ideal. The collection of feedback protocols that can only rotate the Bloch vector in the yz-plane about the x-axis, include both Flux Protocols **I** and **II** (changing rotational frequency) in addition to the no feedback case where the rotational frequency is constant throughout the Bloch sphere, producing three similar but gradually changing figures 5.31C, 5.31D and 5.31E. The transition from the **II** protocols to the **I** schemes is readily apparent, however even the no feedback case is still a reasonable approximation to Ideal Protocol **II**. Indeed, to significantly reduce spread of purification times it is necessary to employ Charge Protocol **I**, however as this protocol momentarily utilises the no feedback condition, this determinism is somewhat limited.

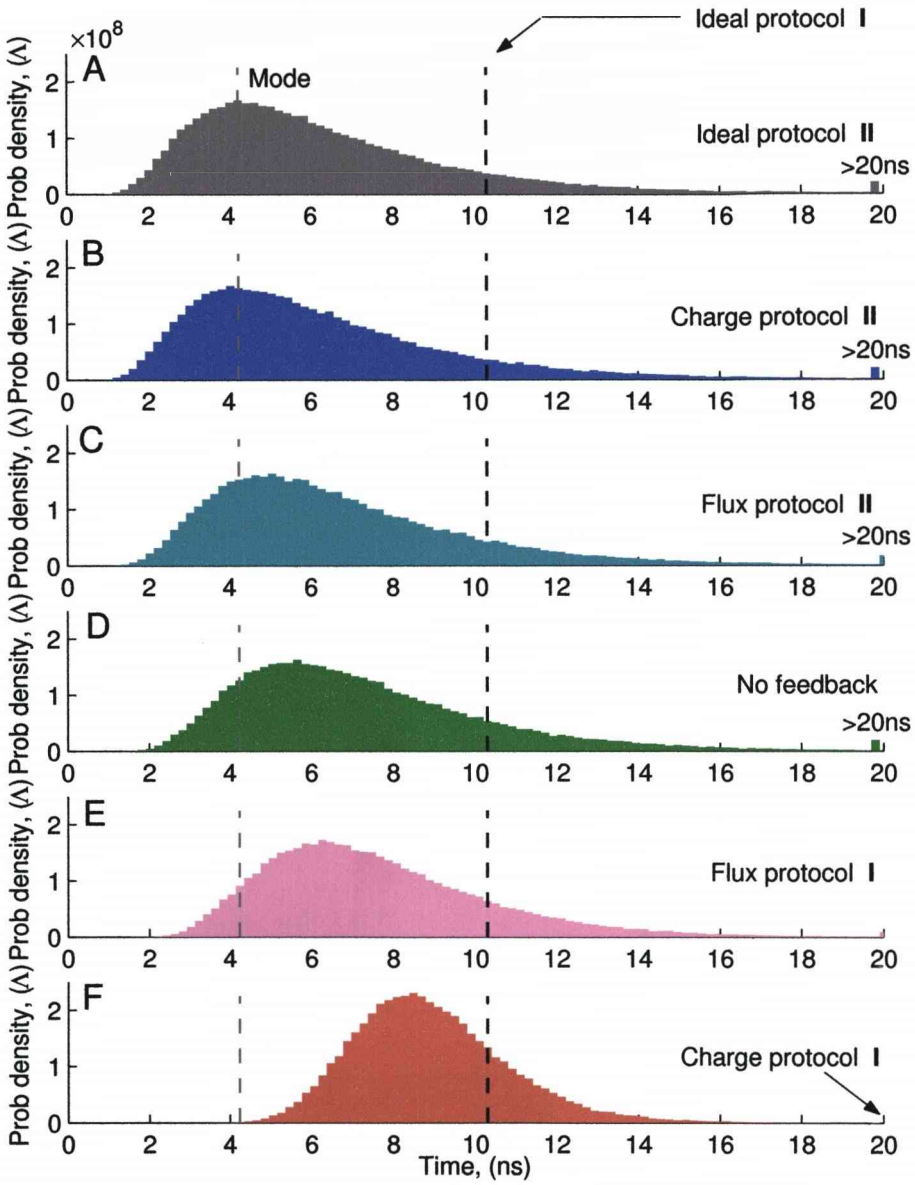

Figure 5.31: Distribution of times to purify to $L = 1 \times 10^{-3}$. The majority of the qubits in an ensemble are quickly purified under the section **II** protocols. However it is most important to understand (for A,B,C and D) that a significant number are not purified at all after 20ns of purification, as indicated by '> 20ns'.

Comparing the average times of first passage against that of Ideal Protocol **I** allows the performance increase of each protocol to be better quantified. Therefore, in addition to plotting histograms, it is also possible to perform a similar analysis to section 5.9.1, although in this case the worst performing protocol is: Ideal Protocol **I** - *Perfect feedback of the Bloch vector to the plane orthogonal to the measurement axis.*

$$S_{first}(L) = \frac{T_{ideal\ \mathbf{I}}(L)}{T_{test}(L)} \tag{5.74}$$

$$L_{ideal\ \mathbf{I}}(t) = 0.5\ e^{-8\gamma t} \tag{5.75}$$

Plotting the "speed-up" as a function of the remaining impurity yields a characteristic similar in shape to figure 5.26.

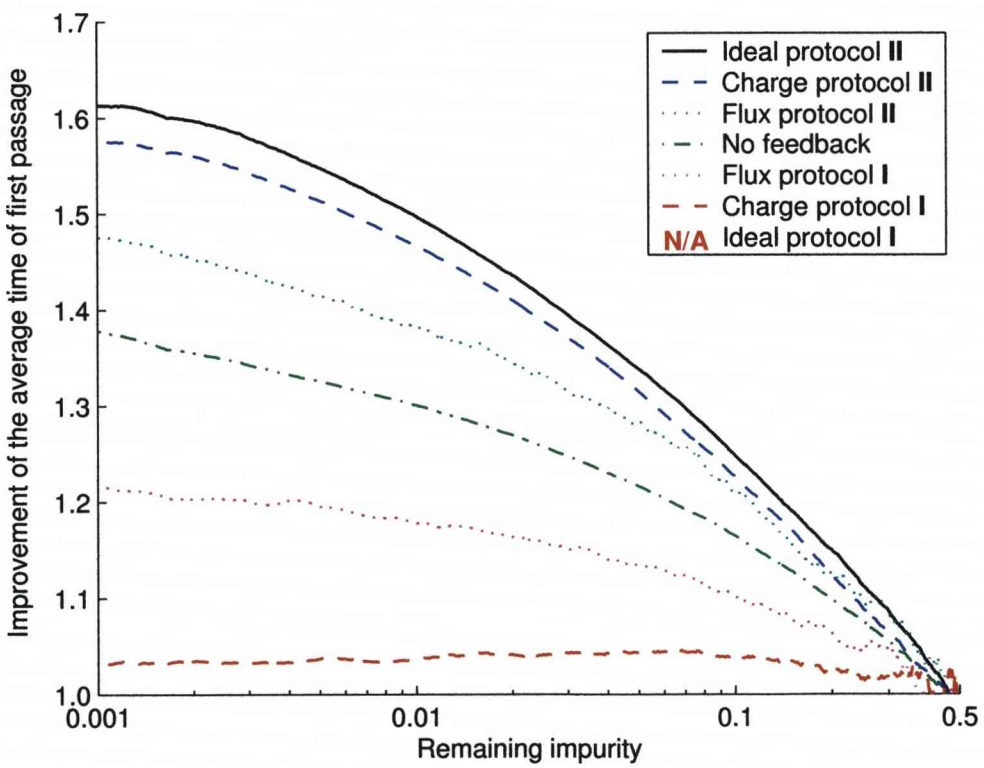

Figure 5.32: The improvement of the average time of first passage as a function of the remaining impurity.

The optimality of Charge Protocol **II** can be immediately seen, with the ordering of the feedback protocols being reversed in comparison with figure 5.26. The average time to reach an impurity of $L = 1 \times 10^{-3}$ is reduced by approximately 60% if either Ideal or Charge Protocol **II** is used.

5.9.5 Protocol specific results

Under Charge Protocol **I**, the Bloch vector takes a relatively complex path therefore a basic analysis of the robustness of the protocol has been performed. The test focuses on the improvement in the average purification rate given systematic errors within the feedback trigger, which could be caused by a combination of errors in the measurement of the z-axis and/or application of the z-control.

Figure 5.33 shows the influence of the thresholding value z_{Limit} on the improvement in the average purification rate. There is indeed an optimum value, however there is also a significant plateau where the improvement is not greatly affected by the value of the thresholding, which would suggest that if there were fluctuations in the accuracy of the thresholding there would be little reduction in performance.

Similarly, figure 5.34 plots the improvement in the average purification rate for the case when the control pulse is applied late at phase delay θ, but with a pulse shape that was designed using values at $\theta = 0^o$. The optimal value of $z_{\text{Limit}} = 0.33$ was used. The phase delay is taken around the x-axis with angular frequency $\omega_z = E_J/\hbar$ as this is the natural rotation of the Bloch vector with no feedback. Ideally, the feedback pulse should be start at $\theta = 0^o$ to achieve the maximum performance however it can be clearly seen that the this level of performance can be obtained until $\theta \approx 45^o$. It is at this point ($\theta \approx 45^o$) that the feedback pulse, that was calculated at $\theta \approx 0^o$, starts to take the vector through the xy-plane and away from the optimal region. Indeed, when $\theta = 90^o$ the Bloch vector starts on the xy-plane and the feedback pulse takes the vector the maximum distance outwards, reversing the very purpose of the protocol.

In addition, the sizable inter-pulse separations are previously indicated by figure 5.16 imply that the application of the feedback pulse can be delayed entire cycles if necessary which corresponds to a change of z_{Limit} as per figure 5.33. The main requirement is the synchronisation with the z-axis, which is quite forgiving as figure 5.34 shows this needs to be within the first 45 degrees of a cycle.

With further regard to the phase delay, it could be possible to apply the feedback pulse at $\theta = 180^o$ if the z-rotation were reversed ($n_g < 0.5$) to take the Bloch vector on to the x-axis. Although applying corrective feedback half a cycle earlier or later will not affect the overall performance and would add unnecessary complication.

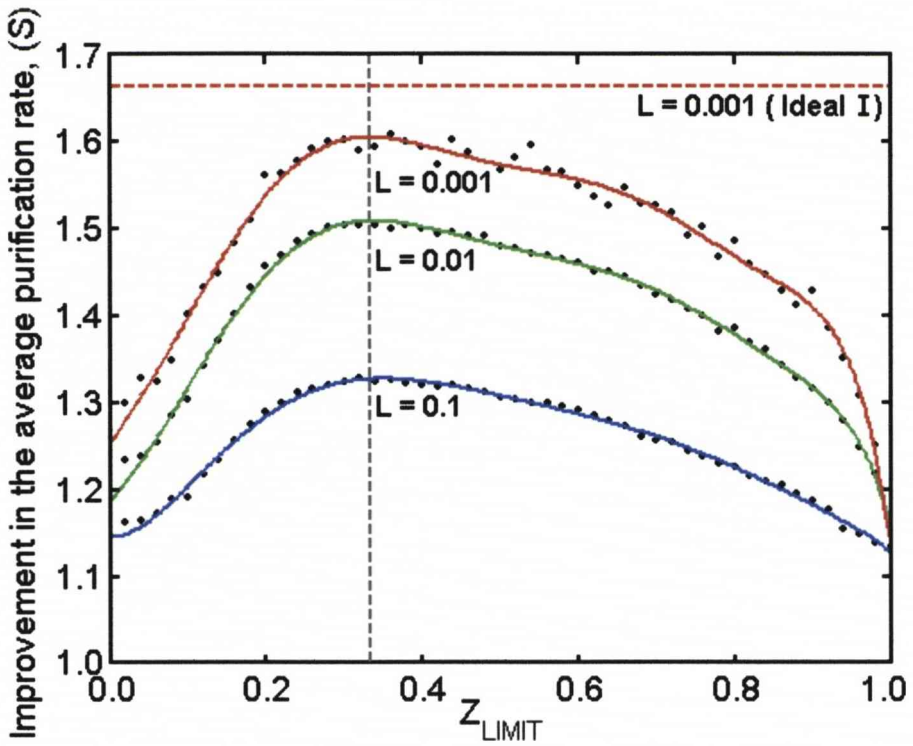

Figure 5.33: Improvement in the average purification rate as a function of z_{Limit} at different levels of impurity.

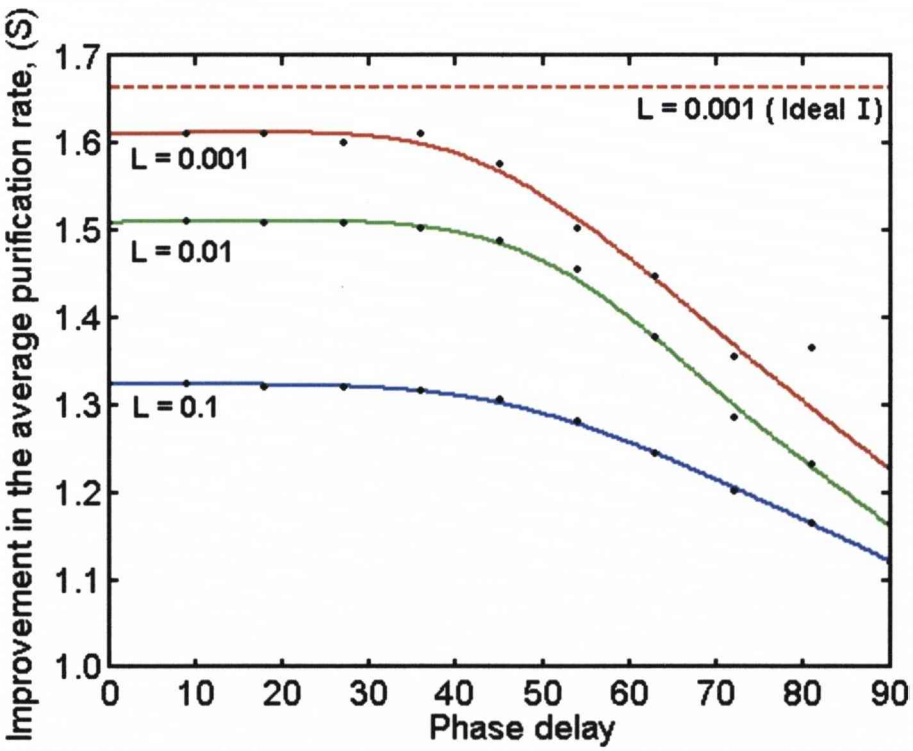

Figure 5.34: Improvement in the average purification rate where the actual application of the feedback pulse is phase-delayed (at the Josephson frequency) starting with $\theta = 0^o$ at the positive z-axis.

5.10 Summary

For each 'Ideal Protocol' devised by Jacobs, Wiseman and Ralph, we have proposed two feedback protocols which would be somewhat more practical to implement, given the available charge (σ_z) and flux (σ_x) controls available for a superconducting charge qubit.

Each feedback protocol is useful, albeit for specific requirements. Although the protocols exhibit advantages in purification speed and reduced stochasticity, these properties are somewhat mutually exclusive. It is the decision of the experimentalist to decide if he or she requires **all** the qubits in the ensemble to gradually purify, or allow the majority of qubits to purify quickly at the **risk** of a number or unpurified qubits remaining. Choosing either a **I** protocol or **II** protocol respectively.

The simulations of each feedback protocol suggest that the charge controlled feedback yield the best performance when attempting to implement rapid state purification within the constraints of a charge qubit system. The significant disadvantage of the flux control schemes is the limitation of only using a single axis of rotation (σ_x) such that the Bloch vector must pass through both the measurement axis and the plane orthogonal to the measurement axis, each of which could be considered optimal or non-optimal dependent on the type of feedback, **I** or **II**. In contrast, the bias charge n_g controls σ_z rotations, combined with the Joesphson tunneling (σ_x) this permits a second axis of rotation which aids in constraining the Bloch vector close to the optimal regions whilst avoiding passage through the non-optimal areas by rotating the Bloch vector out of the nominal yz-plane of rotation and into the previously unused regions of the Bloch sphere.

It is expected that the proposed routines could also be adapted to other quantum information processing technologies that can generate continuous rotations about an axis orthogonal to the measurement axis. The most interesting benefit would be a class of purification protocols that only require modification of a single control field, with the measurement of a single axis.

Protocol	Increase in the average purification rate @ $L=1x10^{-3}$	Increase in the average time of first passage @ $L=1x10^{-3}$	Advantages	Disadvantages
Ideal Protocol **II**	0%	62%	• Fastest available purification. • Highest purity achievable. • Simple, if no Hamiltonian present.	• Final purities vary over many orders of magnitude. • Qubit may not purify at all.
Charge Protocol **II**	3%	58%	• Good approximation of Ideal protocol **II** to some extent. • Single control field is used.	• Can not reach very small levels of impurity due to Hamiltonian. • Very strong controls required.
Flux Protocol **II**	8%	48%	• Reasonable approximation of Ideal protocol **II** • Single control field of practical magnitude.	• Can not reach small impurity • Control field needs to switch four times per tunnelling cycle.
No Feedback	24%	38%	• Combines properties of both types of feedback protocol. • No controls are required.	• No distinct advantage is gained
Flux Protocol **I**	38%	22%	• Reasonable approximation of Ideal protocol **I** • Single control field of practical magnitude.	• Remaining impurity still varies over a wide range of values. • Control field needs to switch four times per tunnelling cycle.
Charge Protocol **I**	60%	4%	• All qubits will purify. • Slow control pulses, applied through a single control	• Timing is important • Not fully deterministic, as it uses "no feedback" temporarily.
Ideal Protocol **I**	67%	0%	• All qubits will purify. • Slow control pulses, applied through a single control	• Fast and accurate control field required. • Measurement of other axes may also be required.

Figure 5.35: Table of the advantages and disadvantages of each feedback protocol, in addition to average performance improvements expressed as a percentage of the relevant worst case protocol (indicated as 0%).

Chapter 6

Conclusions

The overall goal of quantum computing is to make a quantum computer that can be mass marketed to the general public. Unfortunately, this is not likely to happen for many decades, where currently even simple laboratory experiments prove difficult, especially for solid state quantum computation compared with the competing technologies. However, on the path leading to the construction of quantum computers a great many problems will need to be solved, whose solutions may have application *in other areas* even if it eventually proves impossible to build a computer.

To help introduce an engineer to quantum theory we have provided chapter 2 which includes in the authors opinion, a description of the essentials required to understand this thesis whilst avoiding the heavy mathematics and materials which can be explored further in a physics textbook.

The technology we have investigated is the superconducting charge qubit (Cooper pair box) where the island can be coupled by either one or two junctions dependent on the need for flux control. The charge qubit is modelled as an electrical circuit whose Hamiltonian is then quantised to a matrix form for computer simulation. The circuit Hamiltonian was obtained using a loop analysis technique recently proposed for superconducting charge qubits by Burkard, whereby the Hamiltonian is determined by a well defined process and in a consistent manner.

The results of this thesis concerns two subjects, the characterisation and purification of a charge qubit, both are important but sometimes overlooked areas. Stochastic quantum processes are a recurrent theme of this thesis, the dissipative model for the characterisation work uses stochastic Schrödinger equations whilst

the purification work employs a weak measurement theory that is modelled using a stochastic master equation.

Characterisation covers a very wide range of parameters, however we have focused on how the frequency spectrum of biasing circuity can be used to obtain the qubit energy level structure and how additional frequencies can be created by the use of a biasing circuit with an unusually high resonant frequency. This biasing circuit behaves as an RLC oscillator which for this work has been modelled as a classical dampened second order differential equation, and also as a quantised simple harmonic oscillator in which case the dissipation has been implemented using stochastic processes called 'quantum trajectories' [118]. The main objective of this work is to minimise the hardware requirements and hence the externally coupled environment, by using the control fields already in place to estimate the qubit behaviour.

Chapter 4 of this thesis exploits the so called 'backreaction effect' of a coupled system, which allows the bias dependent noise properties of the qubit to drive the coupled biasing circuity, this behaviour of the oscillator circuit should be experimentally accessible allowing the qubit to be potentially characterised without direct measurement. When the qubit is correctly biased with a continuous microwave drive of known frequency, the qubit undergoes Rabi oscillations and is then likely to occupy the excited state where quantum jumps back to the ground state may occur. These discontinuous jumps create broadband noise in the qubit which is coupled back to drive the oscillator circuit at the resonant frequency, thereby increasing the noise power observed at the oscillator frequency. This increase in oscillator power can therefore be used as an indication of a correctly biased system and thereby linking the known microwave frequency (now known to be equal to the qubit energy gap) with a known bias at the laboratory signal generator.

The second part of chapter 4 investigated the use of a biasing circuit with a higher than usual resonant frequency. This was found to mix with the with the microwave drive to create a sideband that is sufficiently strong so this in turn mixes with the Rabi oscillations shifting the Rabi frequency into two side bands centred on $F_{mw} - F_{osc}$. Therefore, the Rabi frequency can be estimated from measurements made in a redefineable bandwidth by suitable selection of the microwave or oscillator frequency. In addition, for large amplitude microwave drive or small microwave oscillator frequency difference, there is a small but distinct splitting at $F_{mw} - F_{osc}$ that indicates (using a discontinuity) when the Rabi

frequency is equal to $F_{mw} - F_{osc}$, also the separation of the split peaks is a maximum when the Rabi oscillations are of maximum amplitude. This minor splitting therefore links the three major frequencies of interest (microwave, oscillator and Rabi) and also the bias required for the microwave transition.

Purification is a rather more specific task, maximising the confidence in the qubit state being the true qubit state from a probabilistic (classical) mixture of pure states. For projective measurements a system purifies instanteously, however the incremental and stochastic nature of weak measurement means the system purifies slowly or even not at all. We have interpreted purification as a geometric problem in Bloch coordinates and have investigated Jacob, Wiseman and Ralph's discovery that the rate at which as system purifies under weak measurement can be quantum mechanically accelerated through the use of quantum feedback. This work is the main focus of the thesis and has yielded several algorithms for implementing these optimal protocols for a charge qubit. The charge qubit has a constant x-axis rotation due to the σ_x term of the qubit Hamiltonian and only limited control over z-axis rotations, with the z-axis being the axis of measurement.

Chapter 5 first examines Jacobs' optimal feedback protocol for maximising the *average purification rate* for an ensemble of generic qubits. This involves returning the Bloch vector back onto the plane orthogonal (xy) to the axis of weak measurement (z) after each measurement step, which given control over all axes and infinite Hamiltonian resources is trivial to solve. However given the constant x-axis rotations of a charge qubit Hamiltonian, the Bloch vector is always taken away from the optimal xy-plane. We have first devised a flux controlled protocol that changes the x-axis rotational frequency to slow the Bloch vector as it passes near the xy-plane and speed it through the non-optimal z-axis poles. Alternatively, using a charge control (bias voltage) yielded near optimal results ($\approx 80\% - 90\%$), by using pulsed rotations about the z-axis it is possible to return the Bloch vector near to the x-axis, as this region is invariant to x-rotations the Bloch vector tends to stay near the xyplane for a much longer duration, increasing the average purification rate. The feedback is a simple π-pulse applied occasionally to return the Bloch vector whenever it strays too far from the xy-plane due to the z-axis meaurement.

The latter part of chapter 5 examines the recently proposed Wiseman and Ralph protocol that resulted from questioning if it is best to maximise the purification rate of the *ensemble average* (Jacobs') or to maximise the purification

rate of *individual qubits* (Wiseman and Ralph). By rotating the Bloch vector onto the measurement axis after each measurement step, the purification rate of individual qubits is faster although the ensemble average purifies slower. The constant x-axis rotations of a charge qubit Hamiltonian moves the Bloch vector away from the optimal region, in this case the z-axis. To correct for this the previous flux protocol was reversed such that the passage of the Bloch vector is slowed through the z-axis and sped through the xy-plane. However for better results, a very simple charge control protocol was designed to lock the path of the Bloch vector in a tight spiral rotating near parallel to the z-axis for the majority of the purification time.

Bibliography

[1] K. Jacobs, "How to project qubits faster using quantum feedback," *Phys. Rev. A* **67**, p. 030301(R), 2003.

[2] H. M. Wiseman and J. F. Ralph, "Reconsidering rapid qubit purification by feedback," *New J. Phys.* **8**, p. 90, 2006.

[3] H.-A. Engel, L. P. Kouwenhoven, D. Loss, and C. M. Marcus, "Controlling spin qubits in quantum dots," *Quantum Information Processing* **3**, pp. 115–132, 2002.

[4] J. Gorman, D. G. Hasko, and D. A. Williams, "Charge-qubit operation of an isolated double quantum dot," *Phys. Rev. Lett.* **95**, p. 090502, 2005.

[5] J. H. Jefferson, M. Fearn, D. L. J. Tipton, and T. P. Spiller, "Two-electron quantum dots as scalable qubits," *Phys. Rev. A* **66**, p. 042328, 2002.

[6] J. E. Mooji, T. P. Orlando, L. Levitov, L. Tian, C. H. van der Wal, and S. Lloyd, "Josephson persistent-current qubit," *Science* **285**, p. 1036, 1999.

[7] D. W. Utami, H. Goan, and G. J. Milburn, "Charge transport in a quantum electromechanical system," *Phys. Rev. B* **70**, p. 075303, 2004.

[8] K. Bladh, T. Duty, D. Gunnarsson, and P. Delsing, "The single cooper-pair box as a charge qubit," *New J. Phys.* **7**, p. 180, 2005.

[9] R. Feynman, "Simulating physics with computers," *International Journal of Theoretical Physics* **21**, p. 467, 1982.

[10] www.magiqtech.com, "Magiq technologies," 10/04/2007.

[11] R. Rivest, A. Shamir, and L. Adleman, "A method for obtaining digital signatures and public-key cryptosystems," *Communications of the ACM* **21**, p. 120126, 1978.

[12] D. Deutsch and R. Jozsa, "Rapid solutions of problems by quantum computation," *Proceedings of the Royal Society of London, Series A* **439**, p. 553, 1992.

[13] P. W. Shor, "Polynomial-time algorithms for prime factorization and discrete logarithms on a quantum computer," *SIAM J.Sci.Statist.Comput.* **26**, p. 1484, 1997.

[14] L. Grover, "Quantum mechanics helps in searching for a needle in a haystack," *Phys. Rev. Lett.* **79**, p. 325, 1997.

[15] M. Nielsen and I. Chuang, *Quantum Computation and Quantum Information*, Cambridge University Press, 2000.

[16] L. M. K. Vandersypen, M. Steffen, G. Breyta, C. S. Yannoni, M. H. Sherwood, and I. L. Chuang, "Experimental realization of shor's quantum factoring algorithm using nuclear magnetic resonance," *Nature* **414**, p. 883, 2001.

[17] J. I. Cirac and P. Zoller, "Quantum computations with cold trapped ions," *Phys. Rev. Lett.* **74**, pp. 4094–4097, 1995.

[18] D. Leibfried, B. DeMarco, V. Meyer, M. Rowe, A. Ben-Kish, M. Barrett, J. Britton, J. Hughes, W. M. Itano, B. M. Jelenkovic, C. Langer, D. Lucas, T. Rosenband, and D. J. Wineland, "Towards quantum information with trapped ions at nist," *J. Phys. B* **36**, pp. 599–612, 2003.

[19] A. Steane, "The ion trap quantum information processor," *Applied Physics B: Lasers and Optics* **64**, pp. 623–643, 1997.

[20] B. Brkic, S. Taylor, J. F. Ralph, and N. France, "High-fidelity simulations of ion trajectories in miniature ion traps using the boundary-element method," *Nature* **73**, p. 012326, 2006.

[21] N. Yu, H. Dehmelt, and W. Nagourney *Proc. Natl Acad. Sci* **86**, p. 5672, 1989.

[22] N. Nakamura, J. Asada, F. J. Currell, T. Fukami, T. Hirayama, K. Motohashi, T. Nagata, E. Nojikawa, S. Ohtani, K. Okaaki, M. Sakurai, H. Shiraishi, S. Tsurubuchi, and H. Watanabe, "An overview of the tokyo electron beam ion trap," *Physica Scripta.* **T73**, pp. 362–364, 1997.

[23] F. Bloch, "Nuclear induction," *Phys. Rev.* **70**, p. 460, 1946.

[24] S. Lloyd, "A potentially realizable quantum computer," *Science* **261**, p. 1569, 1993.

[25] B. E. Kane, "A silicon-based nuclear spin quantum computer," *Nature* **393**, p. 6681, 1998.

[26] J. A. Weil and J. R. Bolton, *Electron Paramagnetic Resonance : Elementary Theory and Practical Applications*, John Wiley and Sons, 2007.

[27] C. R. Myers and R. Laflamme, "Linear optics quantum computation: an overview," *quant-ph/0512104* , 2005.

[28] Q. A. Turchette, "Measurement of conditional phase shifts for quantum logic," *Phys. Rev. Lett.* **75**, p. 4710, 1995.

[29] D. Loss and D. P. DiVincenzo, "Quantum computation with quantum dots," *Phys. Rev. A* **57**, p. 120, 1998.

[30] J. Q. You, J. S. Tsai, and F. Nori, "Scalable quantum computing with josephson charge qubits," *Phys. Rev. Lett.* **89**, p. 197902, 2002.

[31] M. Wulf, T. A. Ohki, Z. Xingxiang, and M. J. Feldman, "Dressed states of josephson phase qubit coupled to an LC circuit," *IEEE trans. appl. supercond.* **15**, pp. 856–859, 2005.

[32] M. J. Everitt, T. D. Clark, P. B. Stiffell, A. Vourdas, J. F. Ralph, R. J. Prance, and H. Prance, "Superconducting analogues of quantum optical phenomena: Macroscopic quantum superpositions and squeezing in a squid ring," *Phys. Rev. A* **69**, p. 043804, 2004.

[33] D. Vion, A. Aassime, A. Cottet, P. Joyez, H. Pothier, C. Urbina, D. Esteve, and M. H. Devoret, "Manipulating the quantum state of an electrical circuit," *Science* **296**, pp. 886 – 889, 2002.

[34] M. Buttiker, "Zero-current persistent potential drop across small-capacitance josephson junctions," *Phys. Rev. B* **36**, pp. 3548–3555, 1987.

[35] I. L. Aleiner, P. W. Brouwer, and L. I. Glazman, "Quantum effects in coulomb blockade," *Phys. Rep.* **358**, pp. 309–440, 2002.

[36] I. L. Aleiner, P. W. Brouwer, and L. I. Glazman, "Reading out charge qubits with a radio-frequency single-electron-transistor," *Phys. Rep.* **358**, pp. 309–440, 2002.

[37] Y. Nakamura, Y. A. Pashkin, and J. S. Tsai, "Coherent control of macroscopic quantum states in a single cooper-pair box," *Nature* **398**, pp. 786–788, 1999.

[38] Y. A. Pashkin, T. Yamamoto, O. Astafiev, Y. Nakamura, D. V. Averin, and J. S. Tsai, "Quantum oscillations in two coupled charge qubits," *Nature* **421**, p. 823, 2003.

[39] W. G. Teich, "Structural basis of multistationary quantum systems. ii. effective few-particle dynamics," *Phys. Rev. B* **37**, pp. 8111–8121, 1987.

[40] D. V. Averin and V. J. Goldman, "Quantum computation with quasiparticles of the fractional quantum hall effect," *Solid State Communications* **121**, pp. 25–28, 2001.

[41] D. DiVincenzo and D. Loss, "Quantum information is physical," *arXiv:cond-mat/0411174* , 1998.

[42] C. J. Isham, *Lectures on Quantum Theory*, Imperial College Press, 1995.

[43] F. Mandl, *Quantum Mechanics*, John Wiley and Sons, 2001.

[44] D. T. Gillespie, *A quantum mechanics primer*, International textbook company, 1983.

[45] R. Eisberg and R. Resnick, *Quantum Physics of Atoms, Molecules, Solids, Nuclei and particles*, John Wiley and Sons, 1985.

[46] A. Sudbery, *Quantum mechanics and the particles of nature*, Cambridge University Press, 1986.

[47] M. O. Scully and M. S. Zubairy, *Quantum Optics*, Cambridge University Press, 1997.

[48] J. Samuel J. Lomonaco, *Proceedings of Symposia in Applied Mathematics*, vol. 58, American Mathematical Society, 2002.

[49] C. D. Hill and J. F. Ralph, "Weak measurement and rapid state reduction in bipartite quantum systems," *arXiv:quant-ph/0610156v2* , 2006.

[50] D. McMahon, *Quantum Mechanics Demystified*, Mc Graw Hill, 2006.

[51] W. Heisenberg, "Ueber den anschaulichen inhalt der quantentheoretischen kinematik and mechanik," *Zeitschrift fr Physik* **43**, pp. 172–198, 1927.

[52] Y. Q. Li and B. Chen, "Quantum theory for mesoscopic electric circuits," *Phys. Rev. B* **53**, p. 4027, 1996.

[53] I. L. Aleiner, P. W. Brouwer, and L. I. Glazman, "Quantum mechanical computers," *Foundations of Physics* **16**, p. 507, 1986.

[54] M. D. Srinivas and E. B. Davies, "Quantum theory for mesoscopic electric circuits," *Opt. Acta* **28**, p. 981, 1981.

[55] M. D. Srinivas and E. B. Davies, "Quantum theory for mesoscopic electric circuits," *Opt. Acta* **29**, p. 235, 1982.

[56] L. Diosi, "Stochastic pure state representation for open quantum systems," *Phys. Rev. Lett.* **114**, p. 451, 1986.

[57] G. Lindblad, "On the generators of quantum dynamical semigroups," *Communications in Mathematical Physics* , 1976.

[58] N. Gisin, T. A. Brun, and M. Rigo, "From quantum to classical: the quantum state diffusion model," *arXiv:quant-ph/9611002v1* , 1996.

[59] H. M. Wiseman, "Optimal unravellings for feedback control in linear quantum systems," *Phys. Rev. Lett.* **94**, p. 070405, 2005.

[60] A. O. Caldeira and A. J. Leggett, "Influence of dissipation on quantum tunneling in macroscopic systems," *Phys. Rev. Lett.* **46**, pp. 211–214, 1981.

[61] K. Hornberger, "Introduction to the theory of decoherence," *arXiv:quant-ph/0612118v1* , 2006.

[62] L. Diosi, *Weak measurements in quantum mechanics*, vol. 4 Encyclopedia of Mathematical Physics, 2006.

[63] T. A. Brun, "A simple model of quantum trajectories," *American Journal of Physics* **70**, pp. 719–737, 2005.

[64] S. Habib, *Nonlinear quantum dynamics*, Springer Netherlands, 2006.

[65] J. Wilkie, "Numerical methods for stochastic differential equations," *Phys. Rev. E* **70**, p. 017701, 2004.

[66] K. Jacobs, "Optimal feedback control for the rapid preparation of a qubit," *Proc. SPIE Vol.* **5468**, p. 355, 2004.

[67] G. Burkard, "Circuit theory for decoherence in superconducting charge qubits," *Phys. Rev. B* **71**, p. 144511, 2005.

[68] A. Barone and G. Paterno, *Physics and Applications of the Josephson effect*, A Wiley-Interscience publication, 1982.

[69] H. Kammerlingh-Onnes *Leiden Commun* , p. 120, 1911.

[70] W. Meissner and R. Ochsenfeld *Naturwissen* **21**, p. 787, 1933.

[71] J. Bardeen, L. N. Cooper, and J. R. Schrieffer, "Theory of superconductivity," *Phys. Rev.* **108**, p. 1175, 1957.

[72] B. D. Josephson, "Possible new effects in superconductive tunnelling," *Phys. Letters* **1**, p. 251, 1962.

[73] B. W. Petley, *An Introduction to the Josephson Effects*, Mills and Boon Limited. London., 1965.

[74] J. R. Waldram, A. B. Pippard, and J. Clark, "Theory of the current-voltage characteristics of sns junctions and other superconducting weak links," *Phil. trans. Roy. Soc. Lond.* **268**, p. 265, 1970.

[75] T. G. Blaney, "A simple point-contact josephson junction for use in the millimetre and submillimetre wavelength regions," *J. Phys. E: Sci. Instrum.* **4**, pp. 945–948, 1971.

[76] P. W. Anderson and A. H. Dayem, "Radio-frequency effects in superconducting thin film bridges," *Phys. Rev. Lett.* **13**, p. 195, 1964.

[77] J. Clarke *Phil. Mag.* **13**, p. 115, 1966.

[78] R. P. Feynman, R. B. Leighton, and M. Sands, *The Feynman Lectures on Physics III*, Addison-Wesley, Reading, Mass., 1965.

[79] J. C. Gallop, *SQUIDs, the Josepshon Effects and Superconducting Electronics*, IOP publishing, 1991.

[80] D. V. Averin, "Quantum computation: Solid-state qubits under control," *Nature* **398**, p. 748, 1999.

[81] L. P. Kouwenhoven, G. Schön, and L. L. Sohn *Mesoscopic Electron Transport* **345**, 1997.

[82] W. H. Hayt and J. E. Kemmerly, *Engineering Circuit Analysis*, McGraw-Hill, 1993.

[83] R. J. Smith and R. C. Dorf, *Circuits, Devices and Systems*, John Wiley and Sons, 1992.

[84] T. L. Floyd, *Electronic devices*, Prentice Hall, 1996.

[85] H. Goldstein, *Classical mechanics, Second Edition*, Addison-Wesley, 1980.

[86] E. J. Griffith, C. D. Hill, J. F. Ralph, H. M. Wiseman, and K. Jacobs, "Rapid state purification protocols for a cooper pair box," *Phys. Rev. B* **75**, p. 014511, 2007.

[87] Y. S. Greenberg, E. Il'ichev, and A. Izmalkov, "Low-frequency rabi spectroscopy for a dissipative two-level system," *Europhys. Lett.* **72**, p. 880, 2005.

[88] T. D. Clark, J. Diggins, J. F. Ralph, M. Everitt, R. J. Prance, H. Prance, R. Whiteman, A. Widom, and Y. N. Srivastava, "Coherent evolution and quantum transitions in a two level model of a squid ring," *Ann. Phys.* **268**, pp. 1–30, 1998.

[89] E. Ilichev, N. Oukhanski, A. Izmalkov, T. Wagner, M. Grajcar, H.-G. Meyer, A. Y. Smirnov, A. M. van den Brink, M. H. S. Amin, and A. M. Zagoskin, "Continuous monitoring of rabi oscillations in a josephson flux qubit," *Phys. Rev. Lett.* **91**, p. 097906, 2003.

[90] M. H. Devoret, A. Wallraff, and J. M. Martinis, "Superconducting qubits: A short review," *arXiv:cond-mat/0411174* , 2004.

[91] A. Aassime, G. Johansson, G. Wendin, R. J. Schoelkopf, and P. Delsing, "Radio-frequency single-electron transistor as readout device for qubits: Charge sensitivity and backaction," *Phys. Rev. Lett.* **86**, pp. 3376–3379, 2001.

[92] I. Chiorescu, Y. Nakamura, C. J. P. M. Harmans, and J. E. Mooij, "Coherent quantum dynamics of a superconducting flux qubit," *Science* **299**, pp. 1869 – 1871, 2003.

[93] R. F. Pease, "Semiconductor technology: Imprints offer moore," *Nature* **417**, pp. 802–803, 2002.

[94] H. M. Wiseman and G. E. Toombes, "Quantum jumps in a two-level atom," *Phys. Rev. A* **60**, pp. 2474–2490, 1999.

[95] H. Carmichael, *An Open Systems Approach to Quantum Optics*, An Open Systems Approach to Quantum Optics, by Howard Carmichael. Lecture Notes in Physics, Monographs Series, v.18. Published by Springer-Verlag (Berlin Heidelberg), 1993.

[96] J. F. Ralph, T. D. Clark, T. P. Spiller, and W. J. Munro, "Entanglement generation in persistent current qubits," *Phys. Rev. B* **70**, p. 144527, 2004.

[97] B. A. Turek, K. W. Lehnert, A. Clerk, D. Gunnarsson, K. Bladh, P. Delsing, and R. J. Schoelkopf, "Single-electron transistor backaction on the single-electron box," *Phys. Rev. B* **71**, p. 193304, 2005.

[98] E. Kreyszig, *Advanced Engineering Mathematics, 8th Edition*, John Wiley and Sons, 1999.

[99] E. J. Griffith, J. F. Ralph, and T. D. Clark, "Superconducting qubits and environmental noise," *Proc. AIP* **734**, pp. 401–404, 2004.

[100] J. F. Ralph, T. D. Clark, M. J. Everitt, and P. Stiffell, "Nonlinear backreaction in a quantum mechanical squid," *Phys. Rev. B* **64**, pp. 180504/1–4, 2001.

[101] E. K. Irish, J. Gea-Banacloche, I. Martin, and K. C. Schwab, "Dynamics of a two-level system strongly coupled to a high-frequency quantum oscillator," *Phys. Rev. B* **72**, p. 195410, 2005.

[102] E. T. Jaynes and F. W. Cummings *Proc. IEEE* **51**, p. 89, 1963.

[103] D. K. Ferry, *Quantum Mechanics An Introduction for Device Physicists and Electrical Engineers*, IOP publishing, 2001.

[104] T. P. Spiller, B. M. Garraway, and I. C. Percival, "Thermal equlibrium in the quantum state diffusion picture," *Phys. Lett. A* **179**, pp. 63–66, 1993.

[105] N. Gisin and I. C. Percival, "The quantum-state diffusion model applied to open systems," *J. Phys. A* **25**, p. 5677, 1992.

[106] L. Diosi, "Calderia-leggett master equation and medium temperatures," *Physica A.* **199**, pp. 517–526, 1993.

[107] T. A. Brun, N. Gisin, P. F. O'Mahony, and M. Rigo, "From quantum trajectories to classical orbits," *arXiv:quant-ph/9608038* , 1996.

[108] A. D. Greentree, C. Wei, S. A. Holmstrom, J. P. D. Martin, N. B. Manson, K. R. Catchpole, and C. Savage, "Probing a doubly driven two-level atom," *Journal of Optics B: Quantum and Semiclassical Optics* **1**, pp. 240–244, 1999.

[109] E. J. Griffith, J. F. Ralph, A. D. Greentree, and T. D. Clark, "Spectroscopy of a cooper-pair box in the autler-townes configuration," *Phys. Rev. B* **74**, p. 094510, 2006.

[110] K. Jacobs and D. A. Steck, "A straightforward introduction to continuous quantum measurement," *Contemporary Physics* **47**, pp. 279–303, 2006.

[111] K. Jacobs and P. L. Knight, "Linear quantum trajectories: Applications to continuous projection measurements," *Phys. Rev. A* **57**, p. 2301, 1998.

[112] Y. Makhlin, G. Schon, and A. Shnirman, "Josephson-junction qubits with controlled couplings," *Nature* **398**, pp. 305–307, 1999.

[113] D. Gunnarsson, T. Duty, K. Bladh, and P. Delsing, "Tunability of a 2e periodic single cooper pair box," *Phys. Rev. B* **70**, p. 224523, 2004.

[114] J. F. Ralph, E. J. Griffith, C. D. Hill, and T. D. Clark, "Rapid purification of a solid state charge qubit," *Proc. SPIE Vol.* **6244**, 2006.

[115] J. Combes and K. Jacobs, "Rapid state-reduction of quantum systems using feedback control," *Phys. Rev. Lett.* **96**, p. 010504, 2006.

[116] J. J. DiStefano, A. R. Stubberud, and I. J. Williams, *Schaum's Outline of Feedback and Control Systems*, McGraw-Hill, 1990.

[117] T. Yamamoto, Y. A. Pashkin, O. Astafiev, Y. Nakamura, and J. S. Tsai, "Demonstration of conditional gate operation using superconducting charge qubits," *Nature* **425**, p. 941, 2003.

[118] H. M. Wiseman, "Quantum trajectories and quantum measurement theory," *Quantum Semiclass. Opt.* **8**, pp. 205–222, 1996.